MONTE-CARLO BASED INVESTIGATIONS OF THE RESPONSE OF CLINICAL DOSIMETERS OVER THE FULL RANGE OF FIELD SIZES INVOLVED IN ADVANCED PHOTON-BEAM RADIOTHERAPY TECHNIQUES

By

Sudhir Kumar
PHYS01200904005
Bhabha Atomic Research Centre

A thesis submitted to the
Board of Studies in Physical Sciences

In partial fulfillment of requirements
For the Degree of

DOCTOR OF PHILOSOPHY
of
HOMI BHABHA NATIONAL INSTITUTE

November, 2015

Homi Bhabha National Institute

Recommendations of the Viva Voce Committee

As members of the Viva Voce Committee, we certify that we have read the dissertation prepared by **Sudhir Kumar** entitled '**Monte-Carlo based investigations of the response of clinical dosimeters over the full range of field sizes involved in advanced photon-beam radiotherapy techniques**' and recommend that it may be accepted as fulfilling the dissertation requirement for the award of Degree of Doctor of Philosophy.

Kailash C. Mittal

Chairman : Prof. K. C. Mittal 19/01/2016 **Date:**

Guide / Convener : Prof. D. D. Deshpande **Date:** 19/01/2016

Member 1 : Prof. R. Sarin **Date:** 19.1.16

Member 2 : Prof. S. D. Sharma **Date:** 19/01/2016

M. Ravi 19.1.16

External Examiner : Prof. M. Ravikumar **Date:** 19.1.2016

Final approval and acceptance of this dissertation is contingent upon the candidate's submission of the final copies of the dissertation to HBNI

I hereby certify that I have read this dissertation prepared under my direction and recommend that it may be accepted as fulfilling the thesis requirement.

Date: 19/01/2016
Place: Mumbai

Prof. D. D. Deshpande
(Guide)

STATEMENT BY AUTHOR

This dissertation has been submitted in partial fulfillment of the requirements for an advanced degree at Homi Bhabha National Institute (HBNI) and is deposited in the library to be made available to borrowers under the rules of the HBNI.

Brief quotations from this dissertation are allowed without special permission, provided that acknowledgement of the source is made. Requests for permission for extended quotations from or reproduction of this manuscript, in whole or in part, may be granted by the Competent Authority of HBNI when, in his or her judgment, the proposed use of the material is in the interests of scholarship. In all other instances, however, permission must be obtained from the author.

SKumar

(Sudhir Kumar)

DECLARATION

I hereby declare that the investigation presented in the thesis has been carried out by me. The work is original and has not been submitted earlier, as a whole or in part, for a degree / diploma at this or any other Institution / University.

(Sudhir Kumar)

List of publications arising from the Thesis

Journal

"Characterizing the influence of detector density on dosimeter response in non-equilibrium small photon fields", Alison J D Scott , **Sudhir Kumar**, Alan E Nahum and John D Fenwick, *Physics in Medicine and Biology*, **2012**, 57, 4461-4476. **(Paper I)**

(Featured as Editor's Choice on 25.6.2012 on www.medicalphysicsweb.org)

"Using cavity theory to describe the dependence on detector density of dosimeter response in non-equilibrium small fields", John D Fenwick, **Sudhir Kumar**, Alison J D Scott and Alan E Nahum, *Physics in Medicine and Biology*, **2013**, 58, 2901-2923. **(Paper II)**

"Monte-Carlo-derived insights into dose-kerma-collision kerma inter-relationships for 50keV to 25MeV photon beams in water, aluminium and copper", **Sudhir Kumar**, Deepak D Deshpande and Alan E Nahum, *Physics in Medicine and Biology*, **2015**, 60, 501-519. **(Paper III)**

"Breakdown of Bragg-Gray behaviour for low-density detectors under electronic disequilibrium conditions in small megavoltage photon fields", **Sudhir Kumar**, John D Fenwick, Tracy S A Underwood, Deepak D Deshpande, Alison J D Scott, and Alan E Nahum, *Physics in Medicine and Biology*, **2015**, 60, 8187-8212. **(Paper IV)**

"Secondary bremsstrahlung and the energy-conservation aspects of kerma in photon-irradiated media", **Sudhir Kumar** and Alan E Nahum, *Physics in Medicine and Biology*, **2016,** 61, 1389-1402. **(Paper V)**

"Dosimetric response of variable-size cavities in photon-irradiated media and the behaviour of the Spencer-Attix cavity integral with increasing Δ", **Sudhir Kumar**, Deepak D Deshpande and Alan E Nahum, *Physics in Medicine and Biology*, **2016** (Provisionally Accepted). **(Paper VI)**

Conference/Workshops

1. "Monte-Carlo study of Dose, Kerma and collision Kerma vs depth for 50 KeV – 25 MeV photons in a range of materials", **Sudhir Kumar S**, M Chandrasekaran, Alison J D Scott, Deepak D Deshpande, Alan E Nahum, *Book of abstracts of International Workshop on Recent Advances in Monte Carlo Techniques in Radiation Therapy* **(McGill University & Universite Laval, June 8-10, 2011, Montreal, Quebec, Canada), 2011,** 23-25.

2. “Small field dosimetry for IMRT and stereotactic radiotherapy”, John D Fenwick, A Scott, **Sudhir Kumar,** T Underwood, H Winter, M Hill and Alan E Nahum, *Book of Extended Abstracts on Workshop on* ‘*IPEM Small Fields Dosimetry*’, **National Physical Laboratory, 29 May 2012, Teddington, Middlesex, UK, 2012**.

3. “A versatile analytical approach to estimate D/K ratios and β for 5 to 25 MeV photon beams in a range of materials”, **Sudhir Kumar**, S. D. Sharma, Deepak D Deshpande, Alan E Nahum, ***Book of Abstracts*** **(AMPICON-2012), 2012,** 197-199.

4. “Target dose verification in gamma knife: comparison of ionization chamber, diamond detector and radiochromic film measurements”, Anil Pendse, **Sudhir Kumar,** R Chaudhary, S. D. Sharma, B. K. Misra, *Medical Physics International Journal*, **2013**, **1, 606**

(Sudhir Kumar)

DEDICATED TO

MY FATHER MR. MANGEY RAM

&

MY UNCLE MR. RAJENDRA KUMAR

ACKNOWLEDGEMENTS

First and foremost I wish to take this privilege to place on record in a very special and distinctive manner, an expression of deep sense of gratitude and indebtedness to my PhD supervisor, Dr. D. D. Deshpande, Head, Department of Medical Physics, Tata Memorial Hospital, Mumbai for his excellent guidance and make himself available whenever I requested to meet him during the thesis work.

I express my gratitude to Drs. S. D. Sharma, Head, MPS, Radiological Physics & Advisory Division (RP&AD), Bhabha Atomic Research Centre (BARC), D. Datta, Head, RP&AD, BARC, Pradeepkumar K. S., Associate Director, HS&EG, BARC, D. N. Sharma, former Director, HS&EG, BARC, Mumbai, India, for their encouragement, supports and allowing me to pursue my PhD project.

I would like to express my sincere gratitude to Commonwealth Scholarship Commission, United Kingdom (UK) for offering me the Split-site Doctoral Scholarship to pursue my partial research work during December 2010 to December 2011. The partial research work was hosted by Prof. Alan E. Nahum, Physics Department, Clatterbridge Cancer Cancer (CCC), Wirral, University of Liverpool, Liverpool, UK. During this prestigious scholarship, Prof. Nahum was designated as my UK supervisor to supervise my PhD research work. I am grateful to Prof. Nahum for taking my tutorial at regular interval to teach me all fundamental concepts of theoretical radiation dosimetry and Monte-Carlo technique to build-up my strong base for pursuing research work in focussed manner, for continuing the strong collaboration and inviting me subsequently twice to the Physics Department, CCC to work in his research group to complete this project. It is his motivation, enthusiasm, immense knowledge, wholehearted guidance and support that helped me to complete this project.

I am deeply grateful to Mr. H. S. Kushwaha, former Director, HS&EG, BARC and Raja Ramanna Fellow, Department of Atomic Energy, India for supporting and helping me to establish this wonderful collaboration with Prof. Nahum.

I am very grateful to Prof. D. W. O. Rogers, Carleton University, Ottawa, Canada for fixing a bug in the scoring of kerma in the DOSRZnrc user-code and for insightful comments on the manuscripts. I am also grateful to Professor Philip Mayles, former head of Physics Department, CCC for his support during this work. I wish to thank Dr. John D. Fenwick, University of Liverpool, UK for constructive and insightful comments on all manuscripts which have resulted in significant improvements and for all discussion and help for the completion of this project. I also wish to thank Professor Frank Verhaegen, Maastro Clinic, Netherlands for his insightful comments on the manuscript and useful discussions on Monte-Carlo simulation during *International Workshop* held at McGill University, Montreal, Canada. I am also grateful to Professor Pedro Andreo, Stockholm University, Dr. David Burns, BIPM, and Professor Jan Seuntjens, McGill University, Canada, for useful discussions during this work. Thanks are also due, amongst others, to Dr. Colin Baker, Alison J. D. Scott, and Julien Uzan, Jothy Basu, Mekala Chandrasekaran, Antony Carver, Dhvanil Karia and

George Georgiou for creating the friendly and helpful atmosphere of the Physics research group at CCC during my all visits and to the IT section for their expertise and for putting extensive computer hardware at my disposal. I am grateful to Mrs. Sue Nixon, secretary Department of Physics, CCC, UK for the extensive supports provided while I was at CCC. I am also thankful to Dr. Tracy S. A. Underwood, Massachusetts General Hospital, Boston, USA for helping me during this work.

I am extremely grateful to all my favourite teachers and seniors Dr. A. N. Nandakumar, former Head, RSD, AERB, Mumbai, India, Mr. U. B. Tripathi, former Head, MP&TS, RP&AD, Dr. B.C. Bhatt, former Head, RP&AD, Dr. B. S. Rao, former Head, RP&AD and Mr. Anil M Pendse, Senior Physicist, Hinduja Hospital, Mumbai for their help and support/advise at each step from my DiP. R. P. Training till now.

Special thanks are due to Dr. K. C. Mittal, Chairman, Doctoral Committee for helping me to maintain the focus by way of critical discussions and constructive suggestions. I also thank all the Doctoral Committee members for their helpful suggestions during the annual reviews.

I would like to thank to all our colleagues in our division, specially, Dr. T. Palani Selvam, Dr. B. K. Sahoo, Mr. Rahul Kumar Chaudhary, Dr. S. P. Tripathy, HPD, Mr. Gurmeet Singh, Computer Division, Mr. R. B. Tokas, AMPD and Mr. Arup Biswas, AMPD, BARC for immense help.

I would like to thank to Dr. Neha Kumar, TMH, Dr. Sudeep Gupta, Deputy Director, CRC, ACTREC, Tata Memorial Centre, Mumbai, Prof. Bipin Jojo, Tata Institute of Social Science, Mumbai and Dr. Om Pal Singh, former Secretary, AERB & Director ITSD, AERB, Mumbai for their encouragement. I express my deep gratitude to Brig. (Dr.) Harinder Pal Singh, Commandant at Command Hospital, Pathankot for motivating me to pursue higher education. Thanks are also due to Drs. Jagadish Sadashivaiah, Norman Main, Harold d'Souza and Richard Buttery and their families who helped me from all angles while I was in UK.

I convey my heartfelt gratitude to all my family members specially my elder brothers Shri Yeshpal Singh and Rajpal Singh who have always inspired me and without their constant support and encouragement, this work would not have reached the present stage. It is very difficult to name all those who have helped me during the various stages of executing work reported in this thesis. I apologize for any omission.

Finally, I would like to thank my wife Rakhi Tomar for her exceptional care, personal support and great patience throughout these years. I am thankful to my daughter Siyona Tomar for bearing with my absence during my visits to UK especially during December 2010 to December 2011 when she learned how to speak and walk.

S Kumar

(Sudhir Kumar)

CONTENTS

Page No.

SYNOPSIS

Radiotherapy treatment involves the precise delivery of the prescribed radiation dose to a defined target volume in the cancer patient. Whilst a high, tumoricidal dose is delivered to the target volume, the surrounding healthy tissue is to be spared as far as possible. The success of radiotherapy depends on the accuracy, precision and conformity of the desired dose distribution over the tumour volume and organs at risk i.e. the accurate delivery of the treatment as planned. The tumour control probability (TCP), and hence the chances of cancer cure, are critically dependent on the dose delivered to the tumour; for many tumour types TCP is a steep function of dose. If the delivered dose is 5% lower than the intended dose, this can decrease the cure rate between 10 and 15% depending on the tumour type whereas if it is 5-10% higher than intended dose, there may be a significant increase in the rate of serious complications/intolerable side effects (ICRU 1976, Brahme 1984). It follows that high accuracy of dose determination is crucial, and this means that a thorough understanding of the response of the various dose-measuring instruments (dosimeters or detectors) in practical use is essential.

Conventional radiotherapy is often performed with 'static' treatment beams with a uniform transverse dose profile. However, due to the location and/or the shape of the tumour, it is often not possible to achieve both a homogeneous dose in the tumour and adequate sparing of the surrounding normal tissues using such beams. In recent years, the introduction of newer technologies in radiation therapy for the delivery of external radiotherapy using x-ray and γ-ray beams produced by linear accelerator machines and a dedicated Gamma Knife system respectively has improved the capability of treating small and irregular lesions. Conformal dose distributions and more accurate dose delivery is offered by radiotherapy techniques such as beamlet-based intensity modulated radiation therapy (IMRT), volumetric modulation arc therapy (VMAT), helical IMRT and high-precision stereotactic radiosurgery (SRS) and stereotactic ablative radiotherapy (SABR). The multileaf collimators (MLCs) of different designs and technology are the core mechanical components which enable the shaping of the treatment fields so that these 'conform' to the tumour geometry. In particular, SRS delivered by Gamma Knife and Cyberknife deliver a large number of very small fields of the order of a few millimeters to treat (small) tumors and spare normal structures. Beamlet-based IMRT uses a large number of fields (also known as 'segments'), designed using 'inverse-planning', some of which are so small that individually they do not yield charged-particle equilibrium, CPE (Dutreix *et al* 1965 Attix 1986). Thus, recent developments in radiotherapy techniques have substantially increased the use of small radiation treatment fields. A 'small' radiation treatment field can be defined as a field with a width smaller than the range of the secondary charged particles. Small radiation fields require their geometry and dosimetry to be accurately characterized so that dose distributions calculated by treatment planning systems correctly reflect the doses delivered. However, accurate measurement of small radiation fields presents some challenges not encountered for large fields.

The ‘physics’ of small, non-equilibrium radiation fields differs from that of large fields; one consequence of this is that the conversion of detector signal to absorbed dose to water is more sensitive to the properties of the radiation detectors used. Differences include loss of lateral electronic equilibrium and source occlusion; the field size at which these effects become significant depends on beam energy, and collimator design (Treuer *et al* 1993, Das *et al* 2008b, Alfonso *et al* 2008, Scott *et al* 2008, 2009, IPEM 2010). Detector-specific effects include fluence perturbation caused by differences between detector material and medium, dose-averaging effects around the peak of the dose distribution, and the uncertainties for very small fields introduced by slight geometrical detector misalignment (Paskalev *et al* 2003, Bouchard *et al* 2009, Crop *et al* 2009, IPEM 2010, Francescon *et al* 2011, Scott *et al* 2012, Fenwick *et al* 2013, Charles *et al* 2013, Underwood *et al* 2013b, Kumar *et al* 2015b). The Monte-Carlo method is especially valuable when the width of the photon field is so small as to make even quasi-CPE impossible (IPEM 2010).There is therefore a need to carry out comprehensive Monte Carlo based dosimetry studies on small, non-standard and standard treatment fields used for advanced radiotherapy techniques, for a range of different types of detectors, and to develop recommendations for the dosimetry of such fields.

***Aims/Objectives of the work undertaken for the thesis*:**

In this thesis the Monte-Carlo (MC) simulation of radiation transport was applied to the following areas:

- A critical re-examination of certain basic concepts of radiation dosimetry **(Papers III and V)**.
- An improvement of our knowledge and understanding of the response of practical dosimeters in the non-equilibrium (small-field) situations commonly encountered in advanced radiotherapy treatments **(Papers I and IV)**.
- A study of certain aspects of ‘cavity theory’ in order to extend the range of validity of this body of theory **(Papers II, IV and VI)**.

This thesis comprises of eight chapters arranged as follows.

Chapter 1: ***Introduction***

This chapter describes briefly the modalities used for the treatment of cancer and emphasises the importance of radiotherapy in the management of cancer patients. A brief overview of the mode of radiotherapy delivery is given. The biological basis of radiotherapy is briefly discussed. The clinical requirement for accuracy in radiotherapy dose delivery is explained by reference to dose-response (dose-effect) curves in terms of tumour control probability (TCP) and normal-tissue complication probability (NTCP). In addition to this, the different techniques for the delivery of external radiotherapy treatments are described with special attention paid to advanced radiotherapy delivery techniques such as beamlet-based IMRT, VMAT, helical IMRT using tomotherapy, SRS and SABR where small radiation fields are produced by secondary/tertiary collimators (cones and multi-leaf collimators, MLCs) to conform to the tumour volume in order to achieve good clinical outcomes. The main challenges faced in small-field dosimetry are briefly discussed. The need for Monte-Carlo (MC) methods in radiation dosimetry, especially in non-equilibrium photon fields, and for a suitable MC code system (i.e. EGSnrc) for relative ionization chamber response calculations is discussed. Finally the aims and scope of the present thesis are presented. The scientific literature related to the thesis is briefly summarized here. However, more specific publications are reviewed in the individual chapters.

Chapter 2: ***Monte-Carlo derived insights into Dose-Kerma-Collision Kerma inter-relationships for 50-keV to 25-MeV photon beams in water, aluminium and copper*** **(Paper III)**

The relationships between D, K, and K_{col} are of fundamental importance in radiation dosimetry. These relationships are critically influenced by secondary electron transport, which makes Monte-Carlo simulation indispensable; we have used Monte-Carlo (MC) codes DOSRZnrc and FLURZnrc. Computations of the ratios D/K and D/K_{col} in three materials (water, aluminium and copper) for large field sizes with energies from 50 keV to 25 MeV (including 6-15 MV) are presented. Beyond the depth of maximum dose D/K is almost always less than or equal to unity and D/K_{col} greater than unity, and these ratios are virtually constant with increasing depth. The difference between K and K_{col} increases with energy and with the atomic number of the irradiated materials. D/K in 'sub-equilibrium' small megavoltage photon fields decreases rapidly with decreasing field size. A simple analytical expression for $\overline{X}$, the distance 'upstream' from a given voxel to the mean origin of the secondary electrons depositing their energy in this voxel, is proposed: $\overline{X}_{\mathrm{emp}} \approx 0.5R_{\mathrm{csda}}(\overline{E_0})$, where $\overline{E_0}$ is the mean initial secondary electron energy. These $\overline{X}_{\mathrm{emp}}$ agree well with 'exact' MC-derived values for photon energies from 5-25 MeV for water and aluminium. An analytical expression for D/K is also presented and evaluated for 50 keV – 25 MeV photons in the three materials, showing close agreement with the MC-derived values.

Chapter 3: ***Secondary bremsstrahlung and the energy-conservation aspects of Kerma in photon-irradiated media*** **(Paper V)**

Kerma, collision kerma and absorbed dose in media irradiated by megavoltage photons are analysed with respect to energy conservation. The user-code DOSRZnrc was employed to compute absorbed dose D, kerma K and a special form of kerma, K_{ncpt}, obtained by setting the charged-particle transport energy cut-off very high, thereby preventing the generation of 'secondary bremsstrahlung' along the charged-particle paths. The user-code FLURZnrc was employed to compute photon fluence, differential in energy, from which collision kerma, K_{col} and K were derived. The ratios K/D, K_{ncpt}/D and K_{col}/D have thereby been determined over a very large volumes of water, aluminium and copper irradiated by broad, parallel beams of 0.1 to 25 MeV monoenergetic photons, and 6, 10 and 15 MV 'clinical' radiotherapy qualities. Concerning depth-dependence, the 'area under the kerma, K, curve' exceeded that under the dose curve, demonstrating that kerma does not conserve energy when computed over a large volume. This is due to the 'double counting' of the energy of the secondary bremsstrahlung photons, this energy being (implicitly) included in the kerma 'liberated' in the irradiated medium, at the same time as this secondary bremsstrahlung is included in the photon fluence which gives rise to kerma elsewhere in the medium. For 25 MeV photons this 'violation' amounts to 8.6%, 14.2% and 25.5% in large volumes of water, aluminium and copper respectively but only 0.6% for a 'clinical' 6 MV beam in water. By contrast, K_{col}/D and K_{ncpt}/D, also computed over very large phantoms of the same three media, for the same beam qualities , are equal to unity within (very low) statistical uncertainties, demonstrating that collision kerma and the special type of kerma, K_{ncpt}, *do* conserve energy over a large volume. A comparison of photon fluence spectra for the 25 MeV beam at a depth of ≈ 51 g cm^{-2} for both very high and very low charged-particle transport cut-offs reveals the considerable contribution to the total photon fluence by secondary bremsstrahlung in the latter case. Finally, a correction to the 'kerma integral' has been formulated to account for the energy transferred to charged particles by photons with initial energies *below* the Monte-Carlo photon transport cut-off *PCUT*; for 25 MeV photons this 'photon track end' correction is negligible for all *PCUT* below 10 keV.

Chapter 4: ***Characterizing the influence of detector density on dosimeter response in non-equilibrium small photon fields*** **(Paper I)**

The impact of density and atomic composition on the dosimetric response of various detectors in small photon radiation fields is characterized using a 'density-correction' factor, F_{detector}, defined as the ratio of Monte-Carlo calculated doses delivered to water and detector voxels located on-axis, 5 cm deep in a water phantom with a source to surface distance (SSD) of 100 cm. The variation of F_{detector} with field size has been computed for detector voxels of various materials and densities. For ionization chambers and solid-state detectors, the well-known variation of F_{detector} at small field sizes is shown to be due to differences between the *densities* of detector active volumes and water, rather than differences in atomic number. Since changes in F_{detector} with field size arise primarily from differences between the densities of the detector materials and water, ideal small-field relative dosimeters should have small active volumes and water-like density.

Chapter 5: ***Using cavity theory to describe the dependence on detector density of dosimeter response in non-equilibrium small fields*** **(Paper II)**

The dose imparted by a small non-equilibrium photon radiation field to the sensitive volume of a detector located within a water phantom depends on the density of the sensitive volume. Here this effect is explained using cavity theory, and analysed using Monte Carlo data calculated for schematically modelled diamond and Pinpoint-type detectors. The combined impact of the density and atomic composition of the sensitive volume on its response is represented as a ratio, $F_{\mathrm{w,det}}$, of doses absorbed by equal volumes of unit density water and detector material co-located within a unit density water phantom. The impact of density alone is characterized through a similar ratio, $P_{\rho\_}$, of doses absorbed by equal volumes of unit and modified-density water. The cavity theory is developed by splitting the dose absorbed by the sensitive volume into two components, imparted by electrons liberated in photon interactions occurring inside and outside the volume. Using this theory a simple model is obtained that links $P_{\rho\_}$ to the degree of electronic equilibrium, s_{ee} , at the centre of a field via a parameter I_{cav} determined by the density and geometry of the sensitive volume. Following the scheme of Bouchard *et al* (2009 Med. Phys. 36 4654–63) $F_{\mathrm{w,det}}$ can be written as the product of $P_{\rho\_}$, the water-to-detector stopping power ratio $s^{\mathrm{SA}}_{\mathrm{w,\,det},\,\Delta}$, and an additional factor $P_{\mathrm{fl}\_}$. In small fields $s^{\mathrm{SA}}_{\mathrm{w,\,det},\,\Delta}$ changes little with field-size; and for the schematic diamond and Pinpoint detectors $P_{\mathrm{fl}\_}$ takes values close to one. Consequently most of the field-size variation in $F_{\mathrm{w,det}}$ originates from the $P_{\rho\_}$ factor. Relative changes in s_{ee} and in the phantom scatter factor s_p are similar in small fields. For the diamond detector, the variation of $P_{\rho\_}$ with s_{ee} (and thus field-size) is described well by the simple cavity model using an I_{cav} parameter in line with independent Monte Carlo estimates. The model also captures the overall field-size dependence of $P_{\rho\_}$ for the schematic Pinpoint detector, again using an I_{cav} value consistent with independent estimates.

Chapter 6: ***Breakdown of Bragg-Gray behaviour for low-density detectors under electronic disequilibrium conditions in small megavoltage photon fields*** **(Paper IV)**

In small photon fields ionisation chambers can exhibit large deviations from Bragg-Gray behaviour; the EGSnrc Monte Carlo (MC) code system has been employed to investigate this 'Bragg-Gray breakdown'. The total electron (+ positron) fluence in small water and air cavities in a water phantom has been computed for a full linac beam model as well as for a point source spectrum for 6 MV and 15 MV qualities for field sizes from 0.25 × 0.25 cm^2 to 10 × 10 cm^2. A water-to-air perturbation factor has been derived as the ratio of total electron (+ positron) fluence, integrated over all energies, in a tiny water volume to that in a 'PinPoint 3D-chamber-like' air cavity; for the 0.25 × 0.25 cm^2 field size the perturbation factors are 1.323 and 2.139 for 6 MV and 15 MV full linac geometries respectively. For the 15 MV 'full linac' geometry, for field sizes of 1×1 cm^2 and smaller, not only the absolute magnitude but also the 'shape' of the total electron fluence spectrum in the air cavity is significantly different to that in the water 'cavity'. The physics of this 'Bragg-Gray breakdown' is fully explained, making explicit reference to the Fano theorem. For the 15 MV full linac geometry in the 0.25×0.25 cm^2 field the directly computed MC dose ratio, water-to-air, differs by 5% from the product of the Spencer-Attix stopping-power ratio (SPR) and the perturbation factor; this 'difference' is explained by the difference in the shapes of the fluence spectra and is also formulated theoretically. It is shown that the dimensions of an air-cavity with a perturbation factor within 5% of unity would have to be impractically small in these highly non-equilibrium photon fields. In contrast the dose to water in a 0.25×0.25 cm^2 field derived by multiplying the dose in the single-crystal diamond dosimeter (SCDDo) by the Spencer-Attix ratio is within 2.9% of the dose computed directly in the water voxel for full linac geometry at both 6 and 15 MV, thereby demonstrating that this detector exhibits quasi Bragg-Gray behaviour over a wide range of field sizes and beam qualities.

Chapter 7: *Dosimetric response of variable-size cavities in photon-irradiated media and the behaviour of the Spencer-Attix cavity integral with increasing* Δ (Paper VI)

Cavity theory is fundamental to understanding and predicting dosimeter response. Conventional cavity theories have been shown to be consistent with one another by deriving the electron (+ positron) and photon fluence spectra with the FLURZnrc user-code (EGSnrc Monte-Carlo system) in large volumes under quasi-CPE for photon beams of 1 MeV and 10 MeV in three materials (water, aluminium and copper) and then using these fluence spectra to evaluate and then inter-compare the Bragg-Gray, Spencer-Attix and 'large photon' 'cavity integrals'. The behaviour of the 'Spencer-Attix dose' (aka restricted cema), $D_{\mathrm{S\text{-}A}}(\Delta)$, in a 1-MeV photon field in water has been investigated for a wide range of values of the cavity-size parameter Δ: $D_{\mathrm{S\text{-}A}}(\Delta)$ decreases far below the Monte-Carlo dose (D_{MC}) for Δ greater than ≈ 30 keV due to secondary electrons with starting energies *below* Δ not being 'counted'. It has been shown that for a quasi-scatter-free geometry ($D_{\mathrm{S\text{-}A}}(\Delta)/D_{\mathrm{MC}}$) is closely equal to the proportion of energy transferred to Compton electrons with initial (kinetic) energies above Δ, derived from the Klein-Nishina (K-N) differential cross section. ($D_{\mathrm{S\text{-}A}}(\Delta)/D_{\mathrm{MC}}$) can be used to estimate the maximum size of a detector behaving as a *Bragg-Gray* cavity in a photon-irradiated medium as a function of photon-beam quality (under quasi CPE) e.g. a typical air-filled ion chamber is 'Bragg-Gray' at (monoenergetic) beam energies ≥ 260 keV. Finally, by varying the *density* of a silicon cavity (of 2.26 mm diameter and 2.0 mm thickness) in water, the response of different cavity 'sizes' was simulated; the Monte-Carlo-derived ratio $D_{\mathrm{w}}/D_{\mathrm{Si}}$ for 6 MV and 15 MV photons varied from very close to the *Spencer-Attix* value at 'gas' densities, agreed well with Burlin cavity theory as ρ increased, and approached *large photon* behaviour for $\rho \approx 10$ g cm^{-3}. The estimate of Δ for the Si cavity was improved by incorporating a Monte-Carlo-derived correction for electron 'detours'. Excellent agreement was obtained between the Burlin '*d*' factor for the Si cavity and $D_{\text{S-A}}(\Delta)/D_{\text{MC}}$ at different (detour-corrected) Δ, thereby suggesting a further application for the $D_{\text{S-A}}(\Delta)/D_{\text{MC}}$ ratio.

Chapter 8: ***Summary and Conclusions***

This chapter summarizes the major findings of the thesis and outlines the scope for *future* work.

A set of D/K, D/K_{col} and $\overline{X}$ values has been generated in a consistent manner by Monte-Carlo simulation for water, aluminium and copper and for photon energies from 50 keV to 25 MeV (including 6-15 MV). Beyond the build-up region dose D is almost never greater than kerma K whilst collision kerma K_{col} is always less than D. A simple analytical expression for $\overline{X}$, denoted by $\overline{X}_{\text{emp}}$, the distance 'upstream' from a given voxel to the mean origin of the secondary electrons depositing their energy in this voxel, was proposed: $\overline{X}_{\text{emp}} \approx 0.5R_{\text{csda}}(\overline{E_0})$, where $\overline{E_0}$ is the mean initial secondary electron energy, and validated (Paper III).

It has been demonstrated that when computed over a large irradiated volume, kerma does not conserve energy whereas collision kerma and a special form of kerma, which is denoted by K_{ncpt}, (ncpt ≡'no charged-particle transport'), do conserve energy. This analysis has also quantified the magnitude of the errors made in deriving kerma by setting a high electron/positron kinetic energy cut-off *ECUT* and has highlighted the role played by secondary bremsstrahlung in determining kerma at large depths (Paper V).

Relative to wide-field readings, it has been found that *high*-density detectors *over*-read, and *low*-density detectors *under*-read (relative to the density of water, the reference medium) in non-equilibrium small photon fields (Paper I).

A modified form of cavity theory has been developed to take account the 'density effect' in small fields. The density-dependence can be minimized either by constructing detectors with sensitive volumes having similar densities to water, or by limiting the thickness of sensitive volumes in the direction of the beam. Regular 3×3 cm^2 or 4×4 cm^2 fields are useful for small-field detector calibration (Paper II).

In small photon fields, even small 'PinPoint 3D' ionisation chambers exhibit large deviations from Bragg-Gray behaviour; the EGSnrc Monte Carlo code system has been employed to quantify this 'Bragg-Gray breakdown'. For the 15 MV 'full linac' geometry, for field sizes of 1 × 1 cm^2 and smaller, not only the magnitude but also the 'shape' of the electron fluence spectra in the air cavity differs from that in the water cavity, due to the combined effect of electronic disequilibrium, source occlusion and volume-averaging; a theoretical expression for this ‘shape factor’ has been formulated. A detailed explanation, also formulated analytically, for the ‘breakdown’ of Bragg-Gray behaviour in low-density (gas) detectors in non-equilibrium field sizes is given, making explicit reference to the Fano theorem (Paper IV).

The self-consistency of conventional cavity theories has been examined in different materials for photon beams of 1 MeV and 10 MeV. The ratio of Spencer-Attix dose to direct Monte-Carlo dose ($D_{\text{S-A}}(\Delta)/D_{\text{MC}}$) decreases steadily as Spencer-Attix cut-off energy Δ increases about $\approx$ 20 keV in photon-irradiated media. The quantity $D_{\text{S-A}}(\Delta)/D_{\text{MC}}$ as a function of a Δ can be used to deduce an air cavity with dimensions corresponding to a Δ, of 10 keV (a value widely applied to the air cavities of practical ion chambers e.g. Farmer and NACP designs) to exhibit Bragg-Gray behaviour. Excellent agreement between $D_{\text{S-A}}(\Delta)/D_{\text{MC}}$ and the Burlin ‘*d*’ weighting factor at different Si pseudo-densities (provided a correction for ‘detour’ is made) suggests a further application for the $D_{\text{S-A}}(\Delta)/D_{\text{MC}}$ ratio: as an alternative way to estimate *d* (Paper VI).

The scope for future work includes (i) formulating a composite expression for a 'quasi-Burlin dose ratio' for an intermediate cavity in a bremsstrahlung beam by recognising that the cavity response can be characterized as a quasi-perfect 'large photon detector' for the lowest energies, an (approximate) ‘Burlin’ detector for the intermediate energies, and a quasi Bragg-Gray detector for the highest energies of the bremsstrahlung beam spectra; (ii) a critical evaluation of the validity of the Fano theorem when the density-dependence of the interaction cross-sections in various media (e.g. the density or polarization effect in condensed media) is explicitly modelled by Monte-Carlo codes.

List of Figures

Page No.

List of Tables

Page No.

CHAPTER 1

Introduction

1.1 The role of radiotherapy in the treatment of cancer

Cancer (also termed as neoplasm) is a mass of tissue that grows in excess of normal tissue in an uncoordinated manner, and continues to grow after the initial stimulus has ceased. Cancer is one of the leading causes of death globally. The incidence of cancer is increasing, particularly because of the increase in life expectancy arising from worldwide improvements in standards of health care. According to recent estimates of the International Agency for Research on Cancer (IARC) and the World Health Organization (WHO), approximately ten million new cases of cancer are being detected per year worldwide, with slightly more than half of the cases occurring in developing countries. By this year the number is expected to increase to about 15 million cases, of which two thirds will occur in developing countries. As people live longer and populations increase, the number of new cancers each year is projected to rise sharply. By 2035, just 20 years from now, there will be an estimated 10 million more people every year facing cancer (Saracci and Wild 2015). Cancer patients primarily undergo surgery, radiotherapy, chemotherapy, or any combination of these treatment strategies to prolong life. Surgery and radiotherapy are aimed for local control whereas chemotherapy acts systemically to treat the disease in all affected parts of the body.

Radiotherapy is currently an essential component in the management of cancer patients. About fifty to sixty percent cancer patients receive radiotherapy at some time or other during the course of the disease, either as part of their primary treatment, in connection with recurrences or palliative treatment, or in combination with surgery or chemotherapy, for cure or palliation (Delaney *et al* 2005, Williams *et al* 2007, Janaki *et al* 2010). Radiotherapy is a multidisciplinary specialty which uses complex equipment and radiation sources for the delivery of a high ‘dose’ of ionizing radiation to the tumour volume. It is estimated that approximately 3300 teletherapy machines are currently installed in developing countries. This figure is significantly below the estimated needs, of about 10,000 machines by the year 2015. In India, the first teletherapy (telecobalt) unit was installed in 1957. Since then, there has been a steady increase in the number of teletherapy unit in the country. By December 2014, there were 359 radiotherapy centres in India. However, due to the lack of adequate radiotherapy facilities, only 1/3rd of the cancer patients get the opportunity to receive radiotherapy. As per international norms, there should be 2 teletherapy units per million of population. Therefore, considering the present population of India of 1.28 billion, 2560 teletherapy unit are required in the country to meet the ideal requirement as against 520 teletherapy units (289 linear accelerator + 231 telecobalt) currently available in the country.

Radiotherapy is defined as the treatment of diseases (mostly malignant) with ionizing radiation. It works by damaging tumour cells to stop them dividing i.e. killing the so-called clonogens. Radiotherapy is delivered through two different modes: teletherapy (or external-beam radiotherapy) and brachytherapy. External-beam radiotherapy (EBRT) is the most common form of radiotherapy, where the source of radiation lies outside the body. Electrons and photons (x-ray and γ-ray) are the two type of ionising radiation widely used in EBRT presently. The γ-ray beams are usually provided by a radioactive source such as Co-60 whereas x-ray and electron beams are produced using linear accelerators (linacs). The treatment with EBRT spares the skin (skin sparing effect). The linac is preferred for the treatment of deep seated tumours like thoracic tumours, pelvic tumours etc. Telecobalt unit is the backbone of any radiotherapy department in developing countries like India because it is cost effective and requires low maintenance cost. EBRT treatment with conventional fractionation is done once a day with 1.8-2 Gy, 5 times a week and lasts for about 5-7 weeks. Majority of the tumours require EBRT doses in the range of 50-70 Gy. It is a painless and non-invasive procedure.

Brachytherapy is another mode of treatment where the radioactive source is placed inside or in close proximity of the tumour mass. Various radioactive sealed sources used for brachytherapy are Co-60, Cs-137, Ir-192, I-125, Au-198 and Pd-103 etc. Currently the brachytherapy treatment is performed with the help of remote afterloading units where there is minimal risk of radiation exposure to the staff. Brachytherapy has the advantage of delivering high dose of radiation in shorter time simultaneously sparing the surrounding normal structures. The usual treatment with high dose rate (HDR) brachytherapy is delivered in minutes but multiple fractions (average 3-7 fractions) are required. The sites where brachytherapy is used as boost are cancers of cervix, endometrium, esophagus, head & neck and chest wall, etc.

In addition to photon and electron beam, heavy charged particles (i.e. hadron) such as protons and carbon ions are also used for the treatment of cancer patients at some radiotherapy centres in world. Although hadron therapy has shown many advantages over photon and electron beams, its use is still limited worldwide due to the complexity and very high cost of the devices required for the production of beams. In India, this facility is not available so far. In this study/thesis the radiation dosimetry concept relevant to external photon beams produced either by Co-60 or linacs has been studied.

1.2 Biological basis of radiotherapy

In broad term, radiotherapy exploits the fact that ionising radiation causes damage to cells within the body. The biological effects of ionizing radiation result mainly from damage to deoxyribonucleic acid (DNA) which is the most critical target in the nucleus of a cell (Hall and Giaccia 2006). The damage to DNA may occur in one of the two ways: direct or indirect action (Podgorsak 2005). In direct action, the ionizing radiations interact directly with the target molecule (i.e. DNA). In this process, ionization or excitation of the atoms of the target may occur, causing a break in one or both strands of the molecule, which if unrepaired or incorrectly repaired, results in a variety of effect such as cell killing, division delay/mitotic inhibition, chromosome aberration and mutation. On the other hand the interaction of radiation with other molecules (mainly water since almost 80 % of a cell is composed of water) results in the formation of reactive species called the 'free radicals'. The interaction of these radicals with targets (i.e. DNA) results in indirect action. In living organisms, almost 70% of the damage results from indirect action. Since most living systems are composed of 80% water, indirect action mainly results from the radiolytic products of water. Absorption of radiation by water results in excitation and ionization, that finally results in the formation of radicals H^0, OH^0 and hydrated electrons ($\bar{e}_{aq}$). The free radicals are highly reactive due to the presence of unpaired electrons. The most biological damage is caused by hydroxyl radical (OH^0). The damage due to irradiation of cells is classified into lethal, sub-lethal and potentially lethal. The lethal damage is irreversible as well as irreparable and ultimately leads to cell death. This type of damage is expected more for cancerous cells in order to produce a positive treatment outcome. In sub-lethal damage, the cells repair in hours when optimal conditions are there for cell death, if additional sub-lethal damage is not added. Potential lethal damage leads to kill the cell unless external interference (Hall and Giaccia 2006).

In radiotherapy, treatments are typically delivered once daily for up to eight weeks using multiple fraction of small dose (i.e. dose fractionation) allowing for the repair of sub-lethal damage between fractions and cellular repopulation of normal tissues while cancer cells are less likely to repair. In addition, dose fractionation increases damage to the tumour due to reoxygenation of hypoxic cells and redistribution of the cells in the sensitive phases of the cell cycle.

1.3 Required accuracy in radiotherapy dose delivery: dosimetry perspective

An understanding of the basic principles of radiotherapy is essential for the successful application of radiotherapy. The higher the dose of radiation delivered to the tumour, the higher the probability of local control of the tumour. Hence the aim of radiotherapy is to deliver a tumoricidal dose of radiation to a well-defined target volume whilst causing an acceptably low probability of damage to the surrounding healthy tissue, in other words an optimum therapeutic ratio.

The clinical requirement for accuracy in radiotherapy dose delivery is explained by reference to dose-response (dose-effect) curves in terms of tumour control probability (TCP) and normal-tissue complication probability (NTCP). These curves have typically sigmoidal shapes, with a quasi-threshold dose, a relatively steep rise and saturation (100% effect) at high enough doses; see the schematic figure 1.1. The TCP is the probability of 'controlling' (i.e. eliminating) the tumour, TCP is critically dependent on the *dose* delivered to the tumour and is, for many tumour types, a relatively steep function of dose. NTCP is the probability of normal-tissue complications; the NTCP must in a general be kept to no more than approximate 10-15% or even lower if the effect is potentially severe or even fatal.

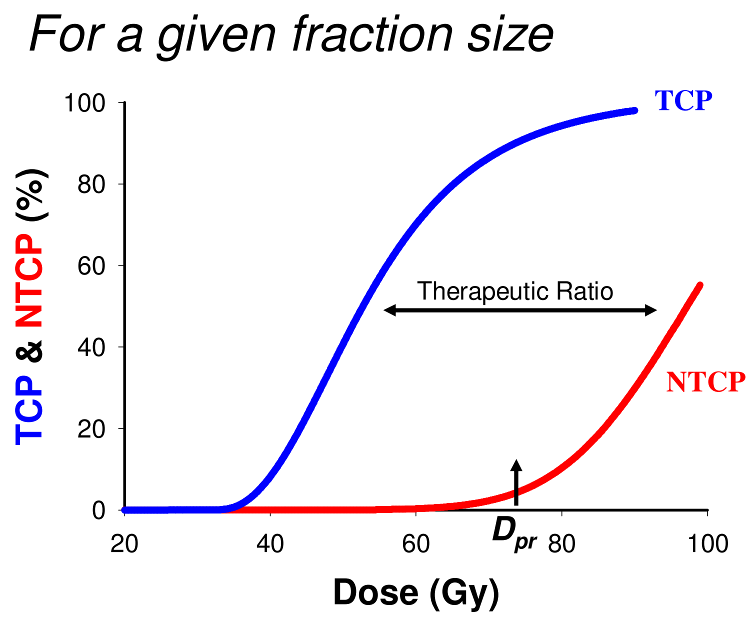

Figure 1.1: **Schematic illustration of tumour control probability (TCP) and normal tissue complication probability (NTCP) as a function of dose. D_{pr} is the suggested optimal dose. (A E Nahum, private communication)**

A relatively common practical radiotherapy situation is an overlapping of the TCP and NTCP curves such that the aim of radiotherapy is compromised (Mayles and Thwaites 2007). Radiotherapy optimisation including advances in beam-delivery technology is aimed at improving this balance, i.e. maximising tumour control while maintaining tissue complications at an acceptable level. The difference between the tumour control curve and the normal tissue complication probability is sometimes known as the *therapeutic ratio*. Dose-response curves depend on a number of parameters, such as fraction size, and tumour or (normal) tissue cell type i.e. radiosensitivity; the latter cannot currently be determined for each individual patient. It is also difficult to define what constitutes an *acceptable* side effect.

The shape of dose-response curves can give an estimate of the required accuracy of dose delivery in radiotherapy and therefore the required accuracy of the determination of the absorbed dose to the patient (in both the tumour and any critical normal tissues). The steepness of the given TCP or NTCP curve versus dose defines the change in response expected for a given change in delivered dose. If the delivered dose is 5% lower than the intended dose, this can decrease the cure rate between 10 and 15% depending on the tumour type whereas if it is 5-10% higher than intended dose, there may be a significant increase in the rate of serious complications/intolerable side effects (ICRU 1976, Brahme 1984). It follows that high accuracy of dose determination is crucial, and this means that a thorough understanding of the response of the various dose-measuring instruments (dosimeters or detectors) in practical use is essential.

Based on the steepness of the dose-response curves from limited routine clinical data available, the International Commission on Radiation Units and Measurements (ICRU), in Report 76 (1976), recommended that ± 5% accuracy is required in the delivery of absorbed dose to the target volume, but that in critical situations ± 2% may be required. Mijnheer *et al* (1987) obtained a figure for required accuracy by considering normal-tissue effects. They considered the steepness of dose-effect curves in terms of the percentage increase in absorbed dose to produce a change in the probability of normal-tissue complications from 25% to 50%. Based on this analysis they recommended a value of 3.5%, one relative SD (standard deviation), as the general accuracy requirement on absorbed dose delivery. Brahme (1988) considered the effects of variations in dose on tumour control for typical values, showing that the largest change in tumour control introduced by dosimetric inaccuracy is found at TCP ≈ 50%. A general figure of 3% (relative SD) on the delivered absorbed dose to the patient was recommended as the tolerance level on accuracy in dose delivery, in order to keep variations in the probability of tumour control within acceptable limits. Thus overall a figure of ± 3% (1 SD) can be taken as the currently recommended accuracy requirement on the value of the dose delivered to the patient at the dose specification point.

Recently Thwaites (2013) stated that general recommendations on achievable dosimetric accuracy in radiotherapy had not changed and concluded that despite the advances in technology and techniques in external-beam megavoltage x-ray therapy, ± 5% was still an acceptable level.

1.4 Dose delivery techniques in external-beam radiotherapy

Different techniques have been developed for the delivery of external radiotherapy treatments using x-ray and γ-ray beams produced by linacs and a dedicated Gamma Knife system respectively. This section gives a brief overview of these techniques, with special emphasis on advanced photon-beam radiotherapy delivery techniques such as Intensity Modulated Radiation Therapy (IMRT) and Volumetric Modulation Arc Therapy (VMAT); Stereotactic Radiosurgery (SRS) and Stereotactic Body Radiotherapy (SBRT) employ so-called ‘small’ radiation fields. Field shaping for all of these machines is produced by secondary/tertiary collimators (cones and multi-leaf collimators, MLCs) which conform the beam cross-section to a projection perpendicular to the beam direction of the outermost margin drawn around the tumour (known as the PTV, planning target volume).

1.4.1 Conventional radiotherapy

Conventional radiotherapy consists of two-dimensional (2D) treatment planning that involves a radiographic film or an image localization procedure. In conventional radiotherapy, the dose is delivered by square or rectangular fields shaped by conventional collimator blocks without any detailed conforming of the field geometry to the treatment volume. The treatment plans for such simple radiotherapy mainly consist of beams with a uniform intensity delivered from several directions to the treatment volume (target volume). This technique is well established at most radiotherapy centres in India and worldwide, because it is generally quick and reliable. However, its use has shown to be limited to the cases where the tumour is symmetrically shaped and centrally located in the body with a minimal surrounding critical organs. Since tumours generally do not have either rectangular or square cross sections seen from any direction, such techniques are not suitable for therapy given with curative intent; this is because, depending on the shape of the tumour, a lot of healthy tissue will be irradiated, leading to high toxicity of the tissues/organs close to the target volume if a curative dose is given to the tumour.

1.4.2 Conformal radiotherapy

The rationale for conformal radiotherapy is straightforward to state. The goal is to achieve a tumoricidal high-dose volume which conforms to (i.e. wraps closely around) the planning target volume (PTV) whilst simultaneously the OARs receive a dose sufficiently low as not to cause any complications. The concept behind this rationale is that if the difference between the doses received by the PTV and the OARs can be made large, then the dose to the PTV can be escalated with consequent expectation of a high TCP without causing unwanted radiation damage to normal-tissues (i.e. a low NTCP).

Conformal radiotherapy techniques are divided into two broad classes: i) techniques which involve only geometrical field shaping, known as three dimensional conformal radiotherapy (3DCRT), and ii) Intensity modulation radiotherapy (IMRT) techniques.

1.4.2.1 Three-dimensional conformal radiotherapy

The goal of three-dimensional (3D) planning is to conform the profile of each radiation beam to the shape of the target volume (i.e. PTV) seen from the beam direction; generally several (static) beams from different directions are employed. The radiation beams normally have uniform intensity across the field and the high-dose volume is made to ‘conform’ to the target volume by putting either metal blocks (e.g. made of cerrobend, a low melting point alloy) in the path of the radiation beams or by a using multi-leaf collimator (MLC) attached to the treatment head of the linac; both methods change the shape of the beam so that it ‘conforms’ closely to the shape of the tumour. A simultaneous goal is to minimize the dose to organs at risk. Radiation delivered by this method can only yield a ‘convex’ 3D dose distribution. The main achievement of techniques involving geometrical collimation alone (i.e. with quasi-uniform intensity across the beam aperture) is the shaping of the radiation field to the beam’s eye-view of the target.

The great advantage of 3*D*-conformal radiotherapy compared to conventional radiotherapy (i.e. few beams with rectangular collimation) is the reduction of radiation dose to the normal tissues adjacent to the PTV. As a consequence, a higher dose of radiation can be delivered to the tumour, thereby increasing the effectiveness of the treatment.

1.4.2.2 Intensity Modulated Radiotherapy

Intensity modulated radiotherapy (IMRT) is now an established paradigm for the treatment of cancer (Staffurth *et al* 2010); IMRT is an advanced form of 3*D* conformal radiotherapy where so-called inverse-planning is applied to calculate a 'modulated' (i.e. non-uniform) x-ray fluence across the treatment field thereby obtaining a potentially 'concave' 3*D* dose distribution. IMRT is a conformal treatment that not only conforms (high) dose to the target volume but also conforms (low) dose to sensitive structures (Nutting *et al* 2011, Miah *et al* 2012). IMRT is also used to deliver different dose prescriptions to multiple target volumes simultaneously (Wong *et al* 2010). Each treatment field is divided into small beams called *beamlets*. The intensity is different for individual beamlets. This is achieved by a set of collimating 'leaves' under computer control. This delivers a spatially non-uniform radiation exposure across the beam aperture and by combining several such beams from different directions, all planned with an inverse algorithm, a quasi-uniform dose distribution can be created in the target volume and steep dose gradients at the edge of the target volume. Steep dose gradients result in the reduction of normal-tissue doses and hence a reduction in morbidity; this affords the possibility of (so-called) 'dose escalation' within the target volume.

Two types of MLC-based IMRT delivery modes are used clinically, namely the 'step-and-shoot' or static (SMLC)' technique and the 'sliding window or dynamic (dMLC)' technique (Ezzell *et al* 2003). With SMLC, the radiation beam is off while the collimator leaves move to shape the field. The beam is turned back on only after the leaf motion has stopped, thereby defining an individual beamlet. In the sliding-window technique, the radiation beam remains on while the leaves are moving. The treatment time using DMLC is much less than for the SMLC technique (Nutting *et al* 2000).

The significant challenge for the practical implementation of IMRT is to ensure the accuracy of dose delivery. The IMRT fields (both step-and-shoot and dMLC) require highly accurate positioning of the MLC leaves, and a number of quality control regimes have been proposed to monitor this (Webb 2001). Inverse treatment planning is used to find the optimal position and movement of the leaves during irradiation. The delivery of modulated beams (i.e. IMRT) is achieved through a large number of small field sizes (< 3 cm in at least one dimension), highly irregular field shapes defined by the MLC and a small number of MUs[1] (≤ 5) per beamlet in step-and-shoot delivery mode. Low *et al* (2011) have provided a detailed discussion on the dosimetry 'tools' required and the techniques used in IMRT.

[1] The integrated current associated with 1 cGy in the standard conditions (source-surface-distance (SSD) of 100 cm for field size 10 × 10 cm^2 at the depth of maximum dose (d_{max})) is defined as one Monitor Unit (MU)

1.4.2.3 Volumetric Modulated Arc Radiotherapy

Yu (1995) introduced the concept of intensity modulated arc therapy (IMAT) on a linac as an alternative to tomotherapy. IMAT combines spatial and temporal intensity modulation with the movement of the gantry. Although Yu first proposed inverse planning for IMAT, forward planning was used for its early implementation (Yu *et al* 2002). The search for an equivalent linac-based solution continued with several authors attempting to determine an inverse-planned technique for IMAT which would result in the desired dose distribution deliverable in a single arc (Otto 2008, Cao *et al* 2009, Pardo-Montero and Fenwick 2009). Since becoming commercially available in 2009, there have been two main implementations of arc radiotherapy: Elekta VMAT (Elekta, Crawley, UK) and Varian RapidArc (Varian Medical Systems, Palo Alto, USA).

Volumetric Modulated Arc Therapy (VMAT) represents a new paradigm in the treatment of patients with external beam radiotherapy. VMAT is a subset of IMRT in which the gantry rotates while the beam is on to deliver dose from a range of coplanar or non-coplanar directions. Gantry speed, MLC leaf position and dose rate vary continuously during the irradiation. Arbitrary intensity distribution at each angle is delivered with multiple arcs. Dose conformity is theoretically equivalent to that achievable with a slice-based treatment technique (cf. tomotherapy). VMAT is ideal for generating conformal dose distributions ‘wrapped around’ critical organs. The demands on accurate dosimetry are even greater for VMAT delivery, as it involves a combination of continuous changes in the dose rate, gantry speed, and MLC leaf positions.

Studies have shown that VMAT dose distributions for prostate and cervical cancer have better sparing of OARs than 3DCRT and even static-field IMRT (Palma *et al* 2008, Zhang *et al* 2010). VMAT reduces the treatment time by a factor of 8 to 2 by using single or two rotations (arcs), respectively, compared to seven-field IMRT treatment plans (Clivio *et al* 2009, Sze *et al* 2011). In complex treatments with concave target volumes, VMAT needs usually at least two or possibly three arcs to be dosimetrically equivalent to fixed-gantry IMRT treatments (Wu *et al* 2009). However, with approximately spherical target volumes, like the prostate gland, one arc has been found to be adequate to achieve comparable dose distributions to conventional IMRT (Fontenot *et al* 2011). The number of MUs has also decreased by a factor of 2-4 by using VMAT techniques when compared to static gantry angle IMRT (Lee *et al* 2011).

1.4.2.4 Tomotherapy

‘Tomotherapy,’ which literally means ‘slice therapy,’ is a term derived from tomography. Tomotherapy is an arc-based approach to IMRT delivered using a fan-beam of radiation in conjunction with a binary multileaf collimator (Mackie *et al* 1993, Shepard *et al* 2000, Welsh *et al* 2002, Mackie *et al* 2006). Tomotherapy was first realized clinically using an approach called serial tomotherapy. Serial tomotherapy, as embodied in the NOMOS PEACOCK system (North American

Scientific, Chatsworth, CA), was delivered as an add-on accessory to a conventional linac. Serial tomotherapy delivers a series of abutted axial arcs. A potential disadvantage of this approach is that it can lead to hot and cold spots due to mismatched divergence. Consequently, it requires very precise placement of the arcs.

More recently, helical tomotherapy has become widely adopted as a new and promising delivery method for IMRT. The first clinical helical tomotherapy (Mackie *et al* 1993, 1999) treatment machine was installed at the University of Wisconsin (UW) Comprehensive Cancer Centre. The UW tomotherapy research group and TomoTherapy Incorporated (Madison, WI) developed the hardware and software. It was named Hi-ART for highly integrated adaptive radiotherapy. It essentially represents the fusion of a computed tomography (CT) scanner and a therapeutic linac. A compact 6 MV flattening filter free linac (waveguide: ~ 40 cm long, S-band (3 GHz)) and megavoltage CT detector sub-system are mounted upon a rotating gantry assembly. They are provided with power via slip-ring technology which also allows the transmission of data, and therefore the unit is capable of continuous rotation around the patient while the couch is moving through the plane defined by the rotating gantry, thus providing smooth helical delivery.

A primary collimator (of tungsten) shapes the 6 MV photon beams. This collimator defines a geometrical projection that is 40 cm wide in the X or transverse direction by 5 cm wide in the Y or patient inferior-superior direction at an isocenter located 85 cm from the x-ray target (source). A single set of moveable (tungsten) jaws further collimates to the fan beam of adjustable thickness up to 5 cm. During the treatment, the radiation fan beam has a fixed thickness (1, 2.5 and 5 cm) and is collimated/modulated along its long axis by a binary multileaf collimator (bMLC) consisting of 64 leaves. There are 32 leaves on each of two opposing sides (64 total) that slide past one another. Each of the leaves projects a shadow of 6.25 mm at the isocenter 85 cm from the x-ray target, thereby generating a total usable fan beam with of 40 cm. The leaves are binary (on or off) in the sense that the transit time from open to close is relatively short (< 25 ms). The open beam components are generally referred to as '*beamlets*'. Thus each leaf therefore defines a beamlet (i.e. 6.25 mm wide in the transverse direction at a distance of 85 cm from the source). The bMLC configuration is optimised and varied as a function of gantry angle using an inverse treatment planning process (Shepard *et al* 2000).

By altering leaf positions as a function of gantry position while the patient advances slowly through the gantry, one has great flexibility to produce the dose distributions with good target coverage and homogeneity together with individualized sparing OARs in a variety of tumours using the helical tomotherapy compare to step-and-shoot IMRT or stereotactic radiotherapy (Penagaricano *et al* 2005, Ramsey *et al* 2006, Soisson *et al* 2006, Vulpen *et al* 2006, Sterzing *et al* 2008).

1.4.2.5 Stereotactic Radiosurgery and Radiotherapy

The term 'stereotactic' defines the three-dimensional localisation of a particular point in space by a unique set of co-ordinates that relate to a fixed, external reference frame. Stereotactic radiosurgery (SRS) is a special radiotherapy technique used to irradiate intracranial lesions with 10-25 Gy dose in a single fraction by means of three-dimensional arrangement using a focused small ionizing radiation beams such as x-rays or γ-rays, eliminating the need for conventional invasive surgery. SRS is used in the treatment of benign and malignant lesions as well as functional disorders (e.g. pituitary adenoma, acoustic neuroma, meningioma, arteriovenous malformations (AVM) etc). The AVM is the most common application of radiosurgery (Webb 1993).

In India, gamma rays from a dedicated Gamma Knife system (Elekta Medical System) and megavoltage x-rays from linac are used to perform SRS. In the linac-based radiosurgery system (X-Knife), field sizes are defined by secondary/tertiary collimators (circular cones or micro multileaf collimator, µMLC) that are either attached to the end of the gantry head or an integral part of the gantry head. Cones are divergent and are used to define circular fields with diameters typically varying from 5 mm to 40 mm (Das *et al* 1996).

In case of stereotactic radiotherapy (SRT), the dose is delivered in multiple fractions (1.8-2 Gy per fraction over 5-6 weeks). The SRT can be used for curative as well as boost to primary lesion/target. The SRT is done by linac using X-Knife system. In general SRS/SRT uses small fields under conditions of lateral electronic disequilibrium and dosimetry is verified by comparing measured data from multiple detectors recommended for small field dosimetry. AAPM TG-135 has provided detailed discussion on the dosimetry tools and techniques for SRS (Dieterich *et al* 2011).

Recently a frameless stereotactic radiosurgical device, called Cyberknife, has been developed. Cyberknife uses a miniature 6 MV linac mounted on a robotic arm. The linac uses an x-band cavity magnetron and a standing wave, side-coupled accelerating waveguide, to produce a 6 MV x-ray treatment beams with a dose-rate of 1000 cGy/min. There is no beam flattening filter in Cyberknife. Secondary collimation is provided using twelve fixed circular collimators with diameters ranging from 0.5- 6 cm. A complete description of this treatment system is given in Kilby *et al* (2010). The system uses on-line x-ray images to continuously monitor the treatment volume within a patient with a high degree of precision. The megavoltage x-ray beam is aimed at the precisely determined treatment volume using pre-planned beam orientation. Cyberknife can be used to treat lesions outside the cranium (e.g. spine, lung, prostate, liver etc.). Skeletal landmarks or fiducial markers implanted in a patient are used to treat lesions of the thorax and the pelvis.

1.4.2.6 Stereotactic Ablative Body Radiotherapy

In the early 1990s, Lax *et al* (1994) and Blomgren *et al* (1995) extrapolated the concept of stereotactic radiosurgery in the treatment of intracranial tumour to extracranial sites like liver and lung with encouraging results. The term ‘stereotactic body radiotherapy’ was coined to describe the precise delivery of a focused small ionizing radiation beams to body lesions (lung, liver and spine tumours) using a 3D coordinated systems/arrangements with reference to a fiducial marker that can be readily detected by imaging system. Its synonym, *stereotactic ablative body radiotherapy* (SABR, pronounced as ‘SAY-BER’) has recently been advocated because the term ‘ablation’ can more accurately reflect the ultra-high radiation dose delivered in each fraction of radiation treatment, so as to overwhelm the normal cellular repair mechanisms and ‘ablate’ the tumour and adjacent tissues (Loo *et al* 2010).

SABR is a form of high-precision radiotherapy characterized by: reproducible immobilization to avoid patient movement during radiation delivery; measures to account for tumour motion during treatment planning and radiation delivery; dose distributions tightly covering the tumour, with steep dose gradients away from the tumour into surrounding normal tissues in order to minimize toxicity.

Non-small cell lung cancer (NSCLC) is the leading cause of cancer-related mortality worldwide, with over 1 million deaths every year (Ferlay *et al* 2010). The SABR delivered to stage I primary NSCLC achieves excellent local control rates.Typical radical radiotherapy regimes for stage I lung cancer, prior to SABR, consisted of total doses of 55-74 Gy in 20-37 fractions of 2-2.75 Gy over a period of 4-7.5 weeks. Typical SABR regimes now deliver a dose of 54-60 Gy in 3-5 fractions of 12-20 Gy per fraction (Goldsmith and Gaya 2012).

The major feature that separates SBRT from conventional radiation treatment is the delivery of large doses in a few fractions, which results in a high biological effective dose (BED). In conventional radiotherapy, fractionated schedules delivering 2 Gy per fraction (e.g. 64 Gy in 32 fractions or 70 Gy in 35 fractions) typically have a BED (for $\alpha/\beta = 10$ Gy) of 70-80 Gy (Fowler *et al* 2004). In contrast, modern SABR schedules use doses equivalent to a BED >100 Gy, resulting in superior tumour cell kill while minimizing the dose to the surrounding tissues, which is a significant improvement compared with conventional fractionated radiotherapy in stage I NSCLC (Nagata *et al* 2005, Chang *et al* 2008, Zhang *et al* 2011). A frequently used schedule for peripheral lung tumours is 20 Gy × 3 fractions, which delivers a BED as high as 180 Gy (McGarry *et al* 2005*)*. The delivery of such high doses of radiotherapy per fraction (hypofractionation) means that the irradiated tumour cells (as well as any normal body cells irradiated to the prescribed dose) cannot possibly repair DNA strand breaks. The prescribed dose (> 8.0 Gy per fraction) is considered ablative (Timmerman 2008).

This unique therapeutic advantage has been exploited with good results for early-stage, inoperable NSCLC (McGarry *et al* 2005, Nagata *et al* 2005, Xia *et al* 2006, Chang *et al* 2008, Lagerwaard *et al* 2008). AAPM TG-101 has provided detailed discussion on SABR including protocols, equipment, and QA procedures etc. (Benedict *et al* 2010).

1.5 Challenges in small-field dosimetry

In modern radiation therapy small photon fields are often used during SRS, SABR, IMRT or VMAT in order to achieve the desired, highly-focused and precisely modulated dose distribution. A photon field is defined as ‘small’ when the field size is not large enough to provide charged particle equilibrium (CPE) at the position of measurement; that is, when the field width is smaller than the (lateral) range of secondary charged particles for the beam quality in question. Accurate determination of the doses delivered by these small or very small radiation fields present many challenges not encountered for large fields (Sánchez-Doblado *et al* 2007, Capote *et al* 2004, Alfonso *et al* 2008, Das *at al* 2008b, Bouchard *et al* 2009, Crop *et al* 2009, IPEM 2010, Francescon *et al* 2011, Scott *et al* 2012, Fenwick *et al* 2013, Kumar *et al* 2015b). The dosimetry of small megavoltage photon fields is challenging for several reasons including a lack of lateral electronic equilibrium, source occlusion, and the size of detector with respect to the field size (Treuer *et al* 1993, McKerracher and Thwaites 1999, Das *et al* 2008b, Alfonso *et al* 2008, IPEM 2010).

1.5.1 Lack of charged particle equilibrium

When a photon interacts with matter, it transfers energy to an electron (or positron). The secondary electrons produced by high-energy photons have long ranges and even though they initially travel predominantly in the forward direction, they will spread laterally because of electron scattering. The longest electron ranges in media irradiated by megavoltage photon beams are of the order of a few centimetres. Near the edges of (very) small fields electrons scatter from inside to outside the field and there is no compensating scatter *into* the field from outside. Since the electron range increases with energy, the minimum beam radius at which lateral electronic disequilibrium becomes significant increases as the beam energy increases (Metcalfe *et al* 1997). Thus material ***laterally*** as well as 'upstream' is necessary for the establishment of CPE. Lateral electronic disequilibrium is said to exist on the central axis for small beam radii/sizes because electrons displaced laterally away from the beam axis are not replaced by equal numbers displaced laterally towards the central axis. This is illustrated in figure 1.2.

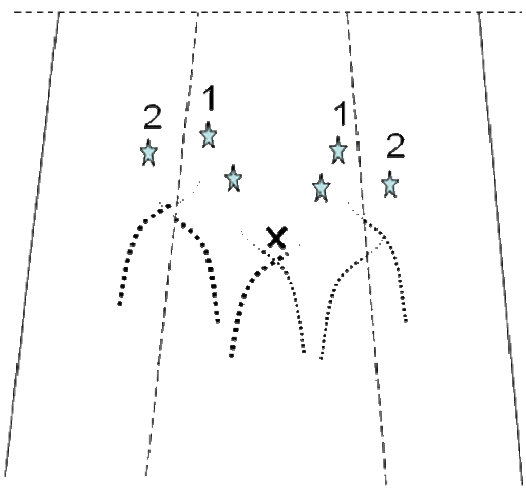

Figure 1.2: **Schematic illustration of charged particle disequilibrium for very narrow fields. For a given incident photon fluence (or kerma), the electron fluence at position × due to the narrow (dashed) photon field is reduced below that obtained for a broader equilibrium photon field (edges indicated by full lines); electrons '1' are not replaced by electrons '2'. (adapted from Gagliardi *et al* (2011))**

At a given photon energy (or MV), as the field size is reduced beyond a certain width the amount of material laterally will no longer be sufficient and the electron fluence and therefore the dose will fall: *electrons leaving the volume laterally (labelled '1') will no longer be replaced by ones entering (labelled '2')*. This results in loss of lateral electronic equilibrium. Lateral charge particle disequilibrium thus *always* occurs at the beam edges and exits at distances from a beam edge up to the maximum lateral secondary electron range. The distance required in a medium for electronic equilibrium depends on the beam energy, and the composition and density of the medium. In non-equilibrium (small) fields, perturbation factors which correct for minor deviations from Bragg-Gray conditions in 'reference conditions' are invalid for converting (air) ionization to dose to water using (conventional) cavity theory (Sánchez-Doblado *et al* 2007, Kumar *et al* 2015b).

Li *et al* (1995) defined the lateral range required for CPE (r_{lcpe}) at a given energy or beam quality, and obtained values of r_{lcpe} from Monte-Carlo-derived ratios D/K_{col} (dose to collision kerma) in water. These authors derived the approximation r_{lcpe} (cm) = 5.973 × $\mathrm{TPR}_{20,10}$ – 2.688, where r_{lcpe} is defined as the maximum radius until which a beam can be considered to be 'small' for the beam quality $\mathrm{TPR}_{20,10}$ of the standard reference field, f_{ref} = 10 cm × 10 cm. Small-beam conditions can be assumed to exist when the external edge of the detector's sensitive volume is at a distance less than r_{lcpe} from the beam edge.

1.5.2 Source occlusion

The bremsstrahlung photon fluence generated by linacs can be divided into two components: i) direct radiation which originates from the effective x-ray source/focal spot in the bremsstrahlung target (usually of tungsten), and ii) indirect or extra-focal radiation which originates when target-generated bremsstrahlung photons are scattered at structures near or below the target (i.e. primary collimator, flattening filter, secondary collimators). The 'direct-beam' source or focal spot is not a point, but has an extended size which is usually defined by the full width at half maximum (FWHM) of the bremsstrahlung photon fluence distribution exiting the target; it is typically represented as a Gaussian distribution.

As collimator aperture of a linear accelerator is decreased, less of the flattening filter is exposed or 'visible' from the position of measurement. In small fields, therefore, indirect/extra-focal becomes less important in the determination of dose. When the beam aperture is extremely narrow, part of the extended source/direct beam source cannot be 'seen' at all at the position of the phantom/patient as shown in figure 1.3.

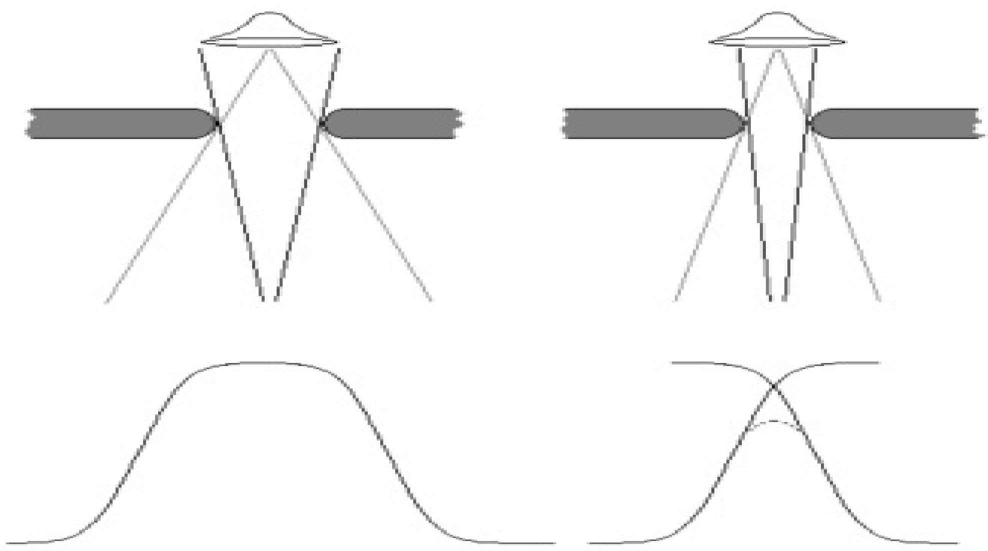

Figure 1.3: **Schematic illustration of the source occlusion effect (adapted from Scott *et al* (2009))**

The larger the focal spot size, the larger the collimator setting/jaw setting at which occlusion of the direct beam source begins (IPEM 2010). For large field sizes (i.e. approx. 4 × 4 cm^2 or greater) the whole of the focal spot can be seen from the detector location on central axis, and so the direct primary fluence component remains approximately constant. For very small fields the jaws are so close together that the outer edges of the focal spot are 'occluded' and therefore the kerma and the dose on the central axis falls significantly.

Focal spot sizes are difficult to determine experimentally, but Monte Carlo phase-space file modelling, where the focal spot FWHM is assumed to be between 1.0 and 1.5 mm, usually produces excellent agreement with measurement for percentage depth-doses (PDD) and beam profiles in water (Wang and Leszczynski 2007). To avoid dose calculation errors when modelling linear accelerators an accurate simulation of the extended source (focal spot) is of great importance (Scott *et al* 2008, Underwood 2013c).

1.5.3 Volume averaging

In addition to the constraints posed by the intrinsic radiation field and beam collimation, the detector size, relative to the dimensions of the field, plays a fundamental role. Due to the finite size of the detector its signal is necessarily an average over its volume. If the dose varies over the volume of the detector, this averaging can yield a different signal compared to that which an infinitesimally small detector would measure when positioned in the centre of the volume of the large detector. This is what is meant by so-called 'volume averaging'.

When the particle fluence crosses the detector volume, the detector signal M_{det} is proportional to the average dose in its sensitive volume, $\overline{D}_{\mathrm{det}}$, (volume-averaging effect). If the field size is smaller than the detector dimensions and therefore particles traverse only a fraction of the sensitive volume, the detector signal *averaged over its entire volume* will be clearly unrepresentative of the dose at the reference position in the uniform medium; a severe *under*-reading may result. Ideally a tiny, medium-equivalent detector is required– which doesn't exist.

In summary, the response of detectors in small fields can vary rapidly with field size due to volume averaging together with source occlusion and the lack of lateral electron equilibrium (Alfonso *et al* 2008, Ding and Ding 2012). During the course of this thesis work, the above mentioned effects have been studied deeply.

1.6 Interaction processes

The most important interactions of radiotherapy-quality photon beams with matter are:

- The attenuation of (primary) photons
- Energy transfer to charged particles, i.e. electrons and positrons
- Transport of charged particles
- Deposition of energy

The three most important photon interaction types at energies used in radiotherapy (Attix 1986, Dance and Carlsson 2007) are photoelectric, Compton and pair production processes. Other interaction processes are the coherent (Classical or Rayleigh) scattering and γ-n interactions, although their cross sections are small at radiotherapy energies. Figure 1.4 summarises the main interaction processes. The probability of each is determined by a cross section which depends on the photon energy and on the density and atomic number of the medium. More detailed information on photon interaction processes can be found in Attix (1986).

1.7 The need for Monte-Carlo simulation in dosimetry studies

Monte-Carlo (MC) calculations are an integral part of many current studies in radiotherapy. Particularly in radiation dosimetry, where experiments are very difficult to perform with an adequate degree of precision, and where many of the correction factors cannot be measured directly, many of the quantities of interest are determined using MC simulations (Mackie 1990, Rogers and Bielajew 1990**,** Andreo 1991, Buckley 2005, Crop *et al* 2009, Seco and Verhaegen 2013).

Monte-Carlo is especially valuable when the width of the photon field is so small as to make even quasi-CPE impossible (IPEM 2010). In small fields, volume-averaging together with source occlusion and loss of lateral electronic equilibrium result in the reduced signal observed in the central part of the beam and a drop in the measured beam output (Metcalfe *et al* 1997, Scott *et al* 2008, Scott 2009a, Underwood 2013c).

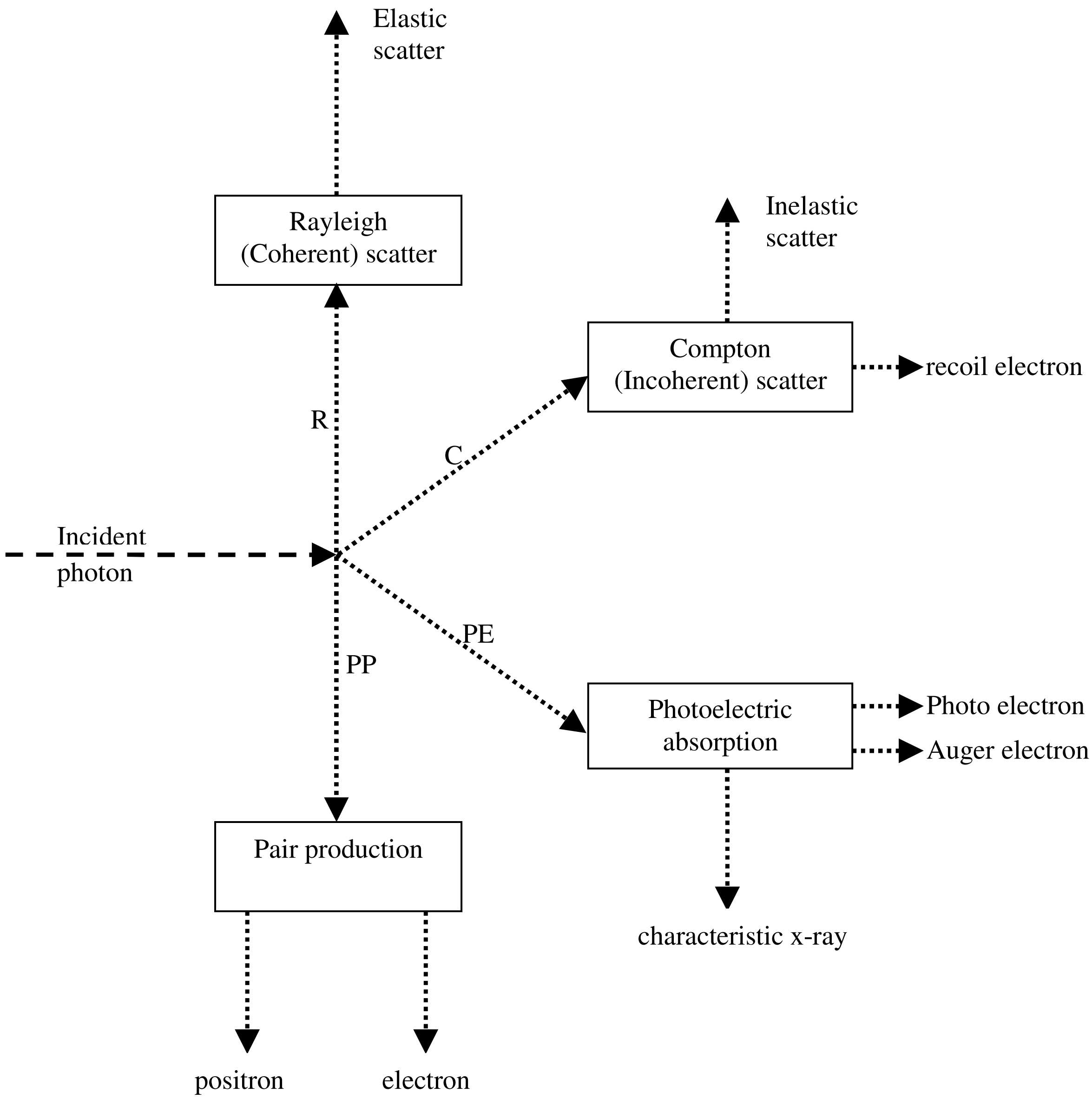

Figure 1.4: **Primary photon interaction processes with their secondary emissions**

Measurement-based effects include fluence perturbations caused by detectors with dimensions similar to the dimensions of the radiation fields, dose-averaging effects for measurements of peak dose distributions, and the increased errors for very small fields introduced by slight geometrical detector misalignment. In order to get the source-occlusion effect right, there is therefore a need to construct *a* detailed *Monte-Carlo model of a medical linear accelerator head using a suitable MC software* system. A validated Monte-Carlo model of accelerators is used further for the prediction of detector response, variations of photon and electron spectra in water and detectors, the calculation of dosimetric parameters (output factors, depth dose curves, and beam profiles) and the calculation of detector correction factors for small, non-standard treatment fields used for the advanced radiotherapy techniques. MC simulation has established itself as a useful tool in radiation therapy dosimetry and more recently for the study of small photon fields (Buckley 2005, Scott *et al* 2008, Scott *et al* 2009, Scott 2009a, Wulff 2010, Francescon *et al* 2011, Cranmer-Sargison *et al* 2011a, 2011b, 2012, Charles *et al* 2012, 2013, Scott *et al* 2012, Fenwick *et al* 2013, Underwood 2013c, Benmakhlouf *et al* 2014, 2015).

1.8 Monte Carlo method

Monte-Carlo simulation of radiation transport is a very powerful technique. There are basically no exact analytical solutions to the Boltzmann Transport equation. Even the 'straightforward' situation (in radiotherapy) of an electron beam depth-dose distribution in water proves to be too difficult for analytical methods without making gross approximations such as ignoring energy-loss straggling, large-angle single scattering and bremsstrahlung production. Monte Carlo is essential when radiation is transported from one medium into another. The MC simulation of particle transport requires a great deal of information regarding the interaction properties of the particle and the media through which it travels. As the particle (be it a neutron, photon, electron, proton) crosses the boundary then a new set of interaction cross sections is simply read in and the simulation continues as though the new medium were infinite until the next boundary is encountered. Details on Monte-Carlo techniques for electron and photon transport are given in Rogers and Bielajew (1990).

Having been used in medical physics for over fifty years (Rogers 2006), MC is considered to be the gold-standard transport simulation method for external-beam radiotherapy, brachytherapy and radionuclide therapy. A variety of different codes exists to enhance and optimise the performance of MC simulations for different particles and different energy ranges, the most widely used for medical application being MCNP (Brown 2003), GEANT (Agostinelli *et al* 2003), FLUKA (Battistoni *et al* 2007), PENELOPE (Salvat *et al* 2014) and EGSnrc (Kawrakow *et al* 2011). The PENELOPE and EGSnrc MC systems are to date the only MC systems capable of simulating accurately the response of ionization chambers; both the above codes pass the stringent test of verifying Fano's theorem (Fano 1954, Smyth 1986, Seuntjens *et al* 2002, Sempau and Andreo 2006). The EGSnrc Monte-Carlo system was chosen for this work.

1.8.1 The EGSnrc Monte Carlo system

The EGSnrc Monte Carlo code system (Electron-Gamma Shower) developed at the National Research Council of Canada (NRC) is a package of codes for the simulation of electron and photon transport through an arbitrary geometry (Kawrakow 2000a, Kawrakow *et al* 2011). It is the most recent version in the family of EGS Monte Carlo codes and is substantial improvement over its predecessor, the EGS4 version (Nelson *et al* 1985). Among other changes, EGSnrc uses an improved multiple-scattering theory which includes relativistic spin effects in the cross section, a more accurate boundary crossing algorithm, and improved sampling algorithms for a variety of energy and angular distributions. For a more detailed description of the features of the EGSnrc system, the reader is referred to the EGSnrc manual (Kawrakow *et al* 2011). The newest version of EGSnrc is a multi-platform version of the EGSnrc code, which retains all the physics of EGSnrc (Kawrakow *et al* 2006).

The EGSnrc Monte-Carlo code (Kawrakow 2000a, Kawrakow *et al* 2011) has been shown to be accurate within 0.1% with respect to its own cross sections for relative ionization chamber response calculations; this is known as the Fano test (Kawrakow 2000b).

1.8.1.1 User-codes of the EGSnrc Monte Carlo system employed in the present work

The EGSnrc system includes a set of user-codes (Rogers *et al* 2011b) developed for specific types of calculations which allows the definition of a geometry, the set-up of various particle sources (e.g. parallel beam of photons with certain spectral distribution), and the scoring of quantities sufficient for most problems. Table 1.1 describes the EGSnrc user-codes previously developed and used in the present study.

Table 1.1: **Brief description of the EGSnrc user-code used in the present study.**

User-code	Description
DOSRZnrc	Computes the dose, kerma and dose to kerma ratios to individual regions within a cylindrically symmetric (RZ) geometry. In the present study, it is used to generate depth dose information for a variety of monoenergetic photon beams as well as for input spectra.
FLURZnrc	Computes the fluence spectra (photon and electron (+ positron)) for designated regions within a cylindrically symmetric (RZ) geometry. It also outputs the mean energy of particles in a given region.
CAVRZnrc	Computes the total dose to a region (or regions) designated as the cavity in a cylindrically symmetric (RZ) geometry and to calculate some correction factors. It is similar to DOSRZnrc but also scores a variety of quantities which are of specific interest to dosimetry calculations for an ion chamber.
SPRZnrc	Computes the mass restricted electronic stopping-power ratio, medium to detector material specified in the input file for each region within the geometry.
'g'	Computes the mass energy-absorption and mass energy-transfer coefficients for the medium of interest.

A detailed description of these *user-codes* is given in Rogers *et al* (2011b).

1.8.1.2 Material data sets required for MC simulation

Prior to all simulations the cross section databases for photon and electron interactions are initialized. The data sets are provided in look-up tables for the materials found in the simulation geometries. PEGS4 is a stand-alone programme that is used to create material data files containing much of the cross section information for the materials of interest in the calculations (Nelson *et al* 1985, Kawrakow *et al* 2006, 2011). When a material data set is created using PEGS4, lower energy bounds AP and AE are defined where AP and AE are the production thresholds for secondary bremsstrahlung photons and knock-on electrons respectively. These parameters represent the lowest energies for which the material data are generated. Among other properties, at the time of creation of a data set, PEGS4 defines the density of the material and whether or not ICRU (or any other) density effect corrections will be applied. In this thesis, the required PEGS4 datafiles were generated depending upon the type of calculation.

1.8.2 Modelling a linac using BEAMnrc

A number of systems have been used for modelling radiotherapy linacs. The three systems most frequently used in medical physics are BEAMnrc (Rogers *et al* 1995, 2011a) which uses the EGSnrc code, PENELOPE (Salvat *et al* 2014) and MCNP (Brown 2003).

In this thesis (chapters 4-6), Monte-Carlo models of a Varian 2100C linear accelerator for photon beams of nominal energy 15 MV (Scott *et al* 2009) and of a Varian 2100 iX linear accelerator (Varian Medical Systems, Palo Alto, CA) for beams of nominal energy 6 MV (Underwood *et al* 2013c) were used. A Monte-Carlo model of both accelerators studied here was constructed in the BEAMnrc system (Rogers *et al* 1995, 2011a). BEAMnrc is a package that allows the user to quickly describe the geometry of their model and choose suitable values for parameters without advanced knowledge of any programming language. One builds a BEAMnrc model of a linear accelerator head by configuring a series of component modules (CM) to dimensions provided by the manufacturer. The typical CM used in modelling an accelerator head are: SLABS, CONS3R, FLATFILT, CHAMBER and JAWS.

The primary output of a BEAMnrc simulation is a phase space file. The measurement of this phase space is nearly impossible and not trivial even for just one of the dimensions. This file contains information on all particles crossing the xy-plane located at a fixed point along the z-axis. The xy-plane is referred to as a scoring plane, where any number of scoring planes can be defined and located along the accelerator head z-axis. A phase space file contains information on each particle: the energy (E), the xy-position (X,Y), the direction cosines with respect to the x and y-axis (U,V), the direction cosine of the angle with respect to the z-axis (SIGN(W)), the particle weight (WT), the charge (IQ), the number of times the particle has crossed the scoring plane (NPASS) and other particle history information (LATCH) (Rogers *et al* 2011a).

The 15 MV and 6 MV Monte-Carlo beam models used for the work described in this thesis were constructed by Scott *et al* (2009a) and by Underwood *et al* (2013c) respectively. Here the outline of a Monte-Carlo model of a Varian 2100C linear accelerator for photon beams of nominal energy 15 MV, adapted from Scott *et al* (2009a), is shown.

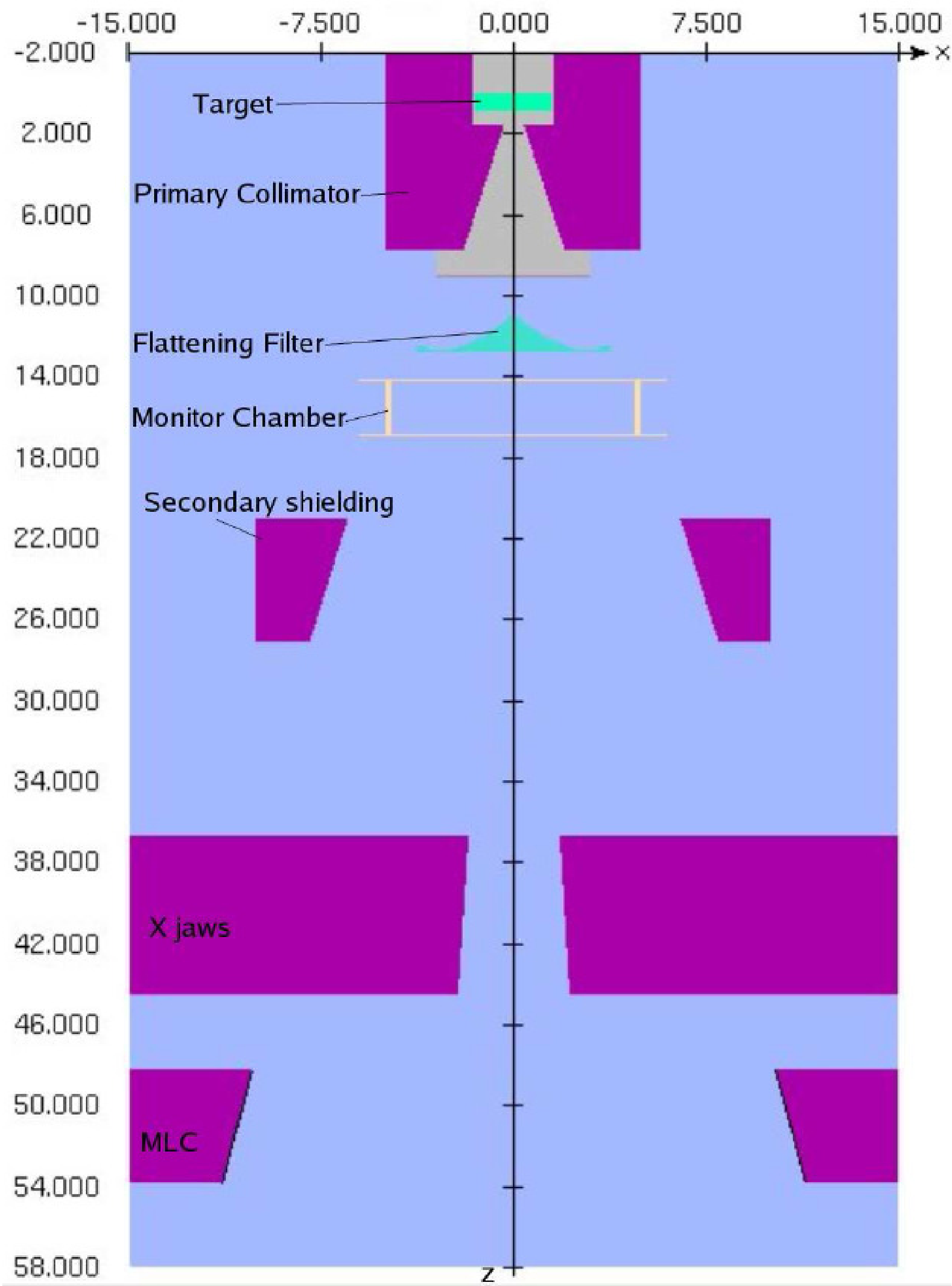

Figure 1.5: **Outline of the MC model of a Varian 2100C linac for photon beams of nominal energy 15 MV, image from BEAMnrc software. The Y jaws are not shown since they are perpendicular to the page, but are positioned above the X jaws. The MLCs are positioned well out of the field (adapted from Scott *et al* (2009a)).**

1.9 Aims/Objectives of the work undertaken for the thesis

In this thesis the Monte-Carlo (MC) simulation of radiation transport was applied to the following areas:

- A critical re-examination of certain basic concepts of radiation dosimetry **(Papers III and V)**.
- An improvement of our knowledge and understanding of the response of practical dosimeters in the non-equilibrium (small-field) situations commonly encountered in advanced radiotherapy treatments **(Papers I and IV)**.
- A study of certain aspects of 'cavity theory' in order to extend the range of validity of this body of theory **(Papers II, IV and VI)**.

1.10 Scope of the present study

During this thesis work the approach has been theoretical i.e. no new measurements were involved and Monte-Carlo simulation was the main computational tool. Certain new analytical expressions have been developed to describe and explain the simulation results. The work presented in this thesis provides guidance on the types of detectors/dosimeters that can be used for reliable absorbed dose determination in certain situations and the ones which cannot. In this thesis, the following areas and associated problems have been approached/solved/tackled:

- Fundamental dosimetry – kerma and its relationship to absorbed dose and to energy conservation **(Papers III and V)**.
- Small megavoltage photon fields – dosimeter response and its relationship to Bragg-Gray cavity theory **(Papers I, II and IV)**.
- Cavity theory – an exploration of the limits of validity of the Spencer-Attix-Nahum cavity theory and aspects of Burlin or general cavity theory **(Paper VI)**.

The scientific literature relevant to the thesis is summarized in this chapter. However, more specific publications are reviewed in the individual chapters. Chapters 2, 4, 5 and 6 of this thesis have already been published in the form of research papers in peer-reviewed international journals; these are denoted by Papers III, I, II and IV in the publications list.

CHAPTER 2

Monte-Carlo derived Insights into Dose-Kerma-Collision Kerma inter-relationships for 50-keV to 25-MeV photon beams in water, aluminium and copper

2.1 Introduction

Energy deposition in a photon-irradiated medium is a two-step process: (i) the photons transfer their energy to atomic electrons (and positrons) via the pair production, Compton and photoelectric processes, and (ii) these charged particles dissipate their kinetic energy in (multiple) coulomb-force interactions with bound atomic electrons in addition to creating bremsstrahlung photons (e.g. Attix 1968). ICRU-85 (2011) defines *kerma*, K, for ionizing uncharged particles, as the quotient of $\mathrm{d}E_{\mathrm{tr}}$ by $\mathrm{d}m$, where $\mathrm{d}E_{\mathrm{tr}}$ is the mean sum of the initial kinetic energies of all the charged particles librated in a mass $\mathrm{d}m$ of a material by the uncharged particles incident on $\mathrm{d}m$. Therefore kerma includes the energy that the charged particles eventually re-radiate in the form of bremsstrahlung photons and can be partitioned into two components, namely collision kerma, K_{col}, and radiative kerma, $K_{\mathrm{rad,}}$ (Attix 1979a, 1979b). The other fundamental quantity is *absorbed dose*, the energy imparted to the medium by ionizing radiation. ICRU-85 (2011) defines *absorbed dose*, D, as the quotient of $\mathrm{d}\varepsilon$ by $\mathrm{d}m$, where $\mathrm{d}\varepsilon$ is the mean energy imparted by ionizing radiation to medium of mass $\mathrm{d}m$. The relationships between D, K, and K_{col}, as a function of depth in photon-irradiated media are of fundamental importance in illustrating and quantifying the two-step process referred to above i.e. firstly transfer of energy in the form of kinetic energy of charged particles and secondly the imparting of this kinetic energy to the medium. Furthermore, absorbed dose and kerma (both types) have the same unit, gray, which emphasises the need for conceptual clarity on the differences between them.

Under charged particle equilibrium (CPE), also known as electronic equilibrium, absorbed dose is exactly equal to collision kerma (Dutreix *et al* 1965, Attix 1979a, 1986). In an irradiated medium, CPE is never exact, with the ratio of absorbed dose at a given point to the collision kerma at the same point often written as $\beta = (D/K_{\mathrm{col}})$ (e.g. Loevinger 1981, Attix 1986, Hannallah *et al* 1996). All these relationships are critically influenced by secondary electron transport, which makes Monte-Carlo simulation essential for obtaining accurate values of the various quantities. Monte-Carlo is especially valuable when the width of the photon field is so small as to make even quasi-CPE impossible (IPEM 2010).

Attix (1979a) illustrated the relationship between D, K, and K_{col} as a function of depth in aluminium (Al) for a 6 MeV broad photon beam. He presented an analytical expression for β in the transient-equilibrium region following Roesch (1958) and evaluated it for the 6 MeV broad photon beam in Al using the effective linear attenuation coefficient to account for scattered photons, as well as estimating the ratio *D/K*. Studies of the relationship between *D*, *K* and K_{col} have also been published by Loevinger (1981), Nilsson and Brahme (1983) and Iwasaki (1994).

In the literature referred to above, the photon energy was limited to either Co-60 γ-rays (mean energy 1.25 MeV) or 6 MeV. To date, there is no comprehensive study of the relationships between *D*, *K* and K_{col} for (broad) beams of kilovoltage (kV) to megavoltage (MV) quality, as a function of depth and in a variety of materials. There are also no systematic data available on how kerma and collision kerma differ from each other in photon beams of much higher energy in media of high atomic number (*Z*). For example, the figures illustrating how dose, kerma and collision kerma vary with depth in the section on *transient charged-particle equilibrium* in the well-respected textbook by Attix (1986) are unrepresentative of photon beams (of radiotherapy quality) in water, as it is shown in what follows.

Furthermore, there is no simple analytical expression in the literature for estimating $\overline{X}$, the mean distance travelled (in the direction of the primary radiation) by the secondary charged particles which deposit energy at the depth of interest; $\overline{X}$ plays a key role in the understanding of the difference between dose and collision kerma in real beams and in the numerical estimation of $D/K_{col.}$ Greening (1981) gives $\overline{X} = d = \mu_e^{-1}$ where μ_e^{-1} is the *linear attenuation coefficient* of the secondary electron energy fluence but it is not straightforward to calculate μ_e. In this chapter an approximate expression for $\overline{X}$ in terms of the *continuous slowing-down approximation,* csda, range of the mean initial energy of the secondary electrons, $R_{csda}(\overline{E_0})$, is derived and compare it to accurate Monte-Carlo-derived values. Using this easy-to-evaluate approximation for $\overline{X}$ in the well-known expression for D/K_{col} (e.g. Attix 1986) leads to an expression for *D/K* which shows explicitly how this key quantity can take values both above and below unity depending on energy and material.

By employing the EGSnrc Monte-Carlo code system (Rogers *et al* 2011b) the values of *D*, *K* and K_{col} as a function of depth in water, aluminium and copper media (thus spanning a range of atomic numbers) for photon energies from 50 keV to 25 MeV, as well as for several clinical x-ray beam qualities ranging from 100 kV to 15 MV in water have been computed. Additionally, the field-size dependence of *D/K* in 'non-equilibrium' small photon fields (e.g. Scott *et al* 2009, IPEM 2010) has been investigated for square fields ranging from 0.25 x 0.25 to 10 x 10 cm^2 in a water phantom for megavoltage beam qualities ranging from 5 MeV to 15 MeV (mono-energetic) and spectra from 6 to 15 MV (from Mohan *et al* (1985)).

The photon fluence, differential in energy (per unit primary photon fluence at a depth of 69 g cm^{-2}), has also been computed for the case of a 25 MeV photon beam in the three materials in order to examine how the low-energy photon fluence (partly due to 'secondary' bremsstrahlung) changes relative to the primary fluence as a function of atomic number. The large depth was chosen to illustrate the effect of secondary bremsstrahlung.

Finally, the mean electron (+ positron) energy has been obtained as a function of depth for a range of megavoltage qualities including some 'clinical' photon beams; this has revealed some intriguing behaviour at very small depths for a 15 MeV monoenergetic beam.

2.2 Materials and Methods

2.2.1 Monte-Carlo Calculations

The EGSnrc user-code DOSRZnrc (version: V4-2.3.2) was employed to compute dose and kerma and the user-code FLURZnrc to generate photon and electron fluence spectra (Rogers *et al* 2011b). The calculations were carried out with the default settings, which include modelling the Compton interaction for bound electrons, the effect of any atomic relaxation events, and relativistic spin effects in the multiple-scattering theory for charged particles.

2.2.1.1 kV region

For 50-250 keV photon beams, the phantom was cylindrical with radius 5 cm and height (minimal) 0.078 cm; note that this very small height will exclude almost all backscatter. The minimum thickness of the scoring voxel was 0.0009 cm (Rogers and Bielajew 1985), chosen in order to reveal the very shallow build-up region. A PEGS4 datafile (pre-processor for EGS (Nelson *et al* 1985)) was generated with the EGSnrcMP package by setting the parameters AP = 1 keV, AE = 512 keV (total energy) where AP and AE are the production thresholds for secondary bremsstrahlung photons and knock-on electrons respectively. Electrons and photons were followed down to 1 keV kinetic energy (i.e. *ECUT* (electron cut-off energy) = 512 keV (total energy) and *PCUT* = 1 keV). The ‘Source 2’ option of the EGSnrc Monte-Carlo code system (i.e. a broad parallel beam) was used for this energy region.

Dose, kerma and *D/K* ratios were computed as a function of depth in the cylindrical phantom for beam qualities 50-250 keV using DOSRZnrc. When dose and kerma versus depth (in water) were plotted for a 100 keV monoenergetic photon beam, a bi-phasic build-up was observed, which warranted further investigation. Consequently FLURZnrc was used to obtain the primary electron fluence per MeV per unit incident photon fluence at each depth in the cylindrical water phantom as described above; the spectral bin width was selected to be 1.0 keV for the lowest energy bin (1.0 keV – 2.0 keV), then 2.0 keV for the next 2 bins and was gradually increased as the energy increased up to 10 keV, and was set at 5 keV thereafter. The beam qualities of 100 and 250 kV using the spectra distributed with the EGSnrc Monte-Carlo code system were added (Rogers *et al* 2011b).

2.2.1.2 MV Region

2.2.1.2.1 Computation of *D*, *K*, K_{col}, *D/K* and β as a function of depth

For Co-60 to 25 MeV photon beams, a beam radius of 5.55 cm (equivalent to a '10 cm ×10 cm' field size; Day and Aird 1996) was defined on the phantom surface. The 'Source 4' option of the EGSnrc Monte-Carlo code system (parallel beam, scoring regions on the central axis for different beam radii) was used; with this option the outer radius of the cylindrical phantom is effectively infinite. The height of the cylindrical phantom was fixed at 75 cm. The scoring cavity had a circular cross-section of 2 cm diameter with a height equal to the slab thickness which was varied from very small in the build-up region (e.g. for Co-60, 0.05 cm in water and 0.005 cm in Cu) to greater values at greater depths. The electron transport cut-off *ECUT* (kinetic energy) was set at 152 keV for water, 220 keV for aluminium and 103 keV for copper, chosen such that the *csda* ranges of electrons with energies equal to *ECUT* were never greater than 1/3 of the slab thickness (Rogers 1984, Rogers and Bielajew 1990). The photon transport cut-off *PCUT* was set at 1 keV in all cases. *D*, *K* and *D/K* were computed along the central axis of the beam from the surface to the end of the cylindrical phantom.

It is emphasised that kerma should not be computed by simply 'switching off' secondary charged-particle transport in the Monte-Carlo photon simulation and scoring energy deposition (per unit mass) as kerma; this approach removes any possibility of 'secondary' bremsstrahlung transport, and therefore underestimates the photon fluence 'downstream' thus distorting the computation of kerma at these greater depths. DOSRZnrc scores kerma by summing the initial kinetic energies of the secondary electrons (and positrons) at their point of creation but these particles are subsequently transported, thus ensuring that secondary bremsstrahlung photons are generated and make their contribution to kerma further downstream. This secondary bremsstrahlung is of critical importance at high energies in high-Z media.

As there is no option available in the user-code DOSRZnrc to compute collision kerma K_{col} directly, the ratio (K_{col}/K) was firstly obtained from the 'photon cavity integrals' given below (equations (2.1) and (2.2)). In order to evaluate equations (2.1) and (2.2) the total photon fluence per MeV per unit incident photon fluence was scored at each depth along the central axis of the cylindrical phantom using FLURZnrc. *K* and K_{col} were then calculated over energy fluence spectrum using the following cavity integrals (e.g. Nahum 2007b):

$$K_{\text{med}} = \int_0^{k_{\max}} k \frac{\mathrm{d}\Phi_{\text{med}}}{\mathrm{d}k} \left(\frac{\mu_{\text{tr}}(k)}{\rho} \right)_{\text{med}} \mathrm{d}k \qquad (2.1)$$

and

$$(K_{\text{col}})_{\text{med}} = \int_0^{k_{\max}} k \frac{\mathrm{d}\Phi_{\text{med}}}{\mathrm{d}k} \left(\frac{\mu_{\text{en}}(k)}{\rho} \right)_{\text{med}} \mathrm{d}k \qquad (2.2)$$

where k is the photon energy, $\mu_{tr}(k)/\rho$ the mass energy-transfer coefficient, $\mu_{en}(k)/\rho$ the mass energy-absorption coefficient, and $\mathrm{d}\Phi_{med}/\mathrm{d}k$ the photon fluence, differential in energy, in the medium[2] (which can also be written $[\Phi_k]_{med}$).

From equations (2.1) and (2.2), $K_{col}/K = (1 - \bar{g})$ was calculated at each depth in the cylinder and multiplied by K from DOSRZnrc to yield K_{col}, and hence D/K_{col} (= β) as a function of depth using the values of D also computed using DOSRZnrc. The *D/K* ratios at corresponding depths were obtained directly from the DOSRZnrc simulations.

Dose, kerma and *D/K* were computed as a function of depth for beam qualities ranging from Co-60 to 25 MeV photon beams in water, aluminium and copper. The parameter β as a function of depth was derived as described above for the three materials. Tables 2.2 and 2.3 compare present study *D/K* and β values with published data. The total photon fluence, differential in energy, as a function of depth was also obtained from FLURZnrc in the three phantom materials irradiated with 25 MeV photon beams in order to investigate the magnitude of the low–energy photon fluence (partly due to 'secondary' bremsstrahlung) relative to the primary fluence.

2.2.1.2.2 Computation of *D*/*K* in 'non-equilibrium' small photon fields as a function of field size

The *D/K* ratios in 'non-equilibrium' small photon fields for square field sizes ranging from 0.25 x 0.25 to 10 × 10 cm^2 were computed in a water medium for a range of beam qualities ranging from 5 to 15 MeV including clinical linac spectra (for point sources) of 6, 10 and 15 MV from Mohan *et al* (1985).

The *D/K* ratios were computed for each field size using DOSRZnrc with the 'source 1' option (i.e. point source, incident on front face). The scoring volume was a cylinder with a circular cross-section of 2.26 mm diameter and 2.0 mm thickness located on the central axis at 10 cm depth in a cylindrical water phantom (radius 15 cm, thickness 30 cm) to ensure sufficient depth beyond the depth of maximum dose (d_{max}) for the absorbed dose and kerma curves to become quasi-parallel to each other (Attix 1986). The source to phantom surface distance was 100 cm. The beam radius equivalent to each square field size (i.e. 0.25 × 0.25 to 10 × 10 cm^2) was defined at the phantom surface. *ECUT* was set at 512 keV (total energy) and *PCUT* at 1 keV, i.e. electrons and photons were generated and followed down to 1 keV.

2.2.1.2.3 Mean electron energy

To see how electron (+ positron) fluence spectra change with depth for megavoltage photons at a range of beam energies/qualities, the mean electron (+ positron) energies were obtained from

[2] Kerma computed from equation (2.1) was compared to the values obtained from DOSRZnrc for a number of data points, with identical normalization, and the agreement was generally within ±0.5%.

$$\overline{E}(z) = \frac{\int_0^{E_{\max}} E\,\Phi_{\mathrm{E}}^{\mathrm{prim}}(z)\,\mathrm{d}E}{\int_0^{E_{\max}} \Phi_{\mathrm{E}}^{\mathrm{prim}}(z)\,\mathrm{d}E} \tag{2.3}$$

where $\Phi_{\mathrm{E}}^{\mathrm{prim}}(z)$ is the 'primary' electron (+ positron) fluence, differential in energy (i.e. excluding 'knock-on' electrons, or *delta-rays*) at different depths z. These fluence spectra were generated for (broad, parallel) beams ranging from Co-60 to 15 MeV including 'clinical' photon beams of 6, 10 and 15 MV using FLURZnrc, with the same *ECUT* and *PCUT* as above. The source spectra employed were those distributed with the EGSnrc code system (Rogers *et al* 2011b) for Co-60 γ-rays (Rogers *et al* 1988), and for 6, 10 and 15 MV 'clinical' photon beams (Mohan *et al* 1985).

2.2.2 Simple analytical expressions for $\overline{X}$, D/K_{col} and D/K

Attix (1979a, 1986) has given the following expression for the absorbed dose to collision kerma ratio for the 'transient CPE' condition:

$$\frac{D}{K_{\mathrm{col}}} = \beta = e^{\frac{\mu_{\mathrm{eff}}}{\rho}\left(\overline{X}\right)} \tag{2.4a}$$

$$\approx\ 1+\ \frac{\mu_{\mathrm{eff}}}{\rho}\left(\overline{X}\right) \tag{2.4b}$$

This is the ratio of the photon fluence (integrated over energy) at the *centre of (secondary) electron production*, CEP (e.g. Boutillon and Niatel 1973), to the photon fluence at the depth of interest P, where $\overline{X}$ is the distance between these depths. Equation (2.4b) assumes that $\overline{X} \ll \rho/\mu_{\mathrm{eff}}$, the photon mean free path in units of mass per distance squared. The 'effective' mass attenuation coefficient μ_{eff}/ρ is smaller than the 'narrow-beam' coefficient μ/ρ due to the build-up of scattered photons; the μ_{eff}/ρ from the gradient of the Monte-Carlo-generated kerma versus depth curves was obtained for each beam quality and material (see tables 2.5a-c).

The factor β is also involved in the determination of primary standards for the quantity air kerma for Co-60 and Ir-192 gamma-ray sources using thick-walled graphite cavity ionization chambers. The secondary electrons that contribute to ionization in the cavity gas originate from photon interactions that take place within the wall at a point *upstream* from the cavity and therefore this photon fluence is not been attenuated by the full wall thickness (see figure 2.1). The factor K_{cep} accounts for the difference in the positions of the centre of electron production and point of interest; it is one of the components of the overall wall correction factor (Boutillon and Niatel 1973, Attix 1984, Sander and Nutbrown 2006, Burns *et al* 2007); K_{cep} is related to D/K_{col} through $(K_{\mathrm{cep}})^{-1} = \beta = D/K_{\mathrm{col}}$.

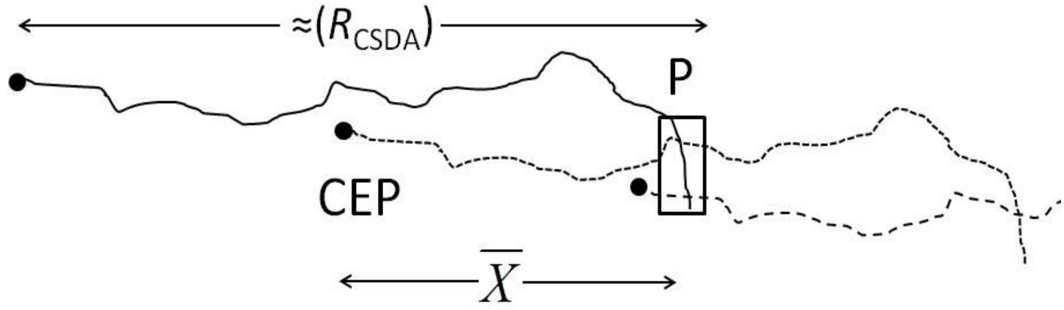

Figure 2.1: **Pictorial explanation of equation (2.5), the simple analytical expression for $\overline{X}_{\mathrm{emp}}$. Three secondary electron tracks of initial energy $\overline{E_0}$, are shown, which contribute fluence (track length per unit volume) and hence deposit energy (and therefore dose) in a small volume at the depth of interest (P), where dose and kerma are required. The CEP is the mean origin of the electrons which contribute fluence to the small volume at P.**

An expression for $\overline{X}$ will now be developed; clearly, it will be related to the ranges of the secondary electrons. Figure 2.1 is a simplified representation of the situation. The quantity $R_{\mathrm{csda}}(\overline{E_0})$, the *continuous slowing-down range*, is taken as a first-order approximation of the mean distance a secondary electron travels in the photon direction, where $\overline{E_0}$ is the mean initial electron energy of the secondary electrons set in motion by photons. Contributions to the electron fluence, and hence to the dose, in a small volume at P arise from electrons with their positions of origin ranging from very close to P to a maximum distance equal to $R_{\mathrm{csda}}(\overline{E_0})$. It is therefore reasonable to assume that *mean* position of the origin of the secondary electrons (i.e. the CEP discussed above) is at a distance approximately equal to $0.5\times R_{\mathrm{csda}}(\overline{E_0})$ from P. Hence the following empirical expression is proposed for $\overline{X}$, denoted by $\overline{X}_{\mathrm{emp}}$:

$$\overline{X}_{\mathrm{emp}} \approx 0.5\times R_{\mathrm{csda}}(\overline{E_0}) \qquad (2.5)$$

The value of $\overline{X}$ is subject to two effects which act in opposite directions. Firstly the csda range automatically includes the *detours* of electron tracks, which are due primarily to elastic nuclear scattering (e.g. Tabata and Andreo 1998); consequently the straight-line distance will be less than the csda range and this will effectively *reduce* the factor multiplying $R_{\mathrm{csda}}(\overline{E_0})$ below 0.5. However, the contribution to the dose at P from electrons originating at different upstream distances will, to first order, be proportional to their contributions to the electron fluence at P (ignoring the relatively minor variation of the electronic stopping power, $(\mathrm{d}E/\mathrm{d}s)_{\mathrm{el}}$ or S_{el}, with energy at relativistic energies). Now the fluence at 'P' per electron will be greater for the more oblique or diffuse electron tracks, and the average degree of obliquity will tend to increase with distance from the point of creation (cf. the build-up of electron fluence, and hence dose, in a broad electron beam); the tracks in the volume at P in figure 2.1 indicate schematically this increasing obliquity. This second effect means that electrons originating furthest away will make the greatest contribution to the fluence at 'P', and this will tend to *increase* the multiplying factor. Due to these two competing effects it has been chosen not to modify the factor 0.5 in equation (2.5).

Combining equations (2.4b) and (2.5), the following approximate expression for β, the dose to collision kerma ratio is arrived:

$$\left(\frac{D}{K_{\mathrm{col}}}\right)_{\mathrm{med}} \approx \left(1+\frac{\mu_{\mathrm{eff}}\left(\bar{k}\right)}{\rho}\left[0.5\times R_{\mathrm{csda}}^{\mathrm{med}}(\overline{E_0})_{\bar{k}}\right]\right) \tag{2.6}$$

An estimate of $\overline{E_0}$ is also required. It is straightforward to show that the mean initial energy of secondary electrons liberated by photons of energy k is given by

$$\overline{E_0} = \left\{k\times\left(\frac{\mu_{\mathrm{tr}}(k)}{\mu(k)}\right)\times\left(\frac{\sigma_{\mathrm{total}}(k)}{\sigma_{\mathrm{pe}}(k)+\sigma_{\mathrm{C}}(k)+2\sigma_{\mathrm{pp}}(k)}\right)\right\} \tag{2.7}$$

where $\sigma_{\mathrm{total}}(k)$, $\sigma_{\mathrm{pp}}(k)$,$\sigma_{\mathrm{C}}(k)$ and $\sigma_{\mathrm{pe}}(k)$ are the total, pair production, Compton and photoelectric atomic interaction cross sections at photon energy k respectively for the medium of interest. In the case of a photon spectrum, e.g. an x-ray beam, the energy k in equation (2.7) should be a *collision-kerma-weighted* mean value over the photon fluence spectrum, $\bar{k}$, i.e. weighted by $\mu_{\mathrm{en}}(k)/\rho$.

An approximate expression for (D/K) now follows. Firstly the equations (2.1) and (2.2) is combined to yield

$$\left(\frac{K_{\mathrm{col}}}{K}\right)_{\mathrm{med}} = 1-\left(\bar{g}_{\bar{k}}\right)_{\mathrm{med}} \tag{2.8}$$

where $\bar{k}$ is the mean energy of the photon beam (for monoenergetic photons $\bar{k} = k$; for a spectrum - see above) and $\bar{g}_{\bar{k}}$ is the average fraction of the secondary electron energy re-radiated as bremsstrahlung for photons of energy $\bar{k}$ in medium *med*. Eliminating K_{col} between equations (2.6) and (2.8) and replacing μ_{eff}/ρ by μ/ρ, the following approximate expression for the dose to kerma ratio is arrived:

$$\left(\frac{D}{K}\right)_{\text{anl, med}} \approx \left(1\text{-}\left(\overline{g}_{\bar{k}}\right)_{\text{med}}\right)\left[1+0.5\frac{\mu\left(\bar{k}\right)}{\rho}R_{\text{csda}}^{\text{med}}(\overline{E_0})_{\bar{k}}\right] \qquad (2.9)$$

It is seen that the first term in equation (2.9) is always less than (or equal to) unity and the second term always greater than unity. The difference between μ_{eff}/ρ and μ/ρ has been ignored, firstly as there is no simple way to estimate this difference, and secondly as equation (2.9) is an approximate expression.

Finally, returning to the more exact expression (2.4a) for D/K_{col} and re-arranging it, $\overline{X}$ can be written as

$$\overline{X} = \left\{ Log_{\text{e}}\left(\frac{D}{K_{\text{col}}}\right) \Big/ \frac{\mu_{\text{eff}}}{\rho} \right\} \qquad (2.10)$$

Values of $\overline{X}$ were obtained from equation (2.10) for photon energies ranging from 5 MeV - 25 MeV for the three materials including clinical beams (Co-60, 6 MV, 10 MV and 15 MV) for water medium; in what follows the $\overline{X}$ obtained from equation (2.10) is denoted by $\overline{X}_{\text{MC}}$ as both D/K_{col} and μ_{eff}/ρ were obtained from Monte-Carlo simulations.

(a)

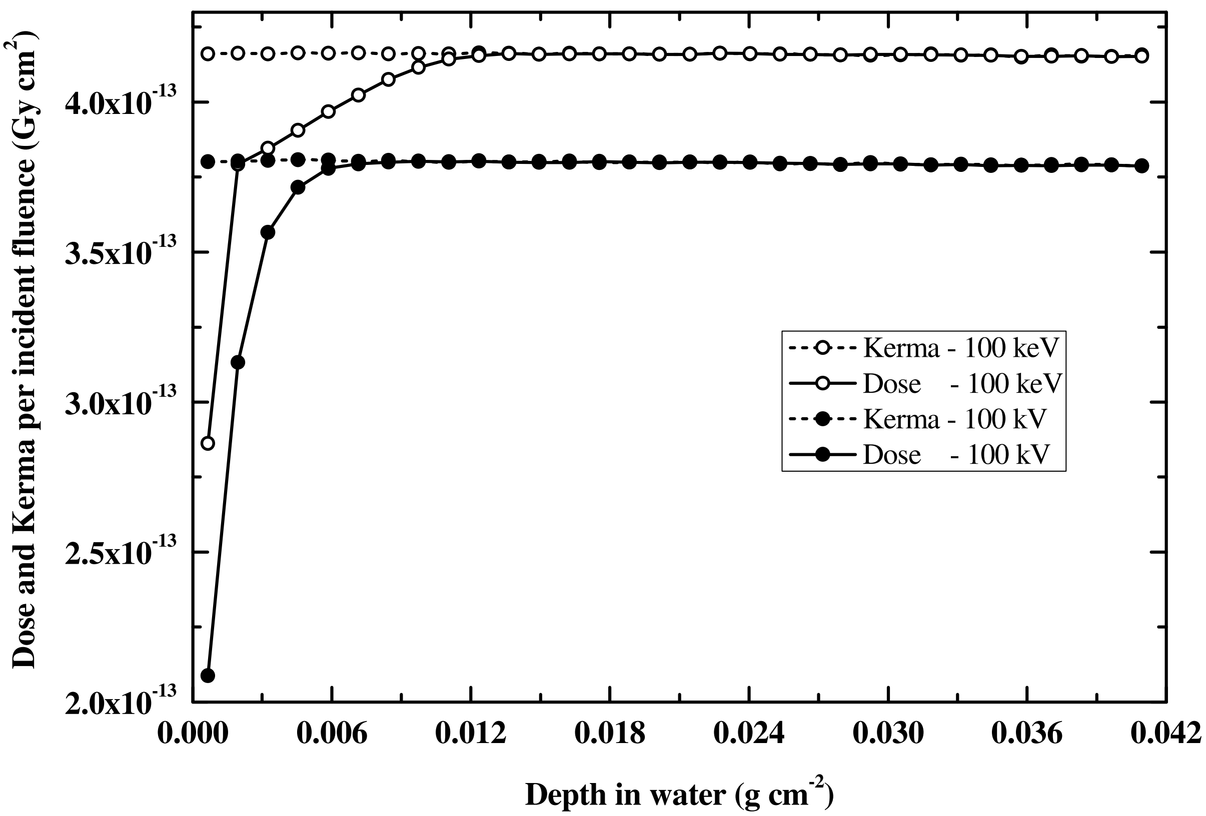

(b)

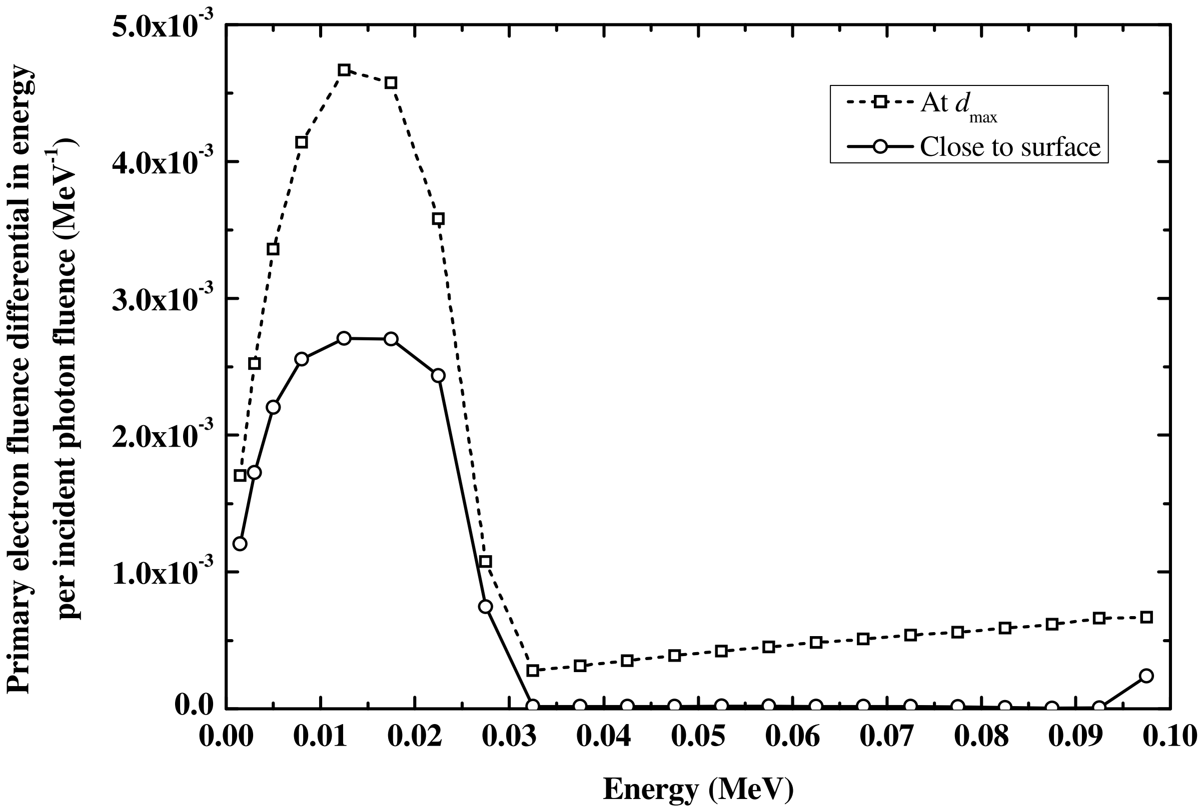

Figure 2.2: **(a) Dose and kerma (Gy/incident fluence) versus depth in water for broad, parallel 100 kV and 100 keV photon beams with *ECUT* (k.e.) = 1 keV. (b) 'Primary' electron fluence (per MeV per incident photon fluence) versus energy (MeV) close to surface and at d_{max} for a broad, parallel 100 keV photon beam with *ECUT* (k.e.) = 1 keV.**

2.3 Results and Discussion

2.3.1 Monte-Carlo calculations

2.3.1.1 kV region

Figure 2.2(a) shows the depth dependence of dose and kerma for a 100 keV monoenergetic photon beam and for a 100 kV spectrum in water. Figure 2.2(b) shows the primary electron fluence, differential in energy, close to surface and at the depth of maximum dose (d_{max}) in water for a 100 keV photon beam. The distribution of (primary) electron energy indicates that there are two distinct components, low-energy Compton electrons giving rise to a very rapid build-up, and a much slower build-up due to the higher-energy photo-electrons (Ma and Nahum 1991). At 250 keV and 250 kV, the bi-phasic build-up was not observed (see figure 2.3). The *D/K* and D/K_{col} values for beam qualities 50-250 keV in the three materials (water, aluminium, copper) are shown in table 2.1a.

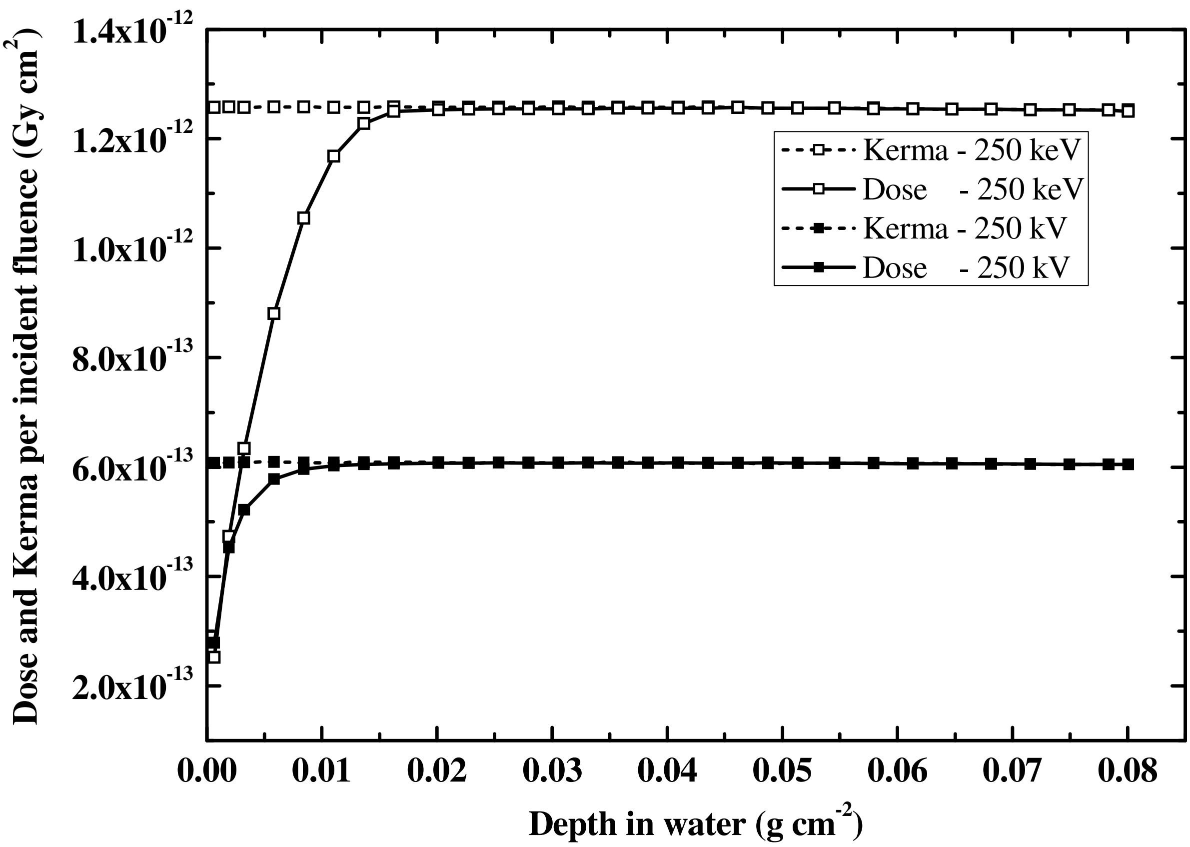

Figure 2.3: **Dose and kerma (Gy/incident fluence) versus depth in water for borad, parallel 250 keV and 250 kV photon beams with *ECUT* (k.e) = 1.0 keV.**

2.3.1.2 MV Region

2.3.1.2.1 D, K, K_{col}, D/K and β as a function of depth

Figures 2.4(a) – 2.4(c) show the depth dependence of dose, kerma and collision kerma for a 25 MeV photon beam in water, aluminium and copper. Beyond the depth of maximum dose, kerma is always greater than dose and collision kerma less than dose. Further, as the Z of the medium increases, and therefore radiative kerma is enhanced due to increased (secondary) bremsstrahlung production, the kerma curve is 'pulled up' over dose curve. Figure 2.4 (d) shows the depth-dependence of the same quantities for the 'clinical' beam quality of 15 MV in water. In this case the kerma and dose curves cannot be separated beyond the depth of maximum dose; Table 2.1 (b) indicates that the numerical difference is only ≈ 0.2%. This can be compared to figure 4.7b in Attix (1986) which shows very different behaviour more representative of high-energy mono-energetic photons in a high-Z material such as figure 2.4(c) presented in this chapter. A further point to note is that the area under the kerma curve exceeds that for either the dose or collision-kerma curves, which demonstrates that kerma does not conserve energy (Kumar and Nahum 2015).

(a)

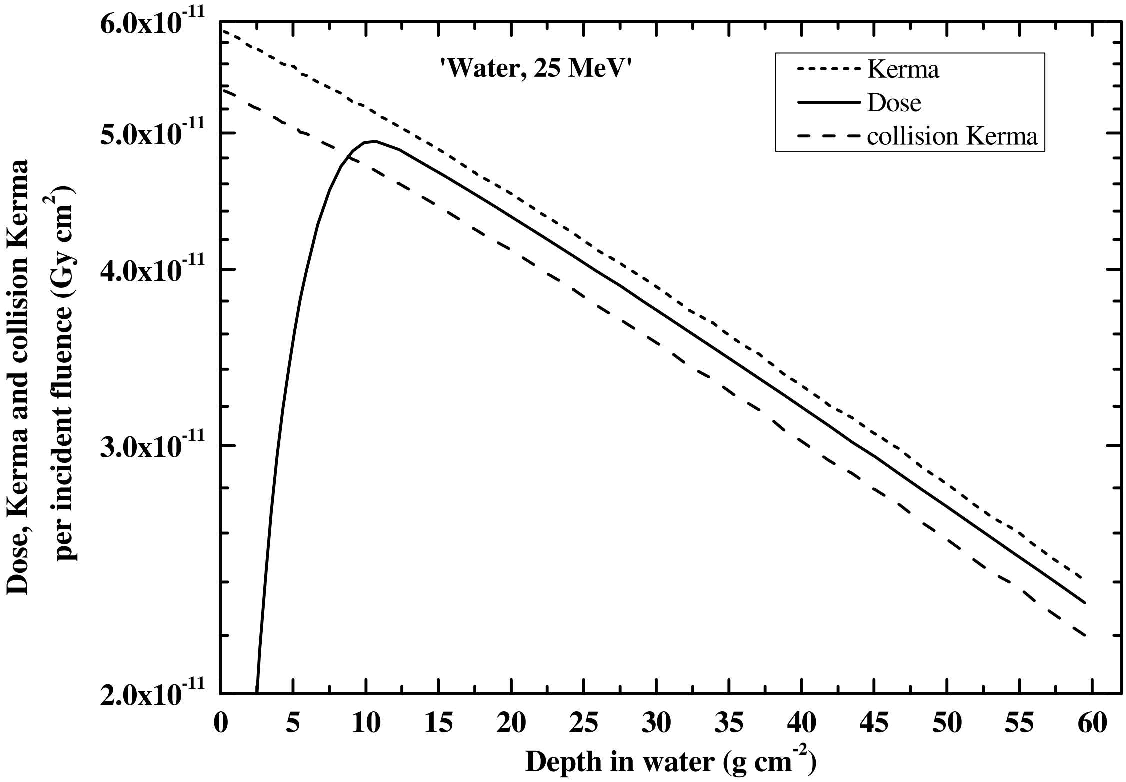
6.0x10^-11
5.0x10^-11
4.0x10^-11
3.0x10^-11
2.0x10^-11
'Water, 25 MeV'
Kerma
Dose
collision Kerma
Dose, Kerma and collision Kerma per incident fluence (Gy cm^2)
0
5
10
15
20
25
30
35
40
45
50
55
60
Depth in water (g cm^-2)

(b)

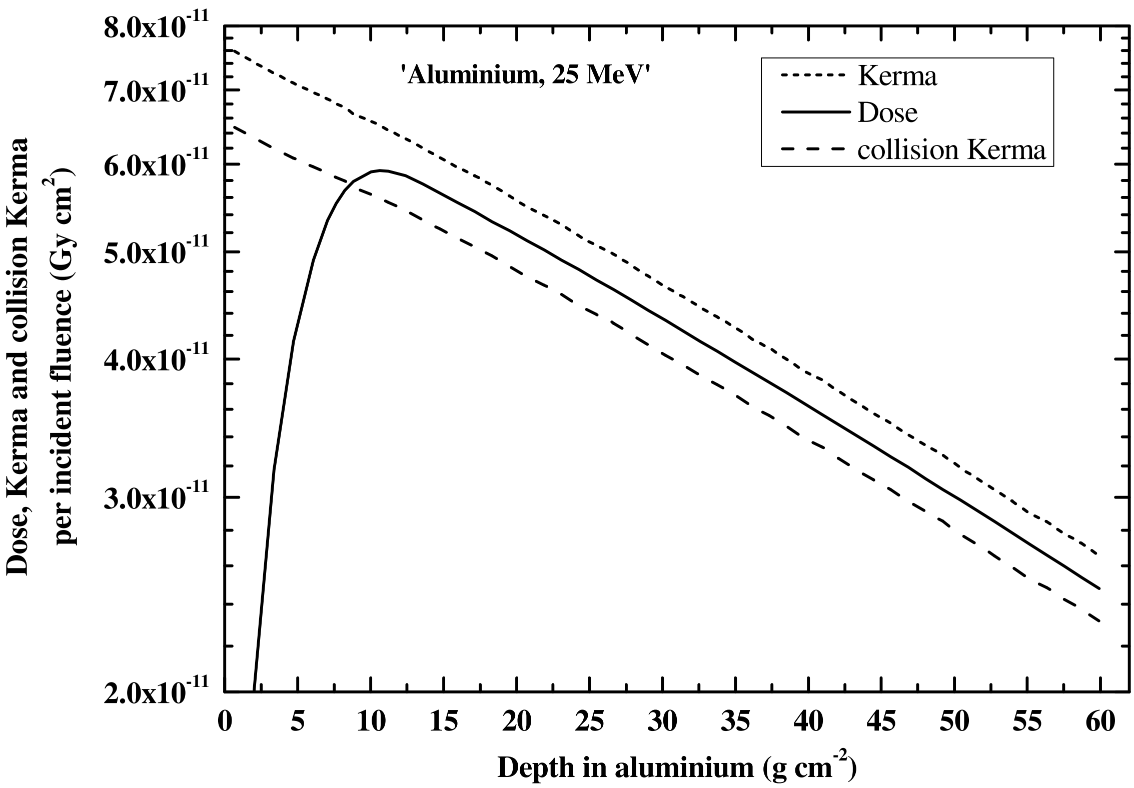
8.0x10^-11
7.0x10^-11
6.0x10^-11
5.0x10^-11
4.0x10^-11
3.0x10^-11
2.0x10^-11
'Aluminium, 25 MeV'
Kerma
Dose
collision Kerma
Dose, Kerma and collision Kerma per incident fluence (Gy cm^2)
0
5
10
15
20
25
30
35
40
45
50
55
60
Depth in aluminium (g cm^-2)

(c)

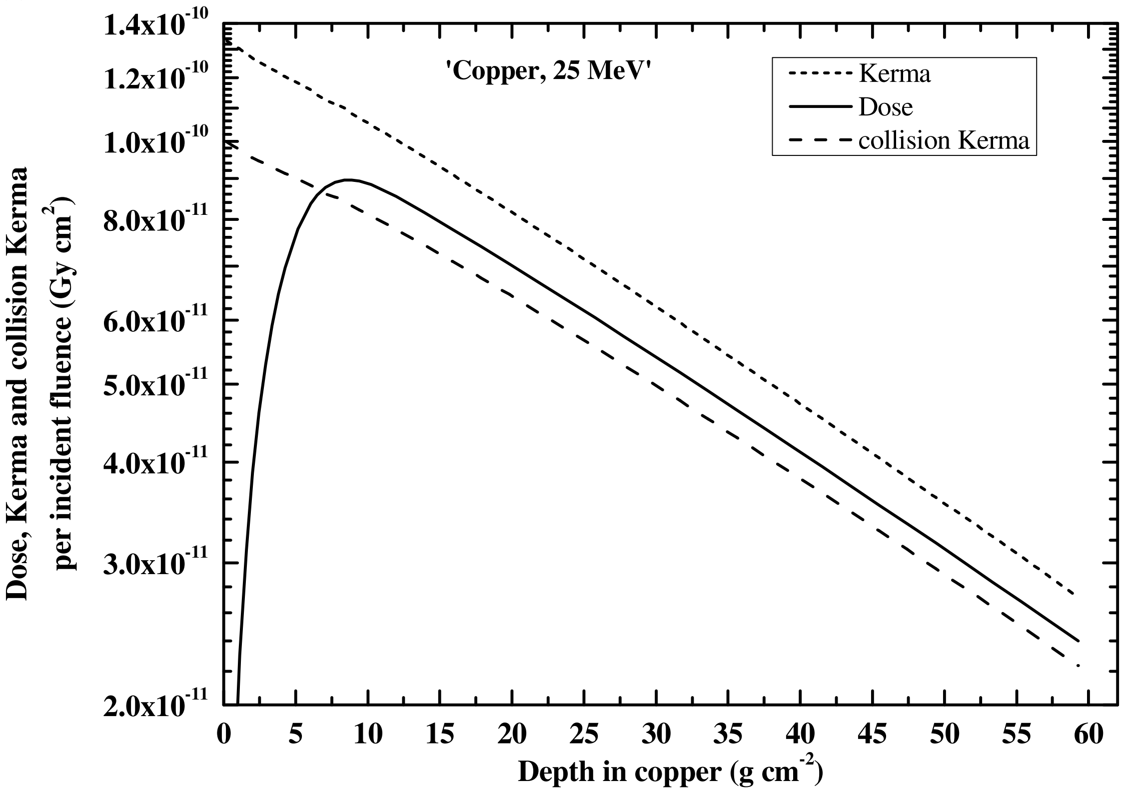

(d)

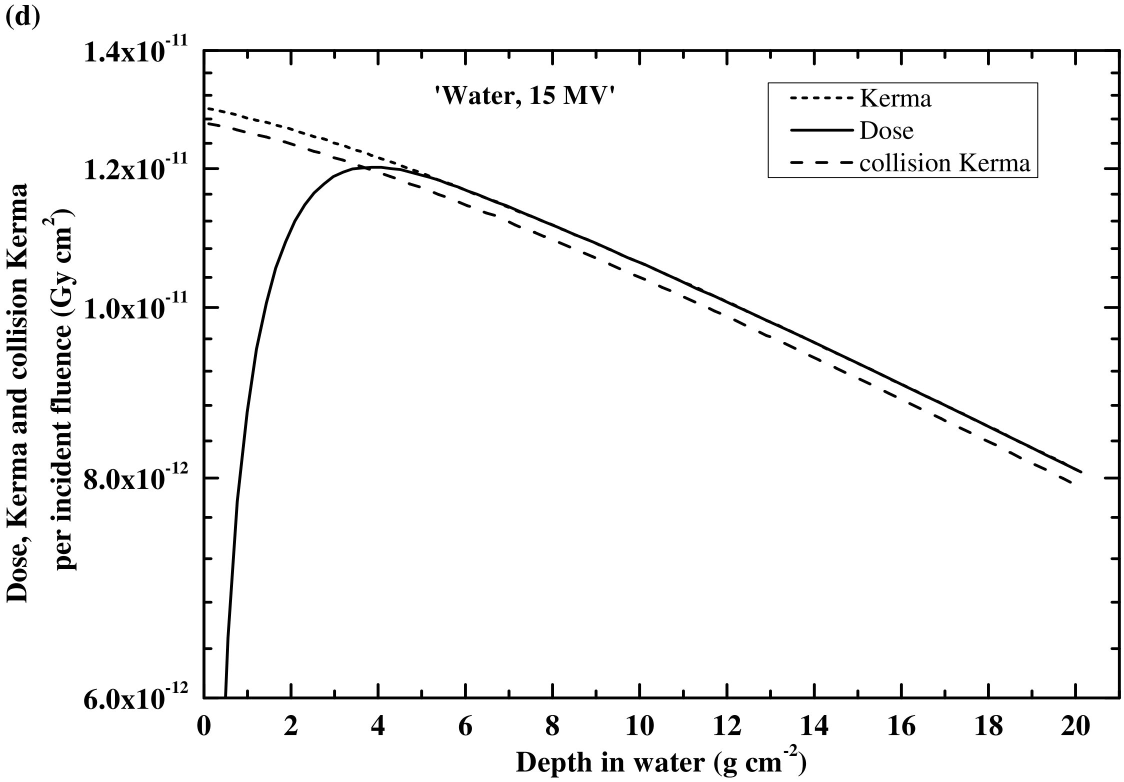

Figure 2.4: **(a) Dose, kerma and collision kerma per incident photon fluence (Gy cm^2) versus depth (g cm^{-2}), for a 25 MeV photon beam in water; (b) same quantities and energy for aluminium (c) same quantities and energy for copper; (d) same quantities, 15 MV 'clinical' photon beam (spectrum form Mohan *et al* (1985)) in water. Dose, kerma and collision kerma were computed using DOSRnrc (and FLURZnrc) along central axis for a field size of 10 × 10 cm^2 defined at the phantom surface.**

Figure 2.5 depicts the variation of the ratios *D/K* and D/K_{col} (= β) as a function of depth for all described materials for 25 MeV photon beams. Beyond the depth of maximum dose *D/K* and β remain very nearly constant, especially in water and aluminium. The variation of β with depth is consistent with that found by Iwasaki (1994). However, a slight depth dependence of the ratios *D/K* and D/K_{col} can be seen, especially in copper, as Bjärngard *et al* (1989) pointed out; *D/K increases* and D/K_{col} *decreases* with depth. In other words the *K* and K_{col} 'curves' converge slowly towards the dose curve as the depth increases. This can be understood by reference to figure 2.6 that shows (at a depth ≈ 69 g cm^{-2}) the fluences of low-energy photons relative to the primary fluence (i.e. at the incident energy); this 'ratio' is significantly higher in copper than in water or aluminium. This will have two effects at large depth: firstly the mean secondary electron energy will be slightly lower than that at shallower depths, which will reduce $\overline{X}$, and therefore cause D/K_{col} to be closer to unity, and secondly less (secondary) bremsstrahlung will be generated by the secondary electrons set in motion by the lower-energy photons, thus making $\overline{g}$ smaller and hence decreasing the difference between *K* and K_{col}. In figure 2.5, for 25-MeV photons, these effects are clearly visible in copper but barely discernible in aluminium or water.

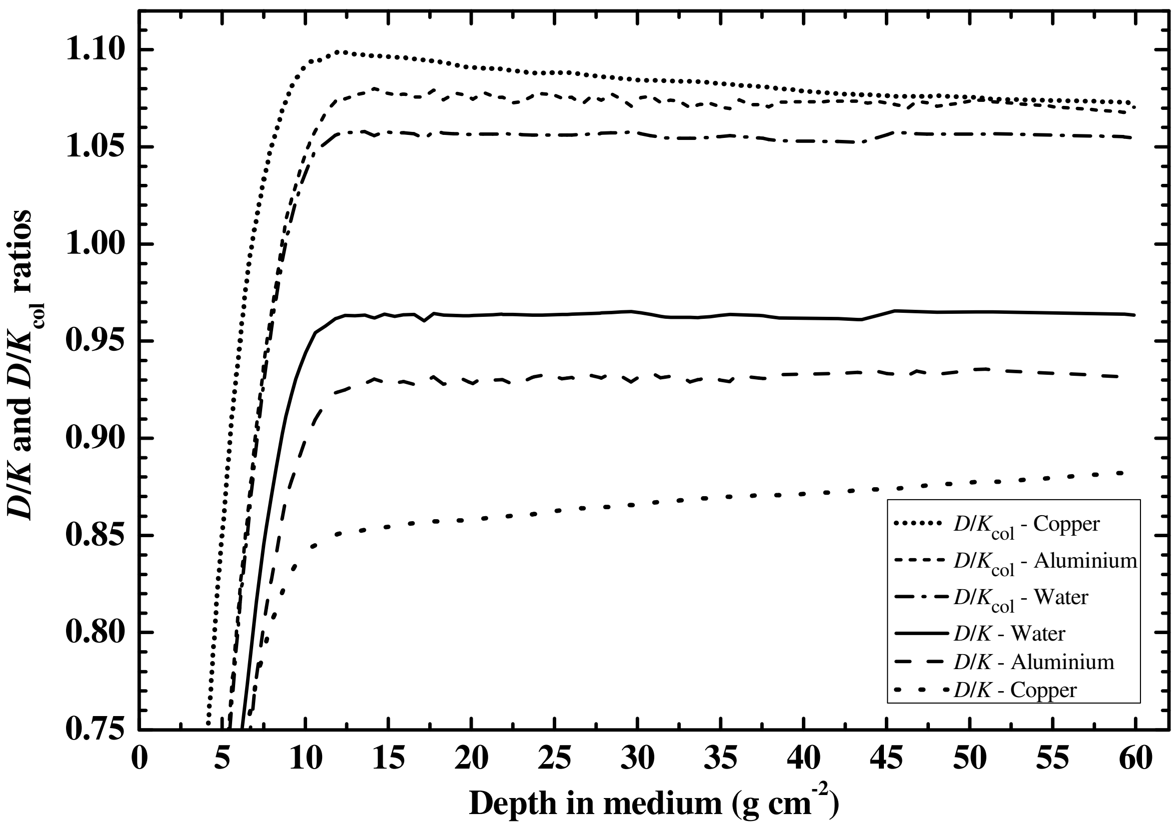

Figure 2.5: **Monte-Carlo-derived dose to kerma (*D/K*) and dose to collision kerma (D/K_{col}) ratios as a function of depth in water, aluminium and copper for a 25 MeV photon beam. The *D/K* and D/K_{col} were computed along the central axis for a field size of 10 × 10 cm^2 defined at the phantom surface.**

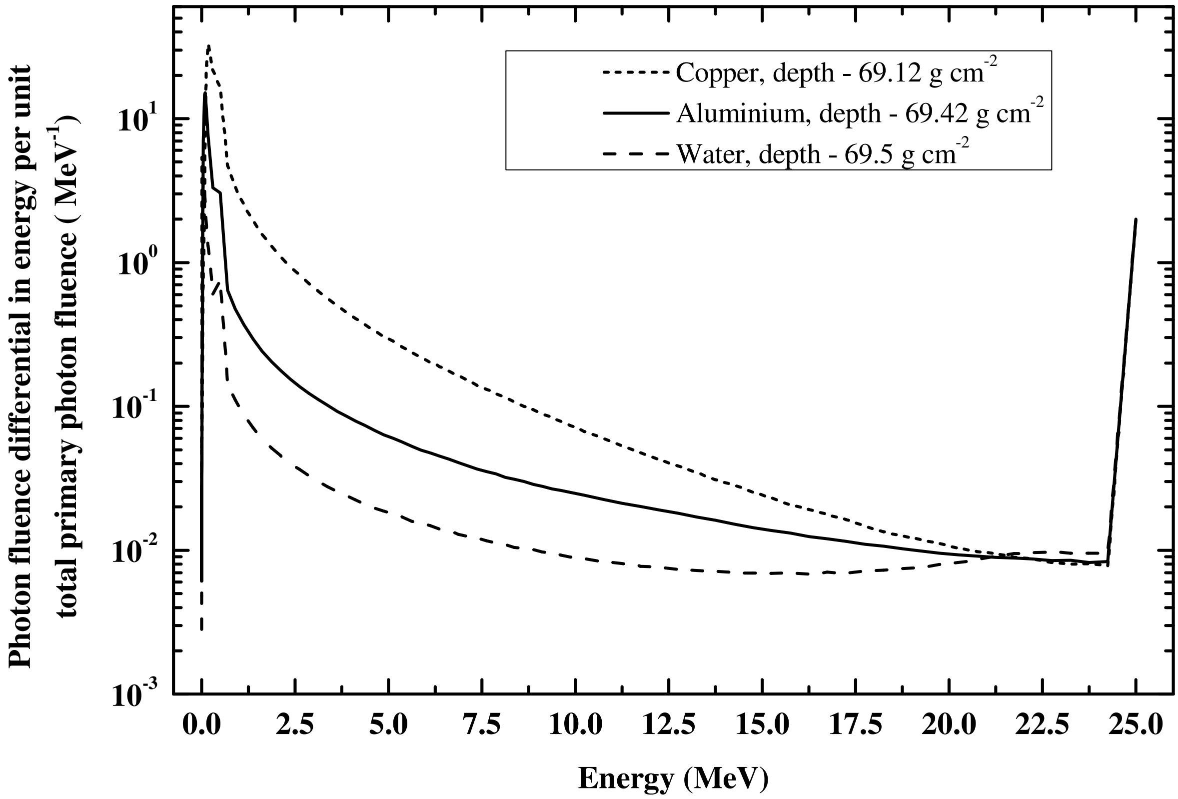

Figure 2.6: **Total photon fluence, differential in energy, along the central axis, normalized to the fluence at the incident energy, for a 25 MeV monoenergetic photon beam, at depths ≈ 69.5 g cm^{-2} in water, aluminium and copper. The field size was 10 × 10 cm^2 defined at the phantom surface.**

Figure 2.7 compares dose to kerma ratios from Monte-Carlo with those from simple analytical expression proposed in this chapter (equation (2.9)) as a function of photon energy in water, aluminium and copper for photon beams over the full energy range from 50 keV to 25 MeV. The agreement is generally good. One can conclude that equation (2.9) reproduces the trends with energy and atomic number very well for these specific materials, energies, and field sizes.

Table 2.1(a) gives the Monte-Carlo-derived values of D/K and D/K_{col} at a depth equal to 1.5 times the depth of maximum dose (d_{max}) from Co-60 γ-ray energy (1.25 MeV) to 25 MeV photon beams, at a field size of 10×10 cm^2 defined at the phantom surface, in water, aluminium and copper. It can be seen that D/K is almost always equal to or less than unity, within Monte-Carlo statistical uncertainties, whereas D/K_{col} (= β) is always greater than unity. Further, these ratios remain almost constant beyond the depth of maximum dose (but see above, especially figure 2.5). It is also clear from table 2.1(a) that D/K decreases and D/K_{col} increases with increasing beam quality. Table 2.1(b) gives the same quantities for clinical beam qualities in water only. It can be noted that the values for the 15 MV spectrum are close to those of the mono-energetic 5 MeV beam.

Tables 2.2 and 2.3 show comparisons of D/K and D/K_{col} from the present study with data available in the literature. There is excellent agreement between values computed in the present study and those from earlier studies for Co-60 energy at field sizes of 4 × 4 and 10 × 10 cm^2 in both water and aluminium. The only significant difference between present study numbers and the previously published ones is for a 6 MeV *broad* photon beam in aluminium where presently computed *D/K* values are ≈ 2% higher than either Attix (1979a) or Nilsson and Brahme (1983).

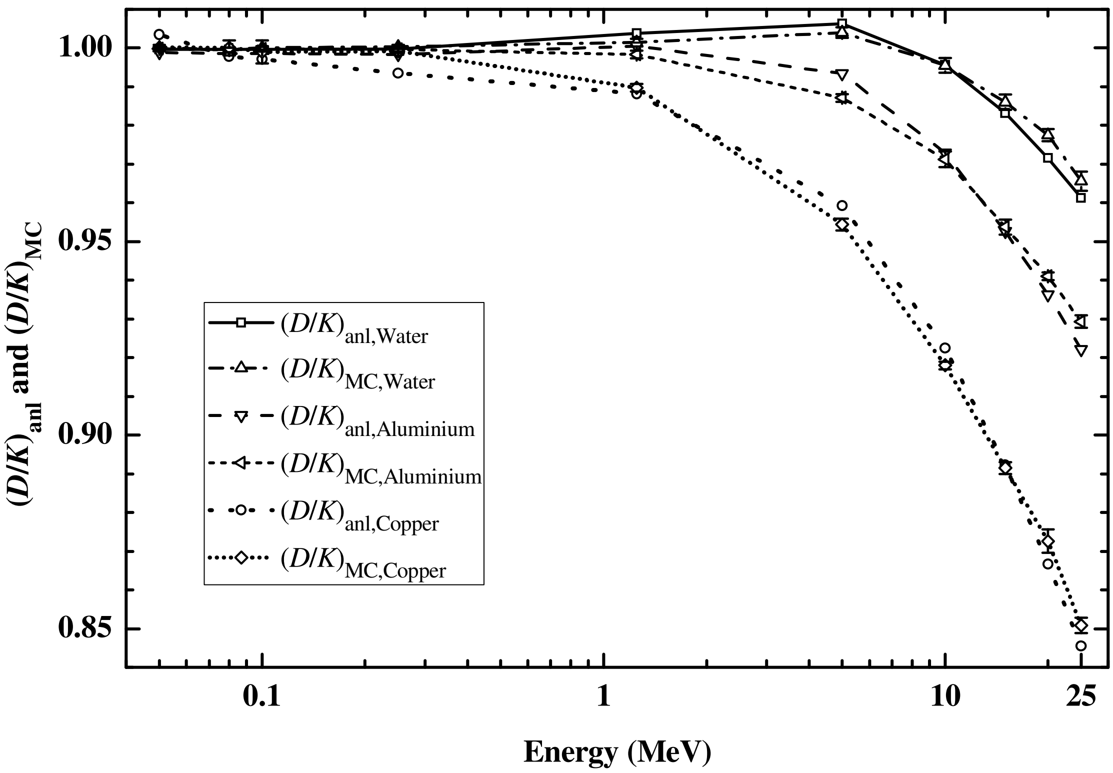

Figure 2.7: **Monte-Carlo-derived dose to kerma $(D/K)_{MC}$ and dose to kerma $(D/K)_{anl}$ evaluated from equation (2.9), as a function of energy, for 0.05–25 MeV photon beams in water, aluminium and copper. The $(D/K)_{MC}$ were computed along the central axis for a 10 × 10 cm^2 field size defined at the phantom surface; the error bars are ± 2 standard deviations and correspond to statistical (Type A) uncertainties.**

2.3.1.2.2 *D/K* in 'non-equilibrium' small photon fields as a function of field size

Figure 2.8 shows the field-size dependence of the *D/K* ratio along the central axis at 10 cm depth in a cylindrical water phantom for megavoltage beam qualities ranging from 5 to 15 MeV, including 'clinical' linac spectra (for point sources) at 6, 10 and 15 MV. It is observed that *D/K* decreases rapidly as the field size decreases below about 3 x 3 cm^2. This decrease is due to the onset of (lateral) electronic disequilibrium as the field width becomes too small to encompass the lateral excursions of the high-energy secondary electrons (e.g. Scott *et al* 2009, IPEM 2010).

2.3.1.2.3 Mean electron energy

Figure 2.9 shows the variation of mean electron (+ positron) energy for 15 MeV and 15 MV photon beams as a function of depth in water. The mean energy was evaluated from equation (2.3), from the 'primary' electron (and positron) fluence spectra generated by FLURZnrc where 'primary' in this context means that knock-on electrons have been excluded.

Table 2.1: **(a) *D/K* and D/K_{col} (= β) at depth = 1.5 × d_{max} from 50 keV to 25 MeV photons in water, aluminium and copper from Monte-Carlo simulation. The *D/K* and D/K_{col} were computed along the central axis for a field size of 10 × 10 cm^2 defined at the phantom surface; the statistical (Type A) uncertainties are ± 2 standard deviations (b) Monte-Carlo-derived *D/K* and D/K_{col} (= β) at depth = 1.5 × d_{max} for clinical qualities from 100 kV to 15 MV in water. The *D/K* and D/K_{col} were computed along central axis for field size 10 × 10 cm^2 defined at the phantom cylindrical phantom surface. The statistical (Type A) uncertainties are ± 2 standard deviations.**

(a)

Photon Energy	*D/K*			D/K_{col} (= β)		
	Water	Aluminium	Copper	Water	Aluminium	Copper
50 keV	1.0000 ± 0.0008	0.9998 ± 0.0005	1.0001 ± 0.0002	1.0003 ± 0.0009	1.0013 ± 0.0006	1.0034 ± 0.0004
80 keV	0.9995 ± 0.0006	0.9994 ± 0.0006	1.0000 ± 0.0020	1.0004 ± 0.0007	1.0008 ± 0.0007	1.0049 ± 0.0004
100 keV	1.0000 ± 0.0005	0.9997 ± 0.0006	0.9990 ± 0.0030	1.0006 ± 0.0005	1.0013 ± 0.0007	1.0047 ± 0.0005
250 keV	1.0003 ± 0.0005	0.9996 ± 0.0005	0.9992 ± 0.0005	1.0007 ± 0.0007	1.0017 ± 0.0006	1.0069 ± 0.0007
Co-60 γ	1.0014 ± 0.0010	0.9983 ± 0.0010	0.9897 ± 0.0010	1.0045 ± 0.0020	1.0046 ± 0.0006	1.0063 ± 0.0030
5 MeV	1.0040 ± 0.0014	0.9871 ± 0.0010	0.9544 ± 0.0015	1.0192 ± 0.0015	1.0193 ± 0.0010	1.0171 ± 0.0030
10 MeV	0.9955 ± 0.0019	0.9712 ± 0.0020	0.9180 ± 0.0010	1.0321 ± 0.0019	1.0328 ± 0.0021	1.0373 ± 0.0013
15 MeV	0.9860 ± 0.0020	0.9537 ± 0.0020	0.8915 ± 0.0015	1.0427 ± 0.0017	1.0475 ± 0.0020	1.0564 ± 0.0030
20 MeV	0.9775 ± 0.0016	0.9410 ± 0.0010	0.8726 ± 0.0030	1.0535 ± 0.0016	1.0627 ± 0.0012	1.0817 ± 0.0032
25 MeV	0.9656 ± 0.0025	0.9293 ± 0.0016	0.8508 ± 0.0200	1.0637 ± 0.0036	1.0782 ± 0.0019	1.0998 ± 0.0020

(b)

Clinical Beam Quality	*D/K*	D/K_{col} (= β)
100 kV	0.9999 ± 0.0005	1.0001 ± 0.0004
250 kV	0.9994 ± 0.0006	1.0002 ± 0.0007
Co-60 γ	1.0014 ± 0.0010	1.0045 ± 0.0020
6 MV	1.0030 ± 0.0002	1.0102 ± 0.0011
10 MV	1.0020 ± 0.0003	1.0145 ± 0.0013
15 MV	0.9981 ± 0.0003	1.0177 ± 0.0013

Table 2.2: **Comparisons of *D/K* computed in this work with values in the literature. The statistical (Type A) uncertainties are ± 2 standard deviations.**

			D/K		
Photon Energy	Material Name	Field Size (cm^2)	Attix (1979a)	Nilsson and Brahme (1983)	Present MC work (1.5 × d_{max})
Co-60 γ	Water	10 × 10	----	1.0011	1.0014 ± 0.0013
		4 × 4	----	1.0019	1.0020 ± 0.0010
	Aluminium	10 × 10	----	0.9980	0.9983 ± 0.0010
		4 × 4	----	0.9970	0.9973 ± 0.0010
6 MeV	Aluminium	Broad Beam	0.9670	0.9660	0.9853 ± 0.0006

Table 2.3: **Comparisons of D/K_{col} from the present work with previously published values. The statistical (Type A) uncertainties are ± 2 standard deviations.**

			D/K_{col}					
Photon Energy	Material Name	Field Size (cm^2)	Attix (1979a)	Loevinger (1981)	Greening (1981)	Nilsson and Brahme (1983)	Iwasaki (1994)	Present MC work (1.5 × d_{max})
Co-60 γ	Water	10 × 10	----	----	1.005	1.0051	1.005	1.0045 ± 0.0012
		4 × 4	----	----	----	1.0059	1.005	1.0053 ± 0.0014
	Aluminium	10 × 10	----	----	----	1.0043		1.0046 ± 0.0006
		4 × 4	----	1.006	----	1.0049		1.0053 ± 0.0006
6 MeV	Aluminium	Broad Beam	1.018	----	----	1.017		1.0208 ± 0.0010

The anomalously low values of the mean energy within a millimetre from the surface for 15 MeV photons must be due to secondary electrons from *backscattered* photons, which will have relatively low energies. The influence of backscattered photons can only be seen at extremely small depths where there is negligible build-up from the forward-directed secondary electrons. Beyond this narrow 'transition layer' the mean energy is at its highest value (≈ 7.5 MeV) and then decreases gradually towards an 'equilibrium' value (≈ 5.2 MeV). At 15 MV a very different behaviour is seen: the highest mean energy is achieved instead not close to the surface but at the depth of the dose maximum and beyond (≈ 2.2 MeV) as a result of the broad distribution of photon energies in the bremsstrahlung spectrum as Andreo and Nahum (1985) discuss in more detail.

The mean electron (+ positron) energies for a range of (broad) beam qualities ranging from Co-60 to 15 MeV, including the 'clinical' photon beams at 6, 10 and 15 MV, in water are given in table 2.4 at two depths, close to the surface and at $z = 1.5 \times d_{max}$. As in figure 2.9, from the surface to a quasi-equilibrium depth there is a clear *decrease* for monoenergetic beams but a modest *increase* for the x-ray qualities (Andreo and Nahum 1985). The numbers for Cobalt-60 gamma rays appear to belong to the results for the bremsstrahlung spectra rather than to those of the mono-energetic beams. This is probably due to the inclusion of a significant component from collimator and internal-source scatter in the source spectrum provided with the EGSnrc code system.

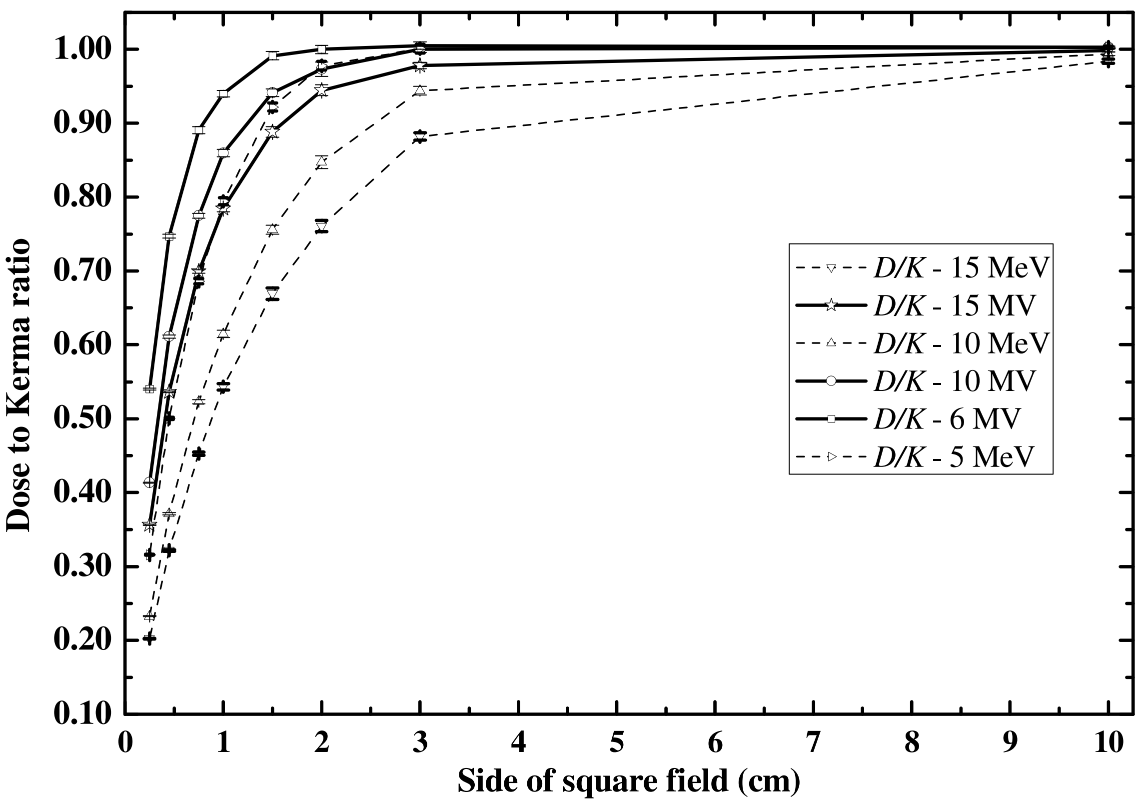

Figure 2.8: **Monte-Carlo-derived ratios of absorbed dose to kerma (*D/K*) on the central axis at 10 cm depth in a cylindrical water phantom for megavoltage beam qualities versus field size defined at 100 cm source-to-phantom surface distance; field sizes are 0.25, 0.5, 0.75, 1, 1.5, 2, 3 and 10 cm respectively; the error bars are ± 2 standard deviations and correspond to statistical (Type A) uncertainties.**

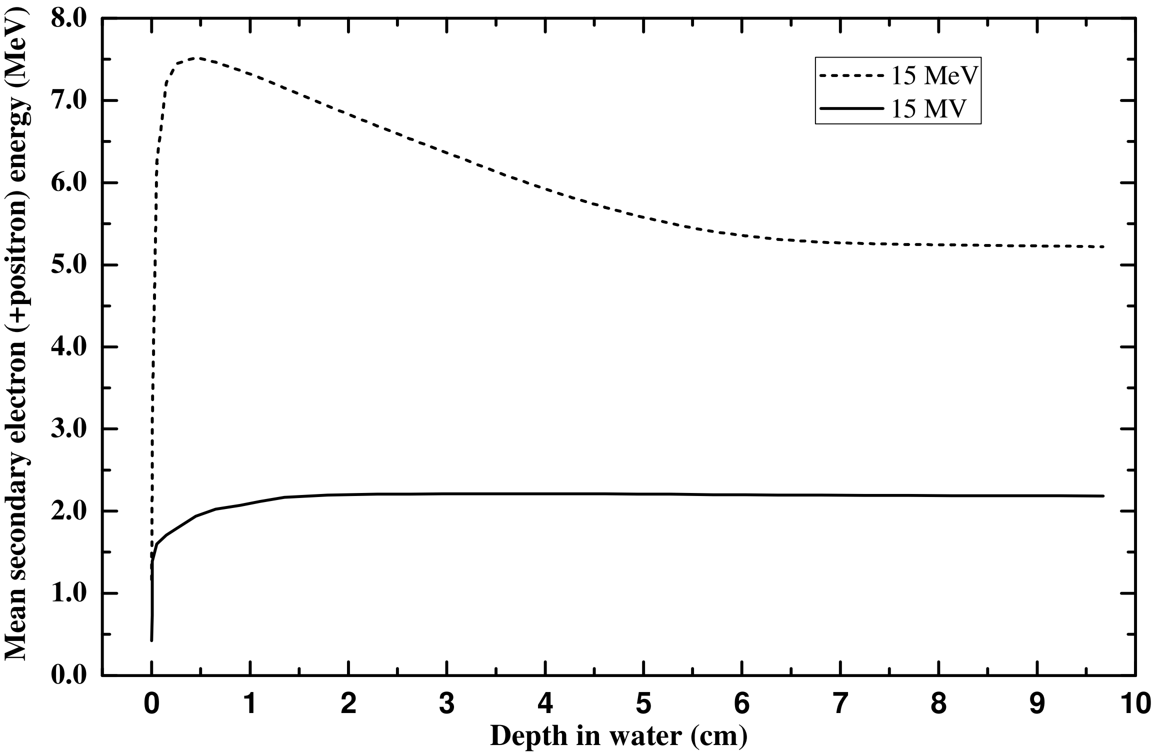

Figure 2.9: **Mean (secondary) electron energy versus depth for 15 MeV and 15 MV photons in water for broad parallel beams.**

Table 2.4: **Mean secondary electron energy $(\overline{E_z})$ at the surface and at a depth of 1.5 × d_{max} in water for broad, parallel beams (evaluated from equation (2.3) using Monte-Carlo-derived 'primary' electron fluence spectra). The statistical (Type A) uncertainties are ± 2 standard deviations. For Co-60 and 5 - 15 MeV qualities the values at the surface are the *maximum* mean energy (see main text) whereas for 6, 10 and 15 MV the 'surface' is at 1.5 mm depth.**

Photon Energy/Quality (megavoltage)	Mean electron Energy (MeV)	
	Surface	1.5 × d_{max}
Co-60 γ	0.45 ± 0.01	0.43 ± 0.01
5 MeV	2.44 ± 0.01	1.89 ± 0.01
10 MeV	5.03 ± 0.01	3.62 ± 0.01
15 MeV	7.52 ± 0.01	5.21 ± 0.01
6 MV	0.81 ± 0.01	0.98 ± 0.01
10 MV	1.25 ± 0.01	1.57 ± 0.01
15 MV	1.60 ± 0.01	2.21 ± 0.01

2.3.2 The analytical and Monte-Carlo evaluations of $\overline{X}$

Tables 2.5 (a) - (c) gives the key quantities from present study MC-derived data involved in evaluating $\overline{X}_{\text{emp}}$ (equation (2.5)) and $\overline{X}_{\text{MC}}$ (equation (2.10)) as well as values of $\overline{X}_{\text{MC}}$ itself, as a function of photon energy/quality and material. In particular it can be noted that $\overline{X}_{\mathrm{MC}}$ is ≈ 0.16-0.19 × $d_{\max}$ for the clinical bremsstrahlung beam qualities and is ≈ 0.33-0.36 × $d_{\max}$ for the monoenergetic beams; this is because the depth of the dose maximum is largely determined by range of the *maximum*-energy secondary electrons whereas $\overline{X}_{\mathrm{MC}}$ is determined by the ranges of the *mean* energy electrons. The final column shows how well the approximate formula for $\overline{X}_{\mathrm{emp}}$ (equation (2.5)) works compared to the 'exact' $\overline{X}_{\mathrm{MC}}$; the ratio is reasonably close to the simple factor 0.5 in equation (2.5) for the monoenergetic beams in both water and aluminium but closer to 0.4 for the clinical beams in water and the monoenergetic beams in copper. The latter difference, for copper, is not surprising as the 'detour' effect (see above) can be expected to dominate in high-atomic number materials where the nuclear elastic scattering of electrons is very strong. Mackie *et al* (1988) employed a convolution method to derive $\overline{X}$ for a water medium for various monoenergetic photon beams of energies 5, 10, 15 and 20 MeV; their values are within 3% of present study $\overline{X}_{\mathrm{MC}}$ values. Present study $\overline{X}_{\mathrm{MC}}$ of 0.413 cm for a 6 MeV broad photon beam is in very good agreement with Attix (1979a).

2.4 Summary and Conclusions

A set of D/K, D/K_{col} and $\overline{X}$ values has been generated in a consistent manner by Monte-Carlo simulation for water, aluminium and copper and for photon energies from 50 keV to 25 MeV. Beyond the build-up region dose D is almost never greater than kerma K whilst collision kerma K_{col} is always less than dose. An expression for $\overline{X}$, denoted by $\overline{X}_{\mathrm{emp}}$, equal to 0.5 × the csda range of the mean initial secondary electron energy, is proposed, based on a simplified picture of energy deposition by secondary electrons, and shown to work well for monoenergetic photons beams in water and aluminium. Expressions for D/K_{col} and D/K based on the above expression for $\overline{X}_{\mathrm{emp}}$ are also given. Further results include the biphasic shape of the dose build-up at 100 keV, the anomalous behaviour of the mean (secondary) electron energy in the build-up region in water at 15 MV and 15 MeV, and the large increase in lower-energy photon fluence at 25 MeV, especially in copper; the latter can explain why the kerma and collision kerma curves converge towards the dose curve at high atomic number and energy.

Table 2.5: **(a) For water: the dependence of $\overline{X}$ on photon energy, including the values of all the terms in equation (2.10) for $\overline{X}_{\mathrm{MC}}$ and in equation (2.5) for $\overline{X}_{\mathrm{emp}}$; the D/K_{col} values correspond to $z = 1.5 \times d_{\mathrm{max}}$.**

Photon Energy	$\mu_{\mathrm{eff}}/\rho\left(\mathrm{cm}^2\mathrm{g}^{-1}\right)$	$\overline{E}_0\,(\mathrm{MeV})$	$R_{\mathrm{csda}}\left(\overline{E}_0\right)\left(\mathrm{g\,cm}^{-2}\right)$	$\left(D/K_{\mathrm{col}}\right)_{\mathrm{MC}}$	$\overline{X}_{\mathrm{MC}}\left(\mathrm{g\,cm}^{-2}\right)$	$\overline{X}_{\mathrm{MC}}/d_{\mathrm{max}}$	$\overline{X}_{\mathrm{MC}}/R_{\mathrm{csda}}\left(\overline{E}_0\right)$
Co-60 γ	0.0524	0.59	0.22	1.0045 ± 0.0020	0.09	0.189	0.409
6 MV	0.0398	1.32	0.61	1.0102 ± 0.0011	0.25	0.161	0.410
10 MV	0.0313	2.27	1.13	1.0145 ± 0.0013	0.46	0.167	0.409
15 MV	0.0260	3.39	1.72	1.0177 ± 0.0013	0.67	0.175	0.393
5 MeV	0.0255	2.96	1.49	1.0192 ± 0.0015	0.75	0.329	0.500
10 MeV	0.0202	5.96	3.03	1.0321 ± 0.0019	1.56	0.332	0.515
15 MeV	0.0176	8.75	4.39	1.0427 ± 0.0017	2.37	0.354	0.541
20 MeV	0.0165	11.43	5.62	1.0535 ± 0.0016	3.16	0.363	0.562
25 MeV	0.0158	14.09	6.81	1.0637 ± 0.0036	3.89	0.363	0.571

Table 2.5: **(b) For aluminium: the dependence of $\overline{X}$ on photon energy, including the values of all the terms in equation (2.10) for $\overline{X}_{MC}$ and in equation (2.5) for $\overline{X}_{emp}$; the D/K_{col} values correspond to z = 1.5 × d_{max}.**

Photon Energy (MeV)	$\mu_{eff}/\rho\left(\mathrm{cm^2g^{-1}}\right)$	$\overline{E}_0\,(\mathrm{MeV})$	$R_{csda}\left(\overline{E}_0\right)\left(\mathrm{g\,cm^{-2}}\right)$	$\left(D/K_{col}\right)_{MC}$	$\overline{X}_{MC}\left(\mathrm{g\,cm^{-2}}\right)$	$\overline{X}_{MC}/d_{max}$	$\overline{X}_{MC}/R_{csda}\left(\overline{E}_0\right)$
5	0.0240	2.84	1.766	1.0193 ± 0.0010	0.80	0.311	0.452
10	0.0204	5.60	3.442	1.0328 ± 0.0021	1.58	0.335	0.459
15	0.0195	8.24	4.779	1.0475 ± 0.0020	2.38	0.338	0.499
20	0.0186	10.75	6.232	1.0627 ± 0.0012	3.27	0.370	0.524
25	0.0183	13.33	7.504	1.0782 ± 0.0019	4.11	0.387	0.548

Table 2.5: **(c) For copper: the dependence of $\overline{X}$ on photon energy, including the values of all the terms in equation (2.10) for $\overline{X}_{MC}$ and in equation (2.5) for $\overline{X}_{emp}$; the D/K_{col} values correspond to z = 1.5 × d_{max}.**

Photon Energy (MeV)	$\mu_{eff}/\rho\left(\mathrm{cm^2g^{-1}}\right)$	$\overline{E}_0\,(\mathrm{MeV})$	$R_{csda}\left(\overline{E}_0\right)\left(\mathrm{g\,cm^{-2}}\right)$	$\left(D/K_{col}\right)_{MC}$	$\overline{X}_{MC}\left(\mathrm{g\,cm^{-2}}\right)$	$\overline{X}_{MC}/d_{max}$	$\overline{X}_{MC}/R_{csda}\left(\overline{E}_0\right)$
5	0.0253	2.64	1.847	1.0171 ± 0.0030	0.67	0.303	0.364
10	0.0262	5.19	3.520	1.0373 ± 0.0013	1.40	0.328	0.397
15	0.0275	7.68	4.966	1.0564 ± 0.0030	1.99	0.356	0.401
20	0.0286	10.20	6.276	1.0817 ± 0.0032	2.75	0.377	0.438
25	0.0292	12.72	7.428	1.0998 ± 0.0020	3.25	0.383	0.438

CHAPTER 3

Secondary bremsstrahlung and the energy-conservation aspects of kerma in photon-irradiated media

3.1 Introduction

In an irradiated medium kerma quantifies the *transfer* of energy from the uncharged ionizing radiation (e.g. photons) to charged-particle kinetic energy (KE), whereas absorbed dose quantifies the energy *imparted* to the medium by these charged particles. Kerma necessarily includes that fraction of the initial charged-particle KE eventually re-radiated in the form of bremsstrahlung photons (ICRU 2011); for this reason kerma is generally partitioned into two components, namely *collision* kerma, K_{col}, and *radiative* kerma, K_{rad} (Attix 1979a, 1979b). Under charged-particle equilibrium (CPE), absorbed dose is exactly equal to *collision* kerma at all positions in the medium (Dutreix *et al* 1965, Attix 1979a, 1986). However, in a medium irradiated by an external beam of uncharged particles, CPE beyond the depth of maximum dose is never complete due to beam attenuation over the range of the secondary charged particles; the ratio of absorbed dose to collision kerma, generally denoted by β, is always greater than unity (Loevinger 1981, Attix 1986, Kumar *et al* 2015a).

Attix (1986) stated, based on a physical model, that the energy obtained from integrating the *dose* curve from zero to infinite depth, should be equal to the energy from the corresponding integration of *collision* kerma (neglecting energy losses due to charged particles scattered out of the front surface of the medium). However, kerma, as opposed to *collision* kerma, includes implicitly the fraction of charged-particle kinetic energy eventually re-radiated as bremsstrahlung. Consequently, if kerma is calculated over a large volume/mass, the energy of these 'secondary bremsstrahlung' photons will inevitably be 'double-counted'.

As far as it is known, no detailed study has been published on the energy conservation aspects of K, K_{col} and D. The K/D and K_{col}/D have therefore been calculated over a large volume by simulating photon transport in a very large (effectively semi-infinite) homogeneous cylindrical phantom for photon beams ranging from 0.1 to 25 MeV (monoenergetic) with water, aluminium and copper as media, and additionally for 'clinical' linac beams of 6, 10 and 15 MV (from Mohan *et al* 1985) in water. Photon energies up to 25 MeV were chosen in order to see by how much K and K_{col} differ from D as a function of atomic number. Further, a special form of kerma have been defined (see below) and computed, which is denoted by K_{ncpt} (ncpt ≡ 'no charged-particle transport'), by preventing any secondary charged-particle transport in the Monte-Carlo simulation in order to see if the K_{ncpt} conserves energy over a large volume.

The photon fluence, differential in energy (per unit primary photon fluence at a depth of ≈ 51 g cm^{-2}), for both very high and very low charged-particle transport cut-offs, has also been computed for a 25 MeV photon beam in the three materials in order to look at differences in the low-energy photon fluence for these two cut-off values as a function of atomic number. The large depth was chosen to highlight the contribution of secondary bremsstrahlung.

Additionally, a 'track-end' correction term to the 'kerma integral', defined by equations (3.7) and (3.8), has been formulated to account for the energy transferred to charged particles by photons *with initial energies below the Monte-Carlo photon transport cut-off PCUT*.

3.2 Materials and methods

3.2.1 The various types of kerma

3.2.1.1 Formal definitions

Attix (1983, 1986), formally defines kerma as

$$K = \frac{\mathrm{d}\left(\varepsilon_{\mathrm{tr}}\right)_e}{\mathrm{d}m} \tag{3.1}$$

where $\left(\varepsilon_{\mathrm{tr}}\right)_e$ is the expectation value of the energy transferred in a *finite* volume during some time interval. For an elementary finite volume V the energy transferred is given by

$$\varepsilon_{\mathrm{tr}} = \left(R_{\mathrm{in}}\right)_{\mathrm{u}} - \left(R_{\mathrm{out}}\right)_{\mathrm{u}}^{\mathrm{nonr}} + \sum Q \tag{3.2}$$

where $\left(R_{\mathrm{in}}\right)_{\mathrm{u}}$ is the energy of uncharged particles entering V and $\left(R_{\mathrm{out}}\right)_{\mathrm{u}}^{\mathrm{nonr}}$ is the energy of uncharged particles leaving V, with the superscript 'nonr' indicating the *non-inclusion* of uncharged particles originating from charged-particle radiative losses while in V, i.e. bremsstrahlung and *in-flight* annihilation of positrons. $\sum Q$ is the *net* energy derived from changes in rest mass in V; for the production of an electron-positron pair this is equal to –1.022 MeV which means that this energy is effectively subtracted from the uncharged radiant energy *entering* the volume and is therefore *not* counted in $\varepsilon_{\mathrm{tr}}$. Equation (3.1) expresses the fact that kerma, K, is the sum of the *kinetic energies* of the charged particles liberated in V divided by the mass of the finite volume element; this is how kerma is conventionally defined and calculated.

The quantity *net energy transferred*, $\varepsilon_{\mathrm{tr}}^{\mathrm{n}}$, from which collision kerma, K_{col}, is derived (by replacing $\varepsilon_{\mathrm{tr}}$ by $\varepsilon_{\mathrm{tr}}^{\mathrm{n}}$ in equation (3.1)), is given by

$$\varepsilon_{\mathrm{tr}}^{\mathrm{n}} = \left(R_{\mathrm{in}}\right)_{\mathrm{u}} - \left(R_{\mathrm{out}}\right)_{\mathrm{u}}^{\mathrm{nonr}} - R_{\mathrm{u}}^{\mathrm{r}} + \sum Q \tag{3.3}$$

which differs from equation (3.2) by the term $-R_{\mathrm{u}}^{\mathrm{r}}$ which is the charged-particle kinetic energy emitted as *radiative losses*, i.e. bremsstrahlung, by the charged particles liberated in V, regardless of where these bremsstrahlung events take place.

The new type of kerma proposed in this chapter, K_{ncpt}, can be defined in terms of the above formalism; in this case the charged particles liberated are not transported and therefore no 'secondary bremsstrahlung' is generated, making the 'nonr' superscript superfluous. The corresponding energy transferred in the finite volume V, $\left\{\varepsilon_{\mathrm{tr}}\right\}_{\mathrm{ncpt}}$, is given by

$$\left\{\varepsilon_{\mathrm{tr}}\right\}_{\mathrm{ncpt}} = \left\{\left(R_{\mathrm{in}}\right)_{\mathrm{u}} - \left(R_{\mathrm{out}}\right)_{\mathrm{u}}\right\}_{\mathrm{ncpt}} + \sum Q \tag{3.4}$$

and therefore K_{ncpt} is defined as

$$K_{\mathrm{ncpt}} = \frac{\mathrm{d}\left(\left\{\varepsilon_{\mathrm{tr}}\right\}_{\mathrm{ncpt}}\right)_{e}}{\mathrm{d}m} \tag{3.5}$$

3.2.1.2 Monte-Carlo 'scoring' of K and K_{ncpt}

In this section it is clarified how two of the types of kerma defined above are 'scored' by Monte-Carlo user-code DOSRZnrc.

Firstly, 'normal' kerma, K: let the initial kinetic energy of each charged particle (both electrons and positrons) liberated in scoring region $\mathrm{P_i}$ of mass M_{i} be denoted by ke_{j}. Then for all the n photon interactions in $\mathrm{P_i}$, K is written as

$$K(\mathrm{P_i}) = \frac{1}{M_{\mathrm{i}}} \sum_{\mathrm{j=1}}^{\mathrm{j=n}} ke_{\mathrm{j}} \tag{3.6}$$

Secondly, kerma K_{ncpt}: this is scored in exactly the same manner, except that in this case the electron/positron kinetic energy cut-off, *ECUT* is set higher than the incident photon energy, thereby ensuring that there is no subsequent transport of the charged particles liberated by photon interactions with the medium, and therefore no possibility of any 'secondary bremsstrahlung' being generated anywhere in the irradiated volume.

3.2.2 Monte-Carlo calculations

3.2.2.1 Setting up the simulations

The EGSnrc user-code DOSRZnrc (version: V4-2.3.2) was employed to compute dose and kerma; photon fluence spectra were generated by the user-code FLURZnrc (version: V4-2.3.2) (Rogers *et al* 2011b). The simulations were carried out with most of the so-called default settings, which include modelling the Compton interaction for bound electrons, and relativistic spin effects in the multiple-scattering of charged particles. However, so-called *electron impact ionization* was switched off. This means that the 'fluorescent' photons resulting from atomic electrons being 'knocked out' of the atom (i.e. the atom being ionized), by fast electron-bound electron 'collisions', are not generated; the binding energies are effectively added to the initial kinetic energy of the knock-on electrons[3]. In addition to the above settings, cross sections for the sampling of bremsstrahlung photon energies from the NIST database (Hubbell and Seltzer 2004) and photon interaction cross sections from the XCOM database were used (Berger *et al* 2010).

The irradiated phantom was cylindrical. The two scoring geometries have been defined: the 'large volume' scoring region (hereafter referred to as LVG ≡ 'large volume geometry') had height and diameter equal to 1308 cm; the 'depth-dependent' scoring geometry consisted of dividing the LVG into many thin layers of circular cross section, each with a diameter of 1308 cm (hereafter referred to as DDLRG ≡ 'depth-dependent large radius geometry'). The 1308 cm dimension was chosen so that the ratio of the number of primary particles reaching the exit surface of the phantom to the number of incident particles was less than 10^{-10} for 25 MeV photons in water (estimated from the total attenuation coefficient); for aluminium and copper and for all lower energies this ratio will be even smaller. These dimensions ensured that a negligible amount of energy, whether carried by charged or uncharged particles, could escape from this phantom, apart from backscattered photons.

The 'Source 2' option (denoted as a 'broad, parallel beam') of the EGSnrc Monte-Carlo code system was used[4]. Source 2 fixes the phantom radius to 1000 cm and the beam area to 1 cm^2 (Rogers *et al* 2011b) i.e. the beam radius is very much smaller than the radius of the scoring regions (here set to 654 cm); due to the 'reciprocity theorem' (Attix 1986) this is equivalent to the distribution along the central axis of a 'broad beam'. Note further that a very large scoring radius (654 cm) was deliberately selected to ensure a negligible probability of any particles escaping through the side walls of the scoring volume.

A PEGS4 datafile (Nelson *et al* 1985; Kawrakow *et al* 2011) was generated with the EGSnrcMP package (Kawrakow *et al* 2006) for parameter values AP = 1 keV, AE = 512 keV (total

---

[3] If electron impact ionization (eii) is simulated (one of the default settings) then the initial kinetic energies of knock-on electrons (aka delta rays) will be reduced by the relevant binding energies, with this energy instead appearing as the energy of fluorescent photons and adding to the photon fluence. This will be reflected in an *increase* in the parameter g compared to *not* simulating eii; for a 25 MeV photons in water the increase is entirely negligible, but with lead as the medium g increases by ≈ 0.9%, from 0.4393 to 0.4435.

[4] Alternatively, 'Source 0' could have been chosen.

energy) where AP and AE are the production thresholds for bremsstrahlung photons and knock-on electrons respectively. Electrons and positrons were followed down to 1 keV kinetic energy (i.e. the electron/positron kinetic energy cut-off *ECUT* = 512 keV) and photons down to 1 keV (photon energy cut-off *PCUT* = 1 keV).

3.2.2.2 Computation of D, K, K_{col}, K_{ncpt}, K/D, K_{col}/D and K_{ncpt}/D

Dose and kerma were computed by the user-code DOSRZnrc in the cylindrical phantom described above for 0.1 to 25 MeV monoenergetic broad, parallel photon beams in water, aluminium and copper media and for 'clinical' linac spectra of 6, 10 and 15 MV (from Mohan *et al* 1985) in water. D, K and K_{ncpt} were scored directly in the DDLRG from the surface to 240 g cm^{-2} depth for the monoenergetic beams and to 20 g cm^{-2} depth for the clinical beams. The scoring regions had very large circular cross sections (radius = 654 cm) with heights/thicknesses varying from very small in the build-up region (e.g. 0.05 cm in water and 0.005 cm in Cu) to larger values at greater depths.

As user-code DOSRZnrc yields kerma K but not collision kerma K_{col}, the ratio (K_{col}/K) was firstly determined by evaluating equations (3.7) and (3.8) for the identical source and geometry. In order to evaluate these expressions the total photon fluence per MeV per unit incident photon fluence was scored in each depth interval in the cylindrical phantom using FLURZnrc, taking care to choose sufficiently narrow energy bins to capture the possible rapid variation in the mass energy-transfer and mass energy-absorption coefficients with photon energy. K and K_{col} were then derived by numerical integration over the energy-fluence spectra according to (e.g. Nahum 2007b):

$$K_{\mathrm{med}} = \int_{PCUT}^{k_{\max}} k \frac{\mathrm{d}\Phi_{\mathrm{med}}}{\mathrm{d}k} \left(\frac{\mu_{\mathrm{tr}}(k)}{\rho} \right)_{\mathrm{med}} \mathrm{d}k \tag{3.7}$$

and

$$(K_{\mathrm{col}})_{\mathrm{med}} = \int_{PCUT}^{k_{\max}} k \frac{\mathrm{d}\Phi_{\mathrm{med}}}{\mathrm{d}k} \left(\frac{\mu_{\mathrm{en}}(k)}{\rho} \right)_{\mathrm{med}} \mathrm{d}k \tag{3.8}$$

where k is the photon energy, $\mu_{tr}(k)/\rho$ the mass energy-transfer coefficient, $\mu_{en}(k)/\rho$ the mass energy-absorption coefficient, and $\mathrm{d}\Phi_{med}/\mathrm{d}k$ the total photon fluence, differential in energy, in the medium (which can also be written $[\Phi_k]_{med}$). The above expressions are sometimes known as 'kerma integrals'. It is emphasised that $\mathrm{d}\Phi_{med}/\mathrm{d}k$ includes secondary bremsstrahlung. For consistency, $\mu_{tr}(k)/\rho$ and $\mu_{en}(k)/\rho$ were computed using the '*g*' user-code of EGSnrc system (Kawrakow *et al* 2011) with the identical PEGS4 datafiles used with DOSRZnrc to compute kerma. Note that the lower limit of the integral is equal to *PCUT* as the fluence spectrum only extends down to *PCUT* in energy. From equations (3.7) and (3.8),

$$K_{col}/K = \left(1-\bar{g}\right) \tag{3.9}$$

was calculated at each depth with the same radius of the scoring volume as above and then multiplied by K from DOSRZnrc to yield K_{col} as a function of depth for each medium in turn. It can be noted that the numerical value of K derived from equation (3.7) with the fluence obtained from user-code FLURZnrc agreed within 0.5% with that obtained directly from the simulations with user-code DOSRZnrc for the same normalization.

From user-code DOSRZnrc, dose D and kerma K were obtained over the LVG for beam qualities ranging from 0.1 to 25 MeV photon beams in water, aluminium and copper and for 'clinical' linac spectra of 6, 10 and 15 MV (from Mohan *et al* 1985) in water; the ratio K/D was then calculated. The value of K_{col} over the LVG was also derived using the methodology described above and hence K_{col}/D could be obtained as D had been computed using DOSRZnrc for the same beam qualities and materials.

The new quantity K_{ncpt} was also computed, firstly as a function of depth in the DDLRG and secondly over the LVG, for the same beam qualities and media as above. This was achieved by setting *ECUT*, the total energy at which charged particle transport is terminated, to a high value; this ensures that there can be no secondary charged-particle transport and hence no generation of secondary bremsstrahlung. A constant value of *ECUT* = 50.511 MeV was chosen in all the simulations where K_{ncpt} was computed[5]. Consequently the initial kinetic energy of each charged particle was added to the total energy deposition in the scoring volume where the charged particle was 'liberated'. K_{ncpt} is then given by the quantity scored as 'dose' (and also 'kerma') in DOSRZnrc. K_{ncpt} cannot possibly include any component due to secondary bremsstrahlung as no charged-article transport is involved. K_{ncpt} scored over the LVG was divided by the dose D, also computed over the LVG using DOSRZnrc (but with the electron transport cut-off *ECUT* now set back to its normal very low value), to yield K_{ncpt}/D.

Regarding the pair-production interaction, as a result of the 'instant termination' of all charged-particle transport, the 0.511 MeV photons due to positron annihilation are set in motion at the position of the pair-production interaction i.e. the EGSnrc code does not 'forget about' these 0.511 gammas.

3.2.2.3 Computation of total photon fluence, differential in energy

In order to determine the amount of low-energy photon fluence (partly due to 'secondary' bremsstrahlung) relative to the primary fluence, the total photon fluence per MeV per unit incident photon fluence, at one single depth, in the large homogeneous cylindrical phantom was computed

[5] In practice *ECUT* = 25.511 MeV would have been sufficient as 25 MeV was the highest incident photon energy in the whole investigation.

using FLURZnrc for our standard low value of the charged-particle transport cut-off (i.e. *ECUT*) of 512 keV (total energy)) and for the very high *ECUT* = 50.511 MeV (total energy) as employed to derive K_{ncpt}, in the three phantom materials irradiated with 25 MeV photon beams. For both settings of *ECUT*, the photons were followed down to 1 keV kinetic energy (i.e. *PCUT* = 1 keV). The spectral energy-bin widths were set at 1 keV for the lowest energy bins (1 keV – 10 keV), then 5 keV for the next 18 bins, then gradually increased as the energy increased up to 400 keV, and thereafter kept at 20 keV. Consequently the 'spike' at 0.511 MeV due to annihilation photons was 'captured' in the 0.50 - 0.52 MeV energy bin. The fluence spectra were scored in a layer centred at a depth of ≈ 51 g cm^{-2}.

3.2.2.4 The influence of *PCUT* on kerma

Here an attempt was made to investigate the effect of the value selected for *PCUT* (the photon transport cut-off energy) on kerma computed using DOSRZnrc at different depths for a 25 MeV photon beam in water, Al and Cu. Therefore *PCUT* was varied between 1 keV and 200 keV in variable intervals, for the geometry and source described in sub-section 3.2.2.1. Kerma obtained from the above DOSRZnrc simulations was compared with kerma derived from equation (3.7) using the photon fluence differential in energy, $\mathrm{d}\Phi/\mathrm{d}k$, computed by FLURZnrc, with the same value of *PCUT*, for the 25 MeV photon beam in the three materials, and with identical normalization (i.e. per unit incident photon fluence).

3.2.3 Formulation of a track-end term in the kerma cavity integral

Ideally, in a Monte-Carlo simulation all photons should be tracked until they disappear (from the fluence spectrum), due to either the pair-production interaction or photoelectric absorption. However, for a finite value of the photon transport cut-off, *PCUT*, there will inevitably be some photons which fall below *PCUT* in energy and are therefore removed from the simulation. The energy deposition by these photons is correctly 'counted' and therefore contributes to absorbed dose but the kinetic energies of any secondary charged particles these sub-*PCUT* photons would have liberated will not be added to kerma via equation (3.6). Consequently, kerma derived from user-code DOSRZnrc will be *underestimated* by an amount depending on the value of *PCUT* in the simulation. When kerma is evaluated from equation (3.7) or (3.8), sometimes referred to as 'large photon cavity integrals', there will also be some 'missing kerma' as the lower limit of the integral cannot be below *PCUT*, the lowest energy in the simulation, and therefore the lowest energy in the fluence spectrum. By analogy with the track-end term in the Spencer-Attix cavity integral (Nahum 1978, 2007b) a kerma track-end term, $\left(K_{\text{T-E}}\right)_{\text{med}}$, can be formulated to be added to equation (3.7):

$$\left(K_{\text{T-E}}\right)_{\text{med}} = \int_{PCUT}^{k_{\max}} k \frac{\mathrm{d}\Phi_{\text{med}}}{\mathrm{d}k} \left(\frac{\mu^{\mathrm{C}}_{\mathrm{tr},\,PCUT}(k)}{\rho}\right)_{\text{med}} \mathrm{d}k \tag{3.10}$$

where $\left(\mu^{\mathrm{C}}_{\mathrm{tr},\,PCUT}(k)/\rho\right)_{\text{med}}$ is a form of restricted energy-transfer coefficient (Brahme 1978) for Compton interactions *which result in* (*scattered*) *photons with energies below PCUT*. By analogy with the derivation of the conventional μ_{tr}/ρ from the (total) mass attenuation coefficient, μ_{tot}, this restricted coefficient is the product of the Compton attenuation coefficient restricted to events producing sub-*PCUT* photons, $\left(\frac{\mu^{\mathrm{C}}_{PCUT}(k)}{\rho}\right)_{\text{med}}$ and ratio of the scattered photon energy to the *primary* photon energy:

$$\left(\frac{\mu^{\mathrm{C}}_{\mathrm{tr},\,PCUT}(k)}{\rho}\right)_{\text{med}} = \left(\frac{\mu^{\mathrm{C}}_{PCUT}(k)}{\rho}\right)_{\text{med}} \times \left[\frac{\overline{k^{\mathrm{C}}}}{k}\right] \tag{3.11}$$

where $\overline{k^{\mathrm{C}}}$ is the mean value of the initial energies of the photons Compton-scattered to energies below *PCUT* generated by photons of energy *k*. Note that the above expression assumes that 100% of the scattered photon energy will eventually be converted into charged-particle kinetic energy (most probably via the photoelectric effect).

3.3 Results and Discussion

3.3.1 *D, K,* K_{col}, K_{ncpt}, *K/D,* K_{col}/D and K_{ncpt}/D

Figures 3.1(a) - (c) show the depth dependence of dose, kerma and collision kerma for a 25 MeV broad, parallel photon beams in water, Al and Cu media respectively[6]. These graphs (and the numbers in Tables 3.1 and 3.2 for energies 0.1-25 MeV) indicate that the 'area under the kerma curve' (i.e. the dashed-dotted line) exceeds the area under either the dose (i.e. dotted line) or collision kerma (dashed) curves, i.e. *over a large volume* the energy content integrated from the kerma distribution is not equal to the energy content integrated from the dose distribution over a large volume. In contrast, the area under the collision kerma curve *is* equal to the area under the dose curve which demonstrates that collision kerma *does* conserve energy (as quantified in Tables 3.1 and 3.2). It can also be noted that as the Z of the medium increases, bremsstrahlung production increases, resulting in the enhancement of radiative kerma, K_{rad}, which 'pulls' the kerma curve up over the dose curve, thus creating a significant difference between dose and kerma.

[6] The absolute value of the kerma very close to the surface (per unit incident photon fluence) obtained from DOSRZnrc, K/Φ was verified and was equal to $k \times \mu_{\mathrm{tr}}(k)/\rho$.

(a)

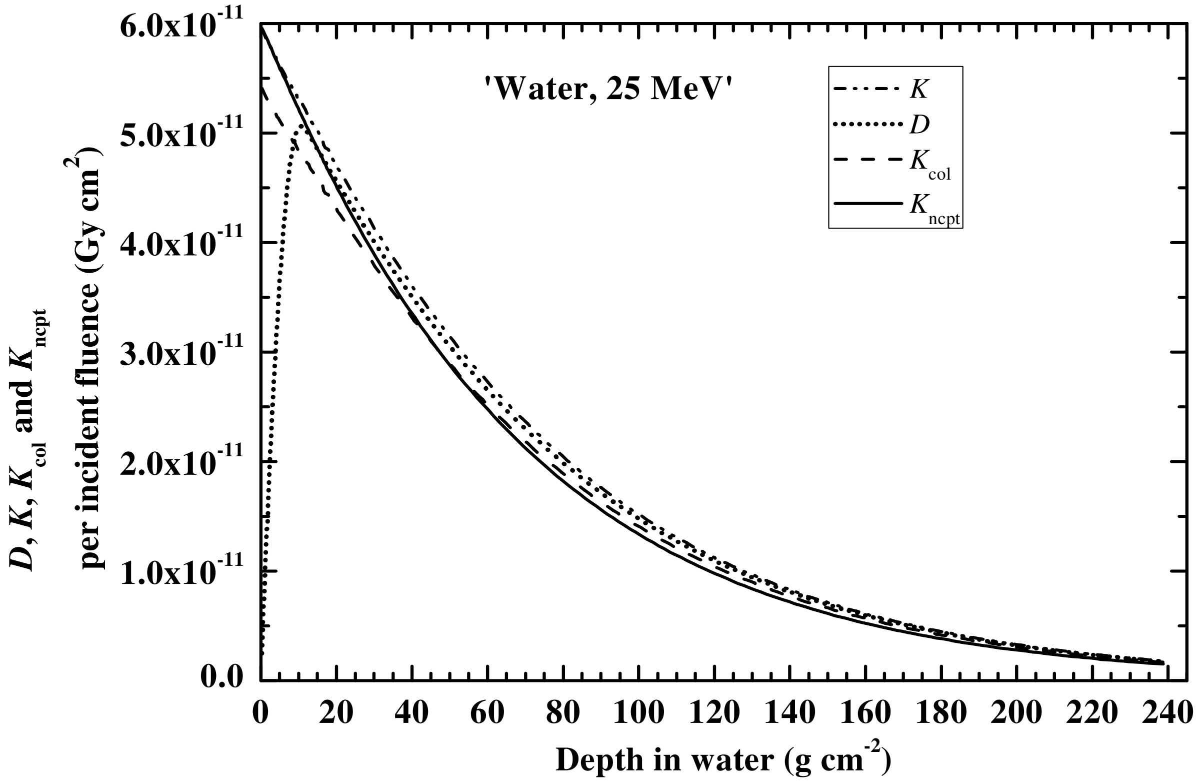
'Water, 25 MeV'
K
D
K col
K ncpt
D, K, K col and K ncpt per incident fluence (Gy cm2)
Depth in water (g cm-2)
6.0x10-11
5.0x10-11
4.0x10-11
3.0x10-11
2.0x10-11
1.0x10-11
0.0
0
20
40
60
80
100
120
140
160
180
200
220
240

(b)

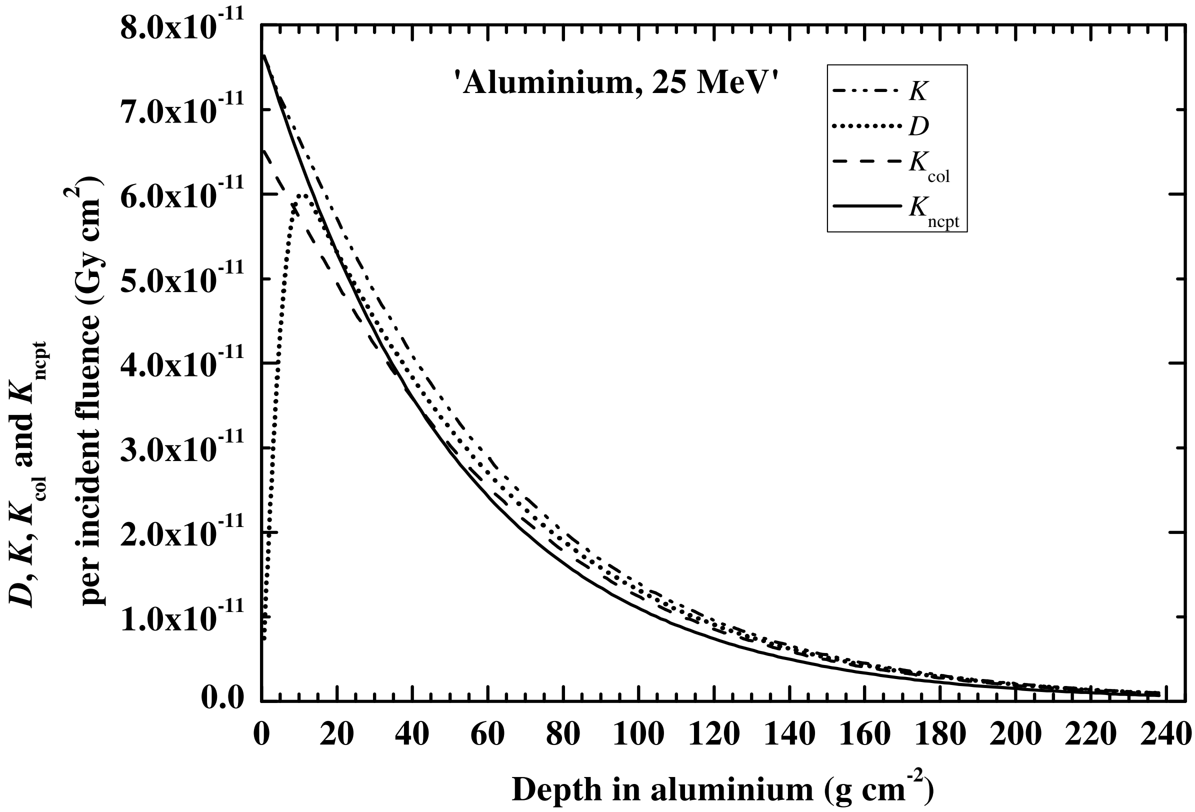
'Aluminium, 25 MeV'
K
D
K col
K ncpt
D, K, K col and K ncpt per incident fluence (Gy cm2)
Depth in aluminium (g cm-2)
8.0x10-11
7.0x10-11
6.0x10-11
5.0x10-11
4.0x10-11
3.0x10-11
2.0x10-11
1.0x10-11
0.0
0
20
40
60
80
100
120
140
160
180
200
220
240

(c)

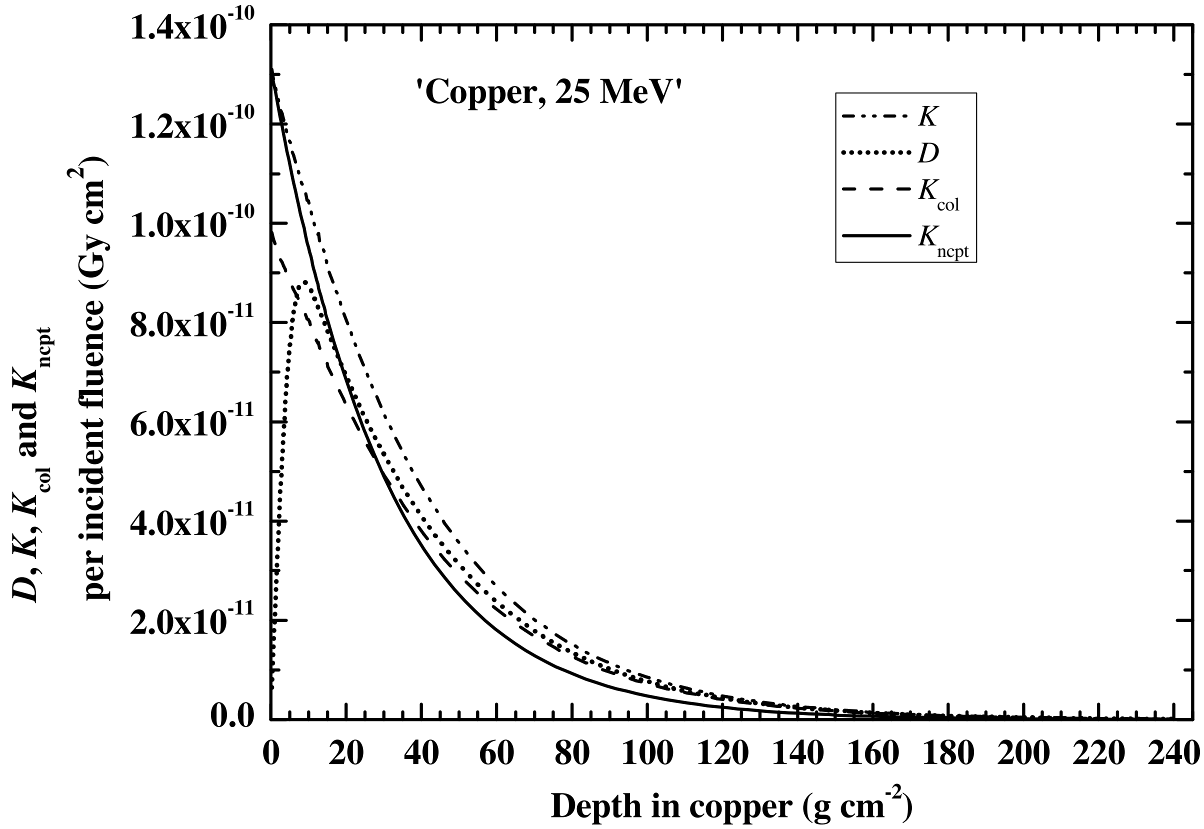

Figure 3.1: **(a) Dose, *D*, kerma, *K*, collision kerma, K_{col} and kerma (no charged-particle transport), K_{ncpt} per unit incident photon fluence (Gy cm^2) versus depth (g cm^{-2}) for the depth-dependent large radius geometry for photon beams with *ECUT* = 512 keV (total energy), and high *ECUT* = 50.511 MeV (total energy) respectively, for a 25 MeV monoenergetic broad, parallel photon beams in water; (b) same quantities and energy for aluminium; (c) same quantities and energy for copper. The data were derived from Monte-Carlo codes DOSRZnrc and FLURZnrc.**

The depth dependence of K and K_{ncpt} are shown on semi-log plots for the three media in Figures 3.2(a) - (c) for a 25 MeV broad, parallel photon beams. It can be seen that the differences between K and K_{ncpt} increase with increasing atomic number (from water to Al to Cu). Figure 3.2(d) shows the depth dependence of the same quantities for the 'clinical' beam quality of 15 MV (for the Mohan *et al* 1985 incident spectrum) in water. Figure 3.2 illustrates more clearly than Figure 3.1 the difference between (normal) kerma and kerma corresponding to no charged-particle transport, K_{ncpt}, and thus gives an idea of the magnitude of the error that could be made over a large volume if kerma is approximated by setting a high value of the charged-particle cut-off in a Monte-Carlo simulation.

(a)

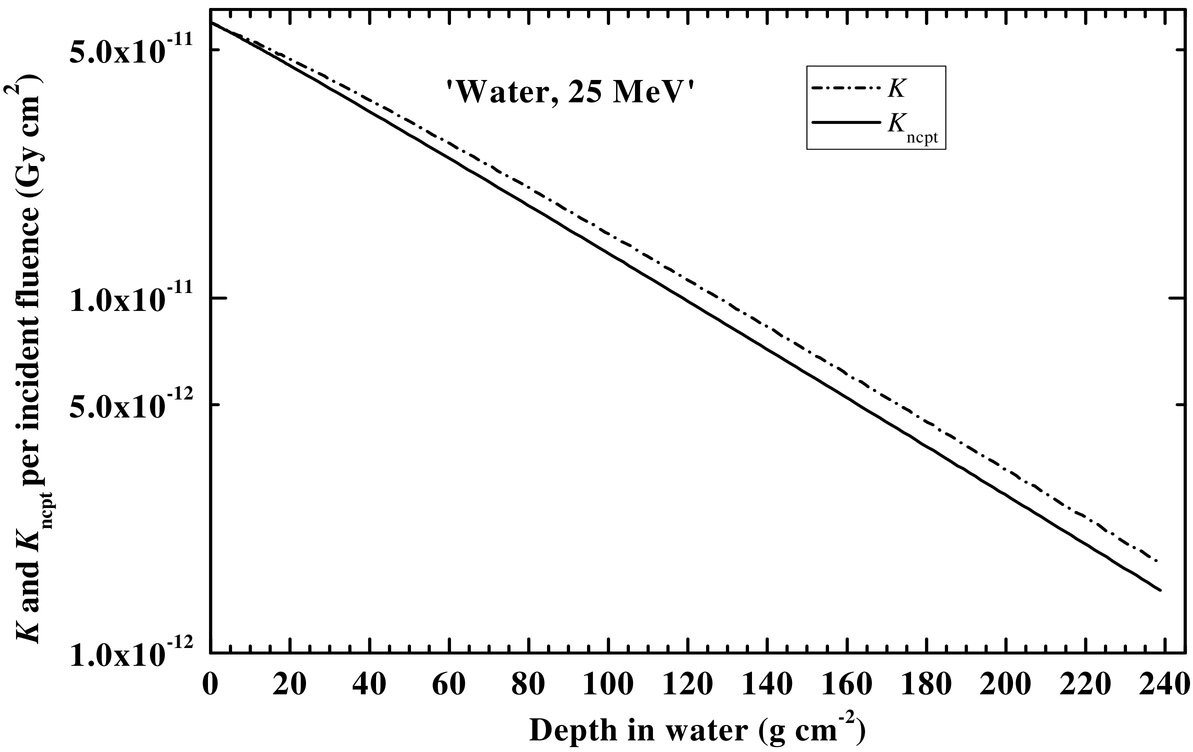
'Water, 25 MeV'
K
K ncpt
K and K ncpt per incident fluence (Gy cm2)
5.0x10-11
1.0x10-11
5.0x10-12
1.0x10-12
0
20
40
60
80
100
120
140
160
180
200
220
240
Depth in water (g cm-2)

(b)

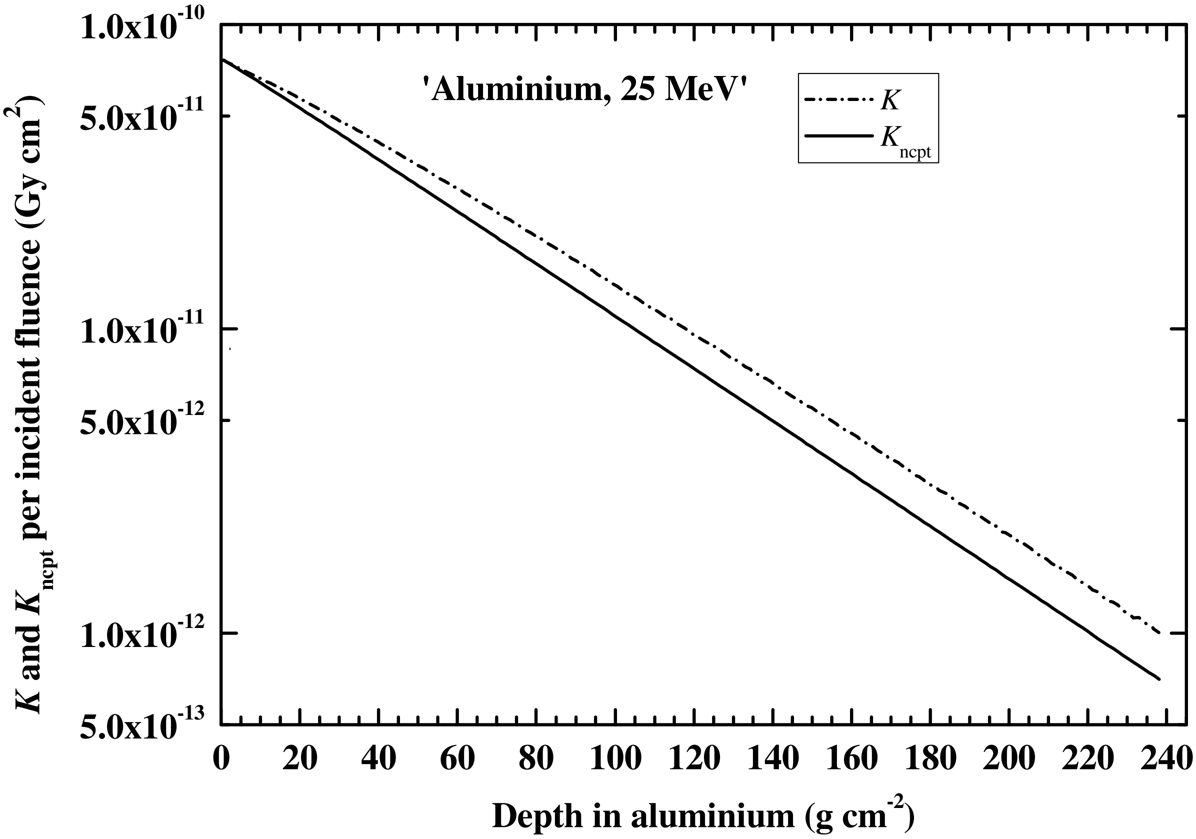
'Aluminium, 25 MeV'
K
K ncpt
K and K ncpt per incident fluence (Gy cm2)
1.0x10-10
5.0x10-11
1.0x10-11
5.0x10-12
1.0x10-12
5.0x10-13
0
20
40
60
80
100
120
140
160
180
200
220
240
Depth in aluminium (g cm-2)

(c)

(d)

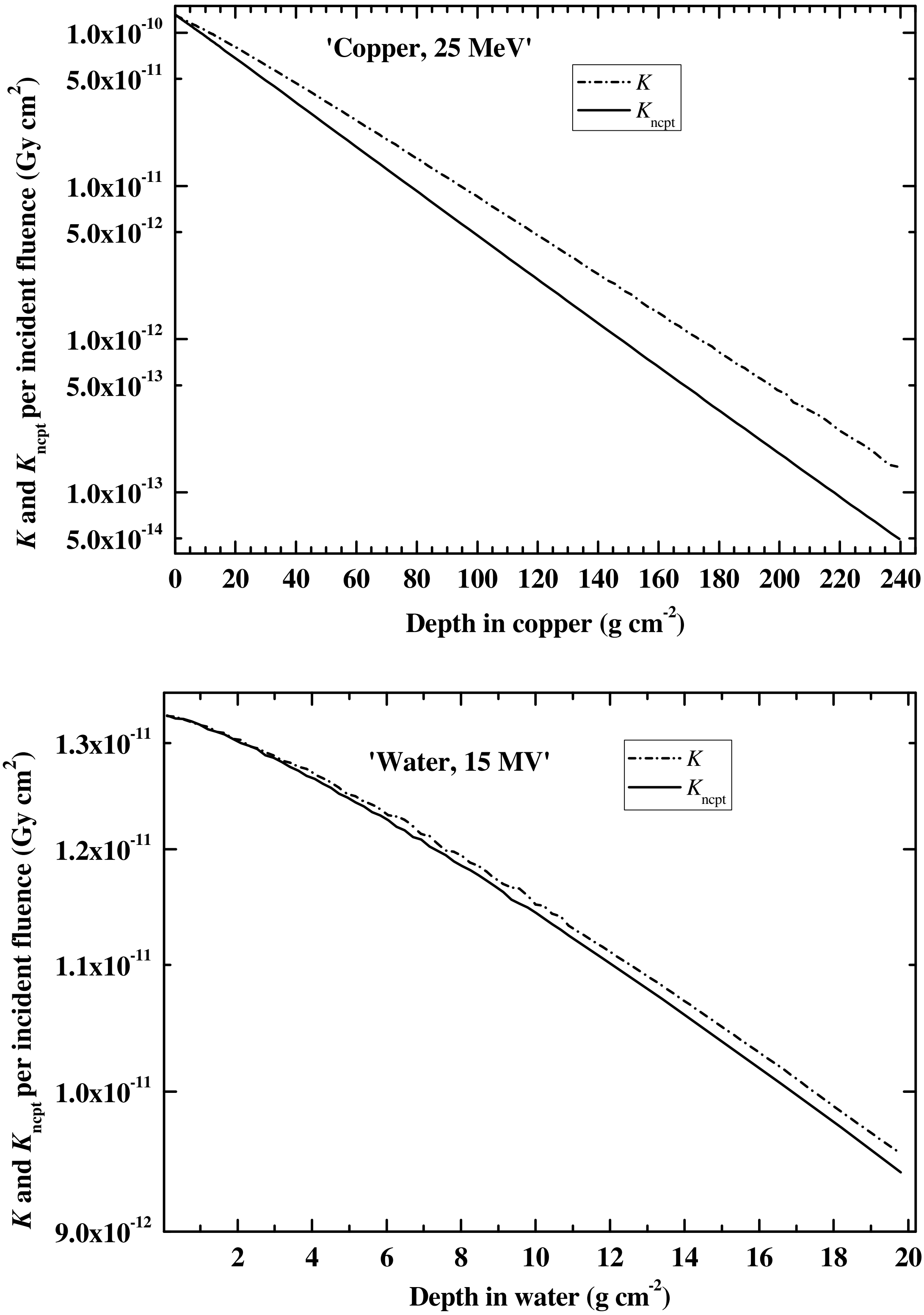

Figure 3.2: **(a) Kerma, *K* and kerma (no charged-particle transport), K_{ncpt} per unit incident photon fluence (Gy cm^2) versus depth (g cm^{-2}) for the depth-dependent large radius geometry for photon beams with *ECUT* = 512 keV (total energy) and high *ECUT* = 50.511 MeV (total energy) respectively, for a 25 MeV monoenergetic broad, parallel photon beams in water; (b) same quantities and energy for aluminium; (c) same quantities and energy for copper; (d) same quantities, 15 MV 'clinical' photon beam (spectrum from Mohan *et al* 1985) in water. Kerma and kerma (no charged-particle transport) were computed using DOSRZnrc.**

Table 3.1: **Kerma K over a large volume, divided by Dose D over the same large volume, K/D, and $1/(1-\bar{g})$ (equation 3.9) for beams of 0.1 to 25 MeV photons in water, aluminium and copper. The statistical (Type A) uncertainties are ± 2 standard deviations.**

Photon energy (MeV)	Water		Aluminium		Copper	
	K/D	$1/(1-\bar{g})$	K/D	$1/(1-\bar{g})$	K/D	$1/(1-\bar{g})$
0.1	1.0002 ± 0.0001	1.0002	1.0009 ± 0.0001	1.0008	1.0032 ± 0.0001	1.0029
0.5	1.0008 ± 0.0001	1.0007	1.0018 ± 0.0001	1.0018	1.0057 ± 0.0001	1.0057
1	1.0017 ± 0.0001	1.0016	1.0037 ± 0.0001	1.0036	1.0100 ± 0.0001	1.0098
5	1.0124 ± 0.0001	1.0128	1.0240 ± 0.0001	1.0238	1.0526 ± 0.0001	1.0524
10	1.0306 ± 0.0001	1.0305	1.0552 ± 0.0002	1.0550	1.1104 ± 0.0002	1.1100
25	1.0857 ± 0.0002	1.0859	1.1417 ± 0.0002	1.1413	1.2547 ± 0.0003	1.2544
25	1.0857 ± 0.0002	1.0859	1.1417 ± 0.0002	1.1413	1.2547 ± 0.0003	1.2544

Table 3.2: **Collision Kerma K_{col} over a large volume, divided by Dose D over the same large volume, K_{col}/D for beams of 0.1 to 25 MeV photons in water, aluminium and copper. The statistical (Type A) uncertainties are ± 2 standard deviations.**

Photon energy (MeV)	K_{col}/D		
	Water	Aluminium	Copper
0.1	1.0001 ± 0.0001	0.9999 ± 0.0002	1.0000 ± 0.0001
0.5	1.0000 ± 0.0001	1.0002 ± 0.0003	1.0001 ± 0.0002
1	1.0000 ± 0.0002	1.0002 ± 0.0002	1.0002 ± 0.0003
5	1.0000 ± 0.0002	1.0002 ± 0.0003	1.0002 ± 0.0003
10	1.0001 ± 0.0003	1.0001 ± 0.0002	1.0002 ± 0.0003
25	0.9998 ± 0.0003	1.0004 ± 0.0005	1.0000 ± 0.0002

Table 3.1 and Table 3.2 give the results of *K/D* and K_{col}/D for the LVG for 0.1 to 25 MeV broad, parallel photon beams in water, Al and Cu. It is observed that *K/D* is always greater than unity whereas K_{col}/D is unity within the very low statistical uncertainties. In other words the energy deposited in the large volume is equal to the energy content of collision kerma in this same volume. This demonstrates that over a large volume collision kerma conserves energy whereas kerma does not; for 25 MeV photons this violation amounts to 8.6%, 14.2% and 25.5% (essentially given by $1/(1-\bar{g})$) in the large volumes of water, aluminium and copper respectively. These results further emphasize that one cannot obtain kerma from the dose yielded by setting a high value of *ECUT* in a Monte-Carlo simulation for a large-volume geometry.

Table 3.3 presents the values of the modified kerma, K_{ncpt}, divided by dose D for the LVG for the same beam qualities and media. It is seen that K_{ncpt} does conserve energy to a very good approximation. The very small excess of K_{ncpt} over D at 5 MeV and above in copper is probably due to the tiny amount of (kinetic) energy backscattered on secondary electrons and thus included in the scoring of kerma but not of dose. Table 3.4 presents the values of *K/D*, K_{col}/D and K_{ncpt}/D for 'clinical' linac spectra of 6, 10 and 15 MV (spectra from Mohan *et al* 1985) in water only. The *K/D* values are 1.018, 1.0011 and 1.006 for 15, 10 and 6 MV respectively. It should be noted that *K/D* is also given by $1/(1-\bar{g})$ derived from the photon fluence spectra via equations (3.7) and (3.8) for the LVG.

Table 3.3: **Kerma (no charged-particle transport), K_{ncpt}, over a large volume, divided by Dose D over the same large volume, K_{col}/D for beams of 0.1 to 25 MeV photons in water, aluminium and copper. The statistical (Type A) uncertainties are ± 2 standard deviations.**

Photon energy (MeV)	K_{ncpt}/D		
	Water	Aluminium	Copper
0.1	1.0000 ± 0.0001	1.0000 ± 0.0001	1.0004 ± 0.0001
0.5	1.0000 ± 0.0001	1.0000 ± 0.0001	1.0002 ± 0.0002
1	1.0001 ± 0.0001	1.0003 ± 0.0002	1.0005 ± 0.0003
5	1.0002 ± 0.0001	1.0006 ± 0.0002	1.0021 ± 0.0003
10	1.0000 ± 0.0001	1.0004 ± 0.0003	1.0028 ± 0.0003
25	0.9997 ± 0.0003	1.0001 ± 0.0003	1.0028 ± 0.0004

Table 3.4: **Kerma K over a large volume, divided by Dose D over the same large volume, K/D, and similarly for K_{col}/D and K_{ncpt}/D for 'clinical' beam qualities from 6 MV to 15 MV for broad, parallel 'clinical' photon beam (spectra from Mohan *et al* 1985) in water. The statistical (Type A) uncertainties are ± 2 standard deviations.**

	Water			
Clinical beam quality (MV)	K/D	$1/(1-\overline{g})$	K_{col}/D	K_{ncpt}/D
6	1.0057 ± 0.0001	1.0056	1.0000 ± 0.0001	1.0000 ± 0.0001
10	1.0110 ± 0.0001	1.0109	1.0002 ± 0.0002	1.0002 ± 0.0002
15	1.0181 ± 0.0002	1.0180	1.0001 ± 0.0002	1.0003 ± 0.0002

3.3.2 Total photon fluence, differential in energy

Figures 3.3(a) - (b) compare photon fluence spectra for the 25 MeV broad, parallel photon beams at a depth of ≈ 51 g cm^{-2} in all three media for both very high and very low charged-particle transport cut-offs, *ECUT*.

(a)

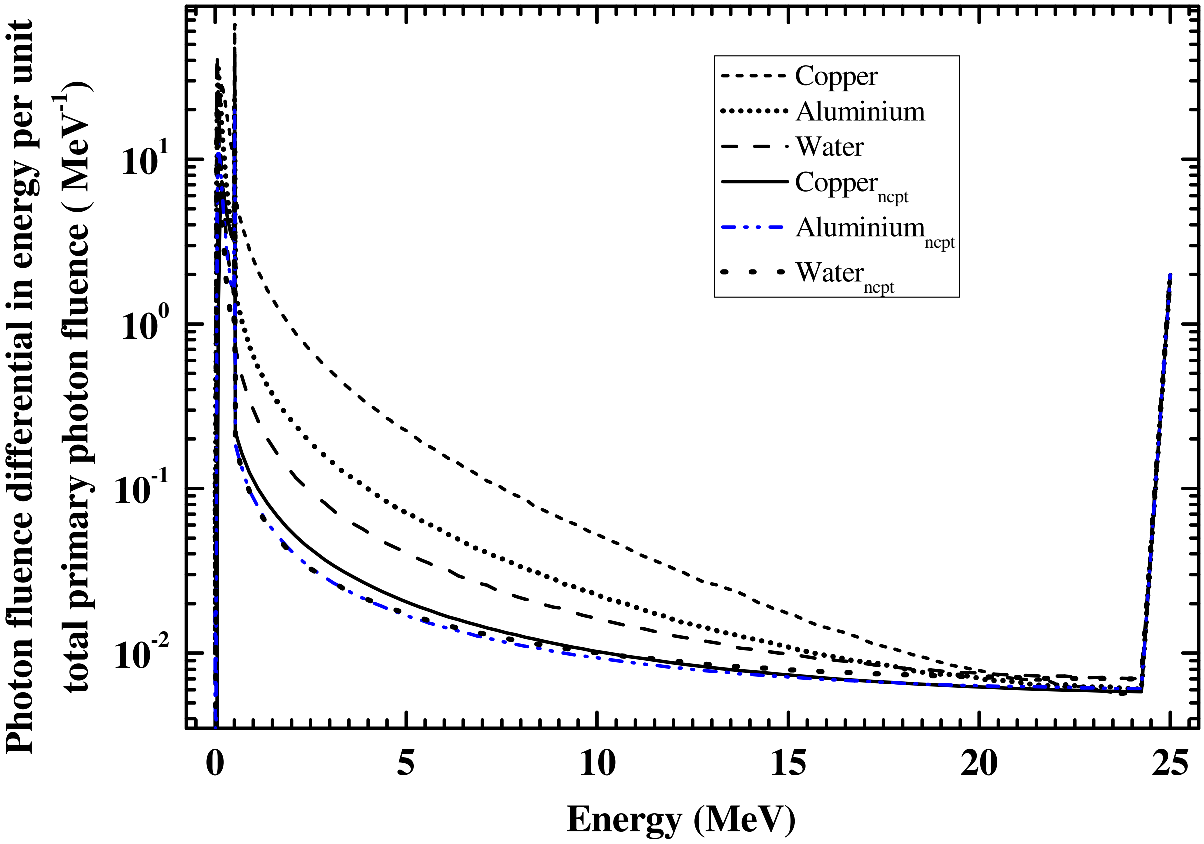

(b)

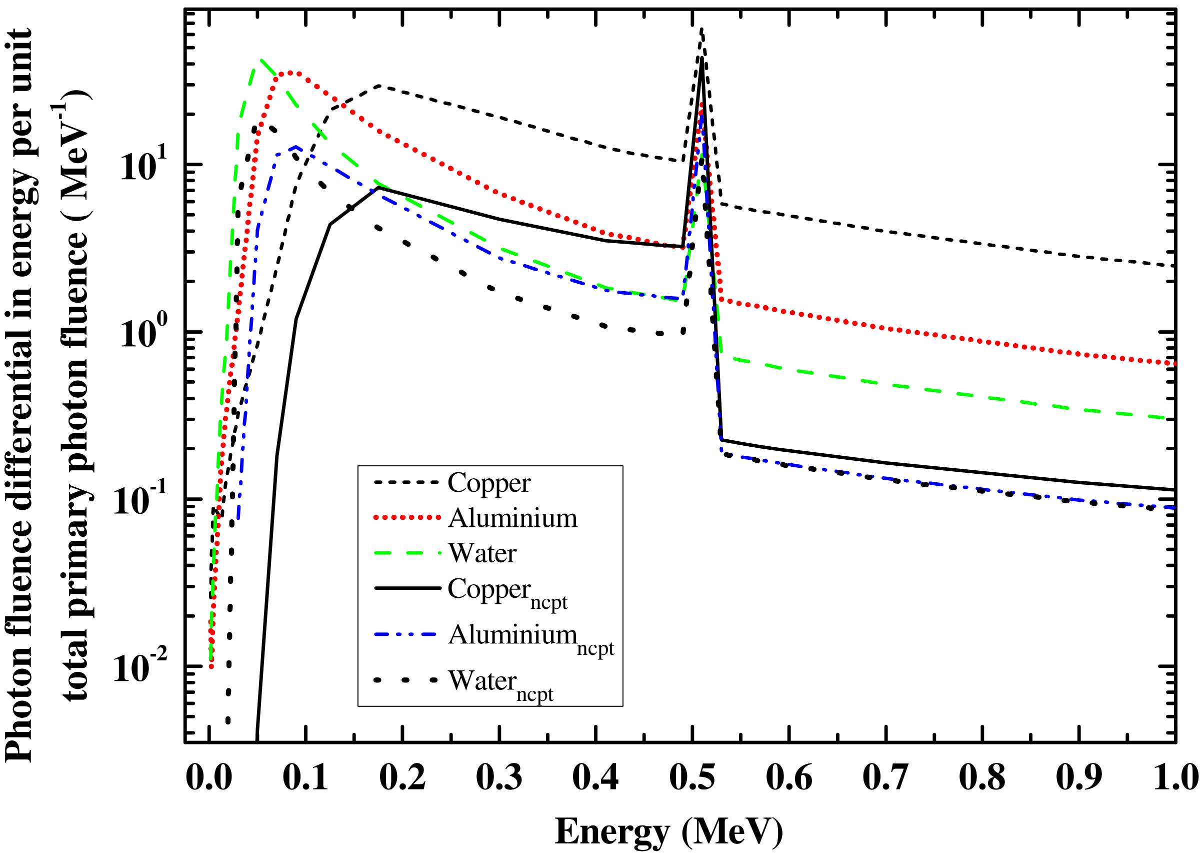

Figure 3.3: **(a) A comparison of total photon fluence, differential in energy, along the central axis, normalized to the fluence at the incident energy, for a 25 MeV monoenergetic broad, parallel photon beams, at depths varying between 51.25 and 52.52 g cm^{-2} in water, aluminium and copper for the DDLRG with very high charged-particle transport cut-off (i.e. *ECUT* = 50.511 MeV (total energy)), labelled with the subscript 'ncpt' and very low charged-particle transport cut-off (i.e. *ECUT* = 512 keV (total energy)), with no subscript; (b) same quantity and media up to a energy range of 1 MeV to visualize the details of the 'spike' at 0.511 MeV due to annihilation photons.**

The difference between the 'low *ECUT*' curves and the 'ncpt' ones is solely due to secondary bremsstrahlung, this being present in the former but not in the latter; this difference is especially marked in copper.

Figure 3.3(b) shows the energy region up to 1 MeV in order to highlight the 'spike' at 0.511 MeV due to annihilation photons. It should be noted that this 0.511 MeV spike is present in the spectra corresponding to both high and low *ECUT*. This is because the Monte-Carlo code DOSRZnrc 'forces' positron annihilation in the scoring volume where these particles fall below *ECUT* i.e. the identical volume where these are created in the case of high *ECUT*. This is consistent with the energy conserving properties of K_{ncpt}. From a careful examination of Figure 3.3(b), in the case of copper a small difference in the height of the low-*ECUT* and high-*ECUT* 0.511 MeV spikes can be discerned; the slightly more pronounced low-*ECUT* spike must be due to the small extra amount of pair-production due to secondary bremsstrahlung photons, while in water this difference is entirely negligible.

3.3.3 The influence of *PCUT* on kerma

Figure 3.4 shows the variation of kerma at depths ≈ 40.0 g cm^{-2} computed by the DOSRZnrc user-code as well as from the cavity integral (equation 3.7) as a function of *PCUT* for values between 1 keV and 200 keV for a 25 MeV broad, parallel photon beam in the three media. As expected kerma decreases as *PCUT* increases. This can be interpreted as an increase in magnitude of the track-end term (see sub-section 3.2.3) with increasing *PCUT*. The decrease in kerma is more pronounced for the high-Z media (Cu, Al) which is probably because the build up of low-energy photon fluence (i.e. due to secondary bremsstrahlung photons) above approximately 100 keV, relative to the primary fluence, is more pronounced at high-Z (cf. Figure 3.3(b)). Kerma values computed by the two different methods, with identical normalization, were found to be in excellent agreement, generally within ± 0.3%.

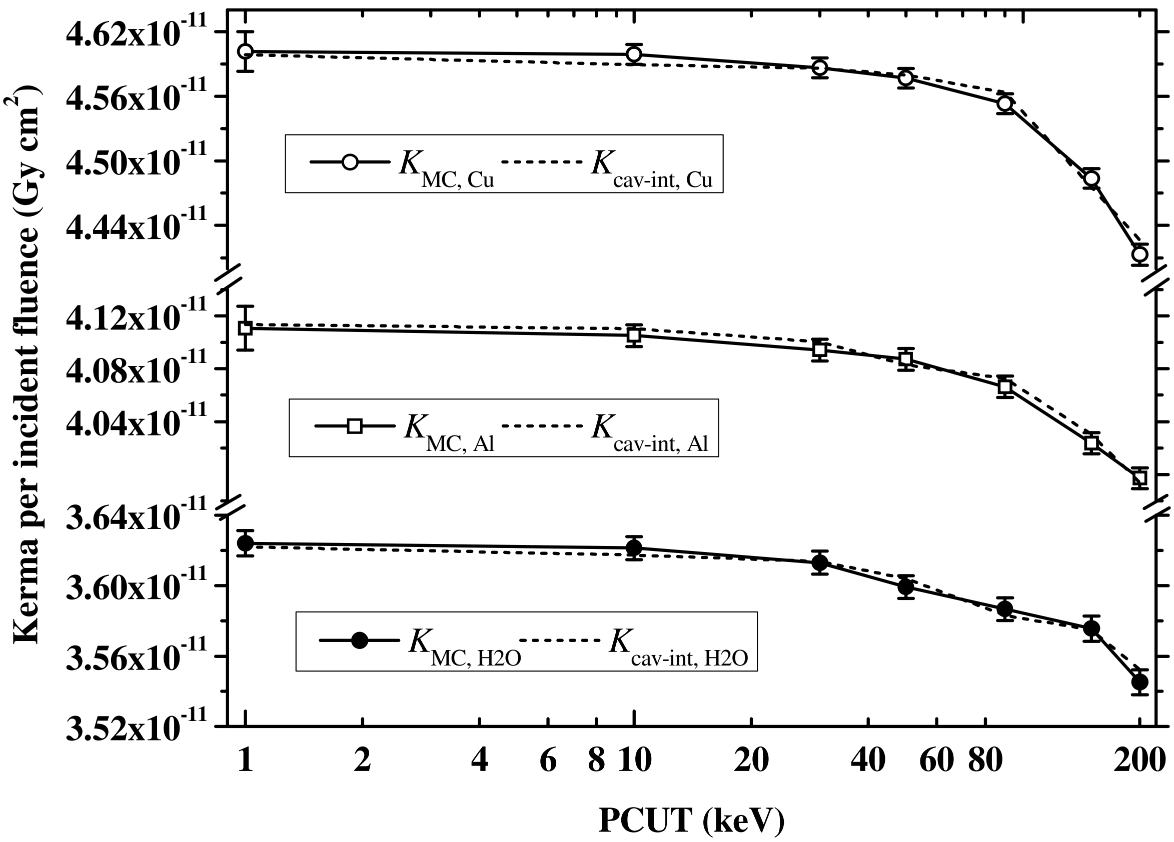

Figure 3.4: **Kerma per unit incident photon fluence (Gy cm^2) versus *PCUT* (keV) for 25 MeV monoenergetic broad, parallel photon beams at depths ≈ 40.0 g cm^{-2} for the depth-dependent large radius geometry in water, aluminium and copper. Kerma derived using DOSRZnrc (full lines). The error bars are ± 2 standard deviations and correspond to statistical (Type A) uncertainties. The short dashed lines represent the values of kerma calculated from the 'cavity integral' (equation 3.7) using fluence spectrum values from FLURZnrc.**

3.4 Summary and Conclusions

The ratios K/D, K_{col}/D and K_{ncpt}/D for 0.1 to 25 MeV 'broad', parallel photon beams in water, aluminium and copper media have been derived from Monte-Carlo simulation in a large phantom of thickness 1308 cm with a scoring volume of radius 654 cm (dimensions chosen to ensure a negligible particle escape). K/D is always greater than unity, by as much as 25% for 25-MeV photons in copper. The ratios K_{col}/D and K_{ncpt}/D are equal to unity (within extremely small statistical uncertainties) and demonstrate that over a large volume, collision kerma and K_{ncpt} conserve energy in contrast to (normal) kerma. However, for a 'clinical' 6 MV beam quality K/D only exceeds unity by 0.6% over the large water volume. This analysis has highlighted the role played by secondary bremsstrahlung in determining kerma at large depths. Additionally the small error made when computing kerma by numerical integration over photon fluence has been quantified as a function of *PCUT* and an expression for a photon track-end correction term has been formulated.

CHAPTER 4

Characterizing the influence of detector density on dosimeter response in non-equilibrium small photon fields

4.1 Introduction

Small radiation fields are increasingly being used in modern radiotherapy techniques such as stereotactic radiosurgery, IMRT and VMAT. The dosimetric measurements required to commission these techniques are the subject of much interest in the literature, both in terms of characterizing small-field detector properties (Westermark *et al* 2000, McKerracher and Thwaites 2002, Pappas *et al* 2008) and developing formalisms relating small-field measurements to conventional dosimetry carried out at standard field sizes and conditions (Alfonso *et al* 2008).

A number of authors have suggested that silicon diodes should make good small-field detectors due to the small size and high sensitivity of their active volume (McKerracher and Thwaites 1999). Sauer and Wilbert (2007) observed a limited variation in the energy response of shielded ('photon') diodes; however studies by Eklund and Ahnesjö (2010) showed that the tungsten shielding of these diodes significantly distorts the radiation energy spectrum at the detector 'cavity', decreasing the low-energy photon scatter and increasing the electron fluence. Unshielded ('electron') diodes do not perturb the radiation fluence in this way; their relatively small size and good directional dependence (McKerracher and Thwaites 2002) ought to make them close to ideal for small-field dosimetry.

Differences between beam profiles measured using various detectors are described in a number of papers. Dose averaging over the finite volume of a detector leads to apparent penumbral broadening (Dawson *et al* 1986), which is offset to some extent by penumbral 'sharpening' and profile distortion by solid-state dosimeters such as silicon diodes and diamond detectors (Pappas *et al* 2008, Beddar *et al* 1994).

Scott *et al* 2008 briefly explored the effect of calculating the dose delivered to a silicon voxel (representing an unshielded diode) located on the axis of a small radiation field in a water tank, rather than directly calculating the dose delivered to a voxel of water. The study was carried out using a Monte-Carlo (MC) model of a 15 MV beam generated by a Varian 2100C linear accelerator (linac) (Varian Medical Systems, Palo Alto, CA). Using photon and electron spectra calculated in the water phantom, it was found that both the Spencer-Attix, or restricted mass stopping-power ratio, water-to-silicon, $s^{\mathrm{SA}}_{\mathrm{w,Si},\Delta}$ and the mass energy-absorption coefficient ratio, water-to-silicon, $\left(\mu_{\mathrm{en}}/\rho\right)_{\mathrm{w,Si}}$ for the 15 MV beam vary minimally with field size and depth as previously shown by Sánchez-Doblado *et al*

(2003) and subsequently confirmed by Bouchard *et al* (2009). However, by directly calculating the doses to water voxels and detector voxels in the water phantom it was showed that the quantity

$$F_{\text{detector}} = \frac{D_{\text{water}}(\text{FS}, d = 5\text{ cm})}{D_{\text{detector}}(\text{FS}, d = 5\text{ cm})} \tag{4.1}$$

changes significantly with field-size, where D_{water} (FS, d = 5 cm) is the dose delivered to a water voxel whose size is roughly that of the sensitive volume of the detector, and which is located on the central axis of a field of size FS at 5 cm depth in a water phantom set up at a source-surface-distance (SSD) of 100 cm, and D_{detector} (FS, d = 5 cm) is the dose delivered to the same voxel with its composition changed to reflect that of the sensitive volume of the detector – silicon in the case of a diode.

Further Scott *et al* (2008) found that although F_{diode} is constant for square fields of around 2 cm width and above (as expected if it is simply a property of the beam quality, detector atomic composition and physical dimensions), it decreases strongly at very small field sizes. Since $s^{\text{SA}}_{\text{w,Si},\Delta}$ and $\left(\mu_{\text{en}}/\rho\right)_{\text{w,Si}}$ change very little with field size, it was inferred that this variation in F_{diode} was not due to the differences in the atomic composition of water and silicon. Therefore F_{diode} was tentatively attributed to the higher physical density of the silicon.

Mobit *et al* (1997) have modelled the response of small chips of diamond in water phantoms irradiated using wide monoenergetic photon and electron beams. They found no energy dependence for electron beams but a significant decrease in sensitivity for very low-energy photon beams (25 kV). Haryanto *et al* (2002) compared output factors measured using a number of detectors with MC calculations of doses delivered to small voxels of detector material placed in a virtual water phantom. They modelled a 6 MV photon beam generated by an Elekta Sl*i* linac (Elekta Oncology Systems Ltd, Crawley, UK), and calculated doses delivered to ‘detector’ voxels from fields of size 1-15 cm. Measurements made using the silicon diode, diamond detector, and PinPoint 3D ionization chamber yielded different small-field output factors, but for each detector the measurements matched their respective MC calculated values. However the dimensions of the voxels were chosen arbitrarily, rather than reflecting those of the detectors modelled, and the density of diamond used in the study was quite low (2.26 g cm^{-3}), closer to that tabulated for graphite than for diamond (3.5 g/cm^{3})[7].

Crop *et al* (2009) used MC methods to determine the effect of individual components of microionization chambers on perturbation factors for small photon fields. They obtained a smaller perturbation factor for the roughly spherical ‘PinPoint 3D’ ionization chamber (Model 31016, PTW,

[7] http://www.mindat.org

Freiburg, Germany) than for the more elongated PinPoint chambers (Models 31006/31014/31015, PTW, Freiburg, Germany). They also found that the perturbation factors changed with the distance off-axis in a small field, suggesting that these detectors may not be ideal for measurement of small-field profiles.

Francescon *et al* (2011) have performed detailed MC calculations of correction factors for a range of commercially available detectors in the 6 MV beams of two clinical linear accelerators. Similarly to Scott *et al* (2008) results they also found that at field sizes of 2 cm and greater the correction factor is constant.

Alfonso *et al* (2008) have defined a factor $k_{Q_{\mathrm{FS}},Q_{\mathrm{FSref}}}^{f_{\mathrm{FS}},f_{\mathrm{FSref}}}$ representing the difference between chamber response in measured and reference fields:

$$k_{Q_{\mathrm{FS}},Q_{\mathrm{FSref}}}^{f_{\mathrm{FS}},f_{\mathrm{FSref}}} = \frac{D_{\mathrm{w},Q_{\mathrm{FS}}}^{f_{\mathrm{FS}}} \Big/ M_{Q_{\mathrm{FS}}}^{f_{\mathrm{FS}}}}{D_{\mathrm{w},Q_{\mathrm{FSref}}}^{f_{\mathrm{FSref}}} \Big/ M_{Q_{\mathrm{FSref}}}^{f_{\mathrm{FSref}}}} = \frac{F_{\mathrm{detector}}(\mathrm{FS})\ P_{\mathrm{vol}}(\mathrm{FS})}{F_{\mathrm{detector}}(\mathrm{FS}_{\mathrm{ref}})\ P_{\mathrm{vol}}(\mathrm{FS}_{\mathrm{ref}})} \tag{4.2}$$

where f_{FSref} and f_{FS} denote the reference field and a nonstandard field of size FS respectively, Q_{FSref} and Q_{FS} describe the radiation qualities of these fields, $D_{\mathrm{w},Q_{\mathrm{FS}}}^{f_{\mathrm{FS}}}$ is the dose to water at a point in the centre of a field of size FS and quality Q_{FS}, and $M_{Q_{\mathrm{FS}}}^{f_{\mathrm{FS}}}$ is the associated detector reading. Assuming that the detector reading is proportional to the integral dose absorbed by its sensitive volume (Francescon *et al* 2011) then it follows that the *k* factor is equal to the ratio of F_{detector} values for the measured and reference fields, multiplied by a ratio of 'P_{vol}' factors which account for $D_{\mathrm{w},Q_{\mathrm{FSref}}}^{f_{\mathrm{FSref}}}$ being defined as dose at a point, in contradistinction to the detector reading which represents the dose absorbed throughout the sensitive volume of the detector. Bouchard *et al* (2009) have developed a formalism linking the dose absorbed by a detector to the dose in water, according to which F_{detector} is equivalent to $P_\rho P_{\mathrm{fl}}\ s_{\mathrm{w,det},\Delta}^{\mathrm{SA}}$ where P_ρ represents the dosimetric impact of any difference in density between water and the detector active volume, and P_{fl} describes the effect of changes in electron fluence within the active volume if its atomic composition differs from that of water. Following the similar formalism of Crop *et al* (2009) F_{detector} is equivalent to $p_{\mathrm{det\text{-}w}}\ s_{\mathrm{med,det},\Delta}^{\mathrm{SA}}$ where $p_{\mathrm{det\text{-}w}}$ is a term equivalent to the product of Bouchard's P_ρ and P_{fl} factors.

In this chapter the computational approach is developed outlined in previous published study (e.g. Scott *et al* 2008), using the Monte-Carlo 15 MV beam model to explore detector response on

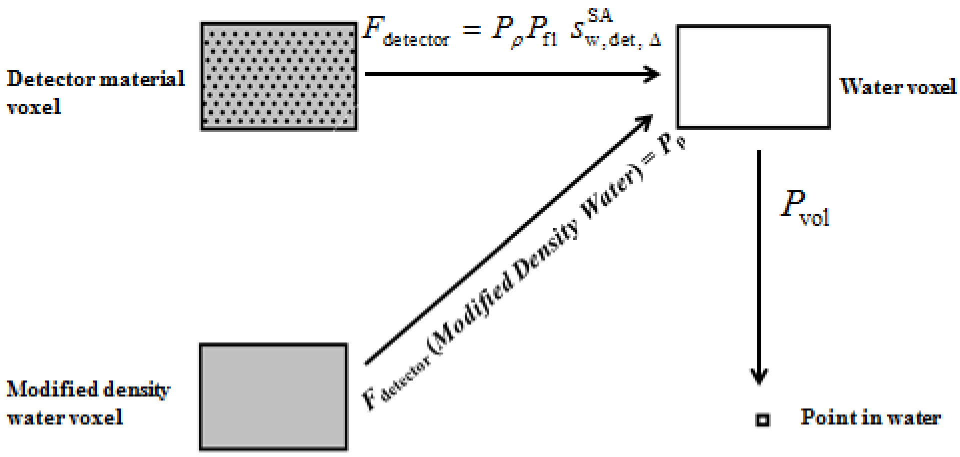

Figure 4.1: **Schematic illustration of the cavities simulated in this work, and the perturbation factors required to obtain the dose to a point in water.**

the central axis. The calculations are presented for active detector volumes of different atomic compositions and densities, broadly representative of a PTW 60003 diamond detector (PTW, Freiburg, Germany), a PTW 31016 PinPoint 3D ionization chamber, and a Scanditronix unshielded electron diode (Scanditronix-Wellhöfer, Uppsala, Sweden). In order to study how detector response changes specifically with the density of the detector active volume, other detector components have been excluded from considerations, and water-to-detector ratios F_{detector} are calculated under two conditions: one for which the density and mass radiological properties of the modelled detector volume are set equal to the real active volume, and the other for which the modelled density is changed to that of the detector, but the mass radiological properties are held fixed at those of unit density water. These latter results allow to isolate the impact of changes in detector density measurements (P_{ρ} in the system of Bouchard *et al* 2009) from the better understood effects of changes in atomic composition (figure 4.1).

4.2 Materials and methods

Monte-Carlo model of a Varian 2100C linear accelerator (Varian Medical Systems, Palo Alto, CA) for photon beams of nominal energy 15 MV developed and validated previously has been used here (Scott *et al* 2008, 2009). A Monte-Carlo model of the accelerator used here was constructed in the BEAMnrc system (Rogers *et al* 1995, 2011a), setting physical machine dimensions to values provided by Varian Medical Systems and achieving good agreement between calculated and measured dose-distributions(within 2%). The phase-space files, generated for previously published study e.g. Scott *et al* (2009) , were scored at a distance of 58 cm from the source, were subsequently used as input for EGSnrc user-code CAVRZnrc (version: V4-2.3.2) using the 'source 21' option (Rogers *et al* 2011b).

The CAVRZnrc user-code of the EGSnrc Monte-Carlo code system has been designed specifically to calculate doses delivered to cylindrically symmetric detectors placed on axis (Rogers 2011b). Different detector voxels have been located at 5 cm depth in a water phantom set up with a SSD of 100 cm. Doses calculated in the detector voxels are compared to those calculated for a voxel of water located at the same place, to establish values for the dose-to-water to dose-to-detector-in-water factor F_{detector} (FS, d) (equation (4.1)). For relative dosimetry it is the variation of this correction factor with field size and depth that matters, rather than its absolute value.

To fully explore the impact of detector density on small-field measurements, the doses for square fields down to a size (width) of 0.25 cm collimated by the linac jaws have been calculated, although the minimum field size currently available on Varian 2100C linear accelerator (Varian Medical Systems, Palo Alto, CA) is 0.5 cm.

4.2.1 Silicon, PTW diamond and PinPoint *3D* detectors

The aim of this work is to characterize the impact of differences in the atomic composition and density of active volumes of detectors on the doses recorded by them, modelling dosimeters as simple homogeneous voxels of detecting material surrounded by water and ignoring any metal contacts or epoxy casing.

All detector active volumes were modelled as having a circular cross-section of 2.26 mm diameter, which has the same area as a 2 × 2 mm^2 square (used as the standard size in previous study, Scott *et al* 2008, 2009) and is close to the area of the circular cross-section of the silicon diode's sensitive region. The thicknesses of the silicon and diamond voxels were chosen to match those of the slim disc- and tablet-like sensitive volumes of the respective detectors, while the PinPoint 3D ionization chamber sensitive volume was modelled as a cuboid of thickness 2 mm, rather than having the 2.9 mm high domed shape of the real air cavity (table 4.1). This results in a modelled air cavity that has half the volume of the physical PinPoint 3D ionization chamber – but this difference between experimental and calculational volumes has no impact on the main focus of this work, which is to compare doses calculated for voxels of different composition, rather than to compare measured and calculated doses. Crop *et al* (2009) found that the central electrode of the PinPoint 3D ion chamber, which is not modelled here, minimally perturbs the dose in the air cavity.

The detector material of the PinPoint 3D and diamond detectors has been represented as single voxels, but for the diode a stack of two silicon voxels is generally used. Only the dose recorded in the upper (0.06 mm thick) voxel which represents the sensitive volume (depletion layer) is used in these calculations; the lower (0.44 mm thick) voxel, which represents the silicon dye, is included in the modelling to fully capture the fluence perturbation caused by the whole silicon crystal.

Table 4.1: **Voxel properties used for simplified model of various detectors.**

	Physical Dimensions			Modelled Dimensions		
Detector name	Diameter (mm)	Depth (mm)	Density (g cm^{-3})	Diameter (mm)	Depth (mm)	Density (g cm^{-3})
Silicon Diode	2.00	0.06	2.3	2.26	0.06	2.3
Silicon Diode (dye)	2.00	0.44	2.3	2.26	0.44	2.3
PTW Diamond (PTW 60003)	3.00*	0.26	3.5	2.26	0.26	3.5
PinPoint 3D ionization chamber (PTW 31016)	2.90	2.90	0.0012	2.26	2.00	0.0012

*The active volume of the diamond detector is a cuboidal chip with a width estimated by the manufacturer of 3 mm.

The radiation interaction cross sections and stopping powers of several materials are provided with the EGSnrc software and stored in a PEGS4 datafile (Pre-processor for EGS (Nelson *et al* 1985, Kawrakow *et al* 2011)). Although graphite is included, diamond with a density of 3.5 g cm^{-3} was not available, in the default version, and so had to be generated independently. First a density correction file was generated to account for the polarisation effect in the denser form of carbon using a program available on the NIST website[8]. Then this was combined with the EGSnrcMP package (Kawrakow *et al* 2006) to generate a PEGS4 datafile, setting the parameters AP=1 keV, AE=512 keV where AP and AE are the production thresholds for secondary bremsstrahlung photons and knock-on electrons respectively.

4.2.2 Varying the density of water

The effect of density on detector response is twofold: firstly it affects the number of atoms a particle encounters on a given path; and secondly it also affects electron stopping powers via the polarisation effect. The changes in mass stopping power caused by the density-dependent polarization effect in small (active) volume of material are eliminated, since the dependence of absorbed dose on stopping power is already well understood. Therefore, the PEGS4 datafiles have been generated for artificial (water) substances having the densities of silicon, diamond and air but the atomic composition and mass stopping power and mass energy-absorption coefficients of unit density water. These artificial materials were then used in calculations of the dose delivered to a nominal detector voxel in a phantom of standard density water. The density-adjusted water voxels have the same dimensions as

[8] http://physics.nist.gov/PhysRefData/Star/Text/ESTAR.html

the corresponding voxels used to represent detector active volumes, and so comparisons between doses delivered to the different voxels are not biased by volume averaging effects.

F_{detector} is determined for these modified density water voxels, as well as for the voxels filled with 'real' detector material, described in sub-section 4.2.1. In the former case, where the atomic number of the detector is identical to water even though the density is not, both the factors P_{fl} and $s^{\mathrm{SA}}_{\mathrm{w,det},\Delta}$ are unity and so F_{detector} is equivalent to the P_{ρ} factor of Bouchard *et al* (2009). Similarly in Crop *et al*'s (2009) formalism F_{detector} for a voxel of modified density water can be interpreted as purely the $p_{\mathrm{det\text{-}w}}$ factor, where 'det' represents this voxel of modified-density water.

4.2.3 Voxel volume effects

Even for a perfect (water-like) detector the size of the active volume will affect the output recorded for very small fields, because the degree of averaging of dose across the peaked distribution will change with both detector size and dose gradient over the detector, which varies with field size. In Bouchard *et al*'s formalism this effect is accounted for by the factor P_{vol}, which is the ratio of the dose absorbed at a point in water to the dose absorbed by a finite volume of water. To characterize this factor, the output has been calculated on central axis for water voxels of various diameters – 2.26 mm representing an unshielded diode, 1.13 mm representing a smaller stereotactic diode or similar and 0.1 mm representing an ideal point-like detector .

In addition to the averaging effect discussed above, the volume of non-unit density material placed in a water phantom will influence the degree to which the electron fluence (in uniform) water is perturbed, and thus influence the magnitude of any resulting changes in absorbed dose in the detector material. To investigate this variation, F_{detector} *(*FS*, d)* values have been calculated for single silicon voxels of different thicknesses (0.5, 1.0 and 2.0 mm). Additionally, F_{detector} *(*FS*, d)* has been calculated for stacks of silicon voxels with diameters of 1.13, 1.70, and 2.26 mm, the upper active voxel having a thickness of 0.06 mm and the underlying dye a thickness of 0.44 mm.

4.2.4 Varying the focal spot size

The size of the x-ray focal spot generated by the incident electron beam in the 'thick' linac target partly determines the penumbral width of the beam in water, and may also influence the central axis dose in very small fields via source occlusion (Scott *et al* 2009). The dose absorbed by a voxel on the central axis will depend on the in-water radiation fluence profile in the vicinity, as well as on any fluence perturbation caused by the presence of the detector material. To check the influence of the focal spot size on F_{detector} ratios, BEAMnrc phase space files have been generated for a range of spot sizes, and used them to calculate F_{detector} values for a diode detector comprising two silicon voxels.

(a)

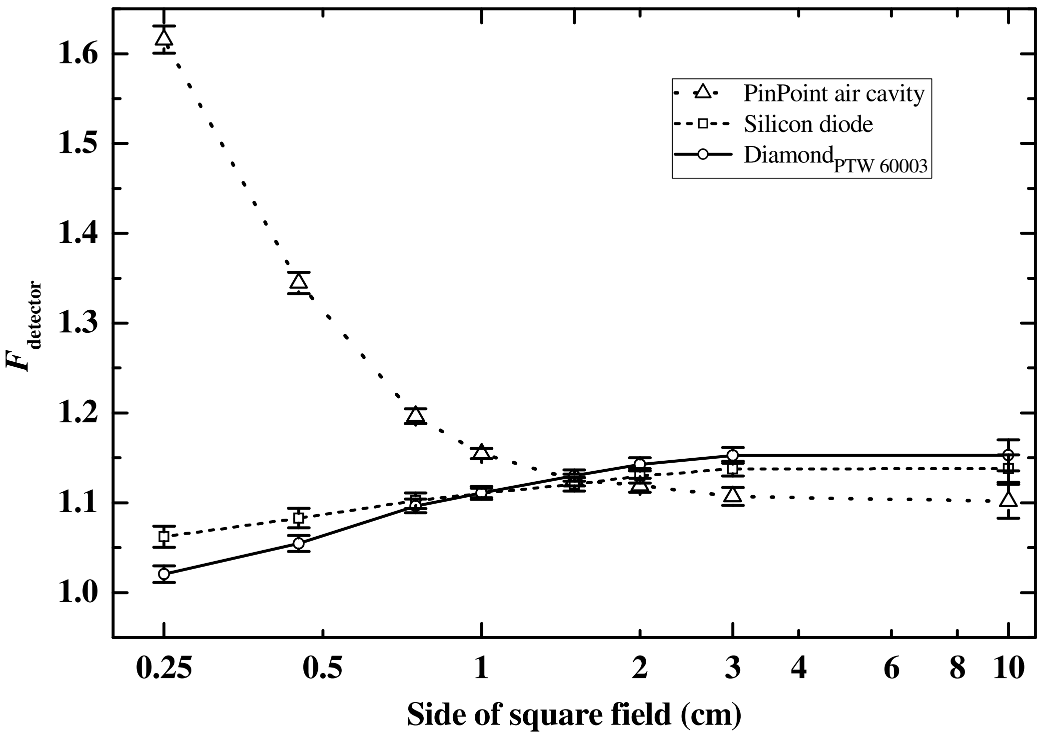

(b)

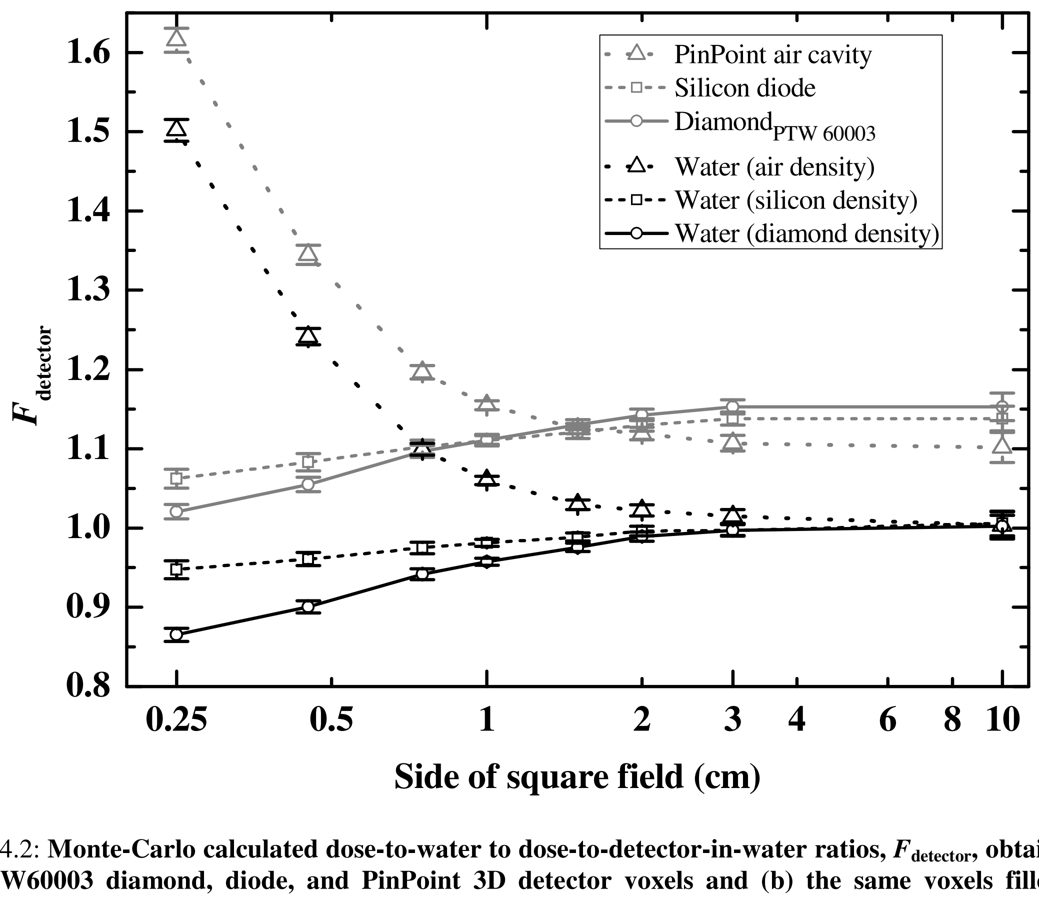

Figure 4.2: **Monte-Carlo calculated dose-to-water to dose-to-detector-in-water ratios, $F_{detector}$, obtained for (a) PTW60003 diamond, diode, and PinPoint 3D detector voxels and (b) the same voxels filled with detector-density water. All points are positioned on-axis at 5 cm depth in a water phantom and displayed with 2 standard deviation (σ) error bars, reflecting statistical uncertainties of the Monte-Carlo calculations. As with all other figures in this chapter the following field sizes have been analysed: 0.25, 0.5 0.75, 1.0, 1.5, 2.0, 3.0 10.0 cm.**

4.2.5 Variation of silicon diode response with depth

Previously it was established that neither $s_{\mathrm{w,Si},\Delta}^{\mathrm{SA}}$ nor $\left(\mu_{\mathrm{en}}/\rho\right)_{\mathrm{w,Si}}$ changes significantly with depth in small fields (Scott *et al* 2008), but it was not checked whether detector response changes with depth. Since F_{detector} varies with field size, it might be expected also to vary with depth because the beam progressively diverges. Therefore the calculations have been carried out, placing a stack of two silicon voxels at various depths in water and determining doses delivered to the upper (active) voxel by a 0.5 × 0.5 cm^2 field, thus simulating the depth dose curve measured by a silicon diode. The curve has been normalized at 5 cm depth, and compared it with a calculated dose-to-water depth dose curve.

4.3 Results

4.3.1 Silicon, PTW diamond and PinPoint 3*D* detectors

In figure 4.2(a) calculated dose-to-water to dose-to-detector-in-water ratios, $F_{\mathrm{detector}}(\mathrm{FS},\ d = 5\mathrm{cm})$ are plotted against square field size for diamond, silicon and air voxels positioned on axis at 5 cm depth in a water phantom positioned at 100 cm SSD. The behaviour of the diamond detector factor, F_{diamond}, is similar to that for silicon F_{diode}, although the diamond factor falls faster at small field sizes. On the other hand, F_{PinPoint}, for the low-density air voxel, varies in the opposite direction to F_{diode} and F_{diamond}, increasing at small field sizes.

4.3.2 Varying the density of water

The variation of F_{detector} values with field size is mirrored by the analogous curves calculated for voxels of water whose densities have been modified to those of the different detectors, figure 4.2(b). Whilst for large fields the values of F_{detector} for water voxels of any density are naturally unity, the F_{detector} values for the voxels of the different detector materials – silicon, diamond, air – reflect the respective combinations of a weighted average of water-to-detector material stopping-power ratio and mass energy-absorption coefficient ratio according to 'classical' cavity theory (Nahum 2009).

4.3.3 Voxel volume effects

In figure 4.3 P_{vol} values (taken as the ratio of average dose-to-water in a very small on-axis voxel of 0.1 mm diameter to that in a wider voxel) are plotted against field-size. In fields wider than 0.5 cm, the effect of dose averaging across water voxels of the same size as detector active volumes is small for commercially available detectors. On-axis in narrower fields, smaller voxels do record higher average doses than those of larger voxels, although the difference in output factor measured by detectors of 1.13 mm and 0.1 mm diameter remains quite small (1.8% relative) in a 0.5 cm field, but rises considerably in a 0.25 cm field.

(a)

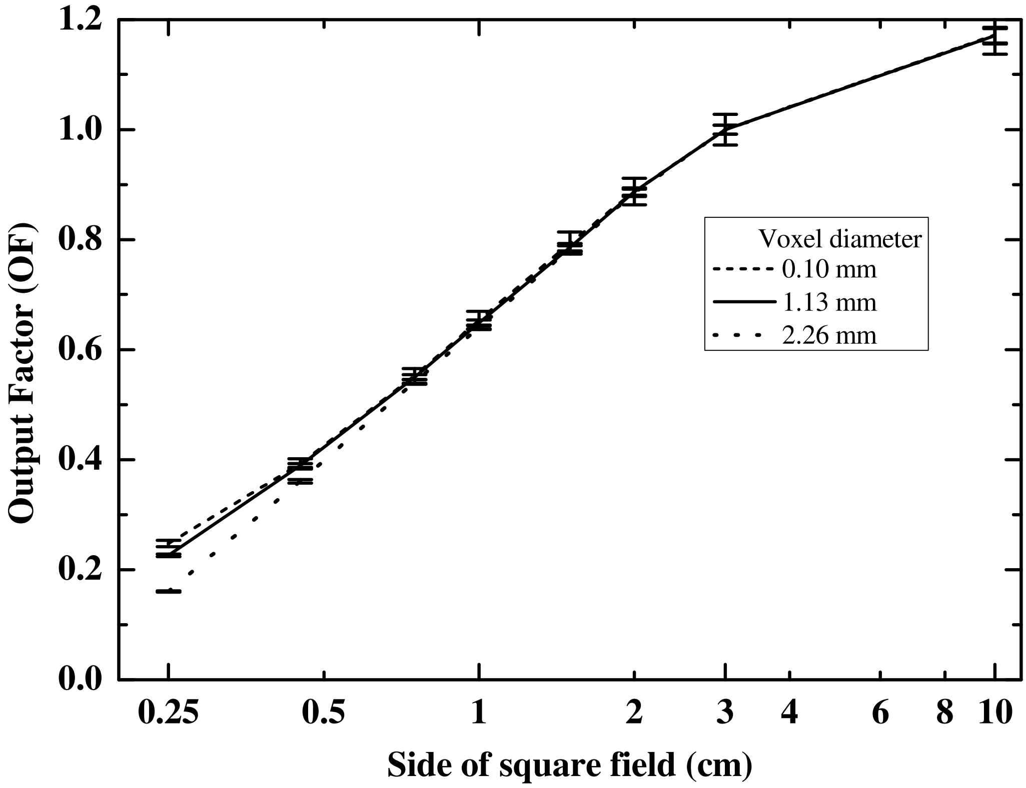

(b)

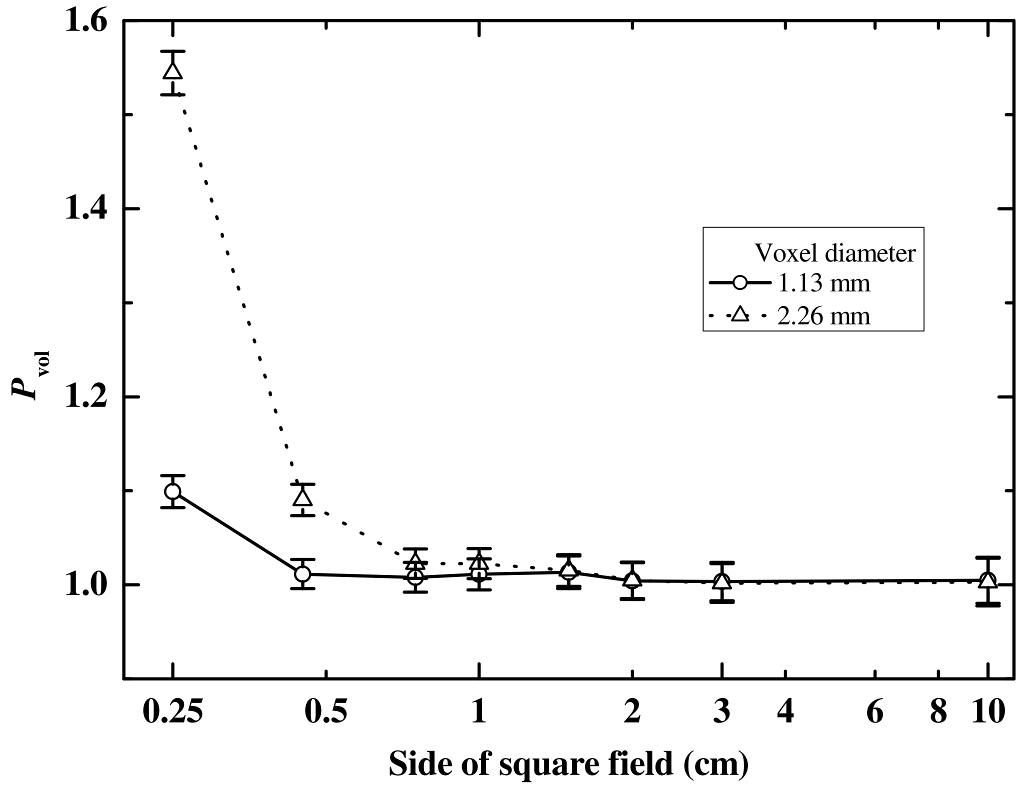

Figure 4.3: **(a) Output factors calculated for 0.26 mm thick water voxels of various diameters, positioned on-axis at 5 cm depth in a water phantom. (b) P_{vol} for the same range of field sizes, calculated as the ratio of average dose-to-water in a 0.1 mm diameter voxel to that in a wider voxel. The uncertainties shown are 2σ.**

(a)

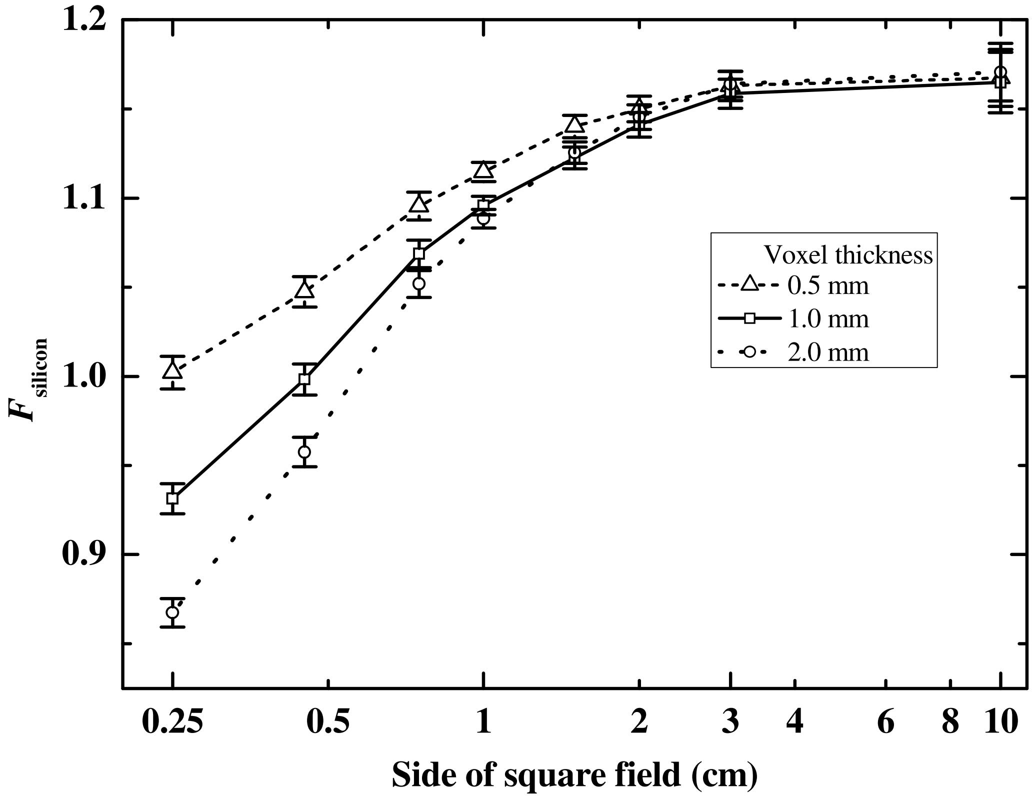

(b)

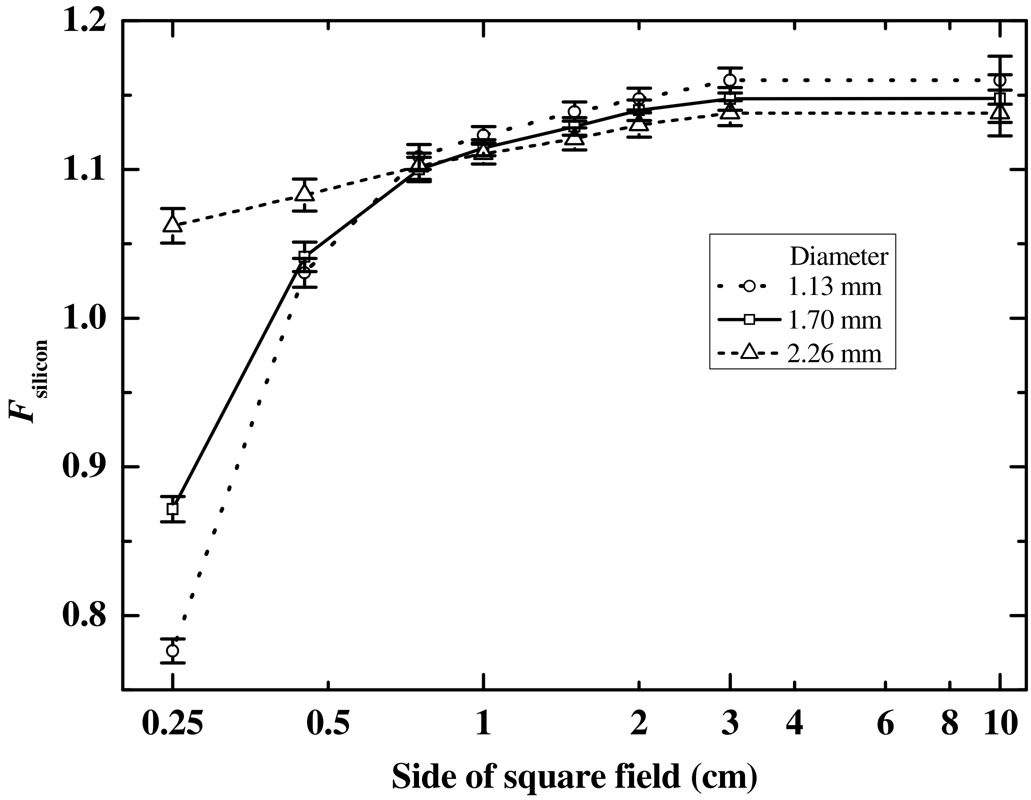

Figure 4.4: $F_{detector}$ **calculated (a) for silicon voxels of 2.26 mm diameter cross-section and various thicknesses and (b) for a stack of silicon voxels (0.06 + 0.44 mm deep) of various diameters. All voxels are located on-axis at 5 cm deep in a water phantom and 2σ uncertainties are indicated.**

In figure 4.4(a) it can be seen that the dose correction factor F_{silicon} decreases as the thickness of the detector increases. This might be expected since the volume of non-water density material is greater in thicker voxels thus increasing the degree of 'perturbation'. Conversely and unexpectedly, however, it can be seen in figure 4.4(b) that the required correction factor becomes closer to unity as voxel widths rise.

4.3.4 Varying the focal spot size

F_{detector} changes little with the width of the incident electron beam (figure 4.5) and therefore with the photon focal spot size. Although penumbra widths and profile shapes of very small fields are partly determined by the focal spot size, the resulting impact on F_{detector} is small compared to the impact of changing field size.

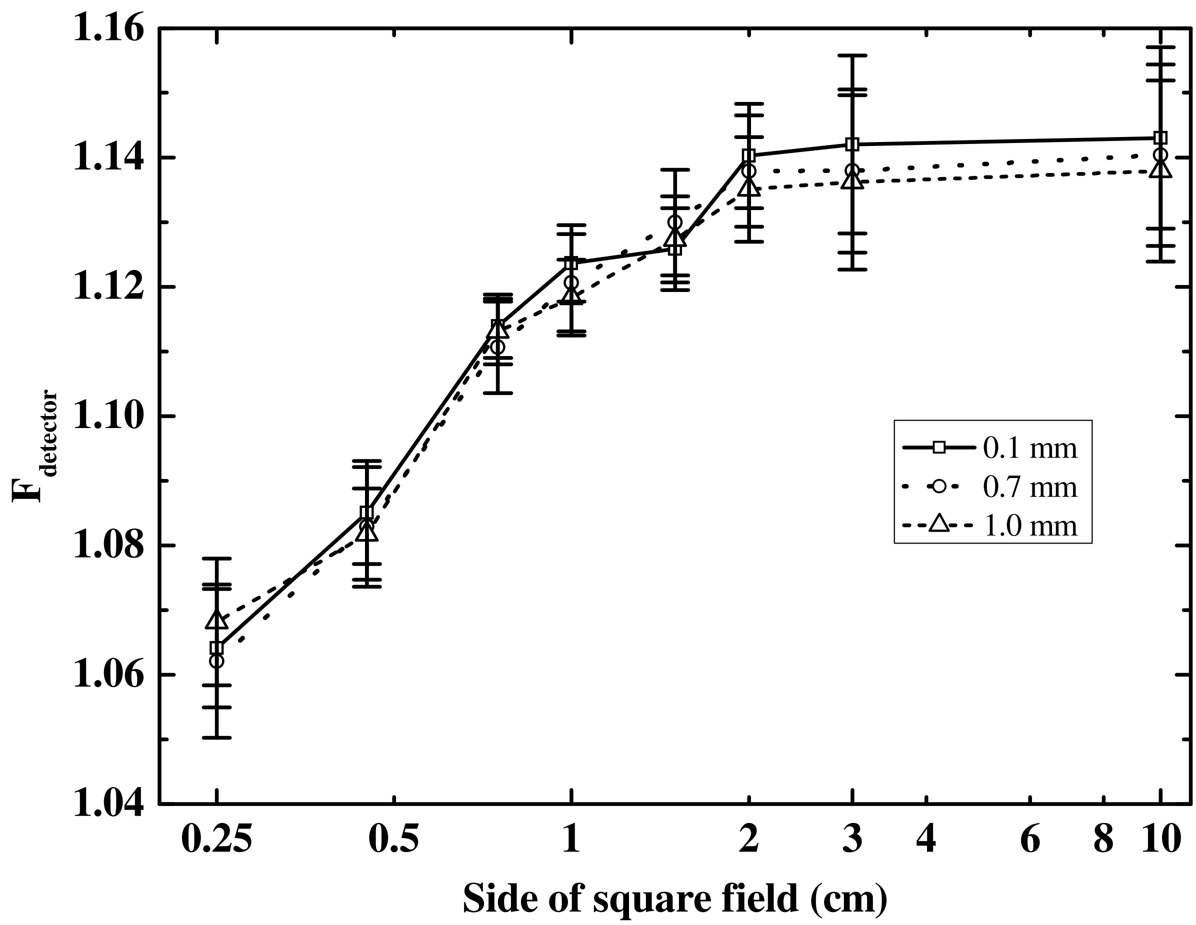

Figure 4.5: **Variation of F_{detector} with field size for different modelled widths of the electron beam incident on the x-ray target. F_{detector} values are plotted with 2σ uncertainties for a 2.26 mm diameter, 0.06 mm depth silicon voxel located on-axis, 5 cm deep in a water phantom (immediately above a 0.44 mm silicon dye).**

4.3.5 Variation of silicon diode response with depth

It can be seen in figure 4.6 that for a 0.5 × 0.5 cm^2 field F_{silicon}, the ratio of dose-to-water to dose-to-silicon-in-water, remains constant with depth from around 2 cm and deeper. The excellent agreement beyond the dose maximum is unsurprising, since for an SSD of 100 cm beam divergence causes the field width to increase by only 20% between measurement depths of 0 and 20 cm. Thus a beam 5 mm wide at isocentre will only have diverged to 6 mm wide at 20 cm depth in water, and from Figure 4.2 it can be seen that the variation in F_{detector} between field sizes of 5 and 6 mm is no more than 1%. It has been shown previously (Scott *et al* 2008) that for small fields the change in energy spectrum with depth minimally affects both the stopping-power and mass-energy-absorption ratios. Consequently it appears that silicon diodes can be used with some confidence to make small-field depth-dose measurements, except possibly in the build-up region.

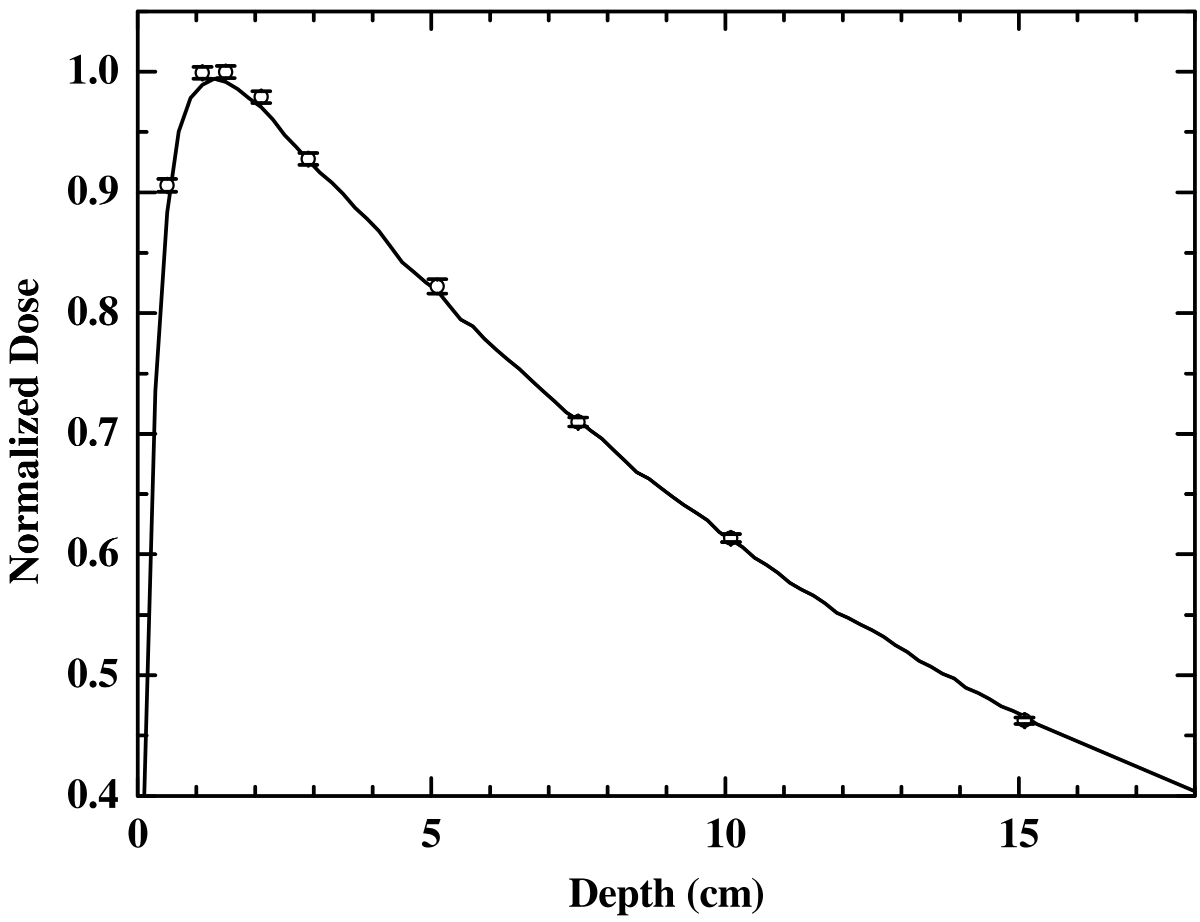

Figure 4.6: **Monte-Carlo calculated depth-dose curves obtained for a 0.5 × 0.5 cm^2 field. The full curve represents calculated doses delivered to water voxels, while the points represent doses calculated for isolated silicon voxels located in a water phantom. The points are normalized to the water values at 5 cm depth.**

4.4 Discussion and conclusions

Working with a previously validated model of a Varian linac 15 MV beam it has been shown that F_{detector}, the ratio of dose-to-water to dose-to-detector-in-water (calculated for finite equal-sized volumes of water and detector material co-located on central axis) varies significantly with field size for ion chambers, silicon diodes and diamond detectors. Relative to wide field readings, it has been found that at the smallest field sizes high-density detectors *over*-read, and low-density detectors *under*-read, to an extent that correlates with the mass density of the detector material relative to that of water. This apparent dependence on density rather than on atomic composition is confirmed by calculations of doses delivered to unit density water voxels and to voxels of water having densities equal to those of detector active volumes, since ratios of the calculated doses change with field size in much the same way as F_{detector}. Of course the average atomic number of the detecting material influences the value of F_{detector} at all field sizes; however this is unimportant for small-field relative detectors, which are used to measure doses in small fields relative to that at the centre of a larger reference field, where absolute dose has previously been determined using an absolute dosimeter.

The relative insensitivity of F_{diode} to variations in spot size means that it should be possible to calculate a set of dose-to-diode to dose-to-water correction factors that might be expected to be valid for a wide range of linac designs.

At first sight it seems appealing to apply the Monte-Carlo-calculated correction factors F_{detector} to convert detector-measured small-field doses into 'true' in-water values. A better approach would be to manufacture small-field relative detectors with active volumes whose densities are similar to water.

Conventional cavity theory has hitherto focussed on differences in the atomic compositions of materials, and thus their stopping-power and mass-attenuation ratios (Nahum 2009). Based on the findings in this chapter, a further work has been extended (chapter 5) to incorporate the effect of 'density' into a theory for F_{detector} – aiming to pin down the causes of the density dependence, determine when it is most likely to be problematic, evaluate ways of minimizing it, and potentially help identify useful reference conditions for calibration of small-field detectors (Alfonso *et al* 2008).

CHAPTER 5

Using cavity theory to describe the dependence on detector density of dosimeter response in non-equilibrium small fields

5.1 Introduction

Small radiation fields are used increasingly often in radiotherapy – a development that has increased the degree of uncertainty in clinical dosimetry because some key properties of these small fields differ from those of the larger fields used classically, on which reference dosimetry protocols are based (Alfonso *et al* 2008, Das *et al* 2008b). In particular, results from several computational studies show that when a detector is placed at a point in a wide radiation field receiving a particular dose-to-water (in the absence of the detector) and where electronic equilibrium holds laterally, its reading may differ from that of the same detector placed in a small field at a point receiving the same dose-to-water but where lateral electronic equilibrium is not established (Bouchard *et al* 2009, Crop *et al* 2009, Francescon *et al* 2011, Scott *et al* 2012). Differences between readings in really small (0.5×0.5 cm^2) fields and in 10×10 cm^2 reference fields can reach several tens of percent, even for small ion chambers, diodes and diamond detectors with sensitive volumes of 1-3 mm diameter (Sánchez-Doblado *et al* 2007).

Monte Carlo calculations show that this effect is largely the result of density differences between detector sensitive volumes and water, and of dose-averaging over detector sensitive volumes. Differences in atomic number generate a smaller effect, even for silicon diodes, because spectral variation between small fields is limited (Bouchard *et al* 2009, Crop *et al* 2009, Ding and Ding 2012, Scott *et al* 2008, 2012). While volume-averaging effects are well understood, the dependence of detector readings on density has been studied less. Here this density-dependence is characterized using two ratios

$$F_{\mathrm{w,det}}(\mathrm{FS}) = \overline{D}_{\mathrm{w}}(\mathrm{FS},\ 5,\ \mathrm{MU}) \big/ \overline{D}_{\mathrm{det}}(\mathrm{FS},\ 5,\ \mathrm{MU}) \tag{5.1}$$

$$P_{\rho\_}(\mathrm{FS}) = \overline{D}_{\mathrm{w}}(\mathrm{FS},\ 5,\ \mathrm{MU}) \big/ \overline{D}_{\mathrm{mdw\_}}(\mathrm{FS},\ 5,\ \rho,\ \mathrm{MU}) \tag{5.2}$$

where $\overline{D}_{\mathrm{w}}$ (FS, 5, MU) is the mean dose absorbed by a unit density water voxel of the same size as the detector sensitive volume, located on-axis at 5 cm depth in a water phantom set up at a source-surface-distance (SSD) of 100 cm and irradiated by a field of size FS delivering MU monitor units; $\overline{D}_{\mathrm{det}}$ is the mean dose absorbed by an equisized voxel of detector sensitive material located in the same place. $\overline{D}_{\mathrm{mdw\_}}$ is the mean dose absorbed by an equisized voxel of 'modified density water', whose density ρ is set to that of the sensitive volume but whose mass stopping power and mass energy-absorption coefficients still match those of unit density water – that is, eliminating changes in mass stopping power caused by the density-dependent polarization effect (Attix 1986, Nahum 2007a) as denoted by the minus suffixes of $\overline{D}_{\mathrm{mdw}\_}$ and $P_{\rho\_}$. Thus $P_{\rho\_}$ describes the impact of density alone on the dose absorbed by a small volume of modified density water, excluding the effects of changes in its mass radiological properties, whereas $F_{\mathrm{w,det}}(\mathrm{FS})$ describes the total impact of changes in the density and atomic composition of the volume.

In this chapter a cavity theory is developed describing $P_{\rho\_}$, aiming to explain the causes of the density-dependence and provide insights into which detector geometries are likely to be most problematic, how the effect might be minimized, and which fields might provide good reference conditions for the calibration of small field detectors (Alfonso *et al* 2008).

To keep the theory reasonably simple detectors are modelled as comprising a single volume (voxel) of sensitive material, surrounded by unit density water. For ion chambers this is often a good approximation: alongside an air cavity these detectors include a central electrode, outer wall and stem, which modify the cavity dose by additional factors P_{cel}, P_{wall} and P_{stem} – but Monte-Carlo simulations of Exradin A12 and A14 detectors show that these extra factors are close to one and differ little between regular 10×10 cm^2 fields and IMRT fields constructed from small field segments (Bouchard *et al* 2009).

Diamond detectors typically comprise an active diamond volume (density 3.5 g cm^{-3}) surrounded by material of density close to one, and so they are also described fairly well by the single voxel cavity model. In diode detectors, on the other hand, a thin active layer of silicon (density 2.3 g cm^{-3}) immediately overlies a thicker inactive silicon layer; and so in this work the single voxel model is used to explore the density-dependence of ionization chambers and diamond detectors but not diodes.

In this analysis Fano's theorem is used to study the case of a unit density water phantom containing a 'water' cavity of modified density ρ. The dose absorbed by the cavity from a wide field is partitioned into two components – firstly that imparted by electrons liberated in photon interactions occurring within the cavity (equal to a particular fraction, J_{cav}, of the total dose absorbed), and secondly that imparted by electrons generated outside it. It is shown that J_{cav} depends on the cavity density, as does the ratio of the two dose components. In smaller fields the ratio also depends on the degree of lateral electronic equilibrium in the vicinity of the cavity, leading to an equation that links $P_{\rho\_}$ to the degree of lateral electronic equilibrium in the smaller fields. This link is compared to data created computationally using a Monte-Carlo model of a 15 MV photon beam, which is studied here because the degree of electronic disequilibrium in small fields is greater at this than at lower energies.

Classical theories of photon dosimetry describe the response of small Bragg-Gray cavities in which all the electron fluence originates outside the cavity volume (J_{cav}= 0), and of large cavities in which the electron fluence is generated entirely internally (J_{cav}=1). Doses absorbed by these small and large cavities are independent of cavity density, However doses absorbed by intermediate-sized cavities (0<J_{cav}<1) located in non-equilibrium fields do depend on cavity density. These 'general' cavities were first studied by Burlin (1966) who characterized them through a parameter (1-*d*), which is loosely analogous to J_{cav} and represents the average electron fluence generated by photon interactions occurring within the cavity, relative to the equilibrium electron fluence generated in an infinitely large volume of cavity material. Burlin's work and that of later investigators (Haider *et al* 1997, Fu and Luo 2002 for example) addressed the dependence of doses absorbed from wide fields on the atomic composition of general cavities and surrounding material. However these workers did not study the response of detectors in the severely non-equilibrium fields that are the subject of this chapter.

The quantities $F_{\mathrm{w,det}}$ and P_{ρ_-} can be linked to other descriptions of small field dosimetry: written in terms of a formalism developed by Bouchard *et al* (2009) from conventional ion chamber dosimetry protocols

$$F_{\mathrm{w,det}} = P_{\rho_+} \times P_{\mathrm{fl}_+} \times s^{\mathrm{SA}}_{\mathrm{mdw}_+,\mathrm{det},\Delta} = P_{\rho_-} \times P_{\mathrm{fl}\_} \times s^{\mathrm{SA}}_{\mathrm{mdw}\_,\mathrm{det},\Delta} = P_{\rho_-} \times P_{\mathrm{fl}\_} \times s^{\mathrm{SA}}_{\mathrm{w,det},\Delta} \tag{5.3}$$

while following the similar formalism of Crop *et al* (2009)

$$F_{\mathrm{w,det}} = p_{\mathrm{det-w}} \times s^{\mathrm{SA}}_{\mathrm{w,det},\Delta} \ ; \ P_{\rho_\pm} = p_{\mathrm{mdw}_\pm\text{ - w}} \tag{5.4}$$

where $s^{\mathrm{SA}}_{\mathrm{mdw}_\pm\text{ , det},\Delta}$ describes the mean modified density water-to-detector mass restricted stopping power ratio for the electron fluence within the sensitive volume of the detector, and $P_{\mathrm{fl}_\pm}$ accounts for any difference between this fluence and that in modified density water; both factors including (+) or excluding (-) the impact of changes in the mass stopping power of water with density. In Bouchard's original formalism the symbols P_ρ and P_{fl} were used to denote P_{ρ_+} and P_{fl_+} , but P_{ρ_-} and $P_{\mathrm{fl}\_}$ are useful variants allowing the effect of density to be studied in isolation from changes in mass radiological properties. The factors $p_{\mathrm{det\text{ - }w}}$ and $p_{\mathrm{mdw}_\pm\text{ - w}}$ are extensions of Crop's $p_{\mathrm{a\text{-}w}}$ factor to situations where air is replaced by detector material and modified density water (± the associated change in mass stopping power from unit density water) respectively (figure 5.1). $p_{\mathrm{det\text{ - }w}}$ equates to $P_{\rho_-} \times P_{\mathrm{fl}\_}$ and accounts for changes in electron fluence due to both the non-water equivalent atomic composition and non-unit density of detector sensitive volumes.

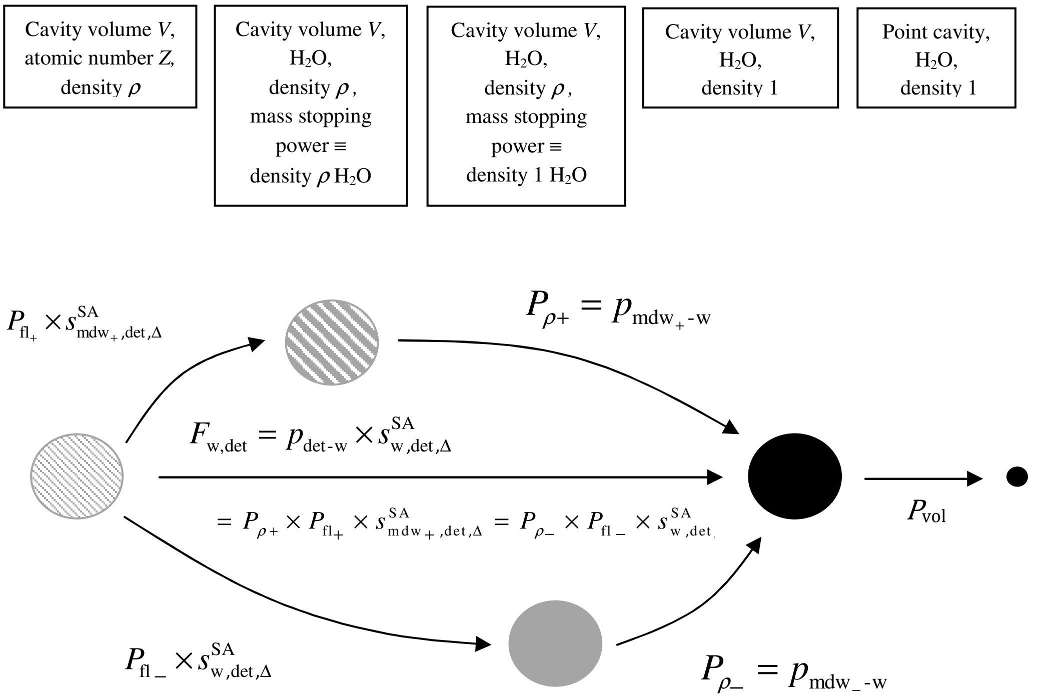

Figure 5.1: **$F_{\mathrm{w,det}}$ and $P_{\rho\_}$ factors illustrated alongside similar factors used in the formalisms of Bouchard *et al* and Crop *et al*. The expression next to each arrow is the term required to correct the average dose in the cavity on the left of the arrow to that in the cavity on the right.**

Alfonso *et al* (2008) have defined a factor

$$k_{Q_{\mathrm{FS}},Q_{\mathrm{FSref}}}^{f_{\mathrm{FS}},f_{\mathrm{FSref}}} = \frac{D_{\mathrm{w},Q_{\mathrm{FS}}}^{f_{\mathrm{FS}}} \Big/ M_{Q_{\mathrm{FS}}}^{f_{\mathrm{FS}}}}{D_{\mathrm{w},Q_{\mathrm{FSref}}}^{f_{\mathrm{FSref}}} \Big/ M_{Q_{\mathrm{FSref}}}^{f_{\mathrm{FSref}}}} \qquad (5.5)$$

in which f_{FSref} and f_{FS} denote the reference field and a nonstandard field of size FS respectively, Q_{FSref} and Q_{FS} describe the radiation qualities of these fields, and $M_{Q_{\mathrm{FS}}}^{f_{\mathrm{FS}}}$ is the meter reading of an on-axis dosimeter at whose point of measurement a dose to water $D_{\mathrm{w},Q_{\mathrm{FS}}}^{f_{\mathrm{FS}}}$ is delivered by a field of size FS in the absence of the dosimeter. Assuming that the meter reading is proportional to the mean dose $\overline{D}_{\mathrm{det}}$ absorbed throughout the detector's sensitive volume (Francescon *et al* 2011) then

$$k_{Q_{\mathrm{FS}},Q_{\mathrm{FSref}}}^{f_{\mathrm{FS}},f_{\mathrm{FSref}}} = \frac{D_{\mathrm{w},Q_{\mathrm{FS}}}^{f_{\mathrm{FS}}} \Big/ \overline{D}_{\mathrm{det},Q_{\mathrm{FS}}}^{f_{\mathrm{FS}}}}{D_{\mathrm{w},Q_{\mathrm{FSref}}}^{f_{\mathrm{FSref}}} \Big/ \overline{D}_{\mathrm{det},Q_{\mathrm{FSref}}}^{f_{\mathrm{FSref}}}}$$

$$= \frac{\left(\overline{D}_{\mathrm{w},Q_{\mathrm{FS}}}^{f_{\mathrm{FS}}} \Big/ \overline{D}_{\mathrm{det},Q_{\mathrm{FS}}}^{f_{\mathrm{FS}}}\right)\left(D_{\mathrm{w},Q_{\mathrm{FS}}}^{f_{\mathrm{FS}}} \Big/ \overline{D}_{\mathrm{w},Q_{\mathrm{FS}}}^{f_{\mathrm{FS}}}\right)}{\left(\overline{D}_{\mathrm{w},Q_{\mathrm{FSref}}}^{f_{\mathrm{FSref}}} \Big/ \overline{D}_{\mathrm{det},Q_{\mathrm{FSref}}}^{f_{\mathrm{FSref}}}\right)\left(D_{\mathrm{w},Q_{\mathrm{FSref}}}^{f_{\mathrm{FSref}}} \Big/ \overline{D}_{\mathrm{w},Q_{\mathrm{FSref}}}^{f_{\mathrm{FSref}}}\right)} = \frac{F_{\mathrm{w,det}}(\mathrm{FS})\,P_{\mathrm{vol}}(\mathrm{FS})}{F_{\mathrm{w,det}}(\mathrm{FS}_{\mathrm{ref}})\,P_{\mathrm{vol}}(\mathrm{FS}_{\mathrm{ref}})} \qquad (5.6)$$

where $F_{\mathrm{w,det}}$ converts the average dose delivered to the detector sensitive volume (Looe *et al* 2013) into the average dose delivered to a co-located volume of water, and P_{vol} (FS) corrects the volume-averaged water dose into the dose at the measurement point.

5.2 Materials and methods

5.2.1 Monte-Carlo modelling of the linear accelerator and detectors

Monte-Carlo techniques has previously been used to study small field measurements of a photon beam of nominal energy 15 MV (Scott *et al* 2008, 2009, 2012) generated by a Varian 2100C linear accelerator (Varian Medical Systems, Palo Alto, CA). A Monte-Carlo model of the accelerator was constructed in the BEAMnrc system (Rogers *et al* 1995), setting physical machine dimensions to values provided by Varian Medical Systems and achieving a good match between calculated and measured dose-distributions through careful selection of user-defined model parameters – an incident electron beam of 14.8 MeV energy, zero energy spread, and a focal spot of 0.7 mm full-width-half-maximum (FWHM).

Table 5.1: **Modelled detector active volumes for which $F_{\mathrm{w,det}}$ and $P_{\rho\_}$ curves have been generated. The physical active volume of the diamond detector is a thin cuboidal wafer, while the physical 31016 PinPoint 3D ionization chamber is a cylinder with a domed end. The modelled volumes are both cylindrical with 4 mm^2 cross-section.**

Detector active volume	Composition	Density (g cm^{-3})	Physical diameter or width (cm)	Modelled diameter (cm)	Physical maximum thickness (cm)	Modelled thickness (cm)
PTW diamond	carbon	3.5	0.30	0.23	0.026	0.026
PTW PinPoint ion chamber	air	0.0012	0.29	0.23	0.290	0.200

As part of the beam-matching process, measurements were compared with doses calculated for water voxels and for voxels whose sizes, densities and atomic compositions were set to the sensitive volumes of the detectors used. The same general approach was taken when calculating $F_{\mathrm{w,det}}$ and $P_{\rho\_}$ values (Scott *et al* 2012); but as this process involved no measurements, being purely a comparison of doses computed for voxels of differing composition, it was possible to simplify the simulated detector geometries for which it was carried out. In this chapter it is focused on calculations made for two geometries loosely corresponding to a ‘PinPoint 3D’ ionization chamber (Model 31016, PTW, Freiburg, Germany), a diamond detector (Model 60003, PTW, Freiburg, Germany). Each detector is represented as a single voxel of sensitive material surrounded by unit density water, and the cross-sections of both sensitive volumes are characterized approximately as circles of 4 mm^2 area;

however the 0.26 mm thickness of the slim cuboidal active volume of diamond is matched exactly whereas the domed active volume of the 'PinPoint 3D' ionization chamber (maximum height 2.9 mm) is represented as a disc of uniform thickness 2 mm (table 5.1). Doses have been computed for these cylindrical geometries using the CAVRZnrc Monte- Carlo user-code (Rogers *et al* 2011b) with ECUT set to 512 keV and PCUT to 1 keV, and $F_{\mathrm{w,det}}$ and $P_{\rho\_}$ values have been calculated from these doses via equations (5.1) and (5.2).

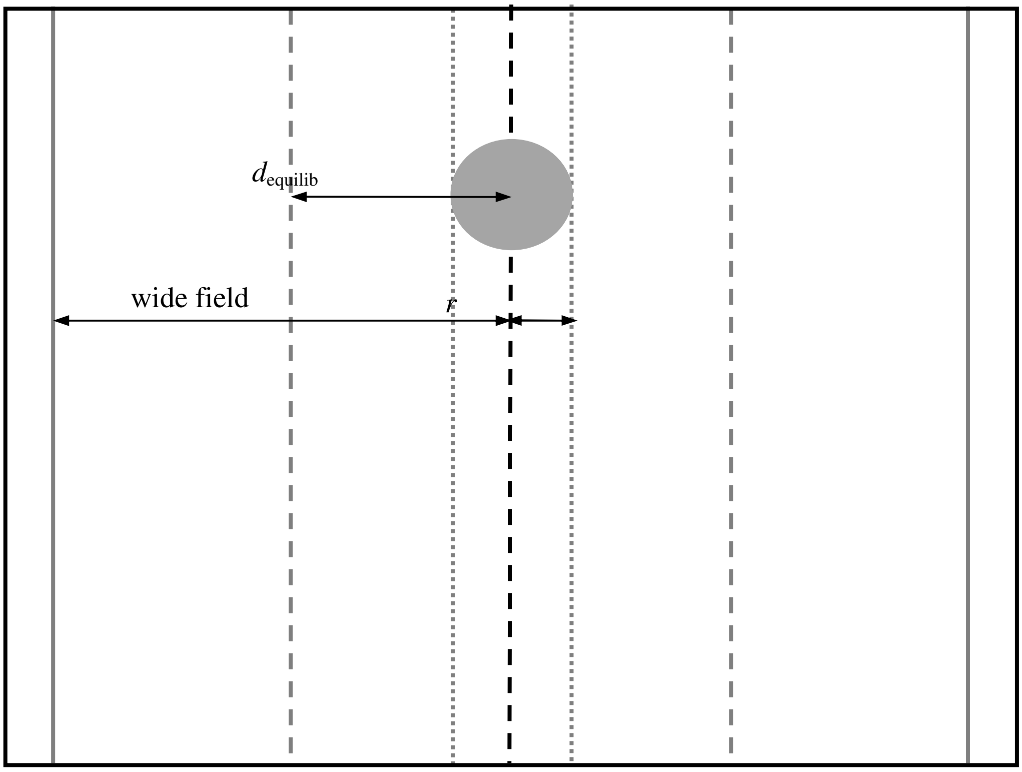

Figure 5.2: **A spherical cavity (grey) of volume *V* and radius *r* contains water of modified density ρ and lies within a large unit density water phantom on the central axis (dark dotted line) of a non-divergent radiation beam. The edges of a wide field and fields of width 2d_{equilib} and 2*r* are shown as grey lines. Lateral electronic equilibrium is just established in the vicinity of the cavity by the 2d_{equilib}wide field, the ranges of electrons at d_{equilib} not quite extending to the cavity.**

5.2.2 Fano's theorem and the dose delivered to a water cavity of modified density ρ

Consider the geometry of figure 5.2 – a small spherical water cavity of density ρ and volume *V* lying within a unit density water phantom irradiated by an idealized wide, uniform, field of primary photon radiation that is non-divergent and attenuation-free. Within the phantom the field generates a photon energy fluence differential in energy $\Psi_{\mathrm{E}}^{\mathrm{p}}(\tilde{x})$ and an electron particle fluence differential in energy $\Phi_{\mathrm{E}}^{\mathrm{e}}(\tilde{x})$, where *E* denotes particle energy and $\tilde{x}$ spatial location, and $\Psi_{\mathrm{E}}^{\mathrm{p}}(\tilde{x})$ accounts for primary, scatter and Bremsstrahlung photons while $\Phi_{\mathrm{E}}^{\mathrm{e}}\left(\tilde{x}\right)$ describes the electrons *directly* energized by interactions of these photons (i.e. it does not include knock-on electrons or delta rays). In the absence of the cavity the photon and electron fluences are uniform throughout the irradiated phantom, delivering a constant dose-level *D*.

Fixing the polarization effect at its unit density water level (and thus eliminating differences between the mass stopping powers of water of different densities) then according to Fano's theorem (Attix 1986)

> 'In an infinite medium of given atomic composition exposed to a uniform field of indirectly ionizing radiation, the field of secondary radiation is also uniform and independent of the density of the medium, as well as of density variations from point to point,'

and so $\Psi_{\mathrm{E}}^{\mathrm{p}}$ and $\Phi_{\mathrm{E}}^{\mathrm{e}}$ remain uniform throughout the irradiated phantom, even when it contains a modified density water cavity, provided it is irradiated by a uniform primary photon field. Consequently the dose-level *D* also remains uniform, being linked to the photon spectrum through

$$D = K_{\mathrm{col}} = \int \Psi_{\mathrm{E}}^{\mathrm{p}} \left(\frac{\mu_{\mathrm{en}}\left(E\right)}{\rho}\right)_{\mathrm{w}} \mathrm{d}E \; = \; \Psi^{\mathrm{P}} \left(\frac{\mu_{\mathrm{en}}}{\rho}\right)_{\mathrm{w}} \tag{5.7}$$

and to the electron spectrum via

$$D = \phi_{\mathrm{E}}^{\mathrm{e}} \left(\frac{S_{\mathrm{el}}\left(E\right)}{\rho}\right)_{\mathrm{w}} \mathrm{d}E = \Phi^{\mathrm{e}} \left(\frac{\overline{S}_{\mathrm{el}}}{\rho}\right)_{\mathrm{w}} \tag{5.8}$$

where K_{col} is the collision kerma in water, $\left(\mu_{\mathrm{en}}\left(E\right)/\rho\right)_{\mathrm{w}}$ and $\left(S_{\mathrm{el}}\left(E\right)/\rho\right)_{\mathrm{w}}$ are the energy-dependent mass energy-absorption coefficient and mass electronic stopping power of unit density water, $\left(\overline{\mu}_{\mathrm{en}}/\rho\right)_{\mathrm{w}}$ and $\left(\overline{S}_{\mathrm{el}}/\rho\right)_{\mathrm{w}}$ are spectral averages of these quantities, Ψ^{p} is the total photon fluence and Φ^{e} the fluence of electrons directly energized by the photons (Attix 1986, Nahum 2007b, ICRU 2011).

Now consider that a volume-averaged component ($J_{\mathrm{cav}}(\rho)$ *D* say) of the dose *D* absorbed by the cavity originates from electrons liberated in photon interactions occurring within it, $J_{\mathrm{cav}}(\rho)$ potentially depending on the cavity density. Correspondingly, the average dose component originating from photon interactions occurring outside the cavity must be

$$\overline{D}_{\mathrm{external}} = D\left(1 - J_{\mathrm{cav}}(\rho)\right) \tag{5.9}$$

J_{cav} can be calculated approximately using the Monte-Carlo approach of Ma and Nahum (1991). This begins by computing the photon spectrum in the cavity when it is located within the water phantom;

then the cavity is computationally relocated in vacuum and re-irradiated with this photon spectrum, now assuming that all the photons are travelling in the forwards (unscattered) direction. Finally J_{cav} is estimated as the ratio of absorbed dose to collision kerma within the vacuum-located cavity, a step whose rationale is set out in figure 5.3. Collision kerma K_{col} is calculated as $\left(1-\overline{g}\right)K$, where kerma K is scored as the dose in the cavity with *ECUT* set high to 30 MeV, precluding electron transport, and where the factor $\left(1-\overline{g}\right)$ is taken as 0.985 for a 15 MV beam with a mean energy of 4.1 MeV (Mohan *et al* 1985, Attix 1986). The assumption that all incident photons are forwards directed introduces some inaccuracy into the calculations, as some photons are scattered in the water phantom. However this approximation might not be expected to substantially bias the J_{cav} estimates obtained, as noted by Ma and Nahum, at least for cavities of similar breadth and depth.

(a)

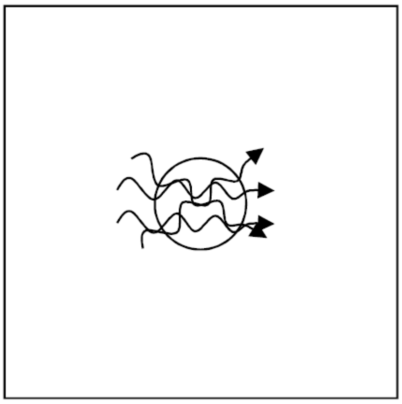

(b)

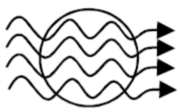

Figure 5.3: **A Monte-Carlo method for estimating J_{cav}. (a) The photon fluence within a large uniformly irradiated phantom is constant, including the fluence within a cavity of modified density water. Electronic equilibrium also holds throughout the phantom, the absorbed dose D equalling the collision kerma K_{col}. (b) If the cavity is relocated in vacuum and irradiated using the same photon fluence (now all forward directed) the same collision kerma is generated within it, still equal to the uniform dose D absorbed in the phantom. However, the dose absorbed by the cavity in vacuum is $J_{\mathrm{cav}}D$, since it is generated only by electrons energized by photon interaction within the cavity. Consequently the ratio of cavity dose to collision kerma is J_{cav}.**

Using this technique J_{cav} values have been calculated for a cylindrical cavity of 4 mm^2 cross-section and 2 mm length (the dimensions used to loosely represent a 'PinPoint 3D' ionization chamber) placed 5 cm deep in a water phantom set up at an SSD of 100 cm and irradiated using a 15 MV 40 × 40 cm^2 field, the cavity's axis being aligned with the central axis of the field. The cavity is filled with modified density water, and J_{cav} computed for densities between 0.0012 g cm^{-3} (air) and 20 g cm^{-3}. Calculated $J_{cav}(\rho)$ values are plotted in figure 5.4 and initially rise roughly linearly with density, in and above the Bragg-Gray region, $J_{cav} \ll 1$, where the cavity absorbs dose almost exclusively from electrons crossing it (Attix 1986). At higher densities J_{cav} approaches a plateau value of 1, the 'photon' detector region where the cavity dose is derived almost exclusively from photon interactions occurring within it (Attix 1986).

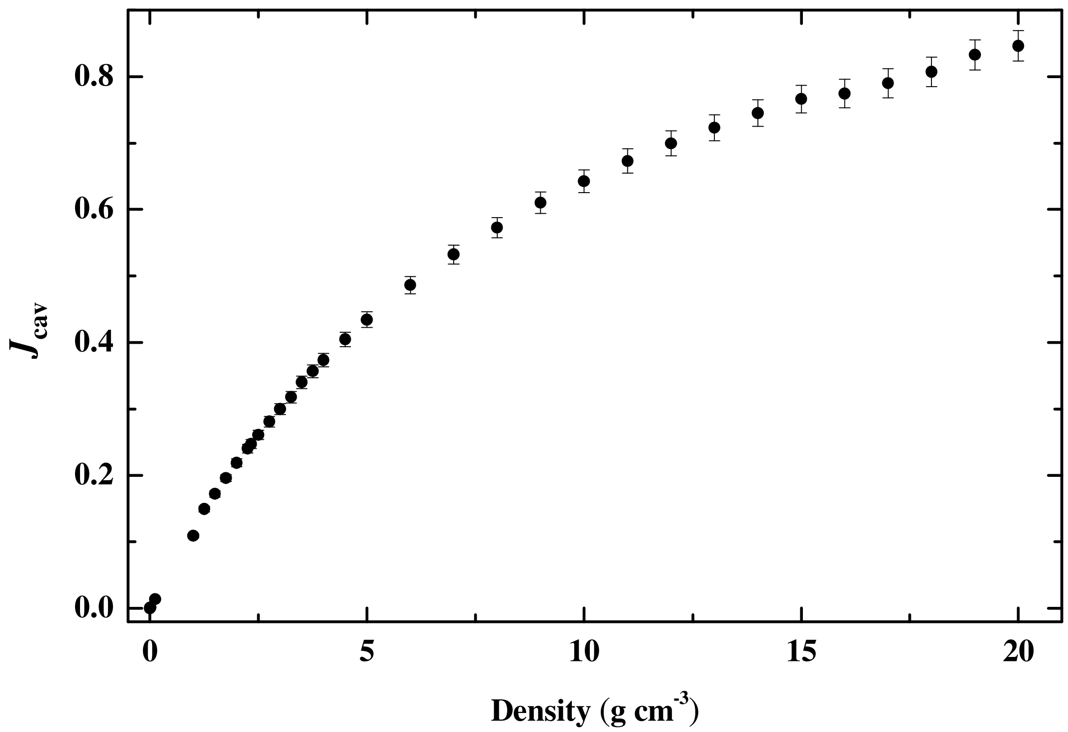

Figure 5.4: **J_{cav} values calculated for a cylindrical cavity of cross-sectional area 4 mm^2 and length 2 mm, located at 5 cm depth in a water phantom set up at an SSD of 100 cm. The axis of the cylindrical cavity is aligned with the central axis of a 15 MV 40 × 40 cm^2 photon field with which the phantom is irradiated. Error bars show ± 2 standard deviation uncertainties on calculated J_{cav} values.**

The initial linear dependence on density can be explained by noting that the total energy transferred to electrons by photon interactions occurring in a cavity of modified density water is the product of the cavity's mass and the average kerma K within it

$$E_{\text{transfer}} = K\rho V = K_{\text{col}}\rho V \Big/ \left(1-\bar{g}\right) = D\rho V \Big/ \left(1-\bar{g}\right) \tag{5.10}$$

Then if most of these electrons escape from the cavity, the fraction of their kinetic energy that it absorbs is

$$F_{\text{abs}} = \left(\frac{\bar{l}(\rho)\bar{L}_{\Delta(\rho)\text{int w}}}{\bar{\bar{T}}_{\text{ep}}} \right) = \rho \left(\frac{\bar{L}_{\Delta(\rho)\text{int w}}}{\rho} \right)_{\text{w}} \left(\frac{\bar{l}(\rho)}{\bar{\bar{T}}_{\text{ep}}} \right) \tag{5.11}$$

where $\bar{l}(\rho)$ is the average path-length traversed by the electrons between their generation and exit from the cavity, $\left(\bar{L}_{\Delta(\rho)\text{int w}}/\rho\right)_{\text{w}}$ is the mean mass restricted electronic stopping power of the internally generated electrons as they cross the cavity (Attix 1986, ICRU 2011), and $\bar{T}_{\text{ep}}$ is their mean initial energy. Consequently the mean dose delivered to the cavity medium by these electrons is

$$\bar{D}_{\text{internal}} = E_{\text{transfer}} F_{\text{abs}} / (\rho V) = D\left(\frac{\rho}{1-\bar{g}}\right)\left(\frac{\bar{l}(\rho)}{\bar{T}_{\text{ep}}}\right)\left(\frac{\bar{L}_{\Delta(\rho)\text{int w}}}{\rho}\right)_{\text{w}} \tag{5.12}$$

and

$$J_{\text{cav}}(\rho) = \frac{\bar{D}_{\text{internal}}}{D} = \rho\left(\frac{1}{1-\bar{g}}\right)\left(\frac{\bar{l}(\rho)}{\bar{T}_{\text{ep}}}\right)\left(\frac{\bar{L}_{\Delta(\rho)\text{int w}}}{\rho}\right) \tag{5.13}$$

The leading ρ term of equation (5.13) accounts for the largely linear form of the initial part of the $J_{\text{cav}}(\rho)$ curve. Even in this region, though, the shape of $J_{\text{cav}}(\rho)$ is also influenced by the mean path-length out of the cavity, $\bar{l}(\rho)$, since electron tracks become more tortuous in denser media; and it is potentially modified further by the threshold energy for electrons to escape the cavity, $\Delta(\rho)$, specified in the restricted stopping power. At higher densities increasing numbers of electrons liberated in internal photon interactions stop within the cavity, and so equations (5.11) and (5.13) are no longer accurate.

5.2.3 Validity of the 'internal' and 'external' split of cavity dose

Two assumptions were made to split the water cavity dose into the 'internal' and 'external' components of equations (5.9) and (5.12). Firstly, the primary photon fluence of a wide 15 MV field was assumed to be uniform throughout the water phantom, which in principle is unphysical since it requires the field to be non-divergent and attenuation-free.

In practice, however, the photon fluence need only be uniform within a distance from the cavity equal to the range of electrons generated by the photon interactions, the fluence further away having far less impact on the cavity dose. The primary photons of a 15 MV beam have a mean energy of 4.1 MeV (Mohan *et al* 1985), and electrons generated by Compton interactions of these photons have a typical initial energy of about 2MeV and a typical *continuous slowing down approximation* (CSDA) range of 1 cm in water (Attix 1986, Berger *et al* 2005), which is consistent with observed build-ups of 80 and 90% of maximum dose at 1 cm depth in water for 15 MV fields of area 4 × 4 and 40 × 40 cm^2 respectively (Scott *et al* 2008). Over this 1 cm distance the photon fluence is indeed reasonably uniform, the depth-dose curve of a 15 MV 40 × 40 cm^2 field varies by only 3% relative (Scott *et al* 2008).

The second assumption was that electrons liberated within the cavity mostly escape from it. For the 'PinPoint 3D' ionization chamber cavity this assumption is good, since the CSDA range of a typical 2 MeV electron directly energized by the 15 MV beam is around 10 m in air (Berger *et al* 2005).Likewise the electrons should escape easily enough from the higher density diamond detector cavity as the CSDA range of 2 MeV electrons in diamond is 3.2 mm, their direction of travel is largely in the direction of the photons that energize them (Attix 1986), and the diamond cavity is just 0.26 mm thick along the beam axis.

However this second assumption was only made in order to explain the initially linear form of $J_{\mathrm{cav}}(\rho)$, and the link between $J_{\mathrm{cav}}(\rho)$ and the density-dependence of detector measurements that will be obtained in *Methods 5.2.4* does not depend on it. Provided *some* internally-generated electrons escape from the cavity its J_{cav} value will still vary with density, driving the density-dependence of detector measurements in lateral disequilibrium situations.

5.2.4 A link between P_{ρ_-} and the degree of lateral electronic equilibrium, s_{ee}

Consider the dose absorbed by a unit density water cavity from a field of size FS, when the average collision kerma throughout the cavity is fixed at K_{col} irrespective of field-size by setting a number of monitor units

$$\mathrm{MU(FS)} = \frac{\mathrm{MU_{ref}}}{\mathrm{OF(FS)} / s_{\mathrm{ee}}(\mathrm{FS})} \tag{5.14}$$

where $\mathrm{MU_{ref}}$ monitor units are required to generate the reference dose-level D at the centre of a wide reference field of size $\mathrm{FS_{ref}}$, and the output factor OF(FS) is the ratio of central axis doses $\overline{D}_{\mathrm{w}}(\mathrm{FS, 5, MU}) / \overline{D}_{\mathrm{w}}(\mathrm{FS_{ref}, 5, MU})$ at 5cm depth in fields of size FS and $\mathrm{FS_{ref}}$ delivering MU monitor units. The degree of lateral electronic equilibrium, s_{ee}(FS) is defined, as

$$s_{\mathrm{ee}}(\mathrm{FS}) = \frac{\overline{D}_{\mathrm{w}}(\mathrm{FS, 5, MU}) / \overline{K}_{\mathrm{w\,col}}(\mathrm{FS, 5, MU})}{\overline{D}_{\mathrm{w}}(\mathrm{FS_{ref}, 5, MU}) / \overline{K}_{\mathrm{w\,col}}(\mathrm{FS_{ref}, 5, MU})} = \frac{\overline{D}_{\mathrm{w}}(\mathrm{FS, 5, MU}) / \overline{K}_{\mathrm{w}}(\mathrm{FS, 5, MU})}{\overline{D}_{\mathrm{w}}(\mathrm{FS_{ref}, 5, MU}) / \overline{K}_{\mathrm{w}}(\mathrm{FS_{ref}, 5, MU})}$$

$$= \frac{\mathrm{OF(FS)}}{\overline{K}_{\mathrm{w}}(\mathrm{FS, 5, MU}) / \overline{K}_{\mathrm{w}}(\mathrm{FS_{ref}, 5, MU})} \tag{5.15}$$

where $\overline{K}_{\mathrm{w}}$ and $\overline{K}_{\mathrm{w\,col}}$ denote on-axis kerma and collision kerma in water, and the normalization by the reference field dose-to-kerma ratio roughly divides out the small degree of longitudinal electronic disequilibrium that exists in all fields, leaving a measure of lateral equilibrium. Dose and kerma values are averaged over the volume of the water cavity in the definition of OF and s_{ee}.

Then for these conditions, the ratio of central axis doses in fields of size *FS* and FS_{ref} works out as

$$\frac{\overline{D}_{\text{w}}\left(\text{FS, 5, }\left\{\text{MU}_{\text{ref}}/\left(\text{OF}(\text{FS})/s_{ee}(\text{FS})\right)\right\}\right)}{\overline{D}_{\text{w}}\left(\text{FS}_{\text{ref}}\text{, 5, MU}_{\text{ref}}\right)} = \frac{\text{OF}(\text{FS})}{\text{OF}(\text{FS})/s_{ee}(\text{FS})} = s_{ee}(\text{FS}) \tag{5.16}$$

And since the average kerma within the unit density water cavity is held constant when the monitor units are set according to equation (5.14), the average dose absorbed by the cavity that originates from photon interactions occurring within it, $\overline{D}_{\text{internal}}$, is also fixed at a field-size independent value of $DJ_{\text{cav}}(1)$. On the other hand, in small fields electronic equilibrium breaks down on axis and $\overline{D}_{\text{internal}}$ will fall below its wide field plateau level of $D\left(1-J_{\text{cav}}(1)\right)$. Consequently under these conditions the total dose absorbed by the unit density water cavity from a field of size FS is

$$\begin{aligned}\overline{D}_{\text{w}}\left(\text{FS, 5, }\frac{\text{MU}_{\text{ref}}}{\text{OF}(\text{FS})/s_{ee}(\text{FS})}\right) &= \overline{D}_{\text{internal}}\left(\text{FS, 5, }\frac{\text{MU}_{\text{ref}}}{\text{OF}(\text{FS})/s_{ee}(\text{FS})}\right)\\ &\quad+\overline{D}_{\text{external}}\left(\text{FS, 5, }\frac{\text{MU}_{\text{ref}}}{OF(\text{FS})/s_{ee}(\text{FS})}\right)\\ &= DJ_{\text{cav}}(1)+D\left(1-J_{\text{cav}}(1)\right)\varepsilon(\text{FS})\end{aligned} \tag{5.17}$$

where ε(FS) is a function that decreases from one as the field-size falls. From equations (5.16) and (5.17) it follows that

$$\begin{aligned}s_{ee}(\text{FS}) &= \frac{\overline{D}_{\text{w}}\left(\text{FS, 5, }\left\{\text{MU}_{\text{ref}}/\left(OF/s_{ee}(\text{FS})\right)\right\}\right)}{\overline{D}_{\text{w}}\left(\text{FS}_{\text{ref}}\text{, 5, MU}\right)} = \frac{DJ_{\text{cav}}(1)+D\left(1-J_{\text{cav}}(1)\right)\varepsilon(\text{FS})}{D}\\ &= J_{\text{cav}}(1)+\left(1-J_{\text{cav}}(1)\right)\varepsilon(\text{FS})\end{aligned} \tag{5.18}$$

Now consider the same conditions, but for a water cavity of non-unit density ρ, again neglecting changes in the mass stopping power of water with density. For a fixed average collision kerma $\overline{K}_{\text{col}}$ within the cavity, the dose due to internally generated electrons will be invariant with field-size at a level of $DJ_{\text{cav}}(\rho)$, while in wide fields the dose due to externally generated electrons is $D(1 - J_{\text{cav}}(\rho))$ (equation (5.9)). For narrower fields $\overline{D}_{\text{external}}$ is modelled as

$$\overline{D}_{\text{external}}\left(\text{FS, 5, }\rho,\frac{\text{MU}_{\text{ref}}}{\left(\text{OF}(\text{FS})/s_{ee}(\text{FS})\right)}\right) \approx D\left(1-J_{\text{cav}}(\rho)\right)\varepsilon(\text{FS}) \tag{5.19}$$

that is, the relative variation of $\overline{D}_{\text{external}}$ with field-size is assumed $\varepsilon(FS)$, the same as for a unit density cavity. This assumption introduces some inaccuracy into the fine detail of $\overline{D}_{\text{external}}(\text{FS})$, but the broad shape of the curve will still be correctly described using the approximation, as outlined in the appendix-A. It follows that

$$\frac{\overline{D}_{\text{mdw}\_}\left(\text{FS},5,\rho,\left\{\text{MU}_{\text{ref}}\big/\left(\text{OF}(\text{FS})/s_{ee}(\text{FS})\right)\right\}\right)}{\overline{D}_{\text{mdw}\_}\left(\text{FS}_{\text{ref}},5,\rho,\text{MU}_{\text{ref}}\right)} \approx \frac{DJ_{\text{cav}}(\rho)+D\left(1-J_{\text{cav}}(\rho)\right)\varepsilon(\text{FS})}{D}$$

$$\approx J_{\text{cav}}(\rho)+\left(1-J_{\text{cav}}(\rho)\right)\varepsilon(\text{FS}) \qquad (5.20)$$

and taking equations (5.2), (5.18) and (5.20) together with the density-independence of the dose-per-monitor unit absorbed by a cavity placed at the centre of a reference field wide enough to establish lateral electronic equilibrium throughout the cavity, then

$$P_{\rho\_}(\text{FS}) = \frac{\overline{D}_{\text{w}}\left(\text{FS},5,\left\{\text{MU}_{\text{ref}}\big/\left(\text{OF}(\text{FS})/s_{ee}(\text{FS})\right)\right\}\right)}{\overline{D}_{\text{mdw}\_}\left(\text{FS},5,\rho,\left\{\text{MU}_{\text{ref}}\big/\left(\text{OF}(\text{FS})/s_{ee}(\text{FS})\right)\right\}\right)}$$

$$= \frac{\overline{D}_{\text{w}}\left(\text{FS},5,\left\{\text{MU}_{\text{ref}}\big/\left(\text{OF}(\text{FS})/s_{ee}(\text{FS})\right)\right\}\right)}{\overline{D}_{\text{mdw}\_}\left(\text{FS},5,\rho,\left\{\text{MU}_{\text{ref}}\big/\left(\text{OF}(\text{FS})/s_{ee}(\text{FS})\right)\right\}\right)}\Bigg/\frac{\overline{D}_{\text{w}}\left(\text{FS}_{\text{ref}},5,\text{MU}_{\text{ref}}\right)}{\overline{D}_{\text{mdw}\_}\left(\text{FS}_{\text{ref}},5,\rho,\text{MU}_{\text{ref}}\right)}$$

$$\approx \frac{J_{\text{cav}}(1)+\left(1-J_{\text{cav}}(1)\right)\varepsilon(\text{FS})}{J_{\text{cav}}(\rho)+\left(1-J_{\text{cav}}(\rho)\right)\varepsilon(\text{FS})} \qquad (5.21)$$

Finally, substituting s_{ee} from equation (5.18) for ε in (5.21) and rearranging leads to

$$P_{\rho-}(\text{FS}) \approx 1\Bigg/\left\{1+\left(\frac{J_{\text{cav}}(\rho)-J_{\text{cav}}(1)}{1-J_{\text{cav}}(1)}\right)\left(\frac{1-s_{ee}(\text{FS})}{s_{ee}(\text{FS})}\right)\right\}=1\Bigg/\left\{1+I_{\text{cav}}\left(\frac{1-s_{ee}(\text{FS})}{s_{ee}(\text{FS})}\right)\right\} \qquad (5.22)$$

where $$I_{\text{cav}}=\left(\frac{J_{\text{cav}}(\rho)-J_{\text{cav}}(1)}{1-J_{\text{cav}}(1)}\right) \qquad (5.23)$$

5.2.5 Exploring the link between $P_{\rho\_}$ and s_{ee}

In the *Results* the ability of equation (5.22) is explored to describe $P_{\rho\_}(\text{FS})$ factors at the centres of fields with lateral electronic equilibrium factors s_{ee}(FS). In particular fits of the equation to $P_{\rho\_}(\text{FS})$ and s_{ee}(FS) data calculated over the field-size range 0.25-10 cm are presented, for the modelled PinPoint 3D and diamond cavities detailed in table 5.1. The $P_{\rho\_}(\text{FS})$ and s_{ee}(FS) values were calculated using the15 MV Monte Carlo beam model, once again computing kerma (for the s_{ee} calculations) by scoring dose with ECUT set high to 30 MeV. For comparison with s_{ee} conventional phantom scatter factors s_p have also been determined, calculated as ratios of the Monte Carlo-computed dose absorbed by a unit density water voxel, having the dimensions of the modelled detector cavity and being located at 5 cm depth in water on the beam's central axis to kerma in the same voxel positioned in vacuum, normalized to one for a 10 cm wide square field (Scott *et al* 2009).

Fitting of equation (5.22) was carried out using maximum-likelihood methods (Thames *et al* 1986), determining model goodness-of-fit via a chi-square measure (Hosmer and Lemeshow 1989). The quantity I_{cav} was treated as a fittable parameter with a 95% confidence interval taken as the range over which the chi-square measure lies below its best-fit value plus $3.84\left(\chi^2_{(1),0.95}\right)$. Good fits of the $P_{\rho_-}\left(s_{\text{ee}}\right)$ model, obtained for physically reasonable I_{cav} values, would lend weight to equation (5.22) which provides a conceptual bridge between s_{ee} and P_{ρ_-}. To check the plausibility of the fitted I_{cav} values they are compared to values calculated via equation (5.23) from direct Monte-Carlo estimates of J_{cav} made using the method of Ma and Nahum (1991).

5.2.6 Extending the $P_{\rho_-}\left(\text{FS}\right)$ model

In this section two limitations of the model derived in *Methods 5.2.4* are discussed. Firstly, noting that photon fluence spectra change with field-size it follows from the reasoning leading to equation (5.13) that $J_{\text{cav}}(\rho)$ might vary with field-size too. In the *Results* this effect for the modelled PinPoint 3D and diamond cavities is quantified – obtaining J_{cav} values by computationally irradiating the cavities in vacuum using forwards-directed photon fluences having the energy spectra calculated to exist within the cavities when located 5 cm deep in water on the axis of 4 × 4, 10 × 10and 40 × 40 cm^2 square fields.

In fact the approach of *Methods 5.2.4* can be extended to account for possible changes of J_{cav} with field-size, generalizing equation (5.17) to

$$\overline{D}_{\text{w}}\left(\text{FS},\,5,\,\frac{\text{MU}_{\text{ref}}}{\text{OF}(\text{FS})/s_{ee}(\text{FS})}\right)=DJ_{\text{cav}}\left(1,\text{FS}\right)+D\left(1-J_{\text{cav}}\left(1,\text{FS}\right)\right)\varepsilon\left(\text{FS}\right) \tag{5.24}$$

and equation (5.19) to

$$\overline{D}_{\text{external}}\left(\text{FS},\,5,\,\rho,\frac{\text{MU}_{\text{ref}}}{\left(\text{OF}(\text{FS})/s_{ee}(\text{FS})\right)}\right)\approx D\left(1-J_{\text{cav}}\left(\rho,\text{FS}\right)\right)\varepsilon\left(\text{FS}\right) \tag{5.25}$$

and thus extending the assumption that ε (FS) is invariant with density to situations in which J_{cav} depends on field-size. Then using equations (5.24) and (5.25) instead of (5.17) and (5.19) it follows that

$$P_{\rho\_} \approx 1 \Bigg/ \left\{ 1 + \left(\frac{J_{\text{cav}}(\rho, \text{FS}) - J_{\text{cav}}(1, \text{FS})}{1 - J_{\text{cav}}(1, \text{FS})} \right) \left(\frac{1 - s_{ee}(\text{FS})}{s_{ee}(\text{FS})} \right) \right\} = 1 \Bigg/ \left\{ 1 + I_{\text{cav}}(\rho) \left(\frac{1 - s_{ee}(\text{FS})}{s_{ee}(\text{FS})} \right) \right\} \quad (5.26)$$

A further limitation of the $P_{\rho\_}$ model is that it focuses on cavity density alone, unlike $F_{\text{w,det}}$ which accounts for the combined effects of density and atomic composition. In the *Results* the $F_{\text{w,det}}$ and $P_{\rho\_}$ values are compared. In particular they are combined with restricted stopping power ratios $s^{\text{SA}}_{\text{w,det},\Delta}(\text{FS})$ to determine the quantity

$$\frac{F_{\text{w,det}}(\text{FS}) / P_{\rho\_}(\text{FS})}{s^{\text{SA}}_{\text{w,det},\Delta}(\text{FS})} = P_{\text{fl}\_}(\text{FS}) \quad (5.27)$$

where the stopping power ratio is calculated for electron fluence spectra computed within a unit density water voxel of 4 mm^2 cross-section, located on-axis at 5 cm depth in water at the centre of a field of size FS. Conceptually $P_{\text{fl}\_}$ accounts for changes in the electron fluence within a detector cavity due specifically to the cavity's non-water-like atomic number rather than to its non-unit density (figure 5.1). In this work, though, $P_{\text{fl}\_}$ is used empirically to study the degree to which the $F_{\text{w,det}}(\text{FS}) / P_{\rho\_}(\text{FS})$ ratio simply reflects the water-to-detector restricted electronic stopping power ratio for the modelled PinPoint 3D and diamond dosimeters. Restricted stopping power cut-off energies, Δ of 10 and 320 keV for the PinPoint 3D and diamond cavities have been chosen respectively, roughly corresponding to the minimum kinetic energies required for electrons to escape from these cavities.

5.3 Results

$F_{\text{w,det}}$ and $P_{\rho\_}$ factors calculated for the modelled PinPoint 3D and diamond cavities by Scott *et al* (2012) are plotted for square fields of width 0.25-10 cm in figure 5.5; the curves are offset but similarly shaped. Spectrally-averaged water-to-air and water-to-diamond restricted electronic stopping power ratios $s^{\text{SA}}_{\text{w,det},\Delta}(\text{FS})$ have been calculated for the computed on-axis electron fluences of these fields and are almost constant (figure 5.6). From these quantities $P_{\text{fl}\_}$ factors have been calculated for the two modelled cavities via equation (5.27) and are plotted against field-size in figure 5.7. For the PinPoint 3D cavity $P_{\text{fl}\_}$ differs insignificantly from one in all the fields studied, whilst for the diamond cavity it lies slightly above one at the smallest field-sizes, dropping to one in fields of width 1.5 cm and greater.

Since $F_{\text{w,det}}$ is the product of $P_{\rho\_}$, $P_{\text{fl}\_}$ and $s^{\text{SA}}_{\text{w,det},\Delta}(\text{FS})$, and the latter two factors are almost field-size invariant for the modelled PinPoint 3D and diamond cavities, most of the field-size dependence of $F_{\mathrm{w,det}}$ stems from the field-size variation of the $P_{\rho_-}(\mathrm{FS})$ factor, focussing attention on its causes and how it might be minimized.

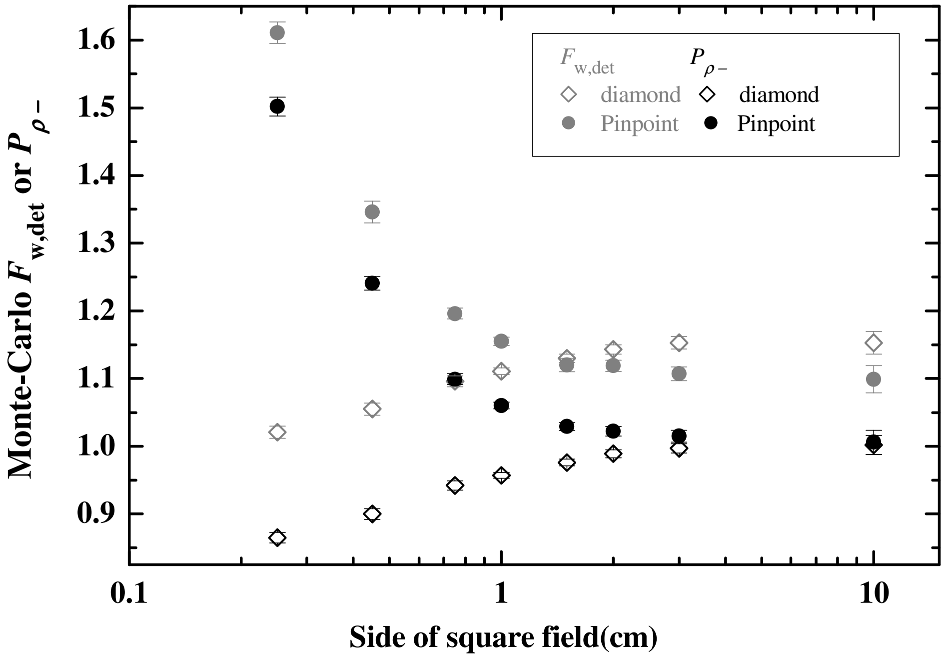

Figure 5.5: **Monte-Carlo calculated $F_{\mathrm{w,det}}$ and P_{ρ_-} factors plotted for the modelled diamond and PinPoint detectors, characterized as isolated voxels of detector material ($F_{\mathrm{w,det}}$) or modified density water (P_{ρ_-}) surrounded by unit density water. Data are taken from Scott *et al* (2012) and graphed for square fields of width 0.25-10 cm, showing the statistical uncertainties of the Monte- Carlo calculations as ± 2 standard deviation confidence intervals.**

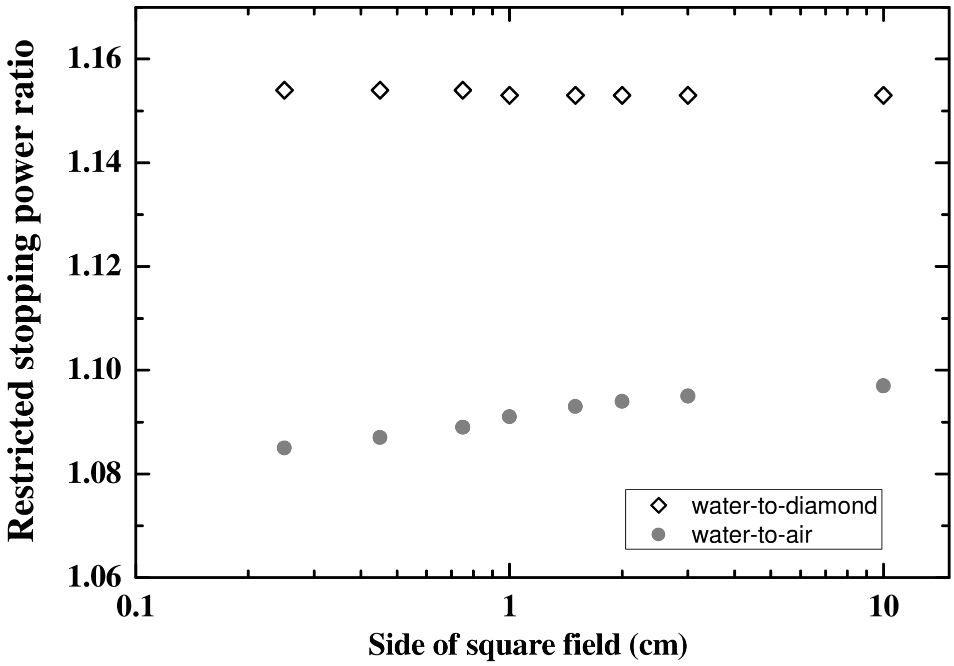

Figure 5.6: **Spectrally-averaged restricted stopping power ratios $s^{\mathrm{SA}}_{\mathrm{w,diamond},\Delta}$ and $s^{\mathrm{SA}}_{\mathrm{w,air},\Delta}$ calculated for Monte-Carlo computed on-axis electron particle spectra in square fields of width 0.25-10 cm. Confidence intervals are narrower than 4×10^{-4}.**

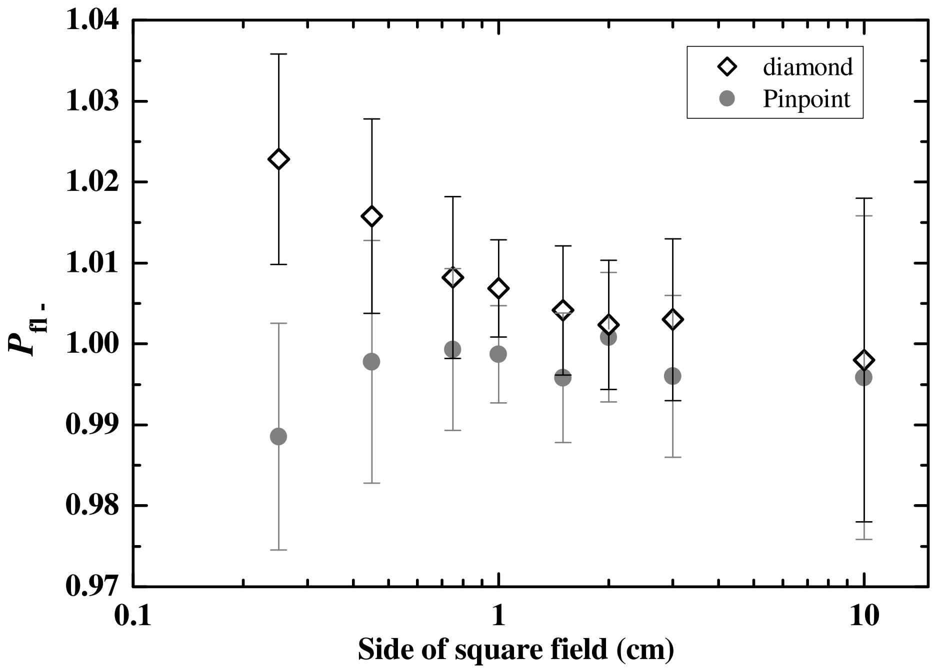

Figure 5.7: $P_{\text{fl}\_}$ **factors (calculated as** $\left\{F_{\text{w,det}} \big/ \left(p_\rho \times s^{\text{SA}}_{\text{w,det},\Delta}\right)\right\}$**) plotted for square fields of width 0.25-10 cm, together with ± 2s.d. confidence.**

Table 5.2: **Values of the conventional photon scatter factor s_p and the lateral electronic equilibrium factor s_{ee}, shown together with (± 2 s.d.) uncertainties.**

Field-size (cm)	s_p	s_{ee}
0.25 × 0.25	0.27 ± 0.01	0.30 ± 0.01
0.45 × 0.45	0.34 ± 0.01	0.38 ± 0.01
0.75 × 0.75	0.49 ± 0.01	0.54 ± 0.01
1 × 1	0.58 ± 0.01	0.63 ± 0.01
1.5 × 1.5	0.71 ± 0.01	0.77 ± 0.01
2 × 2	0.81 ± 0.01	0.85 ± 0.01
3 × 3	0.89 ± 0.02	0.93 ± 0.01
10 × 10	1.00	1.00

Monte-Carlo-calculated s_{ee} factors are plotted against field-size in figure 5.8(a), while ratios of the conventional phantom scatter factor, s_p, to s_{ee} are plotted in figure 5.8(b). Values of s_{ee} and s_p are listed in table 5.2: both describe the impact on central axis doses of the buildup of lateral electronic equilibrium with increasing field-size, but s_p additionally describes the buildup of photon scatter. Consequently s_p varies a little more than s_{ee}, dropping by 73 % between field-sizes of 10 and 0.25 cm compared to 70 % for s_{ee}. However s_{ee} and s_p change very similarly in the narrowest fields whose on-axis dose variation with field-size is dominated by electronic disequilibrium effects, their ratio being almost constant (figure 5.8(b)).

The $P_{\rho\_}$ factors calculated for the modelled diamond and PinPoint 3D cavities are replotted in figure 5.9 alongside fits of the $P_{\rho\_}\left(s_{\mathrm{ee}}\left(\mathrm{FS}\right)\right)$ model of equation (5.22). The diamond $P_{\rho\_}$ factors are described well by the best fit of the model ($p = 0.23$, chi-square test) although the fitted value of I_{cav} is 0.067 ± 0.003 (2 standard deviation (s.d.)), significantly higher than the figure of 0.047± 0.002 calculated from direct Monte-Carlo J_{cav} estimates for the diamond cavity (table 5.3).

Table 5.3: **Monte Carlo calculations of J_{cav} (± 2 s.d.) made for the modelled diamond and PinPoint cavities, and in-vacuum photon fluences oriented at 0˚ and 90˚ to the axes of the modelled cylindrical cavities. The photon fluence energy spectrum (though not angular distribution) was computed on the axis of a 40 × 40 cm² field, at 5 cm depth in water. Calculated J_{cav} values are shown together with ± 2 standard deviation uncertainties.**

Modelled active volume	Density (g cm^{-3})	Modelled fluence direction (˚)	$J_{\mathrm{cav}}(1)$	$J_{\mathrm{cav}}(\rho)$	$I_{\mathrm{cav}} = \left(\frac{J_{\mathrm{cav}}(\rho)-J_{\mathrm{cav}}(1)}{1-J_{\mathrm{cav}}(1)}\right)$
diamond	3.5	0	0.023 ± 0.001	0.070 ± 0.002	0.047 ± 0.002
diamond	3.5	90	0.055 ± 0.002	0.161 ± 0.006	0.106 ± 0.006
PinPoint	0.0012	0	0.107 ± 0.003	$2 \times 10^{-4} \pm 4\times10^{-6}$	- 0.107 ± 0.003
PinPoint	0.0012	90	0.137 ± 0.001	$2 \times 10^{-4} \pm 4\times10^{-6}$	- 0.137 ±0.001

This discrepancy is caused by the difference in angular distributions between the real photon fluence at 5 cm depth in water and the exclusively forwards-travelling in-vacuum fluence used to estimate J_{cav} values. For a thin disc such as the diamond cavity, the mean path-length out of the cavity taken by electrons energized by forwards-directed photons is shorter than the mean length of the paths taken by more laterally-directed electrons energized by the mixture of primary and scatter photons found in water. And since J_{cav} is directly proportional to mean path-length, its value is higher for the in-water photon fluence than for an exclusively forwards-directed fluence. To establish the dependence of J_{cav} on photon fluence direction, J_{cav} values have been re-estimated again using the Monte-Carlo approach of Ma and Nahum but now changing the in-vacuum photon fluence direction to 90˚, impacting the cavity side-on rather than from the front. The resulting I_{cav} estimate obtained for this 90˚ fluence is 0.106 (table 5.3) - the fitted value of 0.067 lying between the Monte-Carlo estimates for 0° and 90° fluences as expected since only a fraction of the photon fluence in water is laterally scattered.

(a)

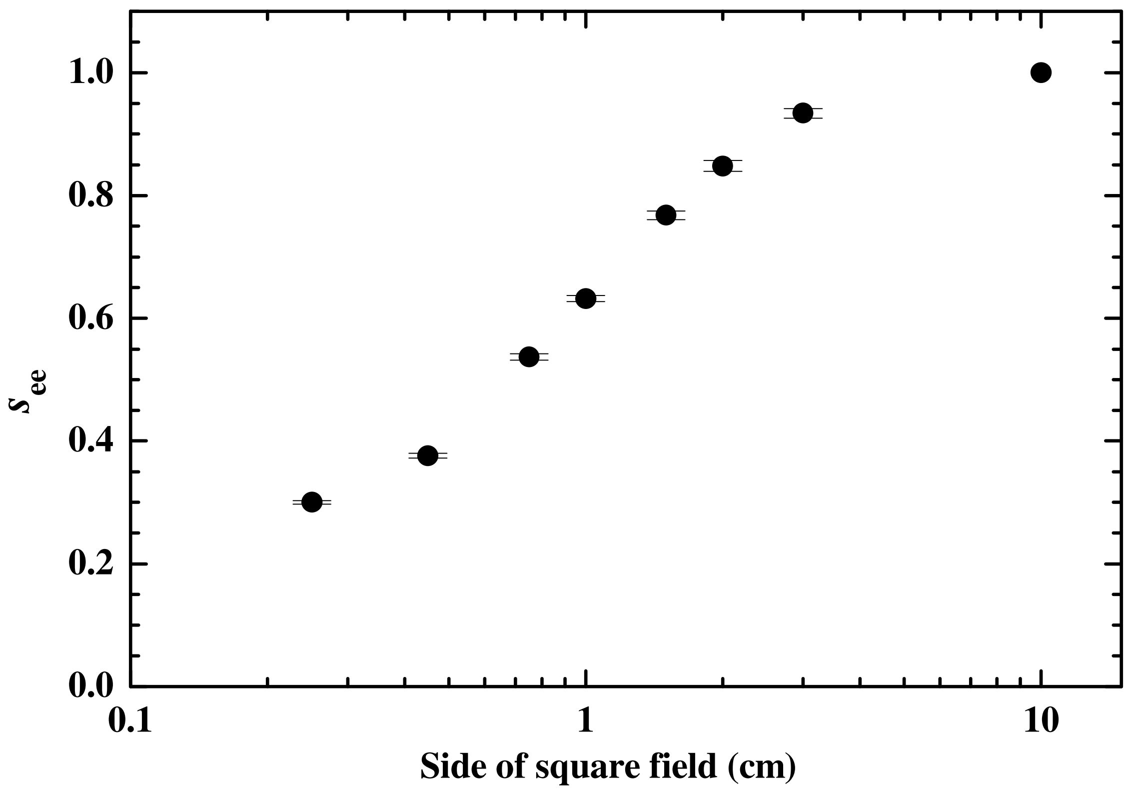

(b)

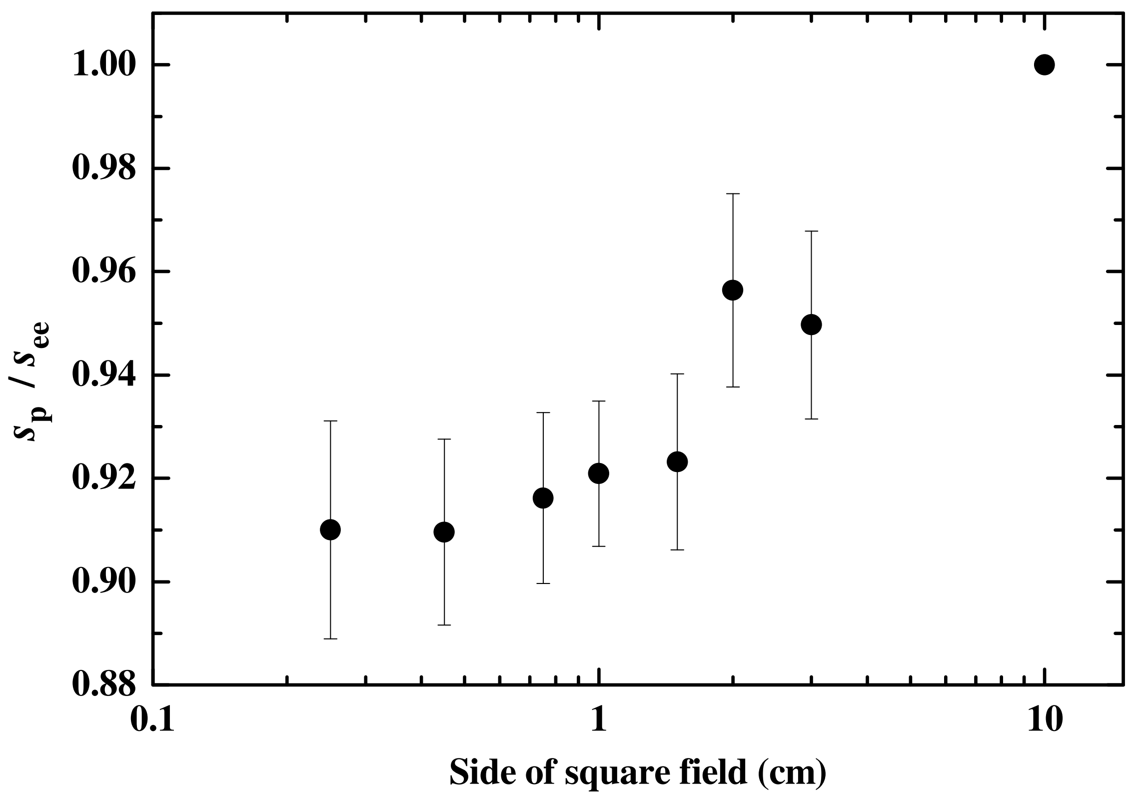

Figure 5.8: **Plots of (a) the lateral electronic equilibrium factor s_{ee} and (b) the ratio of the conventional phantom scatter factor s_p to s_{ee}, for square fields of width 0.25-10 cm.**

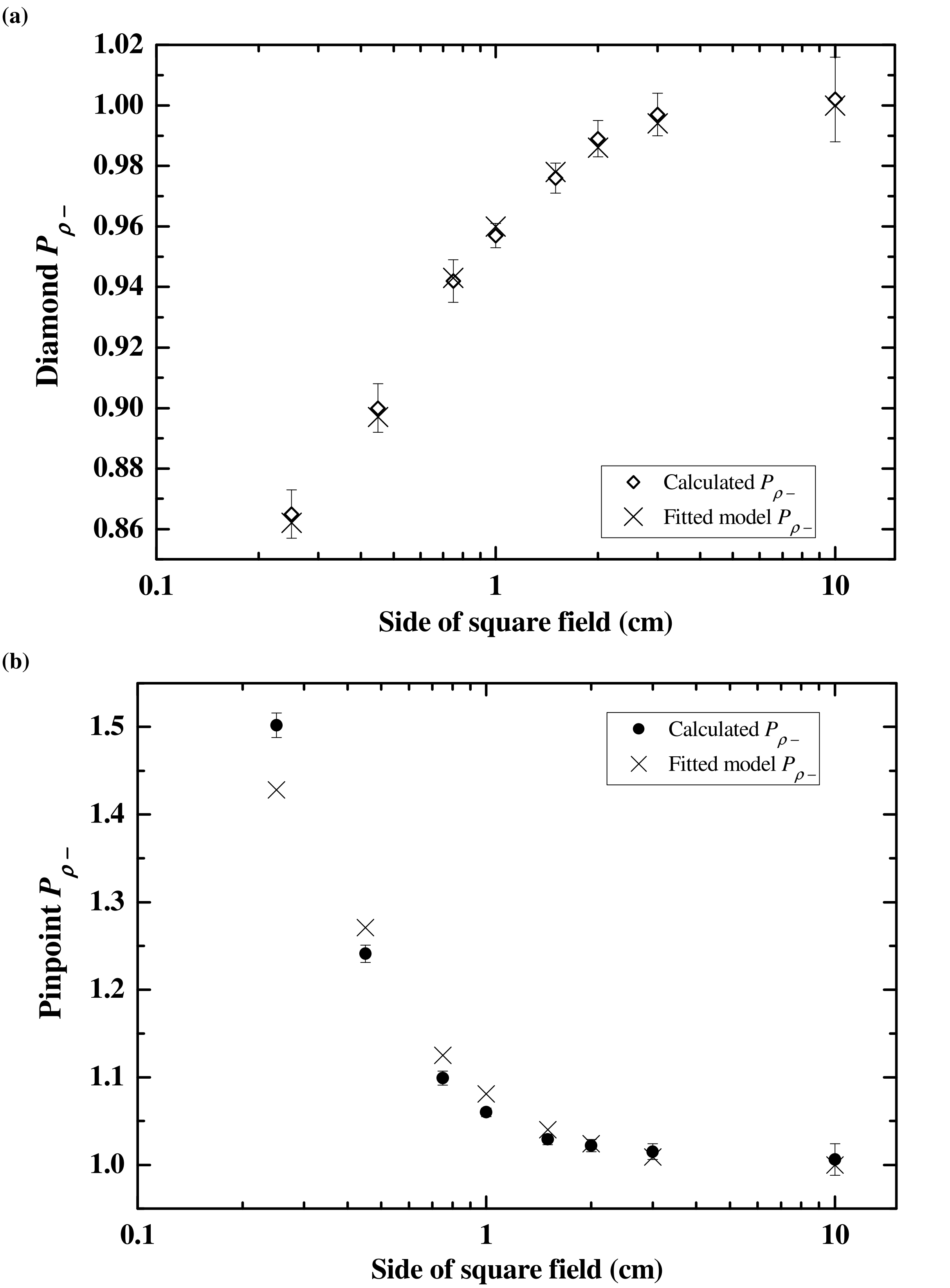

Figure 5.9: **Monte Carlo P_{ρ_-} factors (± 2s.d.) calculated for the modelled cavities of (a) both the diamond detector and PinPoint detectors and (b) the diamond detector alone, together with the best fits of equation (5.22) to the data.**

For the modelled PinPoint 3D cavity, the I_{cav} value obtained from the best fit of equation (5.22) to the $P_{\rho\_}$ data is -0.123± 0.002,which lies in between I_{cav} estimates of -0.107 and -0.137 obtained from Monte-Carlo calculations of J_{cav} made for this cavity using 0° and 90°in-vacuum fluences (table 5.3).Notice that the angular dependence of I_{cav} is less for the modelled PinPoint 3D cavity than for the diamond, because the width and thickness of the PinPoint 3D cavity are much more comparable.

The best fit of equation (5.22) to the Monte-Carlo Pinpoint $P_{\rho\_}$ data is shown in figure 5.9(a). Although the model captures the broad shape of the data, it underestimates $P_{\rho\_}$ for the 0.25 cm field while slightly overestimating it in fields of width 0.5-1.5 cm. The photon fluence profile of the narrow 0.25 cm field is peaked towards the centre of the cavity, increasing the mean exit path-length taken out of the cavity by electrons energized within it, and consequently raising the cavity's $J_{cav}(\rho)$ and I_{cav} values above their levels in wider fields with flatter photon profiles. This effect is greater in the geometrically thicker PinPoint 3D cavity than in the thin sensitive volume of the diamond detector, from which electrons energized by primary photons will exit predominantly through the distal rather than lateral walls, making the mean exit path-length, and thus J_{cav}, insensitive to the shape of the photon fluence profile.

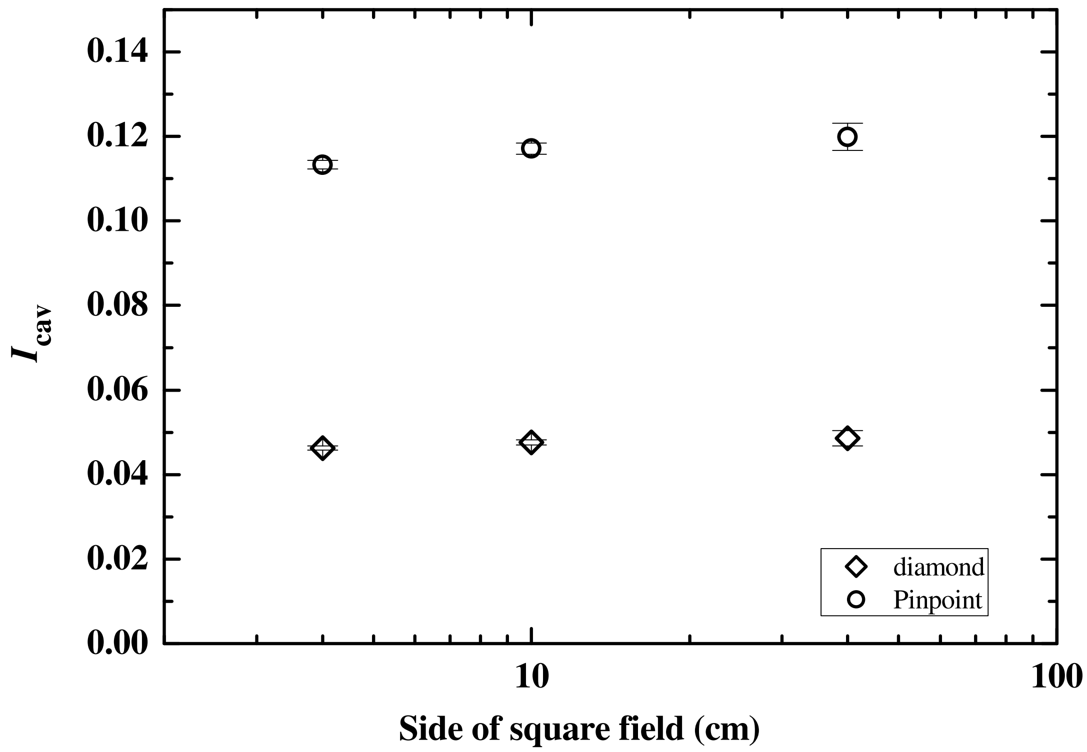

Figure 5.10: **Monte Carlo estimates of I_{cav} (± 2s.d.) plotted against field-size for the modelled diamond (ρ = 3.5 g cm^{-3}) and Pinpoint (ρ = 0.0012 g cm^{-3}) cavities. The I_{cav} estimates were calculated from J_{cav} values obtained using the method of Ma and Nahum, irradiating the cavities in vacuum with forward directed photon fluences having the energy spectra calculated at 5 cm depth in water on-axis in square fields of width 4, 10 and 40 cm.**

Although the simplified method of Ma and Nahum cannot be used to calculate the dependence of J_{cav} on the shapes of very small field photon fluence profiles, it has been used to study the variation of J_{cav} with field-size due to spectral changes resulting from the greater number of scattered photons in wider fields. I_{cav} values obtained from these J_{cav} calculations are plotted in figure 5.10 for the modelled diamond and PinPoint 3D cavities, and change by only 5% between square fields of width 4 and 40 cm. More substantial changes in I_{cav} must, therefore, follow from the peaked photon fluence profiles of very small fields rather than from spectral differences.

5.4 Discussion

Monte-Carlo studies show that when the sensitive volume of a detector is irradiated by a field too small to establish lateral electronic equilibrium, the dose absorbed by the sensitive volume depends on its density (Scott *et al* 2008, 2012). Here this effect has been described using cavity theory, obtaining an approximate formula (equation (5.22)) that links the density-dependence $P_{\rho\_}$ to the degree of on-axis electronic equilibrium s_{ee}, a normalized ratio of dose to collision kerma, whose relative variation in small fields is similar to that of the conventional phantom scatter factor s_p. The form of the $P_{\rho\_}\left(s_{ee}\left(\mathrm{FS}\right)\right)$ link depends on a cavity-specific parameter $I_{cav} = (J_{cav}(\rho) - J_{cav}(1))/(1-J_{cav}(1))$, in which $J_{cav}(\rho)$ describes the fraction of the wide field equilibrium dose that the detector sensitive volume absorbs from internally energized electrons when it is filled with water of density ρ.

Equation (5.22) provides a good description of the field-size variation of Monte-Carlo $P_{\rho\_}$ values computed for a modelled diamond detector cavity, using a fitted I_{cav} value that concords with independent estimates of $J_{cav}(\rho)$. The formula also captures the broad field-size variation of $P_{\rho\_}$ for a modelled PinPoint 3D ionization chamber, again using a fitted I_{cav} value that is consistent with independent computational estimates of $J_{cav}(\rho)$. However the fitted formula does not match the ion chamber $P_{\rho\_}$ data (figure 5.9(b)) for the smallest field-sizes – most likely because for the geometrically thick ion chamber $J_{cav}(\rho)$ values in really small fields with peaked photon fluence profiles are greater than those in wide fields.

Some practical ways of limiting the size of small field $P_{\rho\_}$ density-dependence correction factors can be deduced from the cavity theory – the simplest being to construct a detector whose sensitive volume has a density close to that of water (a liquid ion chamber for example) thereby largely eliminating the problem. Another method is to reduce the dimensions of the sensitive volume so that it approaches the Bragg-Gray limit, making $J_{cav}(\rho)$ very small and $P_{\rho\_}$ correspondingly close to one even in regions of lateral electronic disequilibrium. Immediately above the Bragg-Gray region

$J_{\rm cav}(\rho)$ values are influenced by cavity volume via a linear dependence on $\bar{l}(\rho)$, the mean path-length taken out of the cavity by internally energized electrons (equation (5.13)). It is inefficient to uniformly shrink the cavity volume in order to reduce $\bar{l}(\rho)$, since then the volume of the detector cavity (and so its sensitivity) would decrease as the cube of $\bar{l}(\rho)$ and thus of $J_{\rm cav}(\rho)$. Instead it would be useful just to reduce the thickness of the cavity in the direction of the radiation beam – because this dimension has the most direct impact on $\bar{l}(\rho)$, and reductions in $J_{\rm cav}$ achieved using this approach would scale linearly with associated reductions in detector sensitivity. Alternatively it may be possible to offset the non-water equivalent density of the sensitive volume by building other regions of different density into the detector – adding a high density structure to offset a low density cavity for example.

In the formalism of Bouchard *et al* (2009) the detector correction factor $F_{\rm w,det}$ of equation (5.9) is the product of $P_{\rho\_}$, the water-to-detector restricted stopping power ratio $s^{\rm SA}_{\rm w,det,\Delta}(\rm FS)$, and a further factor $P_{\rm fl\_}$ that accounts for any perturbation of the electron fluence in the cavity caused by its non-water equivalent atomic composition (equation (5.3)). Interestingly, values of $P_{\rm fl\_}$ calculated as $\left(F_{\rm w,det}(FS) \big/ \left(s^{\rm SA}_{\rm w,det,\Delta}(\rm FS)\, P_{\rho\_}(\rm FS)\right)\right)$ lie close to one in square fields of width 0.25-10 cm for the modelled diamond and PinPoint 3D cavities, meaning that $F_{\rm w,det}$ is mostly the product of $P_{\rho\_}$ and $s^{\rm SA}_{\rm w,det,\Delta}(\rm FS)$ for these detectors. And as $P_{\rho\_}$ factors calculated for the diamond cavity depart from unity less rapidly than those calculated for the PinPoint 3D-like cavity, it will be easier to make accurate measurements of small field doses using the diamond detector.

Finally, notice again that $P_{\rho\_}$ takes a value of one at the centre of fields wide enough to establish lateral electronic equilibrium in the vicinity of the cavity, and that this condition is close to being met by a 15 MV 3×3 cm^2 field (figures 5.8(a) and 5.9). Since little difference exists between the water-to-detector restricted electronic stopping power ratios of very small and 3-4 cm wide fields either at this beam energy (figure 5.5) or at 6 MV (Heydarian *et al* 1996), it is convenient to calibrate small field detectors in the 3×3 or 4×4 cm^2 fields: smaller calibration fields would introduce a substantially non-unit $P_{\rho\_}$ factor into the reference conditions (figure 5.9), which would have to be corrected out again, while the spectra of larger fields increasingly differ from those of small fields, again potentially requiring correction. Of course measurements made in small non-equilibrium fields require $P_{\rho\_}$ corrections whose values depends on both field-size and detector location (Scott *et al*

2012), – but the use of a 3 or 4 cm reference field effectively minimizes the number of correction factors needed to move between reference and small field conditions.

5.5 Conclusions

For PinPoint 3D-like ion chambers and diamond detectors most of the field-size variation of $F_{w,det}$, the ratio of doses absorbed by water and the sensitive volume of a detector, originates from the dependence on density of doses absorbed from non-equilibrium small fields. This dependence can be characterized as a ratio $P_{\rho\_}$ of doses absorbed by equal volumes of water of unit and modified density having the same mass radiological properties. $P_{\rho\_}(\mathrm{FS})$ depends on the degree of lateral electronic disequilibrium, which can be defined using a quantity s_{ee} whose variation in small fields is similar to that of the phantom scatter factor s_p. For a diamond detector the relationship between $P_{\rho\_}$ and s_{ee} is described well by a model obtained from a simple cavity theory. The model also captures the overall field-size dependence of $P_{\rho\_}$ for a schematic PinPoint 3D detector, although its accuracy is reduced for the smallest fields whose photon fluence profiles are non-uniform within the sensitive volume.

The density-dependence can be minimized by constructing detectors with sensitive volumes having similar densities to water, or by limiting the thickness of sensitive volumes in the direction of the beam. Regular 3×3 or 4×4 cm^2 fields are useful for small field detector calibration, minimizing the number of correction factors needed for small field measurements.

CHAPTER 6

Breakdown of Bragg-Gray behaviour for low-density detectors under electronic disequilibrium conditions in small megavoltage photon fields

6.1 Introduction

Radiotherapy treatment requires the accurate delivery of the prescribed radiation dose to a defined target volume in the cancer patient. The introduction of new technologies in radiation therapy (intensity modulated radiation therapy (IMRT), stereotactic ablative radiotherapy, (SABR)) enables small and/or irregular shaped lesions to be treated with megavoltage (MV) photon fields often with dimensions of 3 × 3 cm^2 or smaller (Das *et al* 2008a, IPEM 2010). Accurate determination of the doses delivered by these small or very small radiation fields presents some challenges not encountered for large fields (Sánchez-Doblado *et al* 2007, Capote *et al* 2004, Alfonso *et al* 2008, Das *at al* 2008b, Bouchard *et al* 2009, Crop *et al* 2009, IPEM 2010, Francescon *et al* 2011, Scott *et al* 2012).

The 'physics' of small, non-equilibrium radiation fields differs from that of large fields. Differences include loss of lateral electronic equilibrium and source occlusion; the field size at which these effects become significant depends on beam energy, and collimator design (Treuer *et al* 1993, Das *et al* 2008b, Alfonso *et al* 2008, Scott *et al* 2008, 2009, IPEM 2010). Detector-specific effects include fluence perturbation caused by differences between detector material and medium, dose-averaging effects around the peak dose distributions, and uncertainties for very small fields introduced by slight geometrical detector misalignment (Paskalev *et al* 2003, Bouchard *et al* 2009, Crop *et al* 2009, IPEM 2010, Francescon *et al* 2011, Scott *et al* 2012, Charles *et al* 2012, 2013, Underwood *et al* 2013b). In summary, the response of detectors in small fields can vary rapidly with field size (Alfonso *et al* 2008, Ding and Ding 2012).

In a perfect Bragg–Gray cavity the electron fluence spectrum in the detector is identical to that in the uniform medium (i.e. the presence of the detector does not 'perturb' the electron fluence either in magnitude or in 'shape'). It is well established that (air-filled) ionization chambers exhibit Bragg-Gray behaviour in megavoltage photon beams at conventional field sizes i.e. approx. 4 × 4 cm^2 or greater (Ma and Nahum 1991). When the field size is reduced below that required for quasi-CPE[9],

[9] Quasi-CPE corresponds to what Attix (1986) termed 'Transient CPE' i.e. not perfect due to non-negligible photon attenuation over the distance of the maximum secondary electron range.

large perturbations have been observed experimentally and predicted theoretically by Monte-Carlo simulations (Sánchez-Doblado *et al* 2007, Francescon *et al* 2011, Scott *et al* 2012, Fenwick *et al* 2013, Czarnecki and Zink 2013, Benmakhlouf *et al* 2014).

In chapter 4 it was demonstrated that the *physical density* of the active volume of the detector is the key factor in its response in a medium irradiated by beams of non-equilibrium field size, rather than atomic number differences between detector and medium (Scott *et al* 2012). In chapter 5 a modified form of cavity theory was developed to take account of this 'density effect' in small fields (Fenwick *et al* 2013). This effect may also manifest itself in other non-equilibrium situations, such as in the build-up region of a large photon field where a detector with a density *greater* than that of the medium will *over-respond* compared to its behaviour once D_{max} has been reached. Charles *et al* (2013, 2014) and Underwood *et al* (2013b, 2015) showed that for small detector cavities of certain shapes, *mass-density compensation* can be exploited to design a solid-state dosimeter/ionization chamber with a 'perturbation-free' small-field response. Papaconstadopoulos *et al* (2014) have demonstrated that a liquid ionization chamber (microLion 31018, PTW, Freiburg, Germany) and an unshielded diode (Exradin DIV, SI, Middleton, USA) can be re-designed as 'correction-free' detectors for a field size of 0.5×0.5 cm^2; they decreased the radius of the active volume of the microLion from 1.25 mm to 0.85 mm and increased the radius of the active volume of the Exradin diode from 0.5 mm to 1 mm. These authors claimed that this approach was simpler than *mass-density compensation* proposed by Charles *et al* (2013) and Underwood *et al* (2013b).

In this chapter, with the aid of Monte-Carlo simulations, the major deviations from Bragg-Gray behaviour exhibited by ionization chambers with small (air) volumes (e.g. the 'PinPoint 3D' chamber) in small megavoltage photon fields are quantified. With the aid of a diagram it is explained exactly *why* the Bragg-Gray principle breaks down in low-density cavities when CPE is no longer present; an analytical version of this explanation is given in the Appendix-B. The 'textbook' statement that charged-particle equilibrium (CPE) in the undisturbed medium is *not* required for a detector to behave in a Bragg-Gray manner (e.g. Nahum 2007b) is critically examined. As a corollary the sizes of an air cavity and a high-density (diamond) cavity is also determined that *would* fulfil Bragg-Gray conditions, defined as an electron-fluence perturbation factor within 5% of unity, in field sizes of 0.5 $\times$ 0.5 cm^2 and below.

6.2 Theory

The introduction of a measuring device into an irradiated medium perturbs the radiation field unless the device is completely equivalent, in terms of radiation interactions to the medium into which it is introduced (or *displaces*). Here, it is assumed to deal with a *Bragg-Gray* detector, then the quantity 'perturbed' is the charged-particle fluence; if this change in fluence is less than 5%, then the term *perturbation* is generally used (Nahum 1996). An *electron fluence perturbation correction factor*, $\left(p_{\Phi}\right)_{\text{det}}^{\text{med}}$ is defined as

$$\left(p_{\Phi}\right)_{\text{det}}^{\text{med}} = \frac{\left[\Phi^{\text{tot}}(z)\right]_{\text{med}}}{\left[\Phi^{\text{tot}}(z)\right]_{\text{det}}} = \frac{\int_{\Delta}^{E_{\max}} \left[\Phi_{E}^{\text{tot}}(z)\right]_{\text{med}} \mathrm{d}E}{\int_{\Delta}^{E_{\max}} \left[\Phi_{E}^{\text{tot}}(z)\right]_{\text{det}} \mathrm{d}E} \tag{6.1}$$

where $\left[\Phi_{E}^{\text{tot}}(z)\right]_{\text{med}}$ and $\left[\Phi_{\text{E}}^{\text{tot}}(z)\right]_{\text{det}}$ are the *total* electron (+ positron) 'fluence' (i.e. including 'knock-on' electrons, or delta-rays), differential in energy, in the undisturbed medium (water) and averaged throughout the detector/cavity volume, down to energy Δ (determined by the dimensions of the detector cavity), at depth '*z*' respectively. $\left(p_{\Phi}\right)_{\text{det}}^{\text{med}}$ is a function of the medium and detector materials as well as field size FS ,beam quality *Q* and depth '*z*'.

The dose to the medium $D(z)_{\text{med}}$ at a specified position, z, can therefore be written

$$D(z)_{\text{med}} = \overline{D}_{\text{det}} \times s_{\text{med,det},\Delta}^{\text{SA}} \times \left(p_{\Phi}\right)_{\text{det}}^{\text{med}} \tag{6.2}$$

where $s_{\text{med,det},\Delta}^{\text{SA}}$ is the Spencer-Attix, or restricted mass stopping-power ratio, medium-to-detector, for a cut-off energy Δ, appropriate for the dimensions of the detector cavity, and $\overline{D}_{\text{det}}$ is the average dose over the sensitive volume of the detector. It should be noted that the Spencer-Attix ratio, which is the most accurate formulation of the Bragg-Gray principle (Spencer and Attix 1955; Nahum 1978; Nahum 2007b), involves the *total* electron (+ positron) fluence and a perturbation factor defined in terms of total fluence, i.e. equation (6.1), is consistent with this. For a water medium this becomes

$$\frac{D(z)_{\text{w}}}{\overline{D}_{\text{det}}} = s_{\text{w,det},\Delta}^{\text{SA}} \times \left(p_{\Phi}\right)_{\text{det}}^{\text{w}} \tag{6.3}$$

The implicit assumption in the above is that the electron fluences in the detector and water differ in magnitude but that the energy *distribution* is not affected i.e. the spectra have identical 'shapes'; this assumption is investigated later in this chapter.

Alfonso *et al* (2008) defined the output correction factor $k_{Q_{\text{msr}},Q}^{f_{\text{msr}},f_{\text{ref}}}$ accounting for the difference between the responses of an ionization chamber in conventional reference field (f_{ref}) and machine-specific reference field (f_{msr}). Benmakhlouf *et al* (2014, 2015) and Underwood *et al* (2013b, 2015) expressed this composite *k*-factor as

$$k_{Q_{\text{clin}},Q_{\text{msr}}}^{f_{\text{clin}},f_{\text{msr}}} = \frac{D_{\text{w},Q_{\text{clin}}}^{f_{\text{clin}}} \Big/ M_{Q_{\text{clin}}}^{f_{\text{clin}}}}{D_{\text{w},Q_{\text{msr}}}^{f_{\text{msr}}} \Big/ M_{Q_{\text{msr}}}^{f_{\text{msr}}}} \tag{6.4}$$

where $D_{\mathrm{w},Q_x}^{f_x}$ is the dose to water at a point in the centre of a field of size 'x' and beam quality Q_x, and $M_{Q_x}^{f_x}$ is the detector reading in a field of size 'x' ($x \in$ clin, msr). The subscript 'clin' refers to the clinical field size, and 'msr' refers to the machine-specific reference-field size. Following Bouchard *et al* (2009), but using the notation from this work, the composite k-factor can be written:

$$k_{Q_{\mathrm{clin}},Q_{\mathrm{msr}}}^{f_{\mathrm{clin}},f_{\mathrm{msr}}} = \frac{\left[\left(D_{\mathrm{w}} / \overline{D}_{\mathrm{det}}\right)_{\mathrm{MC}}\right]_{Q_{\mathrm{clin}}}}{\left[\left(D_{\mathrm{w}} / \overline{D}_{\mathrm{det}}\right)_{\mathrm{MC}}\right]_{Q_{\mathrm{msr}}}} \tag{6.5}$$

where the subscript MC refers to Monte-Carlo derived dose ratios. It follows from equation (6.3) that

$$k_{Q_{\mathrm{clin}},Q_{\mathrm{msr}}}^{f_{\mathrm{clin}},f_{\mathrm{msr}}} = \frac{\left[s_{\mathrm{w,det},\Delta}^{\mathrm{SA}} \times \left(p_{\Phi}\right)_{\mathrm{det}}^{\mathrm{w}}\right]_{Q_{\mathrm{clin}}}}{\left[s_{\mathrm{w,det},\Delta}^{\mathrm{SA}} \times \left(p_{\Phi}\right)_{\mathrm{det}}^{\mathrm{w}}\right]_{Q_{\mathrm{msr}}}} \tag{6.6}$$

assuming again that the electron fluence spectra in the detector and water volume have identical shapes (see sub-section 6.3.5).

6.3 Materials and methods

6.3.1 Monte Carlo modelling of linear accelerator geometry and detector response

The EGSnrc Monte-Carlo code (Kawrakow 2000a, Kawrakow *et al* 2011) has been shown to be accurate within 0.1% with respect to its own cross sections for relative ionization chamber response calculations; this is known as the Fano test (Kawrakow 2000b). Buckley *et al* (2003) showed that EGSnrc-derived values of thick-walled ionization chamber response differed from Spencer-Attix cavity theory (Spencer and Attix 1955) by 0.15% and 0.01% for graphite and aluminum walled thimble chambers, respectively. Verhaegen (2002, 2003) confirmed the accuracy of the EGSnrc system for near-to-interface dosimetry and also demonstrated that a detailed model of the ion chamber geometry is essential for obtaining good agreement with experimental results.

Monte-Carlo techniques have been previously used to study small-field physics for photon beams of nominal energy 15 MV (Scott *et al* 2008, 2009, 2012; Fenwick *et al* 2013) generated by a Varian 2100C linear accelerator, and beams of nominal energy 6 MV (Underwood *et al* 2013a, 2013b, 2013c) generated by a Varian 2100 iX linear accelerator (Varian Medical Systems, Palo Alto, CA). A Monte-Carlo model of both accelerators used here was constructed in the BEAMnrc system (Rogers *et al* 1995, 2011a), setting physical machine dimensions to values provided by Varian Medical Systems and achieving good agreement between calculated and measured dose-distributions (within 2%) through careful selection of user-defined model parameters (table 6.1). The phase-space files, generated for previously published studies e.g. Scott *et al* (2009) and Underwood *et al* (2013a), were scored at a distance of 58 cm and 100 cm from the source for the 15 MV and 6 MV Monte-Carlo beam models respectively, and were subsequently used as input for EGSnrc user-codes DOSRZnrc, FLURZnrc and CAVRZnrc (all version: V4-2.3.2) using the 'source 21' option (Rogers *et al* 2011b).

Table 6.1: **The user-defined model parameters for Monte-Carlo model of a Varian 2100 iX linear accelerator (Varian Medical Systems, Palo Alto, CA) and Varian 2100C linear accelerator for 6 MV and 15 MV photon beams respectively.**

	User defined model parameters		
Beam quality	Incident electron beam energy (MeV)	Electron source angle γ [10]	Focal spot size (FWHM)[11]
6 MV	6.0	1.5°	0.95 mm
15 MV	14.8	0°	0.70 mm

The simulations with these user-codes employed the default settings, which include modelling the Compton interaction for bound electrons, the effect of any atomic relaxation events, and relativistic spin effects in the multiple scattering of charged particles. In addition to these default settings, cross sections for the sampling of bremsstrahlung photon energies from the NIST database (Hubbell and Seltzer 2004) and photon interaction cross sections from the XCOM database were used (Berger *et al* 2010). A PEGS4 datafile (Nelson *et al* 1985, Kawrakow *et al* 2011) was generated with the EGSnrcMP package (Kawrakow *et al* 2006) with parameters AP = 1 keV, AE = 512 keV (total energy) where AP and AE are the production thresholds for secondary bremsstrahlung photons and knock-on electrons respectively. Electrons and positrons were followed down to 1 keV kinetic energy (i.e. the electron/positron kinetic energy cut-off *ECUT* = 512 keV) and photons down to 1 keV (photon energy cut-off *PCUT* = 1 keV).

6.3.2 Output factor in terms of both kerma and dose

Generally the 'output factor' is defined in terms of absorbed dose (Khan 2010). An output factor has also been calculated in terms of (water) kerma in order to separate the effects of source occlusion, which affects photon fluence, from electron disequilibrium which affects dose but not kerma.

Dose and kerma were computed using the DOSRZnrc user-code for photon beams with square field sizes ranging from 0.25 × 0.25 to 10 × 10 cm^2 in a water medium for the beam qualities

[10] γ is the half angle of the cone in degree (Rogers *et al* 2011a)

[11] FWHM-Full-width-half-maximum

of 6 MV and 15 MV using clinical linac spectra (for point source geometry- PSG) from Mohan *et al* (1985), which are included in the EGSnrc package, and phase-space files generated for these field sizes for *full linac geometry* (FLG) for the 6 MV and 15 MV qualities (see above). The 'source 1' option and 'source 21' option were used to compute the dose and kerma for each field size using the DOSRZnrc user-code, with *ECUT* and *PCUT* given in sub-section 6.3.1.

The scoring volume was a 'point like' water cylinder with a circular cross-section of 0.5 mm diameter and 0.5 mm height (to minimize the volume-averaging effect) located on the central axis of the beam at 10 cm depth in a cylindrical water phantom (15 cm radius, 30 cm thickness) to ensure sufficient depth beyond the depth of maximum dose (d_{max}) for the absorbed dose and kerma curves to become parallel to each other (Attix 1986, Kumar *et al* 2015a). The source to phantom surface distance (SSD) was 100 cm. In the case of PSG, the beam radius equivalent to each square field size (Day and Aird 1996) of the phase-spaces (i.e. 0.25×0.25 to 10×10 cm^2) was defined at the phantom surface.

Output factors[12] in terms of kerma and absorbed dose, *OF*(kerma) and *OF*(dose), were calculated as ratios of either central-axis water kerma, K_w, or dose, D_w, respectively at 10 cm depth in a field of size *FS* to that at the reference field size FS_{ref} for PSG and FLG for both beam qualities (6 MV and 15 MV). The reference field size FS_{ref} was taken as 3×3 cm^2 at 6 MV and 10×10 cm^2 at 15 MV.

6.3.3 Comparison of MC-derived dose to water with 'BG dose to water' for SCDDo, PTW diamond and PinPoint 3*D* detectors

Here the work was focused on three simulation geometries corresponding approximately to the air cavity of a 'PinPoint 3D' ionization chamber (Model 31016, PTW, Freiburg, Germany), a diamond detector (Model 60003, PTW, Freiburg, Germany) and a Single Crystal Diamond Dosimeter (SCDDo) (Marsolat *et al* 2013a, 2013b, Górka *et al* 2006). SCDDo is an 'Element Six' electronic grade, synthetic single-crystal diamond grown by a process of chemical vapour deposition (CVD). The 0.26 mm thickness of the thin cylindrical active volume of the PTW 60003 diamond was modelled exactly while the domed active volume of the PinPoint 3D ionization chamber (maximum height 2.9 mm) was represented by a disc of uniform thickness 2 mm (table 6.2). This results in a modelled air cavity with a volume equal to half that of the PinPoint 3D chamber. Crop *et al* 2009 found that the central electrode of the PinPoint 3D ionization chamber, which is not modelled here, minimally perturbs the dose in the air cavity. The cuboidal sensitive volume of the real SCDDo detector (Marsolat et al 2013a) was modelled as a cylinder with the same thickness (0.0165 cm) and

[12] The Output Factor, also known as field output factor (FOF) or total scatter factor, is often written as the product of two independent effects: collimator (or head) scatter factor (S_c) and phantom scatter factor (S_p) i.e. $FOF = S_c \times S_p$ (Khan 2010).

cross-sectional area (radius 0.0564 cm) (table 6.2) in order to meet the geometrical constraints of the 'RZ user codes' (i.e. CAVRZnrc, FLURZnrc) of the EGSnrc Monte-Carlo code system.

Table 6.2: **Detector details as modelled in the MC simulations. The physical active volume of the PTW 60003 diamond detector is a thin wafer, while the SCDDo detector is a synthetic single crystal diamond dosimeter with tiny cuboidal dimensions and the PTW 31016 PinPoint 3D ion chamber is a cylinder with a domed end. The volumes were all modelled as cylinders.**

Detector name	Material simulated	Density (g cm^{-3})	Diameter or width (cm)	Modelled diameter (cm)	Maximum thickness/ height (cm)	Modelled thickness / height (cm)
PTW diamond (PTW 60003)	Carbon	3.5	0.300	0.230	0.026	0.026
PinPoint 3D ionization chamber (PTW 31016)	air	1.205×10^{-3}	0.290	0.230	0.290	0.200
SCDDo	carbon	3.5	0.113	0.113	0.0165	0.0165

As mentioned above, the radiation interaction cross sections and stopping powers of the selected materials required by the EGSnrc system are stored in a PEGS4 datafile; although graphite is included, diamond (i.e. carbon) with a density of 3.5 g cm^{-3} was not available in the default version and so had to be generated independently for both types of diamond detectors. Firstly a density-effect correction file was generated to account for the density (aka polarisation) effect in the denser form of carbon using the *ESTAR* code/program available on the NIST website[13]. This was then combined with the EGSnrcMP package to generate a PEGS4 datafile, setting the parameters AP=1 keV, AE=512 keV. Note that the EGSnrc Monte Carlo code uses the *ESTAR* code to obtain the density-effect correction to the mass restricted electronic stopping power. Hence there is consistency between our prepared density-effect correction file and the file that the EGSnrc system uses routinely.

The different detector voxels mentioned above (table 6.2) comprising a single volume (voxel) of sensitive material, surrounded by unit density water, were located at 5 cm depth along the central axis of the beam in a cylindrical water phantom (15 cm radius, 30 cm thickness) with an SSD of 100 cm. The 'source 1' option and 'source 21' option as mentioned in sub-section 6.3.2 were again used here to compute the dose to detector using the CAVRZnrc user-code (Rogers *et al* 2011b) for field sizes ranging from 0.25 × 0.25 cm^2 to 10 × 10 cm^2 (for 15 MV FLG and PSG) and 0.25 × 0.25 cm^2 to 3 × 3 cm^2 (for 6 MV FLG and PSG). The dose to water was scored in a 'point like' water voxel

[13] http://physics.nist.gov/PhysRefData/Star/Text/ESTAR.html

(0.5 mm diameter, 0.5 mm thickness) to minimize volume-averaging effects as these are significant for the FL geometry.

The Spencer-Attix mass electronic stopping-power ratio, water to detector material, for energy cut-off Δ, $s^{\mathrm{SA}}_{\mathrm{w,det},\Delta}$, was computed from the total electron fluence at 5 cm depth in the unperturbed medium (i.e. water). This was done with the SPRRZnrc user-code (Rogers *et al* 2011b) for both beam qualities (6 MV and 15 MV) and both source geometries (FLG and PSG) for the above-mentioned field sizes; further, the same PEGS4 datafiles were used as with the CAVRZnrc computation of the dose to the detector. SPRRZnrc calculates restricted stopping power ratios using an 'on the fly' technique in the volume of interest (Kosunen and Rogers 1993). The track-end term was evaluated following Nahum (1978). The cut-off energies Δ of 10 keV, 258 keV and 320 keV have been chosen for the PinPoint 3D, SCDDo and diamond (PTW 60003) cavities respectively, following Fenwick *et al* (2013). The dose to the sensitive volume of each detector, $\overline{D}_{\mathrm{det}}$, was computed using CAVRZnrc (for each field size); this detector dose was then multiplied by $s^{\mathrm{SA}}_{\mathrm{w,det},\Delta}$ to yield the quantity defined here as '*BG dose to water*' for both beam qualities (6 MV and 15 MV) and both source geometries, for field sizes ranging from 0.25 × 0.25 cm^2 to 3 × 3 cm^2 and to 10 × 10 cm^2 respectively.

6.3.4 Total electron (+ positron) fluence spectra in water and detector cavities and the computation of $\left(p_{\Phi}\right)^{\mathrm{w}}_{\mathrm{det}}$

The total electron (+ positron) fluence spectra per MeV per unit incident photon fluence down to 1 keV have been computed using the FLURZnrc user-code, with the same *ECUT* and *PCUT* as above, for PSG and FLG sources of 6 MV and 15 MV, for field sizes ranging from 0.25 × 0.25 cm^2 to 10 × 10 cm^2. These fluence spectra have been scored in the following volumes: a 'point like' water cavity (0.5 mm diameter, 0.5 mm thickness), a 'PinPoint 3D' air cavity and a *single crystal* diamond dosimeter volume (SCDDo) located at 5 cm depth on the beam central axis in a cylindrical water phantom with SSD = 100 cm as described above.

In order to obtain high energy resolution of the fluence spectra at very low energies, energy-bin widths were set at 1 keV for the lowest energy bin (1 keV – 2 keV), then 2 keV for the next 2 bins and then gradually increased until the electron energy was 10 keV, and thereafter kept at 5 keV. The electron (+ positron) fluence, per unit incident photon fluence, obtained directly from FLURZnrc was verified by integrating over the fluence differential in energy, i.e. $\int_{\Delta}^{E_{\max}} \left[\Phi^{\mathrm{tot}}_{E}(z)\right]_{\mathrm{w}} \mathrm{d}E$. The *electron* *fluence perturbation correction factors*, water-to-air, $\left(p_{\Phi}\right)_{\mathrm{air}}^{\mathrm{w}}$, and water-to-SCDDo, $\left(p_{\Phi}\right)_{\mathrm{SCDDo}}^{\mathrm{w}}$, were computed from equation (6.1) for both beam energies and the full range of field sizes.

6.3.5 Comparison of the MC-derived dose ratio with the product of $s_{\mathrm{med,det},\Delta}^{\mathrm{SA}}$ and $\left(p_{\Phi}\right)_{\mathrm{det}}^{\mathrm{w}}$

As discussed in section 6.2, the fluence in the detector may differ from that in the uniform medium not only in magnitude but also in the shape of its energy distribution. This shape 'distortion' may cause the MC-derived dose ratio to differ from the dose ratio derived from cavity theory, given by equation (6.3); these differences are quantified here. The ratio of dose-to-water to dose-to-detector, $\left(D_{\mathrm{w}} / \overline{D}_{\mathrm{det}}\right)_{\mathrm{MC}}$, was computed with user-code CAVRZnrc for the detectors, geometry, field sizes and beam qualities mentioned in sub-section 6.3.3. The mass restricted electronic stopping-power ratio, water to detector material, $s_{\mathrm{med,det},\Delta}^{\mathrm{SA}}$, and the electron fluence perturbation correction factor, water to detector material, $\left(p_{\Phi}\right)_{\mathrm{det}}^{\mathrm{w}}$, were computed as described above from user-codes SPRZnrc and FLURZnrc respectively. These computations were carried out for field sizes ranging from 0.25 × 0.25 cm^2 to 3 × 3 cm^2 and to 10 × 10 cm^2 for 6 MV and 15 MV respectively, for PSG and FLG sources.

6.3.6 Maximum dimensions of perturbation-limited 'Bragg-Gray' detector

Following Nahum (1996) a detector is considered to be 'Bragg-Gray' if the electron (+ positron) fluence perturbation is within 5% of unity. The size of ionization chamber and diamond detector fulfilling this 5% condition has been determined at the two smallest field sizes (0.5 × 0.5 cm^2 and 0.25 × 0.25 cm^2). The response of an air cavity with radius = 0.0564 cm, equal to half of radius of the modelled 'PinPoint 3D-chamber-like' air cavity, and a diamond cavity with radius equal to the radius of the SCDDo, were simulated with the thickness/height varied incrementally. These cavities were placed at 5 cm depth on the beam central axis in a cylindrical water phantom (15 cm radius, 30 cm thickness) at 100 cm SSD. The total electron (+ positron) fluence spectra down to 1 keV (per MeV per unit incident photon fluence) for field sizes 0.25 × 0.25 cm^2 to 0.5 × 0.5 cm^2 was computed using FLURZnrc, with 'source 21', and with the same *ECUT* and *PCUT* as above for the 6 MV and 15 MV FLG sources. The electron fluence perturbation correction factors, water-to-air, $\left(p_{\Phi}\right)_{\mathrm{air}}^{\mathrm{w}}$, and water-to-diamond, $\left(p_{\Phi}\right)_{\mathrm{SCDDo}}^{\mathrm{w}}$, were computed from equation (6.1) for both field sizes. The thickness/height of the modelled cavities were successively adjusted until the above perturbation factors equalled 1.05 and 0.95 respectively.

(a)

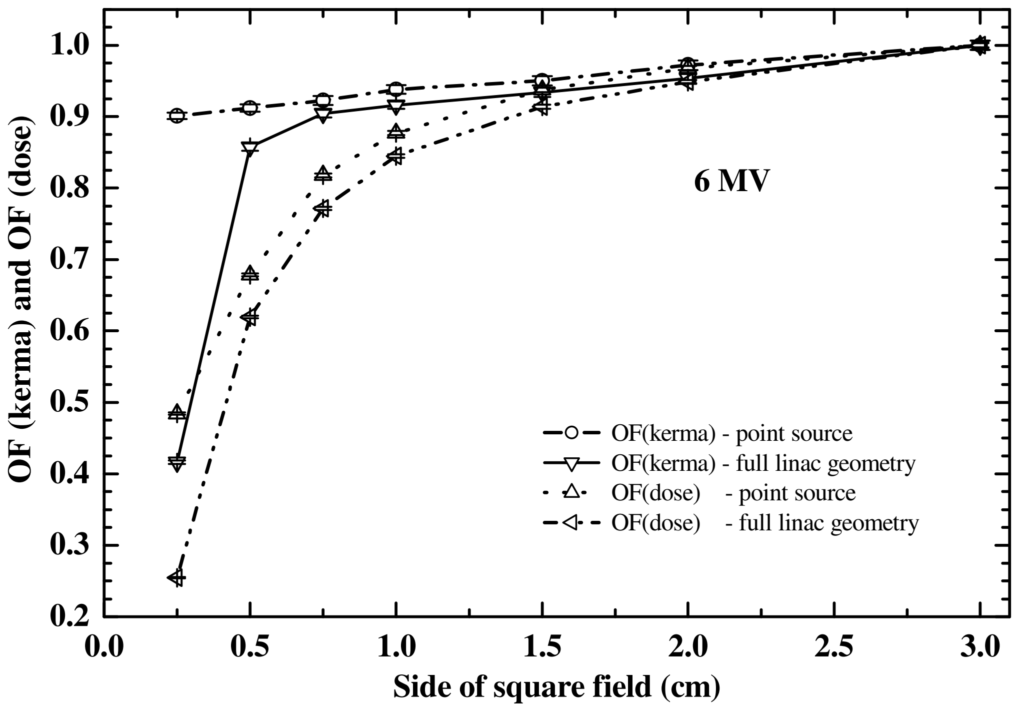

(b)

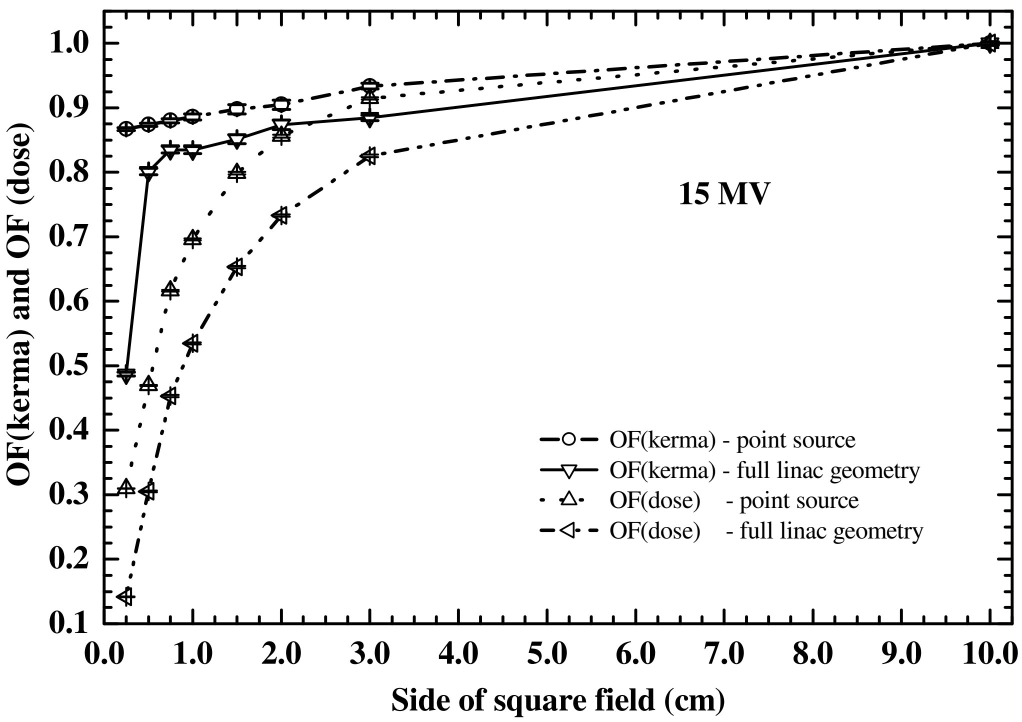

Figure 6.1: **(a) 6 MV photon beams, FLG and PSG: the output factor in term of kerma , *OF*(kerma), and absorbed dose, *OF*(dose), on the beam central axis at 10 cm depth in a cylindrical water phantom versus field size defined at 100 cm SSD; side lengths of square fields are 0.25 cm, 0.5 cm, 0.75 cm, 1 cm, 1.5 cm, 2 cm and 3 cm respectively; the error bars (masked by the symbols) are ± 2 standard deviations and correspond to statistical (Type A) uncertainties. (b) 15 MV photon beams, FLG and PSG: the output factor in term of kerma , *OF*(kerma), and absorbed dose, *OF*(dose), on the beam central axis at 10 cm depth in a cylindrical water phantom versus field size defined at 100 cm SSD; side lengths of square fields are 0.25 cm, 0.5 cm, 0.75 cm, 1 cm, 1.5 cm, 2 cm, 3 cm and 10 cm respectively; the error bars (masked by the symbols) are ± 2 standard deviations and correspond to statistical (Type A) uncertainties.**

6.4 Results and Discussion

6.4.1 Output factor in terms of both kerma and dose

Figures 6.1(a)-(b) show the output factor in terms of kerma, *OF*(kerma), and absorbed dose, *OF*(dose), along the central axis for field sizes ranging from 0.25 × 0.25 cm^2 to 10 × 10 cm^2 at 10 cm depth in water for PSG and FLG for both beam qualities (6 MV and 15 MV). The dramatic decrease in *OF*(kerma) between field sizes 0.5 × 0.5 cm^2 and 0.25 × 0.25 cm^2 for the full-linac geometry at both qualities must be due to source occlusion as this decrease is completely absent for the point source geometry, where source occlusion is not applicable. Turning now to the *OF*(dose) curves, as the field size drops below that necessary for electronic equilibrium, a decrease is clearly seen in the PSG case. For FL geometry, electron disequilibrium (Attix 1986, Kumar *et al* 2015a) combines with source occlusion to produce the greatest decrease in *OF*(dose) with field size.

(a)

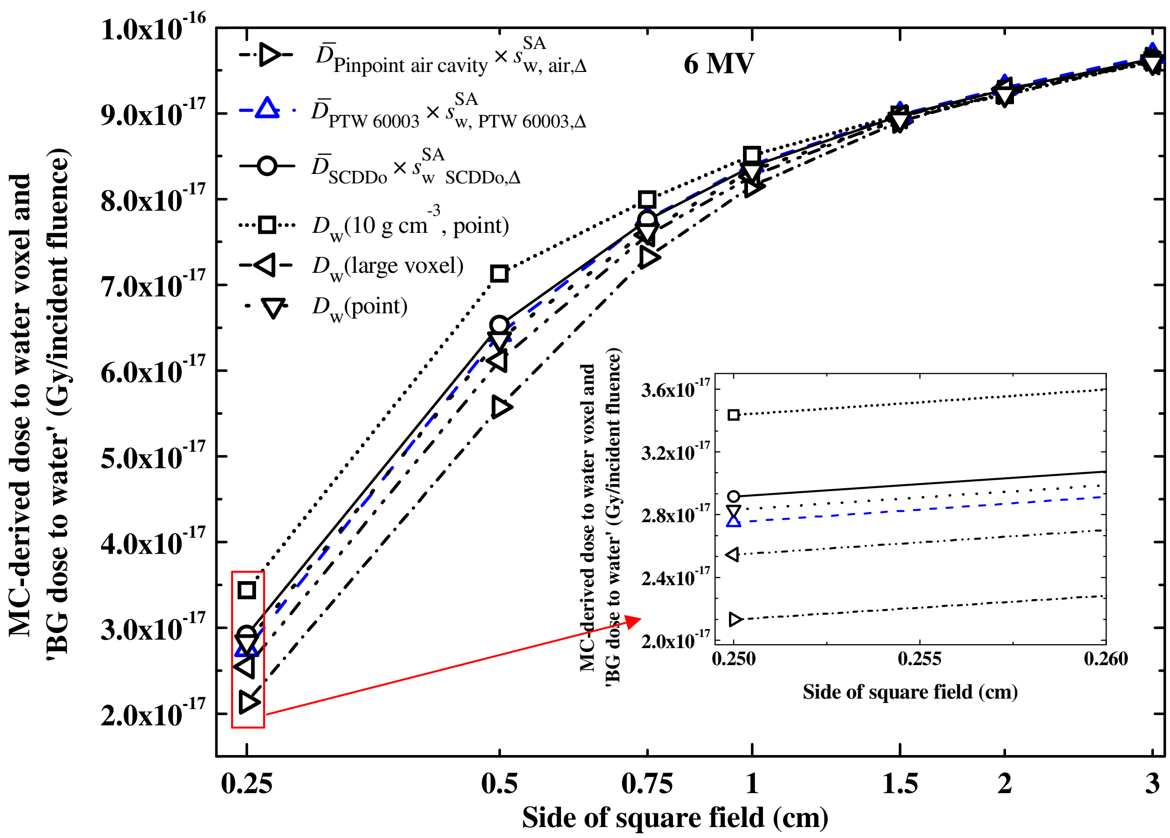

(b)

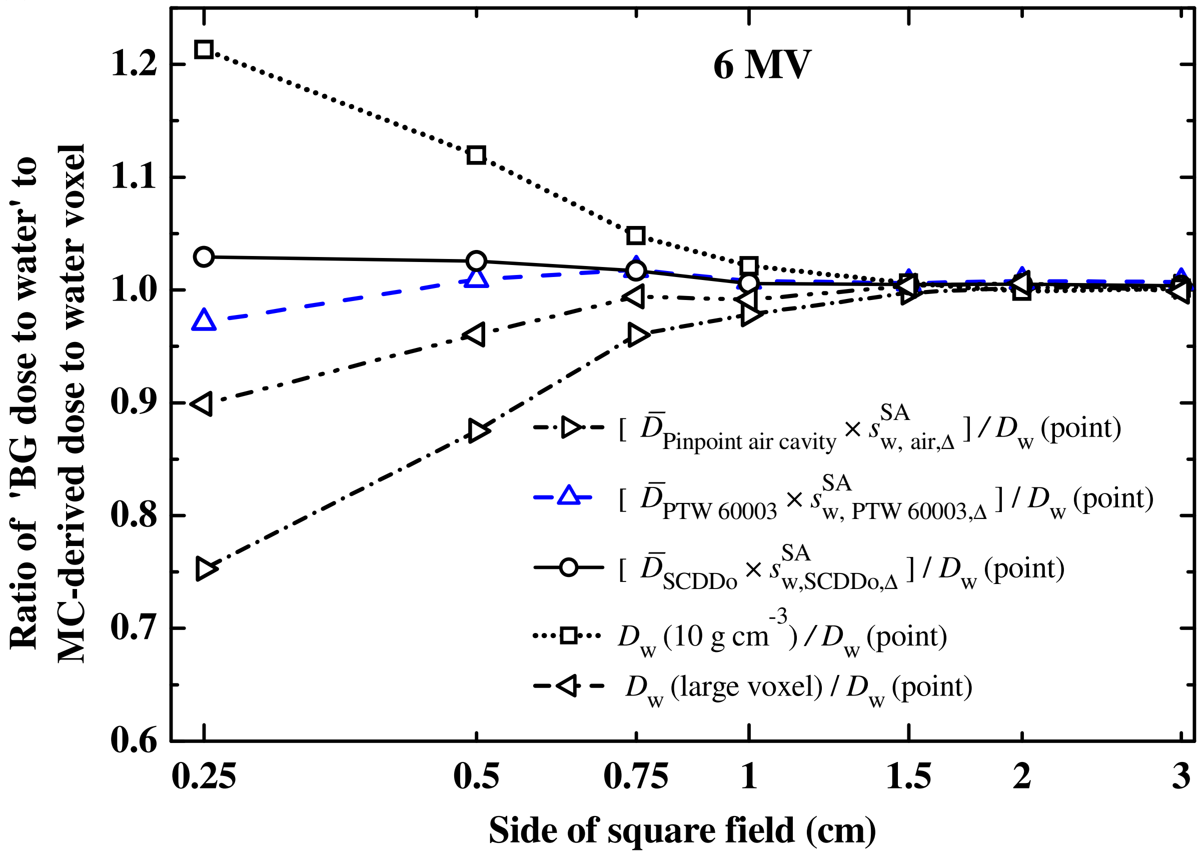

Figure 6.2: **(a) 6 MV photon beams, FLG: comparison of MC-derived dose to water voxel with 'BG dose to water' obtained for SCDDo, PTW diamond and PinPoint 3D detectors, characterized as isolated voxels of material surrounded by water, on the beam central axis at 5 cm depth in a cylindrical water phantom, as a function of field size defined at 100 cm SSD; side lengths of square fields are 0.25 cm, 0.5 cm, 0.75 cm, 1 cm, 1.5 cm, 2 cm and 3 cm. The dose to water (D_w) was scored in a 'point like' water voxel (0.5 mm diameter, 0.5 mm thickness) to minimize the volume averaging effects. The D_w (large voxel) was scored in a larger voxel (2.26 mm diameter, 0.26 mm thickness). The D_w (10 g cm^{-3}) is the dose to water scored again in a 'point like' water voxel (0.5 mm diameter, 0.5 mm thickness) of 'modified density water', with density ρ was set equal to 10 g cm^{-3} but with mass stopping power and mass energy-absorption coefficients equal to those of unit density water i.e. eliminating changes in mass stopping power caused by the density-dependent polarization effect. (b) 6 MV photon beams, FLG: ratio of 'BG dose to water' to water-voxel dose for SCDDo, PTW diamond and PinPoint 3D detectors; other details as for figure 6.2(a).**

6.4.2 Comparison of MC-derived dose to water with 'BG dose to water' for SCDDo, PTW diamond and PinPoint 3*D* detectors

Figures 6.2(a)-6.3(b) show the variation of Monte-Carlo calculated '*BG dose to water*' for the SCDDo, PTW diamond, and PinPoint 3D detectors, characterized as isolated voxels of material surrounded by water, as a function of field size defined at 100 cm SSD, at 5 cm depth on the central axis in a cylindrical water phantom for the FLG source geometry of the 6 MV and 15 MV beams; the side length of square fields are 0.25 cm, 0.5 cm, 0.75 cm, 1 cm, 1.5 cm, 2 cm, 3 cm and 10 cm respectively. It can be seen that even for a perfect water-equivalent detector, the size of the active volume affects the output recorded for very small fields i.e. signal averaging over the detector volume is important.

When the field width is too small for the establishment of lateral electronic equilibrium in the uniform medium, the dose in the sensitive volume of a detector, per unit dose to the uniform medium, depends critically on its density (Scott *et al* 2012). The '*BG dose to water*' at the smallest field sizes (0.25×0.25 cm^2) for the SCDDo is within 2.9% of the dose to water computed directly in the water voxel for FLG at 6 MV and 15 MV, thereby demonstrating that this detector exhibits quasi Bragg-Gray behaviour over a wide range of field sizes and beam qualities; in the case of the other detectors the ratio 'BG dose to water'/MC-derived dose to water deviates significantly from unity as the field size is reduced, as Figures 6.2(b) and 6.3(b) clearly indicate.

(a)

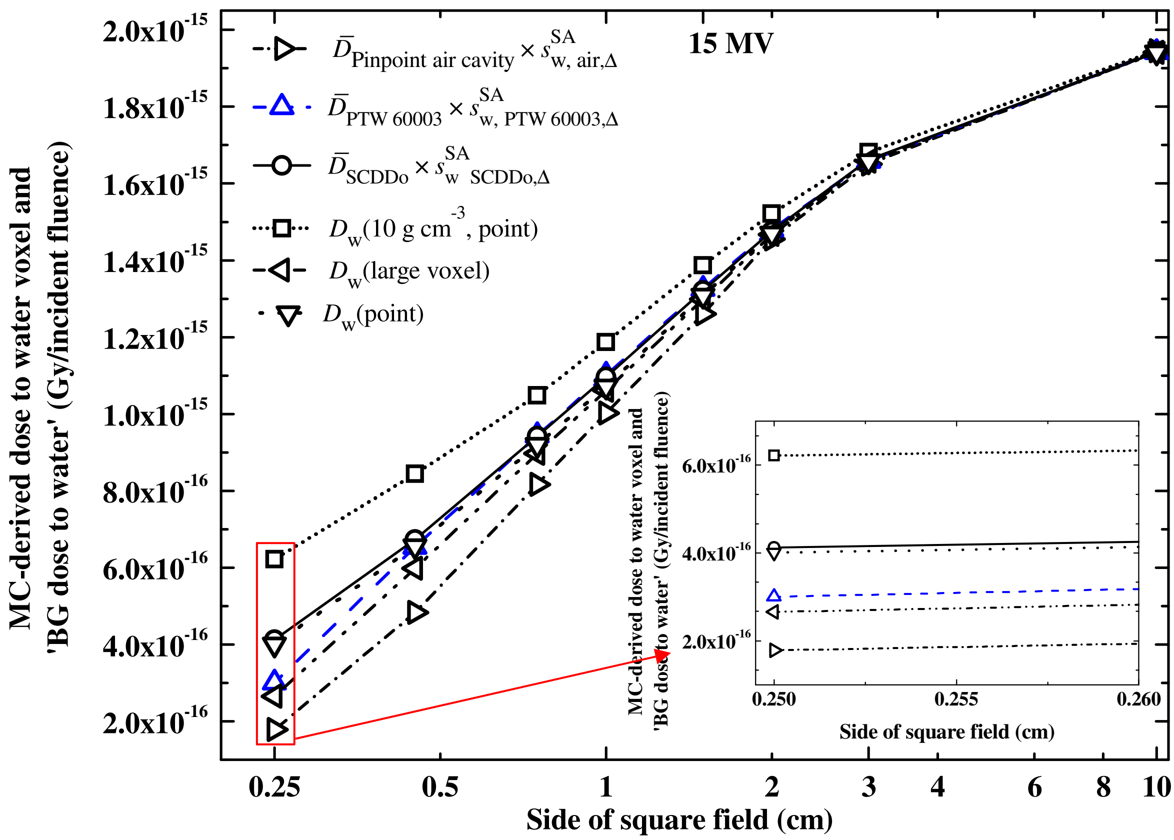

(b)

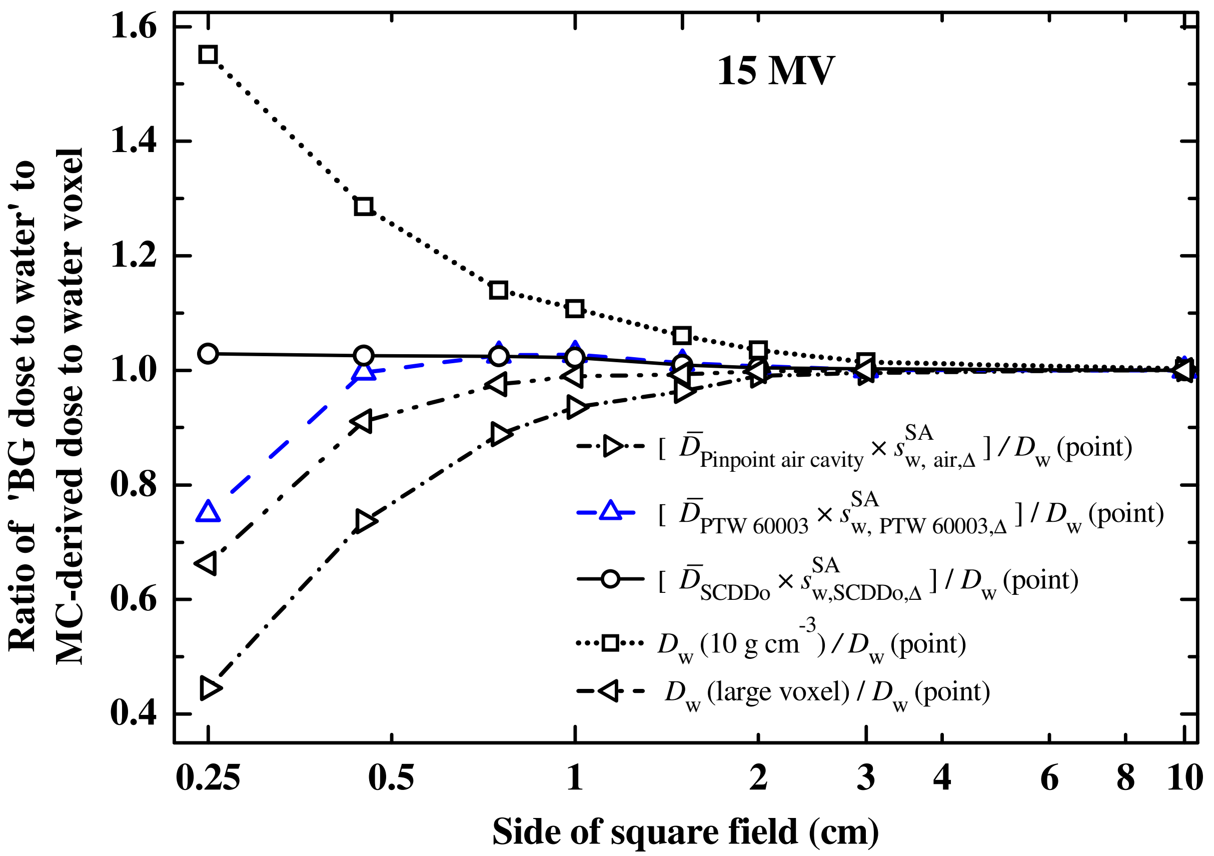

Figure 6.3: **(a) 15 MV photon beam, FLG: comparison of MC-derived dose to water voxel with 'BG dose to water' obtained for SCDDo, PTW60003 diamond and PinPoint 3D (air cavity), characterized as isolated voxels of material surrounded by water, on the beam central axis at 5 cm depth in a cylindrical water phantom, as a function of field size defined at 100 cm SSD; side lengths of square fields are 0.25 cm, 0.45 cm, 0.75 cm, 1 cm, 1.5 cm, 2 cm, 3 cm and 10 cm . For D_w and D_w (10 g cm^{-3}) see figure 6.2(a). (b) 15 MV photon beam, FLG: ratio of 'BG dose to water' to water voxel dose for SCDDo, PTW diamond and PinPoint 3D detectors; details as for figure 6.3(a).**

6.4.3 Total electron (+ positron) fluence spectra in water and in detector cavities and the evaluation of $\left(p_{\Phi}\right)^{\text{w}}_{\text{det}}$

6.4.3.1 Results from Monte-Carlo simulations

Figures 6.4(a), (b) (6 MV, FLG) and 6.5(a), (b) (15 MV, FLG) show explicitly the 'perturbation' of the (total) electron fluence spectrum in small, non-equilibrium photon fields. The dotted curves (corresponding to the 'PinPoint 3D-chamber-like' air cavity) lie significantly below the full curves (water), demonstrating that these air cavities violate the Bragg-Gray principle.

(a)

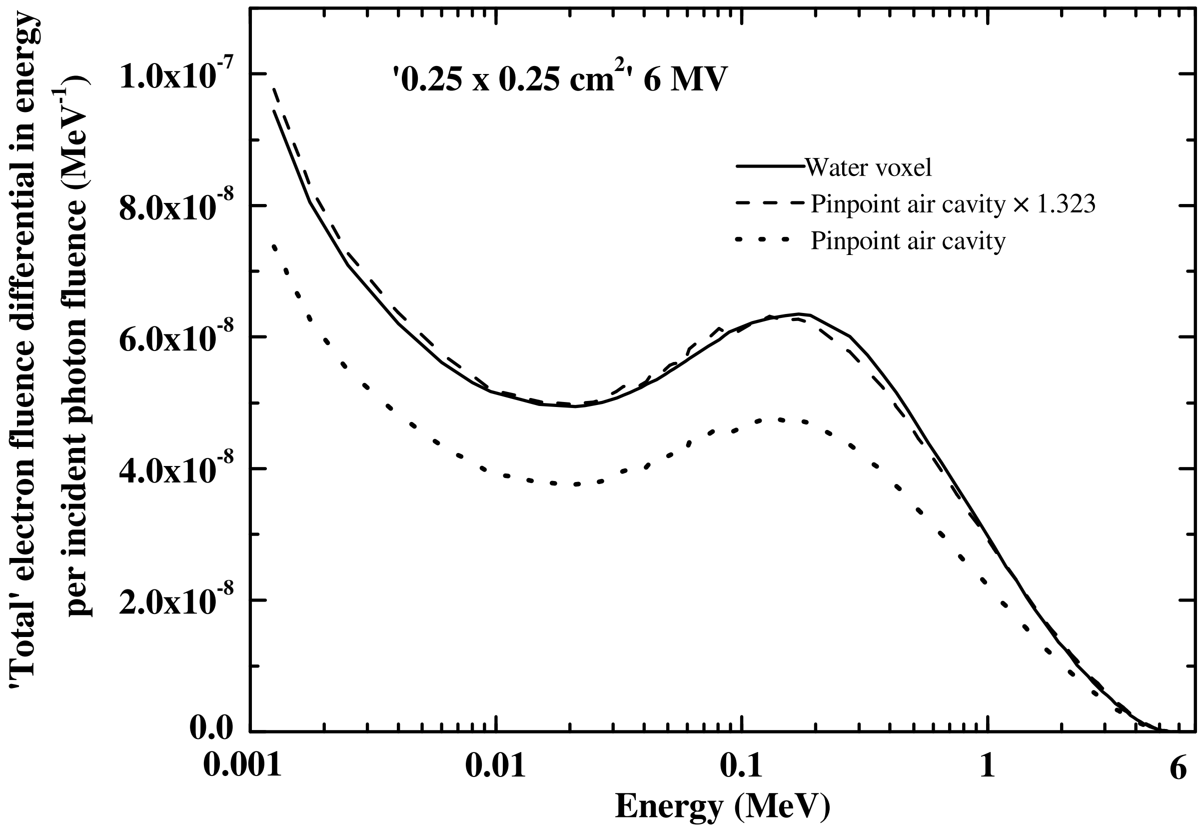
'0.25 x 0.25 cm^2' 6 MV
Water voxel
Pinpoint air cavity × 1.323
Pinpoint air cavity
'Total' electron fluence differential in energy per incident photon fluence (MeV^{-1})
1.0x10^{-7}
8.0x10^{-8}
6.0x10^{-8}
4.0x10^{-8}
2.0x10^{-8}
0.0
0.001
0.01
0.1
1
6
Energy (MeV)

(b)

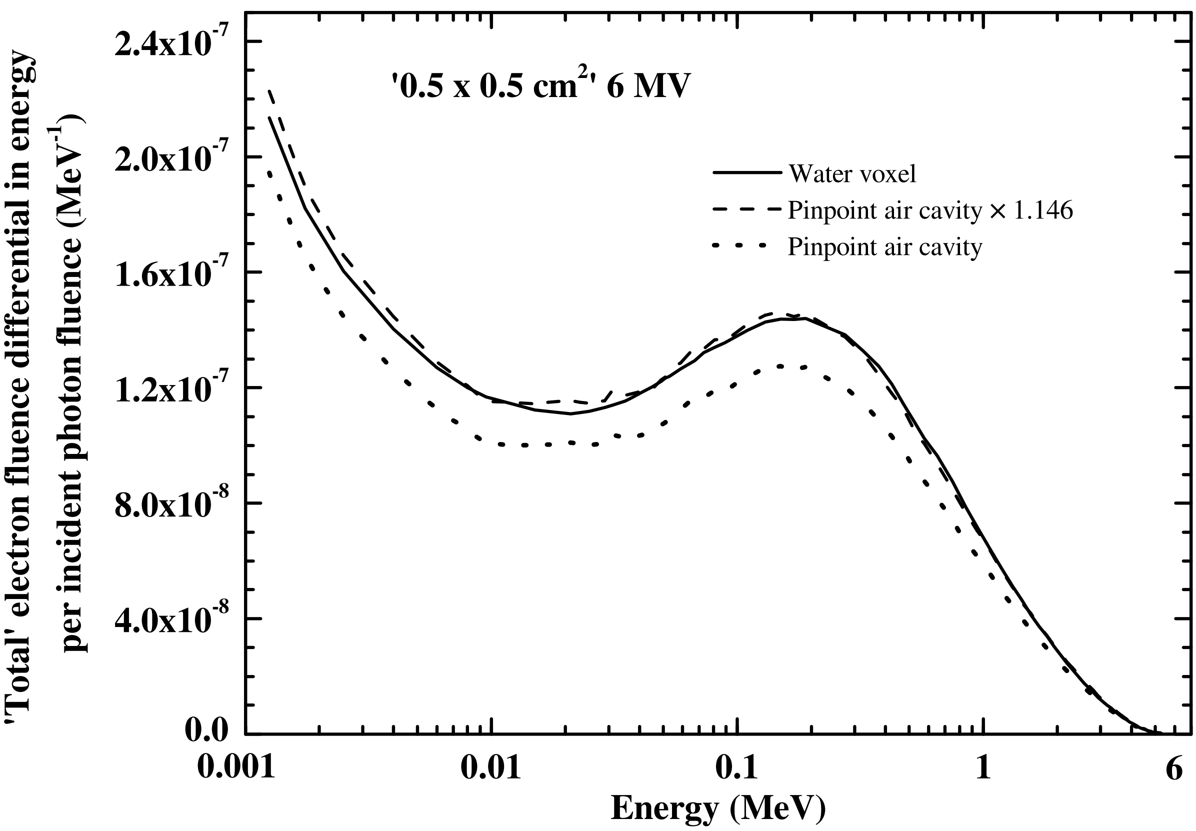
'0.5 x 0.5 cm^2' 6 MV
Water voxel
Pinpoint air cavity × 1.146
Pinpoint air cavity
'Total' electron fluence differential in energy per incident photon fluence (MeV^{-1})
2.4x10^{-7}
2.0x10^{-7}
1.6x10^{-7}
1.2x10^{-7}
8.0x10^{-8}
4.0x10^{-8}
0.0
0.001
0.01
0.1
1
6
Energy (MeV)

(c)

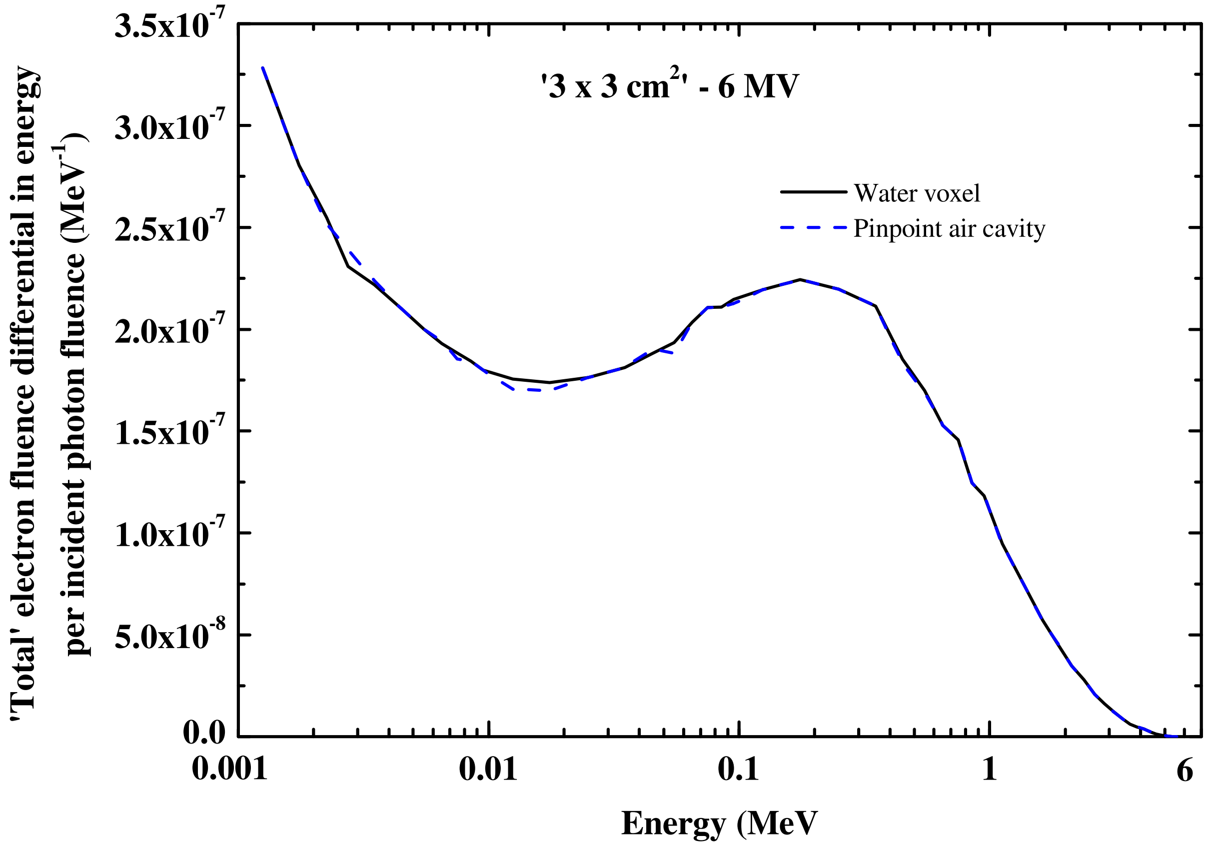

Figure 6.4: **(a) 6 MV photons, FLG, 0.25 × 0.25 cm^2 field size defined at 100 cm SSD: total electron fluence (per MeV per incident photon fluence) as a function of electron kinetic energy (MeV) scored in (i) a 'point like' water voxel (0.5 mm diameter, 0.5 mm thickness), (ii) a Pinpoint 3D air cavity, and (iii) the fluence in (ii) $\times\left(p_{\Phi}\right)^{\mathrm{w}}_{\mathrm{air}}$ (= 1.323); both scoring volumes positioned at 5 cm depth along the beam central axis in a water phantom. (b) 6 MV photons, FLG, 0.5 × 0.5 cm^2 field size defined at 100 cm SSD: total electron fluence (per MeV per incident photon fluence) as a function of electron kinetic energy (MeV) scored in (i) a 'point like' water voxel (0.5 mm diameter, 0.5 mm thickness), (ii) a Pinpoint 3D air cavity, and (iii) the fluence in ii) $\times\left(p_{\Phi}\right)^{\mathrm{w}}_{\mathrm{air}}$ (= 1.146); both scoring volumes positioned at 5 cm depth along the beam central axis in a water phantom. (c) 6 MV photons, FLG, 3 × 3 cm^2 field size defined at 100 cm SSD: total electron fluence (per MeV per incident photon fluence) as a function of electron kinetic energy (MeV) scored in (i) a 'point like' water voxel (0.5 mm diameter, 0.5 mm thickness), and ii) the Pinpoint 3D air cavity; both scoring volumes positioned at 5 cm depth along the beam central axis in a water phantom.**

The dashed curves result from multiplying the fluence (dotted curves) by the water-to-air perturbation factor, defined by equation (6.1). At 6 MV for the 0.25 × 0.25 cm^2 field, for which p = 1.323, this 'corrected' fluence is very close to the unperturbed 'water' fluence at all energies, thereby demonstrating a negligible change in 'shape'. At 15 MV, where p = 2.139, a significant difference between the 'water' and corrected 'PinPoint 3D-chamber-like' air cavity spectra can be observed, especially at low energies i.e. the air cavity perturbs not only the magnitude but also the shape of the electron fluence spectrum.

(a)

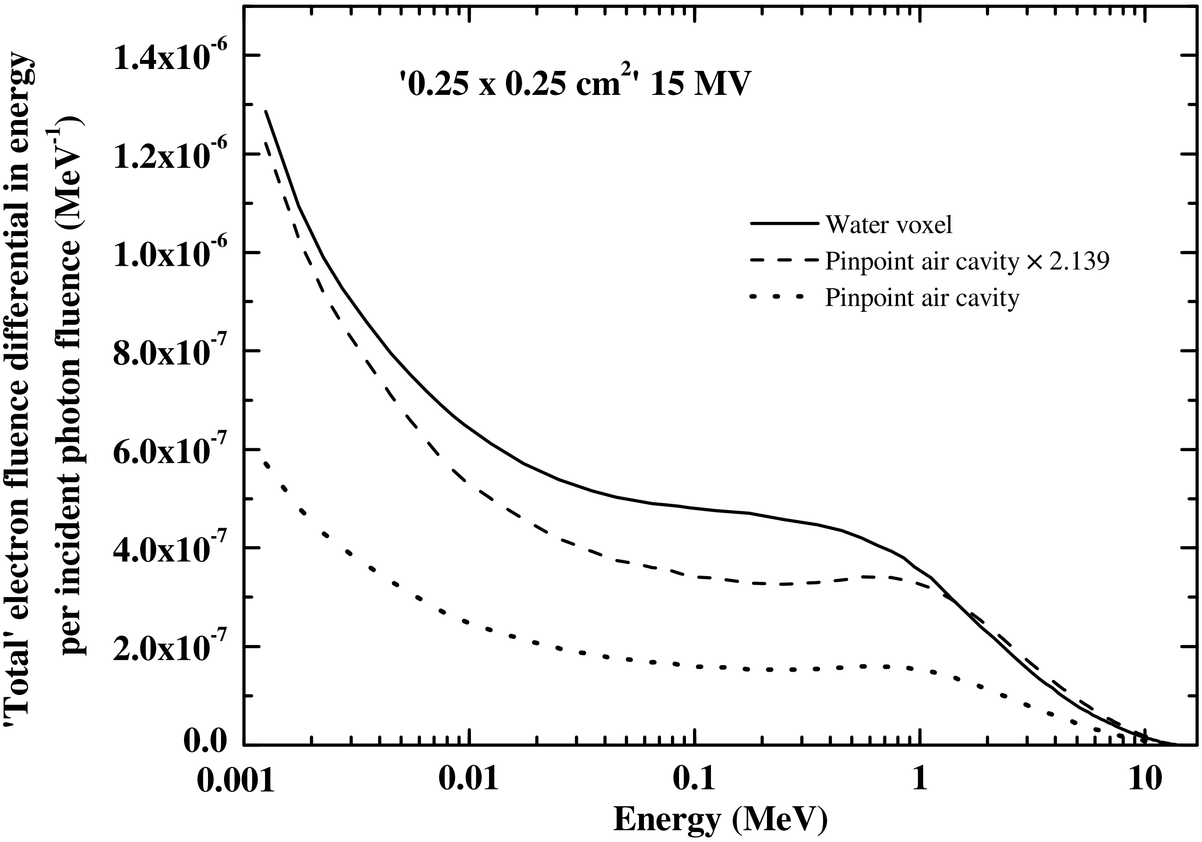
'0.25 x 0.25 cm²' 15 MV
Water voxel
Pinpoint air cavity × 2.139
Pinpoint air cavity
'Total' electron fluence differential in energy per incident photon fluence (MeV⁻¹)
1.4x10⁻⁶
1.2x10⁻⁶
1.0x10⁻⁶
8.0x10⁻⁷
6.0x10⁻⁷
4.0x10⁻⁷
2.0x10⁻⁷
0.0
0.001
0.01
0.1
1
10
Energy (MeV)

(b)

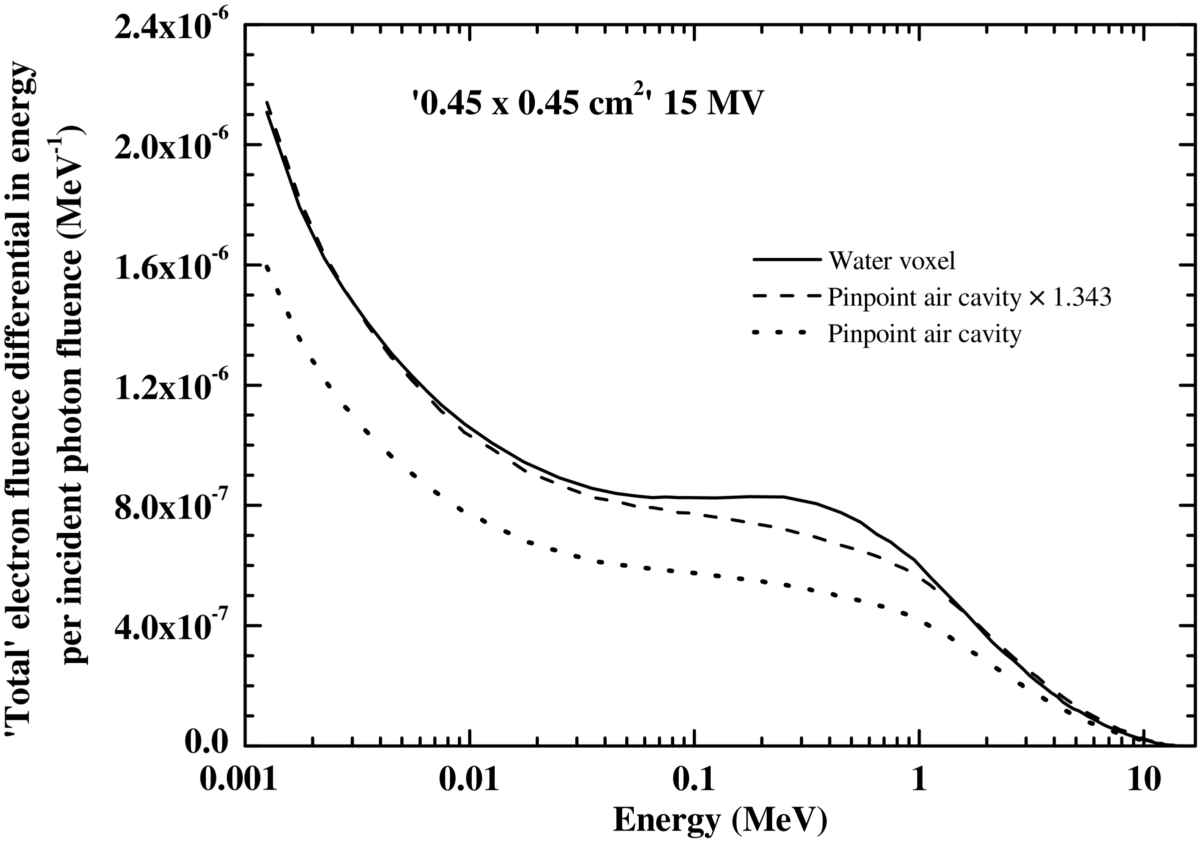
'0.45 x 0.45 cm²' 15 MV
Water voxel
Pinpoint air cavity × 1.343
Pinpoint air cavity
'Total' electron fluence differential in energy per incident photon fluence (MeV⁻¹)
2.4x10⁻⁶
2.0x10⁻⁶
1.6x10⁻⁶
1.2x10⁻⁶
8.0x10⁻⁷
4.0x10⁻⁷
0.0
0.001
0.01
0.1
1
10
Energy (MeV)

(c)

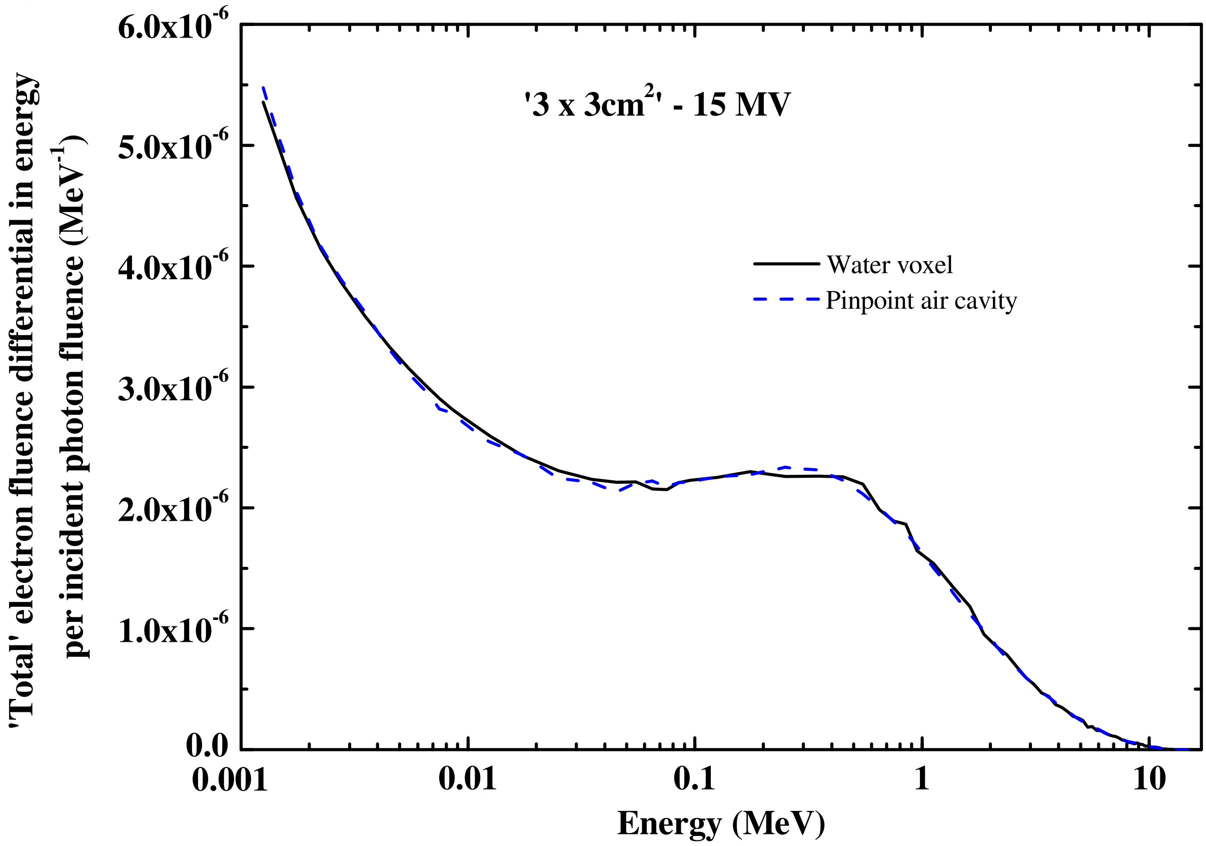

Figure 6.5: **(a) 15 MV photons, FLG: total electron fluence (per MeV per incident photon fluence) along the central axis for a 0.25 × 0.25 cm^2 field size defined at 100 cm source-to-phantom surface distance, as a function of electron kinetic energy (MeV), scored in (i) a 'point like' water voxel (0.5 mm diameter, 0.5 mm thickness), (ii) the PinPoint 3D air cavity, and (iii) the fluence in (ii) ×$\left(p_{\Phi}\right)^{\mathrm{w}}_{\mathrm{air}}$ (= 2.139); both scoring volumes positioned at 5 cm depth along the beam central axis in a water phantom. (b) 15 MV photons, FLG for 0.45 × 0.45 cm^2 field size defined at 100 cm SSD: total electron fluence (per MeV per incident photon fluence) as a function of electron kinetic energy (MeV) scored in (i) a 'point like' water voxel (0.5 mm diameter, 0.5 mm thickness), (ii) the PinPoint 3D air cavity, and (iii) the fluence in (ii) ×$\left(p_{\Phi}\right)^{\mathrm{w}}_{\mathrm{air}}$ (= 1.343); both scoring volumes positioned at 5 cm depth along the beam central axis in a water phantom. (c) 15 MV photons, FLG for a 3 × 3 cm^2 field size defined at 100 cm SSD: total electron fluence (per MeV per incident photon fluence) as a function of electron kinetic energy (MeV) scored in (i) a 'point like' water voxel (0.5 mm diameter, 0.5 mm thickness), and (ii) the PinPoint 3D air cavity; both scoring volumes positioned at 5 cm depth along the beam central axis in a water phantom.**

Note that the logarithmic energy scale over-emphasises the effect of differences between the fluence spectra at the lowest energies on the numerical value of the perturbation factor; the true width of the energy interval between 1 keV and 1 MeV is only equal to that between 1 and 2 MeV. In the interests of graphical clarity the fluence spectra in the SCDDo cavity have not been included; in almost all cases these were virtually indistinguishable from the spectra in the water voxel.

Table 6.4 shows that the water-to-SCCDo perturbation factors were always less than unity (within statistical uncertainties) with the lowest value being 0.957 ± 0.002 at 6 MV, point source geometry, in a 0.25 × 0.25 cm^2 field. Turning now to the larger field sizes (Figures 6.4(c), 6.5(c)), the 'total' electron (+ positron) fluence in these same air and water cavities cannot be separated, which is an explicit demonstration of the Bragg-Gray behaviour of these cavities.

Tables 6.3 and 6.4 present the MC-derived electron fluence perturbation correction factors, water-to-air, $\left(p_{\Phi}\right)_{\text{air}}^{\text{w}}$, and water-to-SCDDo, $\left(p_{\Phi}\right)_{\text{SCDDo}}^{\text{w}}$, versus field size defined at 100 cm SSD for both FLG and PSG source geometries for the 6 MV and 15 MV beam qualities. As expected, the perturbation factors approach unity as the field size increases. It can be noted that even at the very small field size of 0.25 × 0.25 cm^2 the perturbation factor for the SCDDo single-crystal diamond dosimeter is within 4% of unity. These results are consistent with recent studies of the small-field response of the PTW 60019 microDiamond detector in terms of [dose to the detector]/[dose to water] (Chalkley and Heyes 2014, Papaconstadopoulos *et al* 2014, Morales *et al* 2014, Benmakhlouf *et al* 2015); note, however, that the smallest field size simulated by any of these workers had a diameter of 4 mm.

Table 6.3: **6 MV and 15 MV photon beams, FLG and PSG: MC-derived total electron fluence perturbation correction factors for water-to-air, $\left(p_{\Phi}\right)_{\text{air}}^{\text{w}}$, versus field size defined at 100 cm SSD; side lengths of square fields are 0.25 cm, 0.5 cm, 0.75 cm, 1 cm, 1.5 cm, 2cm, 3 cm and 10 cm ; the statistical (Type A) uncertainties are ± 2 standard deviations. The standard uncertainty propagation method was used to derive the statistical (Type A) uncertainties.**

Field Size (cm × cm)	Total electron fluence perturbation correction factors, water-to-air			
	6 MV		15 MV	
	FLG	PSG	FLG	PSG
0.25 × 0.25	1.323 ± 0.003	1.292 ± 0.003	2.139 ± 0.008	1.346 ± 0.001
0.5 × 0.5[14]	1.146 ± 0.003	1.080 ± 0.003	1.343 ± 0.005	1.119 ± 0.001
0.75 × 0.75	1.046 ± 0.002	1.037 ± 0.002	1.165 ± 0.003	1.050 ± 0.001
1 × 1	1.017 ± 0.003	1.017 ± 0.003	1.083 ± 0.002	1.030 ± 0.002
1.5 × 1.5	1.005 ± 0.004	1.002 ± 0.004	1.029 ± 0.002	1.014 ± 0.002
2 × 2	1.003 ± 0.005	1.001 ± 0.004	1.001 ± 0.003	1.007 ± 0.003
3 × 3	1.001 ± 0.005	1.000 ± 0.004	1.000 ± 0.003	1.001 ± 0.003
10 × 10	--------	----------	1.000 ± 0.005	1.000 ± 0.004

[14] Everywhere in the tables for 15 MV the 0.5 × 0.5 cm^2 field size was actually equal to 0.45 × 0.45 cm^2.

Table 6.4: **6 MV and 15 MV photon beams, FLG and PSG: MC-derived total electron fluence perturbation correction factors, water-to-SCDDo, $\left(p_{\Phi}\right)^{\mathrm{w}}_{\mathrm{SCDDo}}$, versus field size defined at 100 cm SSD; side lengths of square fields were 0.25 cm, 0.5 cm, 0.75 cm, 1 cm, 1.5 cm, 2cm, 3 cm and 10 cm; the statistical (Type A) uncertainties are ± 2 standard deviations. The standard uncertainty propagation method was used to derive the statistical (Type A) uncertainties.**

Field Size (cm × cm)	Total electron fluence perturbation correction factors, water-to-SCDDo			
	6 MV		15 MV	
	FLG	PSG	FLG	PSG
0.25 × 0.25	0.968 ± 0.002	0.957 ± 0.002	0.963 ± 0.004	0.967 ± 0.001
0.5 × 0.5	0.979 ± 0.002	0.975 ± 0.003	0.965 ± 0.003	0.976 ± 0.001
0.75 × 0.75	0.983 ± 0.003	0.989 ± 0.002	0.973 ± 0.003	0.985 ± 0.001
1 × 1	0.985 ± 0.004	0.993 ± 0.004	0.979 ± 0.003	0.992 ± 0.002
1.5 × 1.5	1.000 ± 0.004	0.995 ± 0.004	0.992 ± 0.003	0.992 ± 0.003
2 × 2	1.002 ± 0.004	0.996 ± 0.004	0.993 ± 0.003	0.996 ± 0.003
3 × 3	1.001 ± 0.005	1.002 ± 0.006	0.995 ± 0.003	0.997 ± 0.004
10 × 10	----------	------------	0.997 ± 0.004	0.998 ± 0.005

Table 6.5: Comparison of MC-derived dose ratios, water-to-air, for the PinPoint 3D air cavity with MC-calculated output correction factor, $k^{f_{\mathrm{clin}},f_{\mathrm{msr}}}_{Q_{\mathrm{clin}},Q_{\mathrm{msr}}}$ from Benmakhlouf *et al* (2014) versus field size defined at 100 cm SSD. The uncertainties in the present work are ± 2 standard deviations. The standard uncertainty propagation method was used to derive the statistical (Type A) uncertainties.

Beam quality	Field Size (cm × cm)	$k^{f_{\mathrm{clin}},f_{\mathrm{msr}}}_{Q_{\mathrm{clin}},Q_{\mathrm{msr}}}$ (Benmakhlouf *et al* (2014))	$\dfrac{\left[\left(D_{\mathrm{w}}/\overline{D}_{\mathrm{det}}\right)_{\mathrm{MC}}\right]_{Q_{\mathrm{clin}}}}{\left[\left(D_{\mathrm{w}}/\overline{D}_{\mathrm{det}}\right)_{\mathrm{MC}}\right]_{Q_{\mathrm{msr}}}}$ (Present work)
6 MV, FLG	0.5 × 0.5	1.147	1.144 ± 0.006
	1 × 1	1.010	1.024 ± 0.007
	2 × 2	1.000	1.000 ± 0.005

Table 6.5 gives a comparison of $\left[\left(D_{\mathrm{w}} / \overline{D}_{\mathrm{det}}\right)_{\mathrm{MC}}\right]_{Q_{FS}} / \left[\left(D_{\mathrm{w}} / \overline{D}_{\mathrm{det}}\right)_{\mathrm{MC}}\right]_{Q_{ref}}$ for 'det' ≡ air for PTW 31016 'PinPoint 3D' air cavity from this work with the equivalent quantity $k_{Q_{\mathrm{clin}},Q_{\mathrm{msr}}}^{f_{\mathrm{clin}},f_{\mathrm{msr}}}$ derived by Benmakhlouf *et al* (2014), for square fields of side length 0.5 cm, 1 cm and 2 cm for 6 MV full (Varian Clinac) beam geometry. It should be noted that these authors employed a different Monte-Carlo code (PENELOPE) and modelled the PTW 31016 PinPoint 3D ionization chamber in full constructional detail. The excellent agreement between the two studies, despite employing different Monte-Carlo systems and detector geometries, lends considerable confidence to our numbers.

6.4.3.2 Explanation of the breakdown of Bragg-Gray behaviour

In this section the physics behind the 'breakdown' of Bragg-Gray cavity theory is explained as evidenced by the large difference between the (uncorrected) air-cavity fluence spectrum and the water-voxel fluence spectrum for the two smallest field sizes shown in Figures 6.4(a), (b) and 6.5(a), (b). Figure 6.6 is an aid to the explanation; the measurement position, marked by ×, is at a depth beyond D_{max}.. On the left-hand side of the figure the field is broad enough for quasi-CPE ('quasi' in the sense of a real photon beam for which photon attenuation may not be negligible over distances equal to the secondary electron ranges – cf. Kumar *et al* 2015a) to be established at the depth of interest in the uniform medium i.e. the maximum lateral distance any secondary electron can travel (indicated by $r_{\mathrm{max}}^{\mathrm{e-}}$) is less than the field width. It follows that there will be quasi-CPE at × in the uniform medium for all fields wider than the inside edge of the hatched area.

Considering the low-density (gas) cavity, the shortest distance from the cavity edge to the field edge is exactly equal to $r_{\mathrm{max}}^{\mathrm{e-}}$. Therefore in this case the electron fluence in the (gas) cavity will be negligibly different from the equilibrium fluence at × in the uniform medium – in other words the cavity is acting in a *Bragg-Gray* manner. This is because the conditions for the Fano theorem are essentially fulfilled (Harder 1974) even though the atomic composition of the cavity gas may differ from that of the medium; this compositional difference has little significance as here the energy of the photons (and hence of the secondary electrons) is sufficiently high and the density of the cavity sufficiently low that the component of the dose to the cavity (gas) due to photon interactions with the (gas) material *inside* the cavity is a negligible fraction of the dose due to secondary electrons incident from *outside* the cavity (Ma and Nahum 1991).

In case of the *narrow* field on the right-hand side of the figure; the field width is insufficient for quasi-CPE to be established in the uniform medium. Consider first the case of the 'cavity' in the uniform medium. The electron (+ positron) fluence at × (strictly the fluence in a region centred on × giving rise to dose at ×) can be split into two components: Φ_{out} arising from secondary electrons generated *outside* the (virtual) cavity and Φ_{in} arising from photon interactions in that volume of the medium *inside* the virtual cavity boundary. The Φ_{in} component will be very similar to that in the wide-field case described above (as it is assumed that the beam width is greater than the cavity width) but Φ_{out} here will be lower than its wide-field counterpart. Consequently the total charged-particle fluence, and hence the dose, at × will be lower than in the wide-field 'equilibrium' situation discussed above.

Consider now the low-density (gas) cavity in the *narrow* field. Here Φ_{out} will not be too dissimilar in magnitude to that for the uniform medium (but will differ due to the 'attenuation' of the 'out' fluence by the material inside the uniform cavity, whereas there is no such 'attenuation' in the gas cavity). Relative to Φ_{out} , the Φ_{in} contribution to the gas cavity dose will be virtually zero, as it has already been established that the gas cavity acts in a Bragg-Gray manner in this photon quality in a wide field. Consequently the *total* electron (+ positron) fluence in the gas cavity in the narrow non-equilibrium photon field will be *smaller* than its counterpart (the fluence at ×) in the uniform medium, this difference being principally due to the difference in magnitude of the respective Φ_{in} components. Expressed another way, Bragg-Gray behaviour has broken down. An analytical formulation of the above verbal-pictorial explanation is given in the Appendix-B.

Why do the same arguments not apply to the *low*-density cavity in the *wide* field? Because in this case the (same) very low value of Φ_{in} is almost exactly compensated by the added contribution (to Φ_{out}) from the hatched volume shown in the lower part of the wide-field figure; this 'compensation' is due to the (near) fulfilment of Fano conditions in an 'equilibrium' geometry (Harder 1974). It must therefore follow that in a (megavoltage) photon-irradiated (uniform) medium, quasi-CPE *is* required in order for a low-density cavity inserted into the medium to act in a Bragg-Gray manner, as it is only under quasi-CPE conditions that the Fano theorem can be applied, thus ensuring the 'compensation' described above.

The connection between CPE and the Bragg-Gray principle has been insufficiently emphasised in the radiation dosimetry literature. It is frequently argued that because the Bragg-Gray principle is ≈ valid for ion chambers in charged-particle (e.g. electron-beam) irradiated media, where CPE can never exist (as the beam energy is continually decreasing with depth), then neither is CPE necessary for such detectors in photon-irradiated media. However, when the primary radiation is charged particles, the concepts of Φ_{in} and Φ_{out} do not apply and consequently the above reasoning is flawed.

As a corollary, it follows that the *density* of the detector medium will play a major role in the response of a (small) detector in a narrow, non-equilibrium field, as the electron/positron fluence due to photon interactions in the cavity volume, i.e. the Φ_{in} component, will increase with the density of the detector material (Scott *et al* 2012, Fenwick *et al* 2013).

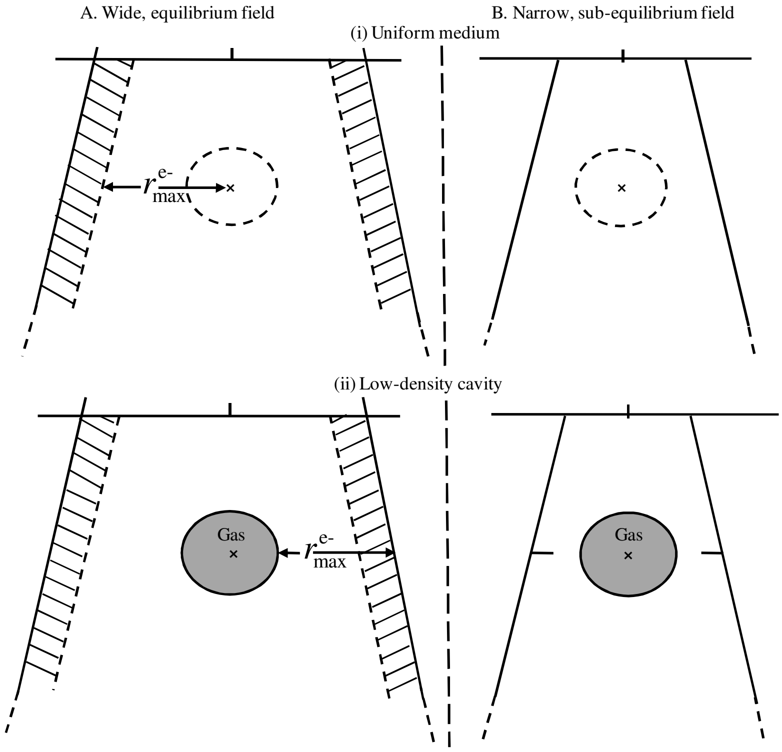

Figure 6.6: **Schematic illustration to accompany the explanation of 'Bragg-Gray breakdown' in narrow, non-equilibrium megavoltage photon fields. The measurement position, marked by '×', is at a depth beyond D_{max}; r_{max}^{e-} is the maximum lateral distance any secondary electron can travel.**

6.4.4 Comparison of the MC-derived dose ratio with the product of $s_{med,det,\Delta}^{SA}$ and $\left(p_{\Phi}\right)_{det}^{w}$

Tables (6.6) - (6.7) present, for both beam qualities and source geometries, a comparison of the ratio of the MC-derived dose-to-water to dose-to-PinPoint-3D-air-cavity-in-water, $\left(D_w / \overline{D}_{air}\right)_{MC}$, with the product of $s_{w,det,\Delta}^{SA}$ and $\left(p_{\Phi}\right)_{det}^{w}$ = $\left(D_w / \overline{D}_{det}\right)_{Eq.(6.3)}$, as a function of field size defined at 100 cm SSD; the side lengths of square fields are 0.25 cm, 0.45 cm, 0.75 cm, 1 cm, 1.5 cm, 2 cm, 3 cm and 10 cm. In the case of field sizes below 1 × 1cm^2 for the 15 MV FLG beam quality, the directly computed MC dose ratios differed from $\left(D_w / \overline{D}_{det}\right)_{Eq.(6.3)}$; in the 0.25 × 0.25 cm^2 field this difference was a non-negligible 5% which must be attributed to the effect of the change in spectral shape.

An expression for the effect of this spectral shape change will now be developed. Firstly the dose ratio can be expressed as:

$$\frac{D_{\mathrm{med}}}{\overline{D}_{\mathrm{det}}} = s^{\mathrm{SA}}_{\mathrm{med,det},\Delta} \times \left(p_{\Phi}\right)^{\mathrm{med}}_{\mathrm{det}} \times \left(\frac{\left(\left\{ \int_{\Delta}^{E_{\max}} \left[\Phi_E^{\mathrm{tot}}(z)\right]_{\mathrm{med}} \times \left[\overline{L}_{\Delta}/\rho\right]_{\mathrm{det}} \mathrm{d}E \right\} + \left\{ \left[\Phi_E^{\mathrm{tot}}(\Delta)\right]_{\mathrm{med}} \times \left[\overline{S}_{\mathrm{el}}(\Delta)/\rho\right]_{\mathrm{det}} \times \Delta \right\} \right) \Big/ \int_{\Delta}^{E_{\max}} \left[\Phi_E^{\mathrm{tot}}(z)\right]_{\mathrm{med}} \mathrm{d}E}{\left(\left\{ \int_{\Delta}^{E_{\max}} \left[\Phi_E^{\mathrm{tot}}(z)\right]_{\mathrm{det}} \times \left[\overline{L}_{\Delta}/\rho\right]_{\mathrm{det}} \mathrm{d}E \right\} + \left\{ \left[\Phi_E^{\mathrm{tot}}(\Delta)\right]_{\mathrm{det}} \times \left[\overline{S}_{\mathrm{el}}(\Delta)/\rho\right]_{\mathrm{det}} \times \Delta \right\} \right) \Big/ \int_{\Delta}^{E_{\max}} \left[\Phi_E^{\mathrm{tot}}(z)\right]_{\mathrm{det}} \mathrm{d}E} \right)$$

which can be re-written as

$$\frac{D_{\mathrm{med}}}{\overline{D}_{\mathrm{det}}} = s^{\mathrm{SA}}_{\mathrm{med,det},\Delta} \times \left(p_{\Phi}\right)^{\mathrm{med}}_{\mathrm{det}} \times \overline{\left(\frac{L_{\Delta}}{\rho}\right)^{\Phi^{\mathrm{e,tot}}_{\mathrm{med}}}_{\mathrm{det}}} \Big/ \overline{\left(\frac{L_{\Delta}}{\rho}\right)^{\Phi^{\mathrm{e,tot}}_{\mathrm{det}}}_{\mathrm{det}}} \tag{6.7}$$

where the final term is the ratio of the restricted mass electronic stopping power averaged over the fluence spectrum in the medium (=1.711 MeV cm^2 g^{-1} for 15 MV FLG at 0.25 × 0.25 cm^2), to the restricted mass electronic stopping power averaged over the fluence spectrum in the PinPoint 3D air cavity (=1.632 MeV cm^2 g^{-1}), yielding a 'shape factor' of 1.049 which is consistent with the ratio $\left(D_{\mathrm{w}}/\overline{D_{\mathrm{air}}}\right)_{\mathrm{MC}} / \left(D_{\mathrm{w}}/\overline{D_{\mathrm{air}}}\right)_{\mathrm{Eq(6.3)}}$ = 1.050 from table 6.6. If the shapes of these two spectra are identical then this factor will be unity.

An alternative approach would be to define an overall or 'global' perturbation factor thus:

$$p_{\mathrm{global}} = p_{\mathrm{fluence}} \times \left(\text{shape - difference factor}\right) \tag{6.8}$$

where the 'shape-difference' factor is given by the final term in equation (6.7).

6.4.5 Maximum dimensions of perturbation-limited 'Bragg-Gray' detector

Table 6.8 presents the dimensions of 'perturbation-free' cavities as per the Nahum (1996) criterion. It can be seen that an ion chamber with a perturbation within 5% of unity in the 0.25 × 0.25 cm^2 field would require the cavity height to be only 0.023 cm at 6 MV and 0.008 cm at 15 MV; these are impractically small dimensions. These results emphasise the magnitude of the breakdown in Bragg-Gray behaviour in very small fields for practical ionisation chambers which easily fulfil Bragg-Gray conditions in conventional, quasi-CPE fields. In contrast, the single-crystal diamond dosimeter, SCDDo, comfortably fulfills the 5% criterion with its actual dimensions.

Table 6.6: **6 MV and 15 MV photon beams, FLG and PSG: comparison of MC-derived ratio, dose-to- water to dose-to-PinPoint 3D-air-cavity-in-water, $\left(D_{\mathrm{w}} / \overline{D}_{\mathrm{air}}\right)_{\mathrm{MC}}$, with the product $s_{\mathrm{w,air},\Delta}^{\mathrm{SA}} \times \left(p_{\Phi}\right)_{\mathrm{air}}^{\mathrm{w}}$ i.e. equation (6.3); the statistical (Type A) uncertainties are ± 2 standard deviations. The standard uncertainty propagation method was used to derive the statistical (Type A) uncertainties.**

	6 MV				15 MV			
	FLG		PSG		FLG		PSG	
Field Size (cm × cm)	$\left(\frac{D_{\mathrm{w}}}{\overline{D}_{\mathrm{air}}}\right)_{\mathrm{MC}}$	$\left(\frac{D_{\mathrm{w}}}{\overline{D}_{\mathrm{air}}}\right)_{\mathrm{Eq.(3)}}$	$\left(\frac{D_{\mathrm{w}}}{\overline{D}_{\mathrm{air}}}\right)_{\mathrm{MC}}$	$\left(\frac{D_{\mathrm{w}}}{\overline{D}_{\mathrm{air}}}\right)_{\mathrm{Eq.(3)}}$	$\left(\frac{D_{\mathrm{w}}}{\overline{D}_{\mathrm{air}}}\right)_{\mathrm{MC}}$	$\left(\frac{D_{\mathrm{w}}}{\overline{D}_{\mathrm{air}}}\right)_{\mathrm{Eq.(3)}}$	$\left(\frac{D_{\mathrm{w}}}{\overline{D}_{\mathrm{air}}}\right)_{\mathrm{MC}}$	$\left(\frac{D_{\mathrm{w}}}{\overline{D}_{\mathrm{air}}}\right)_{\mathrm{Eq.(3)}}$
0.25 × 0.25	1.485 ± 0.007	1.479 ± 0.007	1.464 ± 0.004	1.453 ± 0.006	2.437 ± 0.022	2.321 ± 0.016	1.475 ± 0.004	1.461 ± 0.003
0.5 × 0.5	1.278 ± 0.005	1.281 ± 0.006	1.208 ± 0.005	1.207 ± 0.008	1.474 ± 0.012	1.460 ± 0.010	1.213 ± 0.005	1.217 ± 0.003
0.75 × 0.75	1.165 ± 0.005	1.170 ± 0.005	1.156 ± 0.006	1.161 ± 0.005	1.246 ± 0.009	1.269 ± 0.005	1.144 ± 0.008	1.145 ± 0.003
1 × 1	1.144 ± 0.005	1.138 ± 0.007	1.137 ± 0.008	1.138 ± 0.007	1.166 ± 0.007	1.182 ± 0.005	1.125 ± 0.010	1.124 ± 0.005
2 × 2	1.117 ± 0.010	1.123 ± 0.010	1.162 ± 0.011	1.159 ± 0.010	1.104 ± 0.009	1.094 ± 0.006	1.099 ± 0.012	1.100 ± 0.007
3 × 3	1.117 ± 0.014	1.121 ± 0.010	1.164 ± 0.017	1.166 ± 0.014	1.099 ± 0.010	1.095 ± 0.007	1.097 ± 0.011	1.096 ± 0.007
10 × 10	-------	-------	-------	-------	1.095 ± 0.021	1.098 ± 0.010	1.094 ± 0.028	1.096 ± 0.008

Table 6.7: **6 MV and 15 MV photon beams, FLG and PSG: comparison of MC-derived ratio of dose-to-water to dose-to-SCDDo cavity-in-water,** $\left(D_{\mathrm{w}} / \overline{D}_{\mathrm{SCDDo}}\right)_{\mathrm{MC}}$ **with the product** $s^{\mathrm{SA}}_{\mathrm{w,SCDDo,\Delta}} \times \left(p_{\Phi}\right)^{\mathrm{w}}_{\mathrm{SCDDo}}$ **i.e. equation (6.3); uncertainties are as per table 6.6.**

	6 MV				15 MV			
	FLG		PSG		FLG		PSG	
Field Size (cm × cm)	$\left(\frac{D_{\mathrm{w}}}{\overline{D}_{\mathrm{SCDDo}}}\right)_{\mathrm{MC}}$	$\left(\frac{D_{\mathrm{w}}}{\overline{D}_{\mathrm{SCDDo}}}\right)_{\mathrm{Eq.(3)}}$	$\left(\frac{D_{\mathrm{w}}}{\overline{D}_{\mathrm{SCDDo}}}\right)_{\mathrm{MC}}$	$\left(\frac{D_{\mathrm{w}}}{\overline{D}_{\mathrm{SCDDo}}}\right)_{\mathrm{Eq.(3)}}$	$\left(\frac{D_{\mathrm{w}}}{\overline{D}_{\mathrm{SCDDo}}}\right)_{\mathrm{MC}}$	$\left(\frac{D_{\mathrm{w}}}{\overline{D}_{\mathrm{SCDDo}}}\right)_{\mathrm{Eq.(3)}}$	$\left(\frac{D_{\mathrm{w}}}{\overline{D}_{\mathrm{SCDDo}}}\right)_{\mathrm{MC}}$	$\left(\frac{D_{\mathrm{w}}}{\overline{D}_{\mathrm{SCDDo}}}\right)_{\mathrm{Eq.(3)}}$
0.25 × 0.25	1.131 ± 0.006	1.127 ± 0.005	1.112 ± 0.003	1.115±0.005	1.136 ± 0.009	1.126 ± 0.009	1.127 ± 0.003	1.130 ± 0.003
0.5 × 0.5	1.137 ± 0.005	1.140 ± 0.005	1.138 ± 0.004	1.135±0.007	1.139 ± 0.008	1.128 ± 0.008	1.141 ± 0.004	1.141 ± 0.003
0.75 × 0.75	1.145 ± 0.005	1.144 ± 0.005	1.152 ± 0.006	1.151±0.005	1.140 ± 0.008	1.137 ± 0.006	1.152 ± 0.007	1.150 ± 0.003
1 × 1	1.157 ± 0.007	1.147 ± 0.008	1.156 ± 0.008	1.156±0.008	1.143 ± 0.008	1.144 ± 0.006	1.154 ± 0.009	1.159 ± 0.005
2 × 2	1.158 ± 0.011	1.166 ± 0.010	1.162 ± 0.011	1.159±0.010	1.163 ± 0.009	1.156 ± 0.008	1.169 ± 0.010	1.164 ± 0.008
3 × 3	1.159 ± 0.015	1.165 ± 0.011	1.164 ± 0.017	1.166±0.014	1.165 ± 0.010	1.162 ± 0.008	1.170 ± 0.011	1.165 ± 0.008
10 × 10	-------	-------	-------	-------	1.167 ± 0.021	1.164 ± 0.010	1.170 ± 0.019	1.166 ± 0.011

Table 6.8: **Dimensions of 5% perturbation-limited PinPoint 3D air cavity and diamond cavity (SCDDo) determined by keeping the radii of the cavities constant and reducing the thickness/height until $\left(p_{\Phi}\right)_{\text{air}}^{\text{w}}$ = 1.05 and $\left(p_{\Phi}\right)_{\text{SCDDo}}^{\text{w}}$ = 0.95 for field sizes 0.25 × 0.25 cm^2 and 0.5 × 0.5 cm^2 for FLG of the 6 MV and 15 MV qualities . The 'true' thicknesses/heights are shown in parentheses.**

		Thickness/height of the cavity (cm) for 5% perturbation			
		6 MV		15 MV	
Field size (cm × cm)	Cavity radius (cm)	PinPoint 3D (0.2 cm)	SCDDo (0.0165 cm)	PinPoint 3D (0.2 cm)	SCDDo (0.0165 cm)
0.25 × 0.25	0.0564	0.023	0.028	0.008	0.021
0.5 × 0.5	0.0564	0.122	0.045	0.027	0.024

6.5 Summary and Conclusions

It has been shown that *OF*(kerma) changes minimally with field size for PSG at both beam qualities (15MV and 6 MV) whereas for FLG this quantity decreases dramatically as the field size drops below 0.5 × 0.5 cm^2, thereby demonstrating explicitly the source occlusion effect. For the SCDDo detector, the '*BG dose to water*' in small fields is within 2.9% of the dose computed directly in the water voxel (for the 0.25 × 0.25 cm^2 field size in 6 and 15 MV FLG) whereas these quantities differ significantly in case of a small (air-filled) ionisation chamber. Signal-averaging over the detector volume is also a big effect. A water-to-detector material perturbation factor has been defined and evaluated as the ratio of the (photon-generated) *total* electron (+ positron) fluence in undisturbed water to that in the detector 'cavity', integrated over all energies; for the PinPoint 3D-chamber-like air cavity the values are 1.323 and 2.139 for the 0.25 × 0.25 cm^2 field size in 6 MV FLG and 15 MV FLG respectively. For the 15 MV FLG and fields of 1 × 1 cm^2 and smaller not only the magnitude but also the 'shape' of the electron fluence spectra in the air cavity differs from that in the water cavity due to the combined effect of electronic disequilibrium, source occlusion and volume-averaging; a theoretical expression for this 'shape factor' has been formulated. A detailed explanation for this 'breakdown' of Bragg-Gray behaviour in low-density (gas) detectors in non-equilibrium field sizes is given, which emphasises that for low-density detectors to act as Bragg-Gray cavities in a photon-irradiated medium, quasi-CPE must be present in the undisturbed medium. In contrast to air-filled ionisation chambers, a new type of 'single crystal' diamond detector is predicted to exhibit quasi Bragg-Gray behaviour over a wide range of field sizes and beam qualities despite its high density.

CHAPTER 7

Dosimetric response of variable-size cavities in photon-irradiated media and the behaviour of the Spencer-Attix cavity integral with increasing Δ

7.1 Introduction

The absorbed dose in an irradiated medium, D_{med}, is in practice derived from the reading of a detector (or dosimeter) placed at the desired depth. The energy absorbed in the detector's sensitive material, and hence the absorbed dose in this material, is proportional to the signal, or reading (e.g. charge $\propto D_{\mathrm{det}}$). The ratio of the absorbed dose in the uniform (or undisturbed) medium to the absorbed dose in the detector cavity, $D_{\mathrm{med}}/D_{\mathrm{det}}$, is determined from *cavity theory*, which accounts for the effect of differences between the atomic composition and density of the detector 'cavity' and those of the medium into which it is introduced; $D_{\mathrm{med}}/D_{\mathrm{det}}$ also depends on cavity size and radiation quality (Attix 1986, Nahum 2009).

When the three principal quasi-exact cavity theories, Bragg-Gray (Bragg 1912, Gray 1936), Spencer-Attix (Spencer and Attix 1955) and 'large photon' detector (e.g. Nahum 2009) were developed the theoretical tool to critically examine these theories was not available. Monte-Carlo (MC) codes such as the EGSnrc and PENELOPE systems, with electron transport schemes specifically designed to yield accurate results in gas-filled ion chamber simulations (Kawrakow 2000a, Kawrakow 2000b, Borg *et al* 2000, Mainegra-Hing *et al* 2003, Rogers and Kawrakow 2003, Buckley *et al* 2003, Verhaegen 2002, 2003, Buckley and Rogers 2006, Sempau *et al* 2006, La Russa and Rogers 2006, 2008, 2009, Wulff *et al* 2008, Kawrakow *et al* 2011, Muir and Rogers 2013, 2014, Salvat 2014), together with the high statistical precision which can be obtained today, can critically test these theories for various detector types in different media, for a range of radiation qualities.

Here, a confirmation of the self-consistency of the different cavity theories (Bragg-Gray, Spencer-Attix and large photon detector) with one another is begun by evaluating the so-called 'cavity integrals' (see below) and comparing these to the (direct) Monte-Carlo dose D_{MC} in media of varying atomic number irradiated by high-energy photon beams under (quasi) charged-particle equilibrium. Nahum *et al* (2010) found that if the 'Spencer-Attix dose' $D_{\text{S-A}}(\Delta)$ (also known as restricted cema) was evaluated for value of Δ (the Spencer-Attix cavity-size parameter) much greater than that appropriate for typical gas-filled cavities ($\Delta \approx$ 10-15 keV) then the ratio $D_{\text{S-A}}(\Delta)/D_{\mathrm{MC}}$ fell increasingly below unity; this behaviour is explored in detail here and the dependence of this ratio on Δ is explained in terms of the Klein-Nishina (K-N) differential cross section. For a given radiation quality, it is shown that the maximum value of Δ for which ($D_{S\text{-}A}(\Delta)/D_{MC}$) remains within a few percent of unity can be related to the *maximum* size detector exhibiting Bragg-Gray behaviour. Consequently it is suggested that ($D_{S\text{-}A}(\Delta)/D_{MC}$) can be used as a Bragg-Gray detector criterion.

Finally the variation of D_{med}/D_{det} has been explored for a highly mis-matched (i.e. non-water-equivalent) cavity, irradiated in water by the 'clinical' photon–beam qualities of 6 and 15 MV; by the device of varying the density of the cavity material (silicon), variations in cavity size from that corresponding to a gas to that approaching the 'large photon detector' condition were mimicked, enabling a critical examination of Spencer-Attix and Burlin cavity theories. Furthermore, by employing a Monte-Carlo- electron 'detour factor' to the linking of the Spencer-Attix Δ to cavity size, it is shown that $D_{S\text{-}A}(\Delta)/D_{MC}$ matches closely the (Monte-Carlo-derived) Burlin '*d*' factor at different values of Δ.

7.2 Materials and Methods

7.2.1 Monte-Carlo Calculations

The EGSnrc Monte-Carlo code system (Kawrakow 2000a, Kawrakow *et al* 2011) and its associated user-codes (Rogers *et al* 2011b) have been carefully validated in detector-response studies (Borg *et al* 2000, Mainegra-Hing *et al* 2003, Rogers and Kawrakow 2003, Buckley *et al* 2003, Verhaegen 2002, 2003, Buckley and Rogers 2006, La Russa and Rogers 2006, 2008, 2009, Ali and Rogers 2008, Wulff *et al* 2008, Muir and Rogers 2013, 2014).

The 'user-codes' DOSRZnrc, FLURZnrc and CAVRZnrc (version: V4-2.3.2) were used in the present study. The settings employed in these simulations included modelling Compton interactions for bound electrons, Rayleigh scattering, the effect of any atomic relaxation events and relativistic spin effects in the multiple scattering of charged particles. Electron impact ionization was switched on (in the EGSnrc code system this can be either ON or OFF). Cross sections for sampling photon energies in bremsstrahlung events were taken from the NIST databases (Hubbell and Seltzer 2004) and photon cross sections from the XCOM database were used (Berger *et al* 2010).

A PEGS4 datafile (Nelson *et al* 1985, Kawrakow *et al* 2011) was generated with the EGSnrcMP package (Kawrakow *et al* 2006) with parameters AP = 1 keV, AE = 512 keV (total energy) where AP and AE are the production thresholds for secondary bremsstrahlung photons and knock-on electrons respectively. Electrons and positrons were followed down to 1 keV kinetic energy (i.e. the electron/positron kinetic energy cut-off *ECUT* = 512 keV) and photons down to 1 keV (photon energy cut-off *PCUT* = 1 keV). This ensured that photons and charged particles were explicitly created above 1 keV (i.e. bremsstrahlung photons and knock-on electrons) and transported down to 1 keV.

It is noted that PEGS4 data files with AE = 512 keV and AP = 1 keV generated using the egs_gui of the EGSnrcMP package produce restricted *total* mass stopping powers (IUNRST = 0). The evaluation of the Spencer-Attix cavity integral (see equation (7.3) below) involves the restricted *electronic* mass stopping power. However, for low values of AP (= 1 keV), restricted *radiative* mass stopping powers are extremely close to zero (Rogers and Bielajew 1990, Rogers *et al* 2011b) and hence the difference between the restricted *total* mass stopping power (IUNRST = 0) and the restricted *electronic* mass stopping power is entirely negligible.

7.2.2 Self-consistency of conventional cavity theories

Cavity theory provides several expressions, sometimes known as 'cavity integrals', which essentially yield the absorbed dose to medium, D_{med}, given the particle fluence spectrum, of either photons or charged particles, depending on the cavity integral employed.

The collision kerma in the medium at a depth, z, $\left[K_{\mathrm{col}}(z)\right]_{\mathrm{med}}$, is given by (Mobit *et al* 2000, Nahum 2007b):

$$\left[K_{\mathrm{col}}(z)\right]_{\mathrm{med}} = \int_{0}^{k_{\max}} k\left[\Phi_{k}^{\mathrm{phot}}(\mathrm{z})\right]_{\mathrm{med}}\left(\frac{\mu_{\mathrm{en}}(k)}{\rho}\right)_{\mathrm{med}} \mathrm{d}k \tag{7.1}$$

where k is the photon energy, $\mu_{\mathrm{en}}(k)/\rho$ the mass energy-absorption coefficient at energy k, and $\left[\Phi_{k}^{\mathrm{phot}}(\mathrm{z})\right]_{\mathrm{med}}$ the photon fluence, differential in energy, in the medium (water, aluminium or copper) at depth z. When there is quasi-CPE[15] as is the case here then $\left[D(z)\right]_{\mathrm{med}} = \beta_{\mathrm{med}}\left[K_{\mathrm{col}}(z)\right]_{\mathrm{med}}$ and we can write

$$\left[D(z)\right]_{\mathrm{med}} \overset{\mathrm{CPE}}{=} \beta_{\mathrm{med}}\left[K_{\mathrm{col}}(z)\right]_{\mathrm{med}} = \beta_{\mathrm{med}}\int_{0}^{k_{\max}} k\left[\Phi_{k}^{\mathrm{phot}}(\mathrm{z})\right]_{\mathrm{med}}\left(\frac{\mu_{\mathrm{en}}(k)}{\rho}\right)_{\mathrm{med}} \mathrm{d}k \tag{7.2}$$

where β_{med} is generally unity within a few percent (Kumar *et al* 2015a); in what follows it is $\left[K_{\mathrm{col}}(z)\right]_{\mathrm{med}}$ which has been evaluated. For consistency, $\mu_{\mathrm{en}}(k)/\rho$ was computed using the '*g*' user-code of EGSnrc system (Kawrakow *et al* 2011) with the identical PEGS4 datafiles used with FLURZnrc. In practice the lower limit of the integral is not zero but *PCUT* as the fluence spectrum only extends down to *PCUT* in energy.

[15] In real photon beams CPE is never 'perfect' as a result of finite photon attenuation over the distance of the maximum secondary-electron/positron range; we refer to this as quasi-CPE.

The integral involving the *primary* charged-particle fluence spectrum and the mass electronic stopping power, also known as cema (ICRU 2011), can be written

$$\left[C(z)\right]_{\mathrm{med}} = \int_{0}^{E_{\max}} \left[\Phi_{\mathrm{E}}^{\mathrm{prim}}(\mathrm{z})\right]_{\mathrm{med}} \left[S_{\mathrm{el}}(E)/\rho\right]_{\mathrm{med}} \mathrm{d}E \tag{7.3}$$

where E is the kinetic energy of charged particles, $S_{\mathrm{el}}(E)/\rho$ is the *unrestricted* mass electronic stopping power, and $\left[\Phi_{E}^{\mathrm{prim}}(z)\right]_{\mathrm{med}}$ is the *primary* electron (+ positron) fluence, differential in energy, in the undisturbed medium (water, aluminium or copper) at depth z (the same depth as in equations (7.1) and (7.2)). By *primary* it is meant all charged particles (electrons, positrons) which are not 'delta rays' (aka knock-on electrons); this includes charged particles liberated by *secondary* bremsstrahlung. If there is delta-ray equilibrium in the volume of interest then we can write

$$D(z)_{\mathrm{med}} \overset{\delta-\mathrm{eqm}}{=} \left[C(z)\right]_{\mathrm{med}} = \int_{0}^{E_{\max}} \left[\Phi_{\mathrm{E}}^{\mathrm{prim}}(\mathrm{z})\right]_{\mathrm{med}} \left[S_{\mathrm{el}}(E)/\rho\right]_{\mathrm{med}} \mathrm{d}E \tag{7.4}$$

In general there will be a very good approximation to δ–ray equilibrium (an exception is close to the surface in a medium irradiated by an electron beam). In practice the electron fluence spectrum is only computed down to the Monte-Carlo cut-off energy *ECUT*; however, the numerical difference due to the lower limit of the integral not being zero is entirely negligible in the case here of the primary fluence.

The EGSnrc user-code FLURZnrc was employed to generate the photon and electron fluence spectra per MeV per incident photon fluence down to 1 keV, with the same *ECUT* and *PCUT*, as above at 2.5 g cm^{-2} depth and 10.5 g cm^{-2} on the beam central axis for 1 MeV and 10 MeV photon beams respectively, perpendicularly incident on large homogeneous water, aluminium and copper phantoms (a cylinder with both height and diameter equal to 1308 cm, Kumar and Nahum (2015)). The user-code input parameter setting SLOTE = -999 was chosen i.e. the lowest 90% of the energy range is split into intervals ('bins') with equal logarithmic spacing and the highest 10% into linearly-spaced bins; this was to ensure sufficiently narrow bins to 'capture' the possible rapid variation of the photon mass energy-absorption coefficient with energy. A parallel beam (i.e. source 0) of circular cross-section with a radius of 5 cm was selected. The scoring 'cavity' of water, aluminium or copper, was cylindrical, with radius 2 g cm^{-2}, height 1 g cm^{-2} and with its front face at depths of 2 g cm^{-2} and 10 g cm^{-2} for 1 MeV and 10 MeV photons respectively, perpendicular to the beam direction (i.e. the cavity centres were at depths of 2.5 g cm^{-2} and 10.5 g cm^{-2} respectively).

Again for consistency, a separate PEGS4 datafile was generated for the different media in order to obtain the unrestricted mass electronic stopping power; IUNRST = 1 was set in the PEGS4 input file (this cannot be done from the egs_gui of the EGSnrcMP package (Kawrakow *et al* 2006) so the file was created manually). The IUNRST = 1 option provides a cross-section data set (PEGS4 output) of unrestricted mass electronic stopping powers. The unrestricted stopping powers used in equation (4) were extracted from PEGS4 data files using the user-code EXAMIN, also distributed with the EGSnrc package (Rogers *et al* 2011b).

Finally $D(z)_{\text{med}}$ can also be computed from the 'Spencer-Attix' cavity integral involving the total charged-particle fluence spectra and the restricted electronic stopping power (Nahum 1978, Nahum 2009), also known as restricted cema, $[C_{\Delta}(z)]_{\text{med}}$ (ICRU 2011):

$$\left[D_{\text{S-A}}(z)\right]_{\text{med},\Delta} = \int_{\Delta}^{E_{\max}} \left[\Phi_E^{\text{tot}}(z)\right]_{\text{med}} \left[L_\Delta(E)/\rho\right]_{\text{med}} \mathrm{d}E + \left[\Phi_E^{\text{tot}}(\Delta)\right]_{\text{med}} \left[S_{\text{el}}(\Delta)/\rho\right]_{\text{med}} \Delta \qquad (7.5)$$

where E is the kinetic energy of charged particles, $\left[L_\Delta(E)/\rho\right]_{\text{med}}$ is the mass electronic stopping power restricted to losses less than Δ, and $\left[\Phi_E^{\text{tot}}(z)\right]_{\text{med}}$ is the *total* electron (+ positron) fluence, differential in energy (i.e. including all generations of 'knock-on' electrons, or delta-rays) in the undisturbed medium (water, aluminium , copper), down to the cut-off energy, Δ (1 keV here but any value below around 20 keV could have been chosen –see sub-section 7.2.3) at depth z. For consistency, the restricted mass electronic stopping power $\left[L_\Delta(E)/\rho\right]_{\text{med}}$ was also extracted from the PEGS4 datafiles as described above. The absorbed dose determined using equation (7.5), henceforth written as $\left[D_{\text{S-A}}(\Delta)\right]_{\text{med}}$, will be referred to as the '*Spencer-Attix dose'*.

In the evaluation of the '*track end*' term in the equation (7.5) the total electron (+ positron) fluence and the *unrestricted* mass electronic stopping power are required at an energy exactly equal to Δ. In FLURZnrc it is not possible to derive the fluence at exactly 1 keV, the lower limit of the lowest energy bin. The value of Δ was therefore set equal to the *upper* limit of the lowest bin combined with SLOTE = -999 (see above).

The absorbed dose was computed with DOSRZnrc for the beam qualities, media and source type specified above; we denote this 'direct Monte-Carlo dose' by D_{MC}. The above dose, the photon fluence spectrum, the fluence spectra for the first generation (denoted as 'primary fluence'), and for *all* generations of charged particles (electrons and positrons) i.e. total fluence, have been computed with the identical normalization 'per incident photon fluence'. The ratio of cavity dose (from equations (7.2), (7.4) and (7.5)) to D_{MC} was determined for 1 MeV and 10 MeV photon beams at depths of 2.5 and 10.5 g cm^{-2} respectively in all three media.

7.2.3 The relationship between the direct Monte-Carlo dose and the Spencer-Attix cavity integral at increasing values of Δ

Generally the Spencer-Attix cut-off Δ is either chosen to be as low as possible or, in the context of the S-A stopping-power ratio, is related to the mean chord length across the detector cavity (see sub-section 7.2.4.2). In a critical examination of Spencer-Attix theory for a 10-MeV photon beam in aluminium, Nahum *et al* (2010) observed that whilst for Δ below ≈ 30 keV the ratio [$D_{S\text{-}A}(\Delta)/D_{MC}$] was essentially unity, for Δ above ≈ 30 keV this ratio decreased monotonically with increasing Δ. This decrease was ascribed to the non-inclusion in $D_{S\text{-}A}(\Delta)$ of energy deposition due to secondary electrons and positrons with *initial* energies below Δ. In this section, and in sub-section 7.3.2, this dependence of [$D_{S\text{-}A}(\Delta)/D_{MC}$] on Δ is explored in detail.

7.2.3.1 Investigation of the dependence of ($D_{S\text{-}A}(\Delta)/D_{MC}$) on Δ

The Klein-Nishina (K-N) differential cross section gives the probability that a single photon will undergo a Compton interaction in traversing a layer containing one electron/cm^2, transferring kinetic energy between E and $E + \mathrm{d}E$ to the (Compton) electron (Attix 1986):

$$\frac{d_e\sigma}{dE} = \frac{\pi r_o^2 m_o c^2}{\left(k'\right)^2} \times \left\{ \left[\frac{m_o c^2 E}{\left(k\right)^2}\right] + 2\left[\frac{k'}{k}\right]^2 + \frac{k'}{\left(k\right)^3}\left[\left(E - m_o c^2\right)^2 - \left(m_o c^2\right)^2\right] \right\} \tag{7.6}$$

where $m_o c^2$ is the electron rest mass energy (= 0.511 MeV), k' is the energy of scattered photon, E is the electron kinetic energy, ${}_e\sigma$ is the total K-N cross section per electron and $r_o = e^2/m_o c^2 = 2.818 \times 10^{-13}$ cm is the so-called 'classical electron radius'; the above expression applies to 'free' electrons i.e. no corrections for binding energies. Starting from equation (7.6) the fraction of the *total* energy (i.e. over all energies) transferred to Compton electrons with initial k.e. above energy Δ was calculated. Let us denote the upper and lower limits of energy transfer to Compton electrons by E_{min} and E_{max}. The total energy in the Compton electron spectrum will be proportional to $\int_{E_{min}}^{E_{max}} \left[\frac{d_e\sigma}{dE}\right] E\, dE$ and the energy above Δ proportional to $\int_{\Delta}^{E_{max}} \left[\frac{d_e\sigma}{dE}\right] E\, dE$. Consequently, the fraction of the total (kinetic) energy transferred to electrons with k.e. > Δ for a photon of energy k, $F(k, \Delta)$, is given by[16]

$$F(k,\Delta) = \frac{\int_{\Delta}^{E_{max}} \left[\frac{d_e\sigma}{dE}\right] E\, dE}{\int_{E_{min}}^{E_{max}} \left[\frac{d_e\sigma}{dE}\right] E\, dE} \tag{7.7}$$

The maximum Compton electron energy, E_{max}, due to a 'head-on' collision (photon deflection angle θ = 180° i.e. the photon is backscattered) is

[16] The evaluation of equation (7.7) was 'validated' by computing the *mean energy* of the Compton electrons, E_{mean}, from k = 0.01 MeV to 100 MeV; the numbers were consistent with the data in figure 7.7 in Attix (1986).

$$E_{\max} = \frac{2k^2}{2k + 0.511} \tag{7.8}$$

where the incident photon has energy k in units of MeV. The minimum energy, $E_{\min}$, (see equation (7.7)) is technically zero; in practice this is set at 500 eV as reducing it further had a negligible effect on the results. Equation (7.7) was evaluated for 1 MeV photons for energy Δ = 1 keV and 10 - 200 keV in steps of 10 keV. In the evaluation of the numerical integrals of equation (7.7) the widths of the energy intervals were successively reduced until the value of $F(k, \Delta)$ ceased to change.

The ratio ($D_{\text{S-A}}(\Delta)/D_{\text{MC}}$) was derived for a 1-MeV photon beam incident on a cylindrical water phantom (2 cm diameter, 3 cm height/thickness) suspended in a vacuum. The dimensions were chosen in order to eliminate as much photon scatter as possible, as the quantity $F(k, \Delta)$ was evaluated for photons of exactly 1 MeV energy. The source geometry was a parallel beam of circular cross-section with a radius of 1 cm (equal to the radius of modelled water phantom). The scoring volume was a cylinder with a circular cross-section of 2 cm diameter and 1 cm thickness located on the central axis centered at 2.5 cm depth in the cylindrical water phantom to ensure sufficient depth beyond the depth of maximum dose ($d_{\max}$). The absorbed dose, D_{MC}, was computed using DOSRZnrc with *ECUT* = 512 keV (total energy) and *PCUT* = 1 keV. Using FLURZnrc , the total electron (+ positron) fluence per MeV per incident photon fluence was scored for the same geometry, scoring volume and source described above; the spectral bins were selected as described in sub-section 7.2.2 with *ECUT* and *PCUT* as above. $D_{\text{S-A}}(\Delta)$ was evaluated from equation (7.5) for Δ = 1 keV and 10-200 keV in steps of 10 keV. The ratio ($D_{\text{S-A}}(\Delta)/D_{\text{MC}}$) was compared to $F(k, \Delta)$ evaluated from equation (7.7) for the same values of Δ.

7.2.3.2 The interpretation of the numerical value of ($D_{\text{S-A}}(\Delta)/D_{\text{MC}}$) in terms of cavity theory

The magnitude of ($D_{\text{S-A}}(\Delta)/D_{\text{MC}}$) expresses the fraction of the total energy deposited in a cavity (of dimensions such that electrons of energy Δ can just cross the cavity) by electrons (and technically also positrons) incident on the cavity from the surrounding medium. This can be 'seen' more easily by considering the quantity ($[D_{\text{MC}} - D_{\text{S-A}}(\Delta)]/D_{\text{MC}}$) or 1- ($D_{\text{S-A}}(\Delta)/D_{\text{MC}}$); this is the fraction of energy deposition in the cavity by those electrons and positrons *with initial energies below* Δ (see previous sub-section). It is precisely this component of the total energy deposition which must be negligible for a cavity to exhibit Bragg-Gray behaviour. It follows that if ($D_{\text{S-A}}(\Delta)/D_{\text{MC}}$) is very close to unity then the cavity is *Bragg-Gray* in the radiation quality under study. Thus a cavity with a value of Δ such that $D_{\text{S-A}}(\Delta)/D_{\text{MC}}$ = 0.95-0.98 (or similar) has the *maximum* size for consideration as a Bragg-Gray detector. The computation of $D_{\text{S-A}}(\Delta)/D_{\text{MC}}$ is described in the following sub-section.

7.2.3.3 $\left(D_{\text{S-A}}(\Delta)/D_{\text{MC}}\right)$ as a function of Δ and radiation quality

The scoring volume was a (water) cylinder with a circular cross-section of 20 mm diameter and 6 mm height located on the central axis with its front face at 2.0 cm depth for 50-300 keV photon beams and kilovoltage beam qualities (50-250 kV), 2.5 cm depth for a 10 MeV electron beam, 5 cm depth for Co-60 γ-rays, 6 10 and 15 MV x-rays and 10 cm depth for a 10 MeV photon beam. The scoring cylinder was placed in a cylindrical water phantom (radius 15 cm, thickness 30 cm) to ensure sufficient depth beyond the depth of maximum dose. The source to phantom surface distance (SSD) was 100 cm. A beam radius of 5.55 cm (equivalent to a '10 cm ×10 cm' field size; Day and Aird 1996) was defined on the phantom surface. The 'Source 1' option of the EGSnrc Monte-Carlo code system (i.e. point source, incident on front face) was used. The above geometry mimicks the measurement set-up in radiotherapy clinics. The total electron (+ positron) fluence per MeV per incident photon fluence down to 1 keV was computed using FLURZnrc with the same beam qualities and geometry as above. *ECUT* was set at 512 keV (total energy) and *PCUT* at 1 keV. The spectral bin widths were selected in the same way as in sub-section 2.2. The source spectra employed were those distributed with the EGSnrc code system (Rogers *et al* 2011b) for beam qualities of 50-250 kV, Co-60 γ-rays (Rogers *et al* 1988), and 6, 10 and 15 MV 'clinical' photon beams (Mohan *et al* 1985).

The Spencer-Attix dose $D_{\text{S-A}}(\Delta)$ was derived from equation (7.5) for all the above-mentioned beam qualities for Δ values from 1 keV up to a maximum of 2000 keV depending upon beam quality (see below). The 'direct' Monte-Carlo dose to water, D_{MC}, was computed for the same geometry, source type and radiation beam qualities described above, using CAVRZnrc with *ECUT* and *PCUT* as above. Subsequently $(D_{\text{S-A}}(\Delta)/D_{\text{MC}})$ for all radiation qualities was plotted as a function of Δ. Further, $\Delta_{0.95}$ and $\Delta_{0.98}$ corresponding to $(D_{\text{S-A}}(\Delta)/D_{\text{MC}}) = 0.95$ and 0.98 respectively were determined for all radiation beam qualities. The *continuous slowing-down range* in air, $\left[R_{\text{csda}}(\Delta)\right]_{\text{air}}$, for $\Delta = \Delta_{0.95}$ and $= \Delta_{0.98}$ (see above) was also calculated for each radiation beam quality.

7.2.4 Transition in detector behaviour from 'Bragg-Gray' towards 'large cavity'

The size, density and atomic composition of the cavity in combination with the radiation quality determines whether it behaves as a 'small' or *Bragg-Gray* cavity, an 'intermediate'-size or *Burlin* cavity, or a 'large photon cavity' in an irradiated medium (Attix 1986). We set up a simulation firstly to demonstrate this transition in *behaviour* and secondly to test how well the three 'established' cavity theories (Spencer-Attix, Burlin or general, 'large photon detector' – see below) predicted this transition. The detector/cavity was modelled as a single cylindrical volume (voxel) of silicon (Si), diameter 2.26 mm and height/thickness 2 mm (in the beam direction) surrounded by liquid water (i.e. there was no wall) located with its centre at 5 cm depth on the central axis of a cylindrical water phantom (15 cm radius, 30 cm thickness). Silicon was chosen as it is appreciably different in atomic composition (principally atomic number) from the surrounding water medium and therefore the medium-to-detector stopping-power ratio will differ significantly from the 'large photon cavity' ratio. The intention with this part of the investigation was to compute the response of a detector with a significantly non-water-equivalent atomic composition and constant volume/shape but a density varying from extremely low, corresponding to Bragg-Gray (gas) cavity conditions, to very high, corresponding to that of a 'large photon detector'; in-between these extremes the detector would be 'Burlin' in its response.

The phantom was irradiated by 6 MV and 15 MV x-ray beams with SSD = 100 cm; the clinical linac spectra from Mohan *et al* (1985) were employed. High-energy bremsstrahlung beams were chosen partly as these are representative of clinical radiotherapy beams and partly because small gas-filled detectors unambiguously exhibit Bragg-Gray behaviour in such beams (Nahum 2007b, 2009). The *physical* dimensions of the cavity were kept constant and instead varied the *density* of the cavity material, silicon, over a very wide range so that the detector response would change from Bragg-Gray towards 'large photon cavity', whilst keeping the atomic properties constant. The alternative, of successively increasing the cavity size from extremely small, i.e. Bragg-Gray, all the way to the 'large photon' condition (i.e. quasi-CPE in the detector) would have resulted in unwieldy dimensions, especially at 15 MV, and necessitated unfeasibly large perturbation corrections for the finite size of the detector (Andreo *et al* 2000, Nahum 2009).

7.2.4.1 MC derivation of the dose-to-water to dose-to-silicon ratio, $\left[\left(D_{\mathrm{w}}\right)_{\mathrm{MC}} / \left(D_{\mathrm{w}}\right)_{\mathrm{MC}}\right]$

As mentioned in sub-section 7.2.1, the radiation interaction cross sections and stopping powers (of the selected materials) required by the EGSnrc system are stored in a PEGS4 datafile. Although Si with density 2.33 g cm^{-3} is included as standard, PEGS4 datafiles for Si with (pseudo) densities ranging from 0.002 g cm^{-3} to 10 g cm^{-3} had to be created. Firstly a density-effect correction file was generated for the individual pseudo-densities of Si by keeping the density (aka polarisation) effect *constant* i.e. at the value corresponding to the *true* silicon density (2.33 g cm^{-3}). This was then combined with the EGSnrcMP package (Kawrakow *et al* 2006) to generate PEGS4 datafiles for all the pseudo-densities of Si (0.002, 0.005, 0.01, 0.05, 0.1, 0.25, 0.5, 1, 1.75, 5, 10) with electron transport parameters unchanged at AP=1 keV, AE = 512 keV.

The 'source 1' option (see sub-section 7.2.3.3.) with a beam radius of 5.55 cm (equivalent to a '10 cm × 10 cm' field size) defined on the phantom surface was used to compute the dose to water and the dose to the Si cavity for each pseudo-density of silicon using CAVRZnrc. It is emphasised that the dimensions of the scoring volumes (1.13 mm radius, 2 mm thickness) were identical for the water and silicon cavities and were kept constant. These simulations thus yielded the ratio dose-to-water to dose-to-Si, $\left[\left(D_{\mathrm{w}}\right)_{\mathrm{MC}} / \left(D_{\mathrm{w}}\right)_{\mathrm{MC}}\right]$, for each silicon pseudo-density.

7.2.4.2 Estimation of the Spencer-Attix cut-off energy Δ as a function of silicon density

In order to evaluate the Spencer-Attix stopping-power ratio, water-to-silicon, values of Δ corresponding to each value of the Si density were required. These were estimated starting from the mean chord length, L, of the cavity volume, taken as equal to four times the volume V divided by its surface area S i.e. $L = 4V/S$ (Rogers and Kawrakow 2003, Buckley *et al* 2003, La Russa and Rogers, 2009). The standard method of estimating Δ consists of finding the energy E of an electron for which the *continuous slowing-down approximation* range for the detector material, $[R_{\text{csda}}(E)]_{\text{det}}$, is equal to L. However, this simple method implicitly assumes that these (low-energy) electrons have straight trajectories, whereas in reality their tracks are highly tortuous.

Harder (1970) coined the concept of the term *detour factor*, *DF*, to take account of the vast number of (predominantly small) changes of direction (due to elastic scattering with the nucleus) when charged particles slow down in matter. Several definitions of detour factor have appeared and the *DF* has been evaluated accordingly (Bethe *et al* 1939, Harder 1970, ICRU 1993, Sorcini and Brahme 1994, Fernández-Varea *et al* 1996, Tabata and Andreo 1998) though this was always for megavoltage electrons whereas in the present study primarily interest in *DF* was for kilovoltage electrons. The detour factor has been computed from:

$$DF = \frac{R_{\text{csda}}}{R_{50}} \tag{7.9}$$

where R_{50} is the (half value) depth at which the dose is 50% of the maximum dose; R_{50} is a good estimate of the average maximum penetration depth. R_{50} was computed using DOSRZnrc, for a broad parallel electron beam incident on silicon, for energies between 10 and 4000 keV. Additionally, *DF* was computed for air for electron beam energies ranging from 10 keV to 300 keV, as Spencer-Attix theory is generally applied to the air-filled cavities of ionisation chambers. For each value of the silicon pseudo-density (0.002 g cm^{-3} to 10 g cm^{-3}) a value of Δ was found which satisfied

$$\frac{[R_{\text{csda}}(\Delta)]_{\text{Si}}}{DF} = L \tag{7.10}$$

The detour factor was treated as a constant as its energy dependence was found to be negligible, except in silicon above ≈ 1 MeV (see table 7.3a).

7.2.4.3 Computation of the Spencer-Attix mass electronic stopping-power ratio, water to Si, for cut-off Δ, $s^{\text{SA}}_{\text{w,Si},\Delta}$

The evaluation of the Spencer-Attix ratio requires electronic mass stopping powers restricted to losses less than Δ for the medium and cavity material (Nahum 1978, 2009):

$$s^{\mathrm{SA}}_{\mathrm{med,det},\Delta} = \frac{\int_{\Delta}^{E_{\max}} \left[\Phi_E^{\mathrm{tot}}(z)\right]_{\mathrm{med}} \times \left[L_{\Delta}(E)/\rho\right]_{\mathrm{med}} \mathrm{d}E + \left[\Phi_E^{\mathrm{tot}}(\Delta)\right]_{\mathrm{med}} \times \left[S_{\mathrm{el}}(\Delta)/\rho\right]_{\mathrm{med}} \times \Delta}{\int_{\Delta}^{E_{\max}} \left[\Phi_E^{\mathrm{tot}}(z)\right]_{\mathrm{med}} \times \left[L_{\Delta}(E)/\rho\right]_{\mathrm{det}} \mathrm{d}E + \left[\Phi_E^{\mathrm{tot}}(\Delta)\right]_{\mathrm{med}} \times \left[S_{\mathrm{el}}(\Delta)/\rho\right]_{\mathrm{det}} \times \Delta} \tag{7.11}$$

In practice the Spencer-Attix stopping-power ratio, water to Si, for cut-off energy Δ, $s^{\mathrm{SA}}_{\mathrm{w,Si},\Delta}$, was computed not from equation (7.11) but with the SPRRZnrc user-code (Rogers *et al* 2011b) – see below; PEGS4 datafiles were created for all the cut-off energies Δ (see above, especially equation (7.10). These computations were carried out for both beam qualities (6 MV and 15 MV) with the source, field size, scoring volume, and depth exactly as specified in sub-sections 7.2.4 and 7.2.4.1. SPRRZnrc calculates restricted stopping power ratios using an 'on the fly' technique in the volume of interest[17] (Malamut *et al* 1991, Kosunen and Rogers 1993) with the track-end term evaluated following Nahum (1978) – see also equation (7.11).

7.2.4.4 Evaluation of the water-to-silicon dose ratio from Burlin or general cavity theory

For the case of a silicon cavity in an irradiated water medium, the Burlin ratio can be written as (cf. Attix 1986)

$$\left(f_{\mathrm{Si,w}}\right)_{\mathrm{Bu}} = \left[d \times s^{\mathrm{SA}}_{\mathrm{Si,w},\Delta} + (1-d) \times \left(\frac{\overline{\mu}_{\mathrm{en}}}{\rho}\right)^{\mathrm{Si}}_{\mathrm{w}}\right] \tag{7.12}$$

where $s^{\mathrm{SA}}_{\mathrm{Si,w},\Delta}$ is the Spencer-Attix stopping-power ratio, Si-to-water, for Δ appropriate to the cavity size, and $\left(\overline{\mu}_{\mathrm{en}}/\rho\right)^{\mathrm{Si}}_{\mathrm{w}}$ is the mass energy-absorption coefficient ratio, Si-to-water (see below). The weighting factor d gives the fractional contribution to the total cavity dose from electrons incident from the surrounding medium; (1-*d*) is therefore contribution due to *photon interactions in the detector* (i.e. the silicon cavity). The ratio $\left(f_{\mathrm{w,Si}}\right)_{\mathrm{Bu}}$ is simply the inverse of equation (7.12).

Burlin (1966) proposed that *d* be estimated as $(1-e^{-\beta L})/\beta L$ where L is the mean chord-length of the cavity and *β* is the effective attenuation coefficient[18] of the electron fluence (incident from the medium) as it crosses the cavity. Values of *β* for the Si cavity for each pseudo-density were

[17] In earlier (unpublished) work it was verified that Spencer-Attix stopping power ratios obtained from equation (7.11) with the electron fluence spectrum given by FLURZnrc were in excellent agreement with those derived from SPRRZnrc.

[18] Note that this *β* is not the same quantity as in equation (C.1). In the literature, *β* is used for both of these quantities.

derived from $e^{-\beta R_{\mathrm{csda}}} = 0.04$ (Janssens *et al* 1974) where R_{csda} corresponds to the maximum energy of the secondary electrons, $E_{\max}$; we used equation (8) with k taken as the fluence-weighted mean energy in the bremsstrahlung spectrum (1.9 MeV and 4.1 MeV for 6 MV and 15 MV respectively)[19].

For each silicon pseudo-density at 6 MV and 15 MV we have also determined (1- d) from Monte-Carlo simulation as follows. By selecting the parameter PHOTON REGENERATION = 'no electrons from wall' (i.e. IFANO = 2) in the input file for CAVRZnrc[20], the scoring routine (AUSGAB) in CAVRZnrc scores the absorbed dose resulting from electrons generated by photon interactions in the cavity region (Si cavity) and in the surrounding medium (water) separately (Mobit *et al* 1996, 1997, Borg *et al* 2000). We denote the Monte-Carlo computed values by $(1\text{-}d)_{\mathrm{MC}}$ and d_{MC} and the Burlin-Janssens values by $(1\text{-}d)_{\mathrm{Bu}}$ and d_{Bu} .

The second term in equation (7.12) involves $\left(\bar{\mu}_{\mathrm{en}}/\rho\right)_{\mathrm{w}}^{\mathrm{Si}}$; this is given by (Nahum 2007b):

$$\left(\frac{\bar{\mu}_{\mathrm{en}}}{\rho}\right)_{\mathrm{w}}^{\mathrm{Si}} = \frac{\int_0^{k_{\max}} k\left[\Phi_k^{\mathrm{phot}}(z)\right]_{\mathrm{w}}\left(\frac{\mu_{\mathrm{en}}(k)}{\rho}\right)_{\mathrm{Si}} \mathrm{d}k}{\int_0^{k_{\max}} k\left[\Phi_k^{\mathrm{phot}}(z)\right]_{\mathrm{w}}\left(\frac{\mu_{\mathrm{en}}(k)}{\rho}\right)_{\mathrm{w}} \mathrm{d}k} \qquad (7.13)$$

Each of the terms in the numerator and denominator was defined in sub-section 7.2.2. In order to evaluate equation (7.13), the photon fluence per MeV per incident photon fluence down to *PCUT* (negligibly different from zero for these purposes) was scored at 5 cm depth on the central axis of the cylindrical water phantom (15 cm radius, 30 cm thickness) using FLURZnrc with same *ECUT* and *PCUT* as above (see sub-section 7.2.3.3) for point sources of both beams (6 MV and 15 MV) for the field size specified above (see sub-section 7.2.4). The interaction coefficients $(\mu_{\mathrm{en}}(k)/\rho)_{\mathrm{w}}$ and $(\mu_{\mathrm{en}}(k)/\rho)_{\mathrm{Si}}$ were computed as described in sub-section 7.2.2.

With each of the terms in equation (7.12) evaluated as described above, $\left(f_{\mathrm{w,Si}}\right)_{\mathrm{Bu}}$ was calculated, for the 6 MV and 15 MV qualities at each silicon pseudo-density; d and (1 - d) were obtained from the Burlin and Janssens expressions, not from MC.

[19] Alternatively the Burlin 'd' could be estimated using the *maximum* photon energy in bremsstrahlung spectrum but this would place too much weight on the very small proportion of photons at this energy.

[20] With this special option (i.e. IFANO = 2), the prepared input file has to be executed using the egs_gui of the EGSnrcMP package (Kawrakow *et al* 2006).

Table 7.1: **(a) The direct Monte-Carlo (MC) dose (Gy/incident photon fluence) compared with dose estimated by three different cavity integrals in a small cylindrical cavity in a homogeneous water phantom irradiated by a 1 MeV photon beam: The 'large cavity' integral, B-G cavity integral and S-A cavity integral are also known as collision kerma, cema and restricted cema respectively. The dose and the photon and electron fluences were scored in a voxel of dimensions 2 g cm^{-2} diameter, 1 g cm^{-2} thickness located at 2.5 g cm^{-2} depth; the statistical (Type A) uncertainties are ± 1 standard deviations.**

	1 MeV photon beam					
	Water		Aluminium		Copper	
Alternative dose computation	Dose (Gy cm^2)	$\frac{\text{Cavity Dose}}{\text{MC Dose}}$	Dose (Gy cm^2)	$\frac{\text{Cavity Dose}}{\text{MC Dose}}$	Dose (Gy cm^2)	$\frac{\text{Cavity Dose}}{\text{MC Dose}}$
Direct Monte-Carlo	4.860×10^{-12} ± 0.03%	-------	4.878×10^{-12} ± 0.13%	-------	6.491×10^{-12} ± 0.22%	-------
'Large cavity' integral	4.841×10^{-12} ± 0.06%	0.996 ± 0.001	4.857×10^{-12} ± 0.15%	0.996 ± 0.002	6.449×10^{-12} ± 0.24%	0.994 ± 0.003
B-G cavity integral	4.844×10^{-12} ± 0.09%	0.997 ± 0.001	4.855×10^{-12} ± 0.20%	0.995 ± 0.002	6.452×10^{-12} ± 0.26%	0.994 ± 0.003
S-A cavity integral (Δ = 1.004 keV)	4.881×10^{-12} ± 0.11%	1.004 ± 0.001	4.910×10^{-12} ± 0.2%	1.007 ± 0.003	6.531×10^{-12} ± 0.36%	1.006 ± 0.005

Table 7.1: **(b) The direct Monte-Carlo (MC) dose (Gy/incident photon fluence) compared with dose estimated by three different cavity integrals in a small cylindrical cavity in a homogeneous water phantom irradiated by a 10 MeV photon beam: The 'large cavity' integral, B-G cavity integral and S-A cavity integral are also known as collision kerma, cema and restricted cema respectively. The dose and the photon and electron fluences were scored in a voxel of dimensions 2 g cm^{-2} diameter, 1 g cm^{-2} thickness located at 10.5 g cm^{-2} depth; the statistical (Type A) uncertainties are ± 1 standard deviations.**

	10 MeV photon beam					
	Water		Aluminium		Copper	
Alternative dose computation	Dose (Gy cm^2)	$\frac{\text{Cavity Dose}}{\text{MC Dose}}$	Dose (Gy cm^2)	$\frac{\text{Cavity Dose}}{\text{MC Dose}}$	Dose (Gy cm^2)	$\frac{\text{Cavity Dose}}{\text{MC Dose}}$
Direct Monte-Carlo	$2.233\times10^{-11} \pm 0.08\%$	-------	$2.395\times10^{-11} \pm 0.18\%$	-------	$3.066\times10^{-11} \pm 0.23\%$	-------
'Large cavity' integral	$2.168\times10^{-11} \pm 0.15\%$	0.971 ± 0.002	$2.322\times10^{-11} \pm 0.18\%$	0.969 ± 0.002	$2.960\times10^{-11} \pm 0.25\%$	0.966 ± 0.004
B-G cavity integral	$2.230\times10^{-11} \pm 0.10\%$	0.999 ± 0.001	$2.393\times10^{-11} \pm 0.25\%$	0.999 ± 0.003	$3.058\times10^{-11} \pm 0.28\%$	0.998 ± 0.004
S-A cavity integral (Δ = 1.007 keV)	$2.244\times10^{-11} \pm 0.10\%$	1.005 ± 0.001	$2.411\times10^{-11} \pm 0.23\%$	1.007 ± 0.003	$3.087\times10^{-11} \pm 0.\ 3\%$	1.007 ± 0.004

7.3 Results and Discussion

7.3.1 Self-consistency of conventional cavity theories

Tables 7.1(a) and (b) compare the direct MC-derived absorbed dose in the cylindrical scoring voxel, $(D_{\text{med}})_{\text{MC}}$, with the expressions for dose of the various 'cavity integrals', using the photon and electron fluence spectra at 2.5 g cm^{-2} depth in 1 MeV (table 7.1(a)) and at 10.5 g cm^{-2} in 10 MeV (table 7.1(b)) photon beams in the three media (water, aluminium and copper); note that these depths ensure quasi-CPE. The data demonstrate firstly a high degree of consistency between the different forms of cavity integral and secondly the very good agreement between the dose derived from equations (7.2)–(7.5) and the dose computed with DOSRZnrc. It can be noted that the 'dose' from the 'large cavity' integral, equation (7.2), which is the collision kerma, $(K_{\text{col}})_{\text{med}}$, is expected to be lower than $(D_{\text{med}})_{\text{MC}}$ as the factor β ($=D/K_{\text{col}}$) is always greater than unity (Attix 1986, Kumar *et al* 2015a). The difference is ≈ 0.5% at 1 MeV (table 7.1a) and ≈ 3% at 10 MeV (table 7.1b); the increased discrepancy at the higher photon energy is due to the greater range of the secondary electrons. Further, the dose determined using the Bragg-Gray integral, or cema (equation (7.4)), might be expected to be very slightly lower than $(D_{\text{med}})_{\text{MC}}$ due to contributions to the 'cavity' dose from the *incoming* (energetic) δ-rays generated 'upstream' being slightly greater than the energy removed by δ-rays of corresponding energy exiting the cavity. The S-A cavity dose $[D_{\text{S-A}}(\Delta)]_{\text{med}}$ (equation (7.5)) was consistently about 0.6% greater than $(D_{\text{med}})_{\text{MC}}$ for reasons which are not clear; note that Δ was set to the lowest possible value (≈ 1 keV). The next section deals with what happens to $D_{\text{S-A}}(\Delta)/D_{\text{MC}}$ at increasingly large Δ.

7.3.2 The relationship between the direct Monte-Carlo dose and the Spencer-Attix cavity integral at increasing values of Δ

7.3.2.1 The physics behind the decrease of ($D_{\text{S-A}}(\Delta)/D_{\text{MC}}$) with increasing Δ in photon-irradiated media

Figure 7.1 shows ($D_{\text{S-A}}(\Delta)/D_{\text{MC}}$) as a function of the cut-off energy, Δ, in water irradiated by 1-MeV photons; the scoring region is a small cylinder at 2.5 cm depth. The geometry was carefully designed to minimize the amount of photon scatter (see sub-section 7.2.3.1). Also shown is the fraction of the total energy transferred (in Compton interactions) to electrons with initial kinetic energies above Δ, $F(k, \Delta)$, where k = 1 MeV. There is very close agreement between these two quantities, thereby confirming our explanation for the decrease of ($D_{\text{S-A}}(\Delta)/D_{\text{MC}}$) with increasing Δ. Furthermore, it is seen that ($D_{\text{S-A}}(\Delta)/D_{\text{MC}}$) lies slightly below F(1 MeV, Δ), which is consistent with the simulated irradiation geometry not being 100% free from scattered photons.

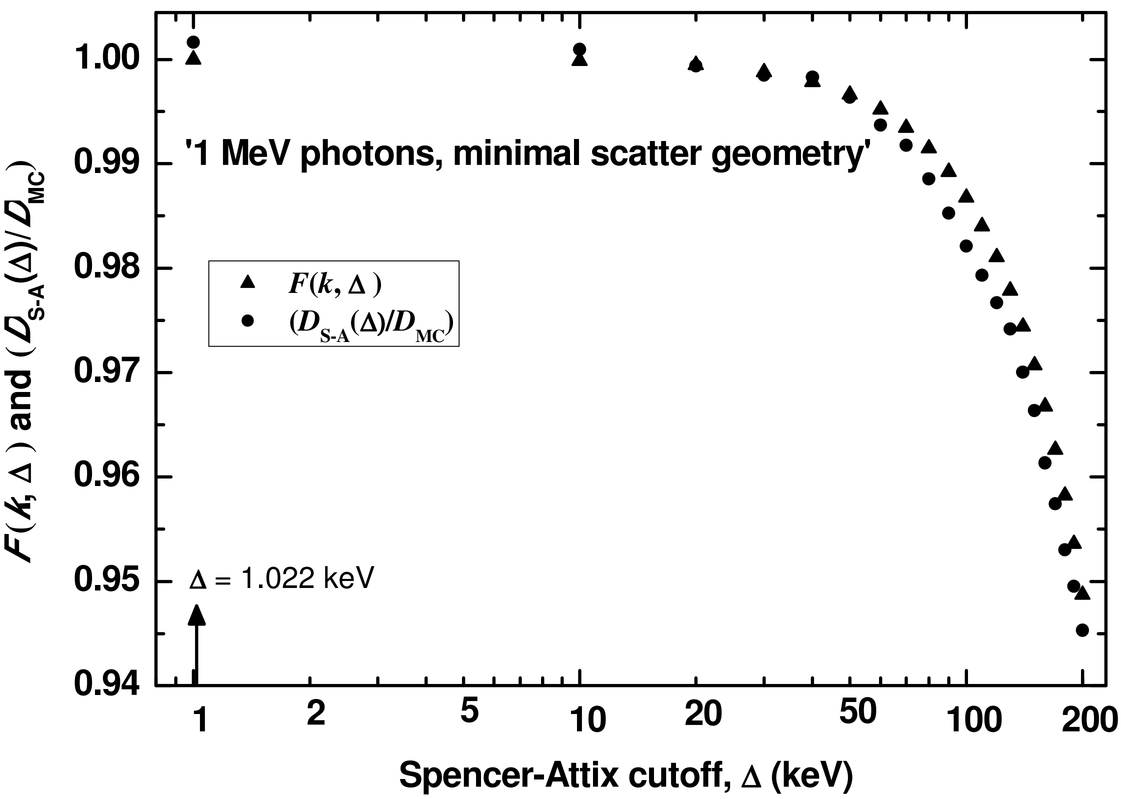

Figure 7.1: **The ratio of Spencer-Attix dose to direct Monte-Carlo dose, ($D_{S\text{-}A}(\Delta)/D_{MC}$), as a function of the cut-off delta for a 1-MeV photon beam in water, minimal scatter geometry (see below),compared to the fraction of the total energy transfer to Compton electrons from electrons with initial (kinetic) energy above delta $F(k, \Delta)$ (see equation (7.7)). The Monte-Carlo dose, D_{MC}, per incident fluence, was scored in a water voxel (2 cm diameter, 1cm thickness) at 2.5 cm depth. The total electron (+positron) fluence spectrum, per incident fluence, was scored in the identical water voxel. The dimensions of the water phantom (a cylinder of 2 cm diameter, 3 cm height/thickness) were chosen to minimize the amount of (Compton) scatter.**

7.3.2.2 $\left(D_{S\text{-}A}(\Delta)/D_{MC}\right)$ as a function of Δ and radiation quality

Figures 7.2(a)-2(c) show ($D_{S\text{-}A}(\Delta)/D_{MC}$) versus Δ, in water, for beam energies ranging from 50 to 300 keV as well as 'clinical' kilovoltage (50 kV to 250 kV) and megavoltage beams (Co-60 γ-rays and clinical linac spectra (for point sources) of 6, 10 and 15 MV); figure 7.2(c) also contains results for monoenergetic 10 MeV photon *and* electron beams.

Energy deposition by 'primary' charged particles (i.e. pair electrons and positrons, Compton electrons and photoelectrons) that have *initial* energies *below* Δ is excluded from the Spencer-Attix cavity integral which, by definition, only extends down to Δ. Consequently the Spencer-Attix cavity dose falls for all Δ above a quasi-threshold energy Δ_{th}, defined (loosely) such that 'primary' electrons with initial energies below Δ_{th} make a negligible contribution to the total energy deposition; a reasonable 'working definition' is that Δ_{th} is the value of Δ such ($D_{S\text{-}A}(\Delta)/D_{MC}$)=0.98. Figures 7.2 (a)-(c) demonstrate the strong beam-quality dependence of Δ_{th} (see the discussion below on tables 7.2a and 7.2b).

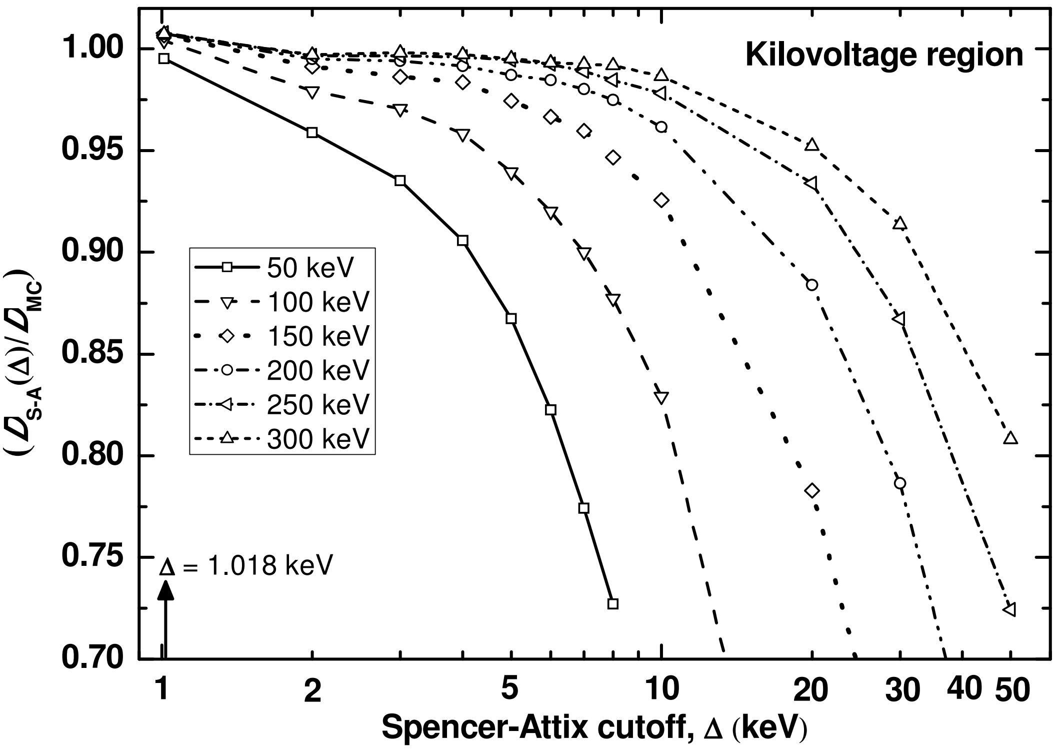

Figure 7.2: **(a) Ratio of Spencer-Attix dose to MC-dose, ($D_{S\text{-}A}(\Delta)/D_{MC}$), as a function of the cut-off energy Δ, for a scoring 'cavity' (20 mm diameter, 6 mm thickness) at 2.0 cm depth along the beam central axis, in a cylindrical water phantom (30 cm diameter, thickness 30 cm) for monoenergetic beams of energy 50 to 300 keV.**

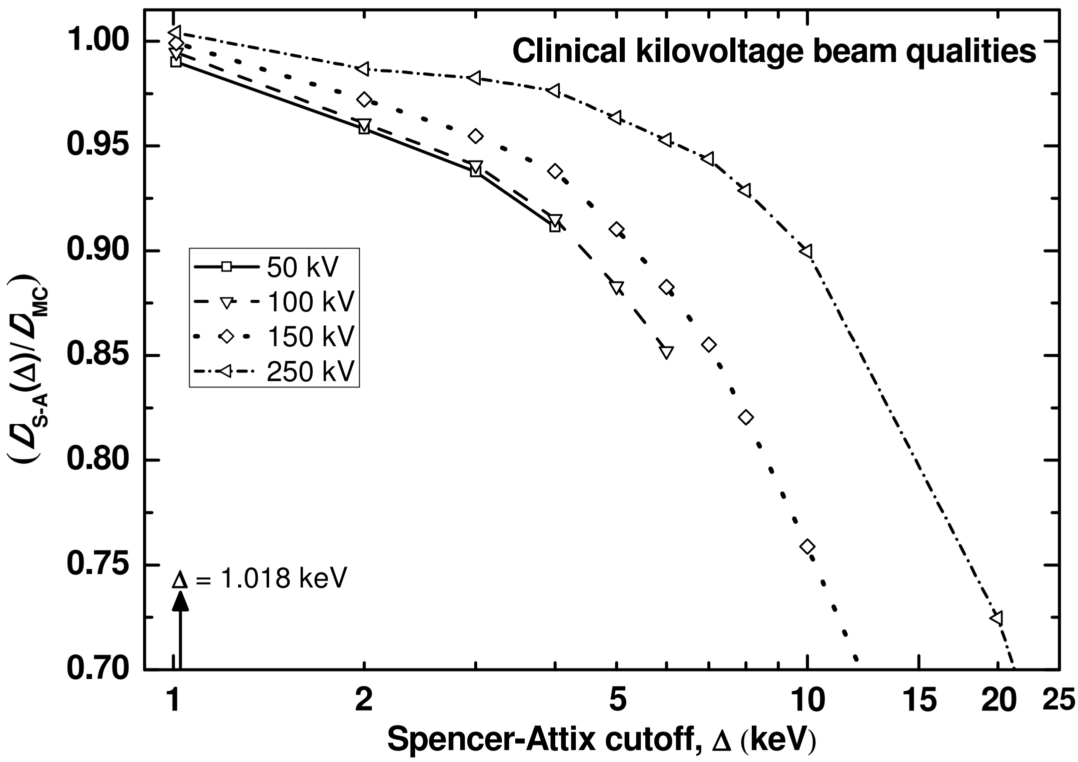

Figure 7.2: **(b) Ratio of Spencer-Attix dose to MC-dose, ($D_{S\text{-}A}(\Delta)/D_{MC}$), as a function of the cut-off energy Δ, for a scoring 'cavity' (20 mm diameter, 6 mm thickness) at 2.0 cm depth along the beam central axis, in a cylindrical water phantom (30 cm diameter, thickness 30 cm), for clinical kilovoltage beam qualities from 50 kV to 250 kV.**

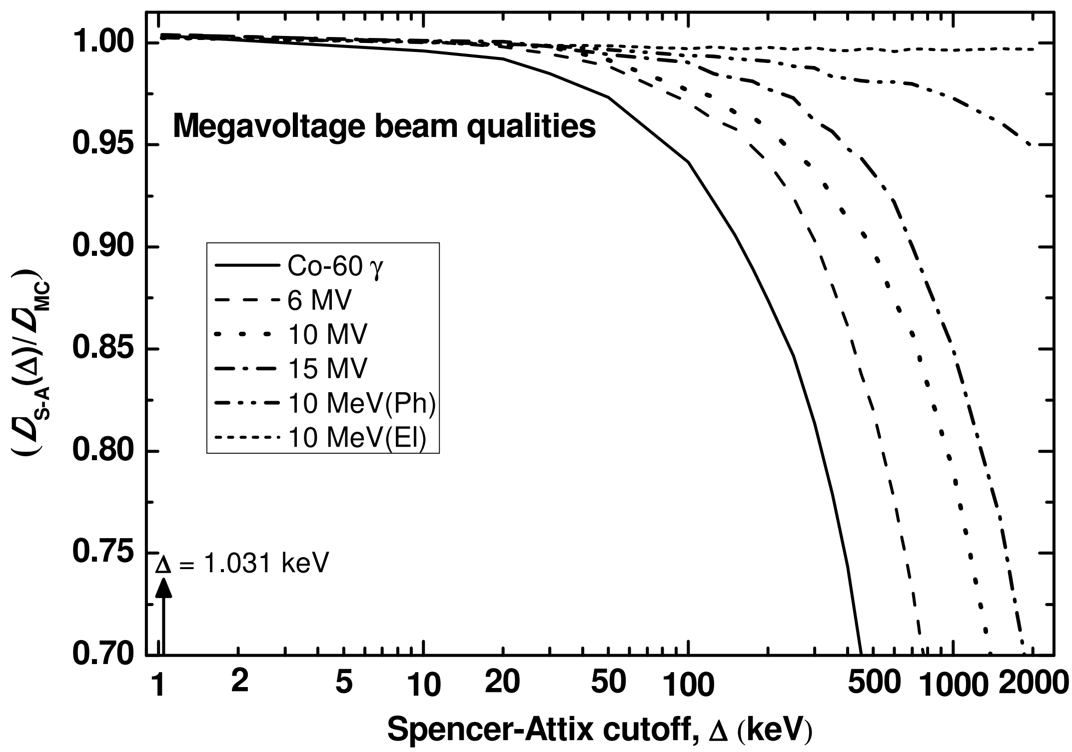

Figure 7.2: **(c) Ratio of Spencer-Attix dose to MC-dose, ($D_{S\text{-}A}(\Delta)/D_{MC}$), as a function of the cut-off energy Δ, for a scoring 'cavity'(20 mm diameter, 6 mm thickness) at 2.5 cm depth for a 10 MeV electron beam, 5 cm depth for Co-60 γ-rays, 6 10 and 15 MV x-rays and 10 cm depth for a 10 MeV photon beam, along the beam central axis in a cylindrical water phantom (diameter 30 cm, thickness 30 cm).**

($D_{S\text{-}A}(\Delta)/D_{MC}$) decreases with increasing Δ for *all* photon qualities, though much more slowly at high photon energies (figure 7.3c). However, in the case of the (10 MeV) *electron* beam it remains constant; the lack of any dependence on Δ in this case is due to the complete absence of any electrons with *initial* energies below any of the Δ values in the figure. There is an alternative way to interpret the dependence of ($D_{S\text{-}A}(\Delta)/D_{MC}$) on Δ and in particular how the curves in figures 7.2(a)-(c) vary with beam quality. For detectors with cavity sizes such that (the Spencer-Attix) $\Delta > \Delta_{th}$ (noting that Δ_{th} depends on photon beam quality, being higher for higher energies) the dose from photon interactions in the cavity material is non-negligible and therefore such detectors no longer fulfil the key Bragg-Gray condition that the 'direct photon dose' must be negligible compared with the dose due to electrons incident from outside the cavity. For such detector-beam quality combinations Spencer-Attix cavity theory is not applicable; instead one must resort to Burlin cavity theory (see sub-section 7.3.3).

Table 7.2(a) shows the values of Δ for which ($D_{S\text{-}A}(\Delta)/D_{MC}$) is equal to 0.98 and 0.95 respectively (i.e. moderately and less rigorous choices of Δ_{th} respectively), for photon energies from 50 keV to 300 keV; the values of R_{csda} and R_{csda}/DF in mm. of air corresponding to the above Δ_{th} are also given.

Figure 7.2: **(a) Ratio of Spencer-Attix dose to MC-dose, ($D_{S\text{-}A}(\Delta)/D_{MC}$), as a function of the cut-off energy Δ, for a scoring 'cavity' (20 mm diameter, 6 mm thickness) at 2.0 cm depth along the beam central axis, in a cylindrical water phantom (30 cm diameter, thickness 30 cm) for monoenergetic beams of energy 50 to 300 keV.**

Photon Energy	$(D_{S\text{-}A}(\Delta)/D_{MC}) = 0.95$			$(D_{S\text{-}A}(\Delta)/D_{MC}) = 0.98$		
	$\Delta_{0.95}$ (keV)	$R_{csda}(\Delta_{0.95})$ (mm)	$\frac{R_{csda}(\Delta_{0.98})}{DF}$ (mm)	$\Delta_{0.98}$ (keV)	$R_{csda}(\Delta_{0.98})$ (mm)	$\frac{R_{csda}(\Delta_{0.98})}{DF}$ (mm)
50 keV	2.38	0.20	0.14	1.42	0.08	0.05
100 keV	4.44	0.58	0.40	1.97	0.14	0.10
150 keV	7.74	1.53	1.05	4.40	0.57	0.39
175 keV	9.88	2.35	1.61	5.50	0.86	0.59
200 keV	11.50	3.08	2.11	7.04	1.30	0.89
250 keV	16.37	5.72	3.92	9.43	2.16	1.48
300 keV	20.59	8.58	5.88	11.91	3.27	2.24

Table 7.2: **(b) The Spencer-Attix cut-off energies Δ and corresponding R_{csda} in mm. of air for ($D_{S\text{-}A}(\Delta)/D_{MC}$) equal to 0.95 and 0.98 for various clinical photon beam qualities. The detour factor for air was taken as 1.46 (average value) as it varies very little with electron energy (see table 7.3(a)).**

Clinical beam quality	$(D_{S\text{-}A}(\Delta)/D_{MC}) = 0.95$			$(D_{S\text{-}A}(\Delta)/D_{MC}) = 0.98$		
	$\Delta_{0.95}$ (keV)	$R_{csda}(\Delta_{0.95})$ (mm)	$\frac{R_{csda}(\Delta_{0.98})}{DF}$ (mm)	$\Delta_{0.98}$ (keV)	$R_{csda}(\Delta_{0.98})$ (mm)	$\frac{R_{csda}(\Delta_{0.98})}{DF}$ (mm)
50 kV	2.44	0.21	0.14	1.33	0.07	0.05
100 kV	2.54	0.22	0.15	1.44	0.08	0.06
150 kV	3.28	0.34	0.24	1.71	0.11	0.08
250 kV	6.31	1.07	0.74	3.39	0.37	0.25
Co-60 γ	75.03	82.71	56.65	39.49	26.99	18.48
6 MV	170.24	326.18	223.41	74.18	81.10	55.55
10 MV	233.88	541.66	371.00	87.31	107.12	73.77
15 MV	379.91	1119.79	766.98	182.83	366.01	250.69

Table 7.2(b) gives the same quantities for clinical beam qualities 50-250 kV, Co-60 γ-rays and clinical linac spectra of 6, 10 and 15 MV. From these data it can be deduced that an air cavity with dimensions corresponding to a Spencer-Attix cut-off energy, Δ, of 10 keV (a value widely applied to

the air cavities of practical ion chambers e.g. Farmer and NACP designs (Andreo *et al* 2000)) will respond in a Bragg-Gray manner in photon beams of (monoenergetic) energies greater than 262 keV for ($D_{S\text{-}A}(\Delta)/D_{MC}$) = 0.98 or 177 keV for ($D_{S\text{-}A}(\Delta)/D_{MC}$) = 0.95. The data in table 7.2(b) are consistent with the findings of Ma and Nahum (1991) that no practical ionisation chamber fulfills the Bragg-Gray assumptions in kilovoltage x-ray beam qualities (i.e. 300 kV and below). Table 7.2(b) shows further that at megavoltage qualities, air cavities with dimensions of several centimetres (up to 25 cm in the case of 15 MV x-rays) should still behave in a Bragg-Gray manner. However, this does not imply that all other sources of deviation from B-G behaviour would remain negligible for such large air cavities e.g. displacement effects (Andreo *et al* 2000; Nahum 2009); see also the next section.

Table 7.3: **(a) Monte-Carlo derived R_{50}, R_{csda} and detour factors (=R_{csda}/ R_{50}) in silicon and air for electron energies from 10 keV to 4000 keV; R_{csda} values were generated with the *ESTAR* code/program (http://physics.nist.gov/PhysRefData/Star/Text/ESTAR.html).**

Photon Energy (keV)	Silicon (ρ = 2.33 g cm^{-3})			Air (ρ = 1.205×10^{-3} g cm^{-3})		
	R_{50} (cm)	R_{csda} (cm)	Detour factor (DF)	R_{50} (cm)	R_{csda} (cm)	Detour factor (DF)
10	7.547×10^{-5}	1.485×10^{-4}	1.968	1.628×10^{-1}	2.393×10^{-1}	1.470
15	1.518×10^{-4}	2.981×10^{-4}	1.963	3.325×10^{-1}	4.885×10^{-1}	1.469
20	2.508×10^{-4}	4.901×10^{-4}	1.957	5.531×10^{-1}	8.117×10^{-1}	1.468
30	5.091×10^{-4}	9.906×10^{-4}	1.946	1.133×10^{0}	1.661×10^{0}	1.467
50	1.239×10^{-3}	2.400×10^{-3}	1.937	2.781×10^{0}	4.076×10^{0}	1.466
100	4.045×10^{-3}	7.820×10^{-3}	1.933	9.200×10^{0}	1.347×10^{1}	1.464
150	7.907×10^{-3}	1.528×10^{-2}	1.933	1.812×10^{1}	2.650×10^{1}	1.462
200	1.255×10^{-2}	2.423×10^{-2}	1.931	2.888×10^{1}	4.217×10^{1}	1.460
300	2.344×10^{-2}	4.524×10^{-2}	1.930	5.430×10^{1}	7.907×10^{1}	1.456
500	4.912×10^{-2}	9.429×10^{-2}	1.920	-------	-------	-------
800	9.180×10^{-2}	1.754×10^{-1}	1.910	-------	-------	-------
1000	1.213×10^{-1}	2.312×10^{-1}	1.906	-------	-------	-------
2000	2.826×10^{-1}	5.099×10^{-1}	1.804	-------	-------	-------
3000	4.549×10^{-1}	7.781×10^{-1}	1.711	-------	-------	-------
4000	6.329×10^{-1}	1.036×10^{0}	1.636	-------	-------	-------

7.3.3 Transition in detector behaviour from 'Bragg-Gray' towards 'large cavity'

Table 7.3(a) presents the Monte-Carlo derived R_{50}, R_{csda} and the detour factor *DF* for silicon and air media for electron energies from 10 keV to 4000 keV. It is observed firstly that *DF* is greatest at low energies and secondly that it is higher in silicon, due to its higher atomic number, than in air. This is consistent with electron interactions in matter - multiple (elastic) scattering is strongest at low energies and at high atomic number. Table 7.3(b) presents the Spencer-Attix cut-off energies Δ corresponding to the silicon cavity at each pseudo-density, with and without the detour factor, derived from equation (7.10). The inclusion of the detour factor results in a near doubling of Δ, especially at silicon pseudo-densities of unity and above.

Table 7.3: **(b) The Spencer-Attix cut-off energies, Δ, derived from equation (7.10) as a function of the silicon pseudo-density. Δ_{DF} indicates that the Monte-Carlo-derived detour factors (equation (7.9)) were used; Δ indicates that the detour factor was assumed to be unity. The mean chord length (in cm) , *L*, of the cavity is equal to 0.144.**

Si density (g cm^{-3})	Δ(keV)	Δ_{DF}(keV)
0.002	9	13
0.005	15	23
0.01	20	34
0.05	50	86
0.10	80	129
0.25	150	229
0.50	207	362
1.00	321	592
1.75	520	913
2.33	634	1151
5.00	1263	2161
10.00	2160	3924

Figure 7.3(a) shows the S-A stopping power ratio, water-to-Si, $s^{\text{SA}}_{\text{w,Si},\Delta}$,as a function of the pseudo-density of the silicon detector for the 6 MV and 15 MV photon beams; the S-A cut-off energy, Δ, at the different ρ_{Si} was determined from equation (7.10) with *DF* from equation (7.9) and also *DF* = 1, as in table 7.3(b). The inclusion of the detour factor decreases the S-A water-to-Si ratio by ≈ 0.8% at a given value of the silicon pseudo-density. As Δ increases from ≈ 10 keV to ≈ 2 MeV, $s^{\text{SA}}_{\text{w,Si},\Delta}$ decreases

by almost 7% at both megavoltage qualities. This is in marked contrast to the extremely weak variation of the *clinically* relevant water-to-air ratio, $s^{SA}_{w,air,\Delta}$, with Δ: a decrease of only 0.25% as Δ increases from 10 to 50 keV (at any depth beyond the build-up region) in either a 6 MV or 15 MV beam[21]. This weak variation justifies the use of a 'nominal' Δ = 10 keV for the air cavity of the commonly employed *Farmer* design of ionisation chamber (Andreo *et al* 2000); Δ ≈ 16 keV results from using the mean chord length of the Farmer geometry (Buckley *et al* 2003) which further increases to Δ ≈ 20 keV with the application of *DF* = 1.46 from table 3(a). Increasing Δ from 10 to 20 keV results in only a 0.12% decrease in $s^{SA}_{w,air,\Delta}$.

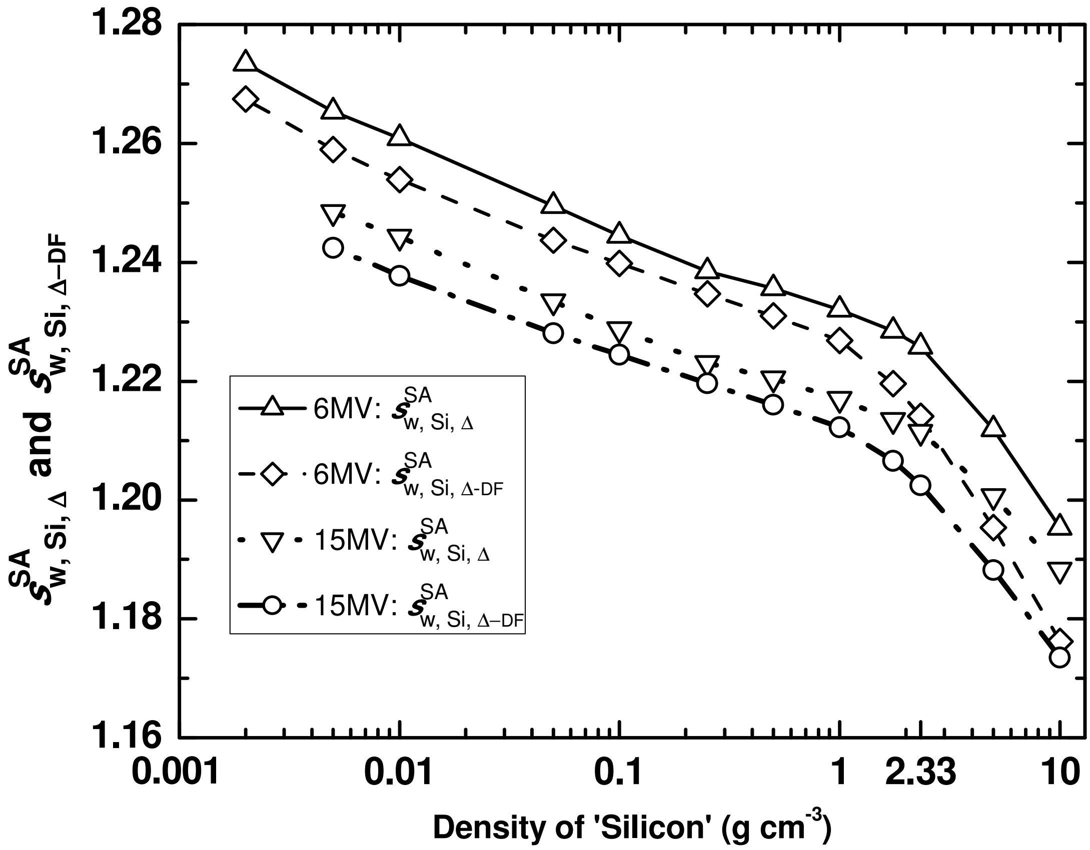

Figure 7.3: **(a) The variation of the S-A stopping-power ratio (spr), water-to-Si, with Δ-values corresponding to silicon pseudo-densities, determined with and without the detour factor *DF*, for 6 MV and 15 MV photon beams at 5 cm depth for a beam radius of 5.55 cm (equivalent to a '10 cm ×10 cm' field size) defined on the phantom surface (the S-A spr curves incorporating the detour factor are also given in figures 7.3(b) and 7.3(c)).**

Figures 7.3(b)-(c) shows the variation of the Monte-Carlo dose ratio, $(D_w/D_{Si})_{MC}$, the S-A stopping power ratio, water-to-Si, $s^{SA}_{w,Si,\Delta}$, the Burlin dose ratio i.e. $\left(f_{w,Si}\right)_{Bu}$ (left hand ordinate) and

[21] Unpublished calculations consistent with e.g. the data in Table 10.2 of Attix (1986).

the fraction of dose in the Si cavity due to direct photon interactions (right hand ordinate) for the 6 MV and 15 MV photon beams. At the lowest densities in the simulation, corresponding to those of a gas, the silicon cavity should act in a quasi-perfect Bragg-Gray manner. A comparison between $(D_w/D_{Si})_{MC}$ and $s^{SA}_{w,Si,\Delta}$ shows virtually perfect agreement at 6 MV i.e. within the MC error bars (Si densities of 0.002-0.005 in figure 7.3(b)) and differences of ≈ 0.6% or less at 15 MV. In contrast, the unrestricted (aka 'Bragg-Gray') stopping-power ratio, $s^{BG}_{w,Si}$, is a full 2.6% and 2.5% below $s^{SA}_{w,Si,\Delta}$ in the 'gas density' (i.e. Bragg-Gray) region, at 6 MV and 15 MV respectively. The superior agreement at gas densities of $(D_w/D_{Si})_{MC}$ with the S-A ratio compared with the unrestricted, or BG, stopping-power ratio constitutes a powerful validation of Spencer-Attix cavity theory.

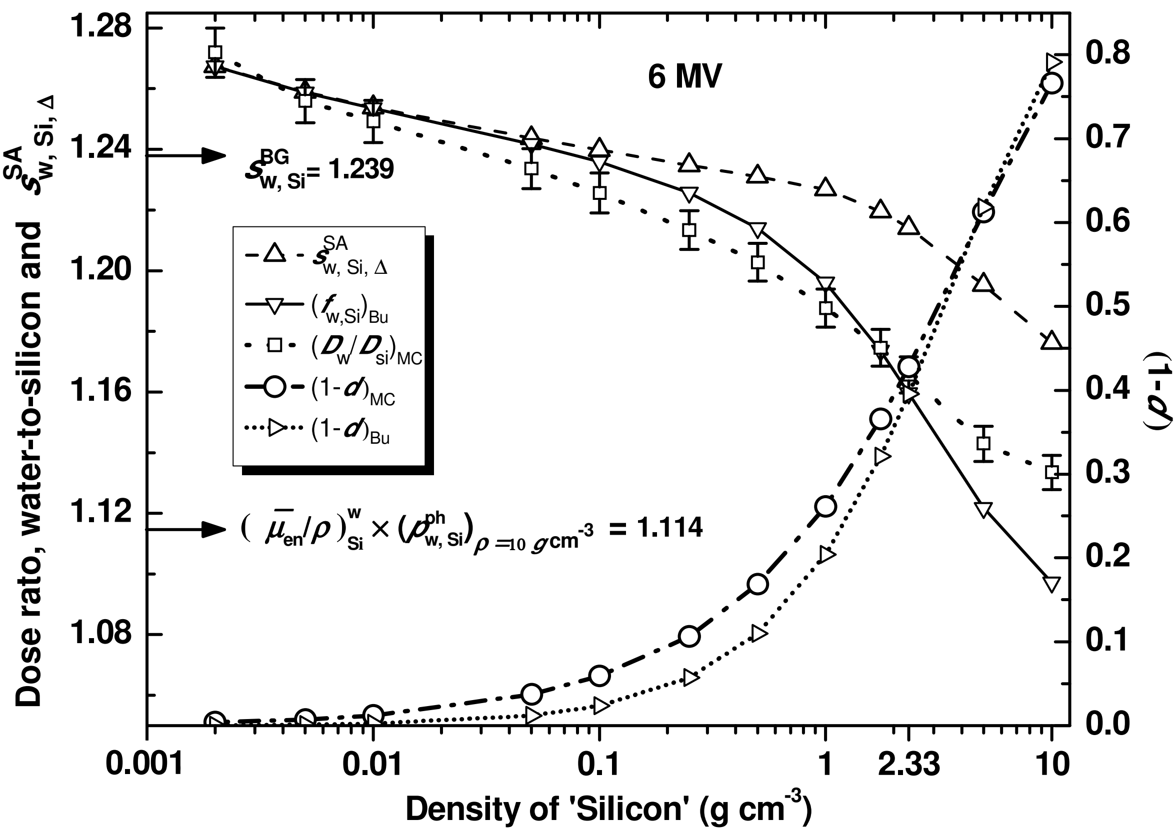

Figure 7.3: **(b) 6 MV photon beam: variation of the Monte-Carlo dose ratio, $(D_W/D_{Si})_{MC}$, the S-A stopping power ratio (spr), water-to-Si, $s^{SA}_{w,Si,\Delta}$, and the Burlin cavity ratio, $\left(f_{w,Si}\right)_{Bu}$ (l. h. axis) with the pseudo-density of the silicon cavity (of fixed dimensions) located at depth 5 cm. The r.h. axis shows the fraction of dose to the Si cavity due to *direct photon interactions*, (1-*d*), derived from Monte-Carlo and from the Burlin-Janssens approximate formulas. An arrow indicates the value of the (density-independent) unrestricted spr, $s^{BG}_{w,Si}$. A second arrow indicates the position of the 'large photon cavity' dose ratio, corrected for photon fluence perturbation, $\left(\overline{\mu_{en}}/\rho\right)^{w}_{Si} \times \left(p^{ph}_{w,Si}\right)_{\rho=10\,g\,cm^{-3}}$.**

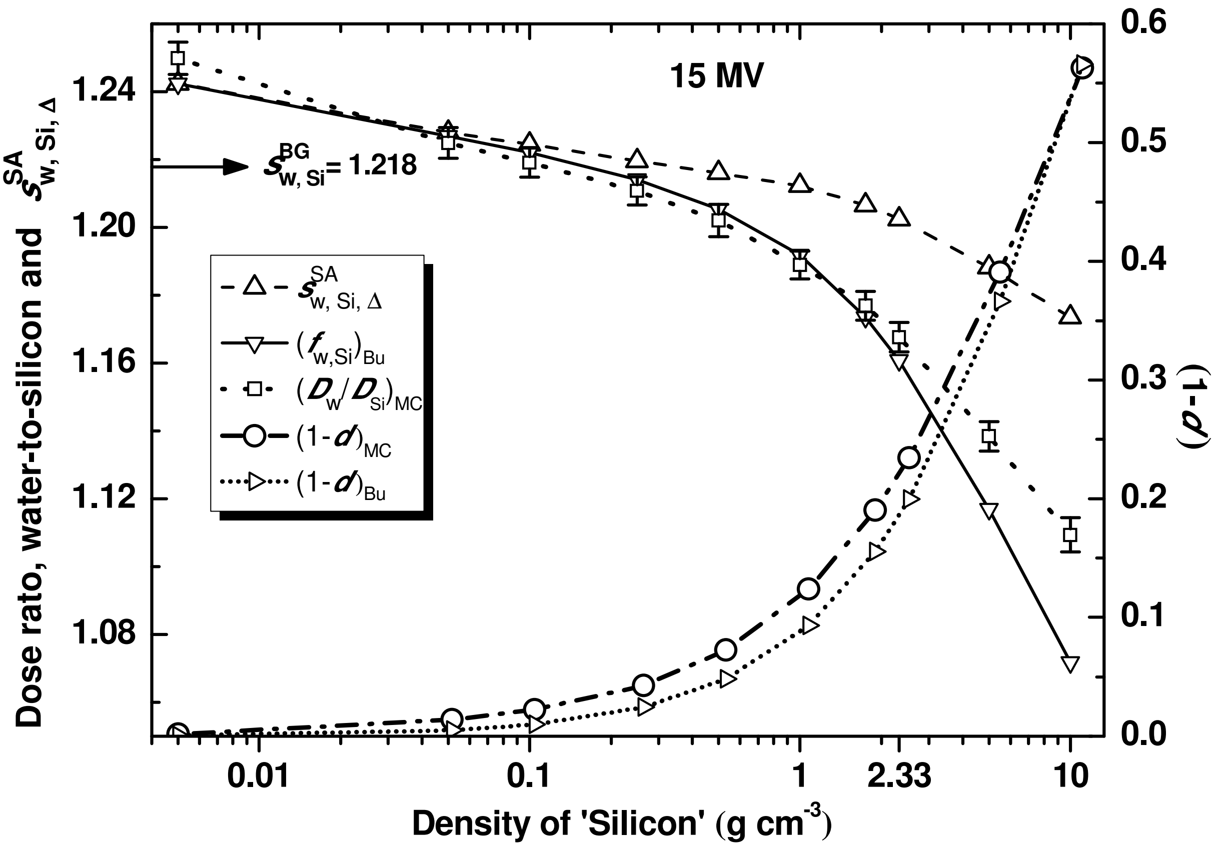

Figure 7.3: **(c) 15 MV photon beam: variation of Monte-Carlo dose ratio, $(D_W/D_{Si})_{MC}$, the S-A stopping power ratio (spr), water-to-Si, $s^{SA}_{w,Si,\Delta}$, and the Burlin cavity ratio, $\left(f_{w,Si}\right)_{Bu}$ (l. h. axis) with the pseudo-density of the silicon cavity (of fixed dimensions) located at 5 cm depth. The r.h. axis shows the fraction of dose to the Si cavity due to *direct photon interactions*, (1-*d*) derived from Monte-Carlo and with the Burlin-Janssens approximate formulas. An arrow indicates the value of the (cavity size/density-independent) unrestricted spr, $s^{BG}_{w,Si}$. The 'large photon cavity' dose ratio $\left(\mu_{en}/\rho\right)^{w}_{Si}\times\left(p^{ph}_{w,Si}\right)_{\rho=10\text{ g cm}^{-3}}$ = 0.996 lies outside the range of dose ratios on the l.h.s. ordinate.**

Should a 'displacement' correction be made for the finite size of the silicon gas density as is commonly applied to typical 'clinical' instruments such as a Farmer chamber (Andreo *et al* 2000, Nahum 2009)? In principle such a correction, generally denoted by p_{dis}, is required but in this case the very small dimension (in the beam direction) of the silicon cavity, 2.0 mm, renders this effect negligible (p_{dis} < 1 but is within 0.1% of unity at 6 MV, and even closer to unity at 15 MV)[22].

As the detector density increases, the secondary electron ranges in the silicon cavity decrease and the detector response moves into the 'intermediate' region. The Burlin ratio is within ≈ 2% of the MC dose ratio all the way from ρ = 0.002 g cm^{-3} to 5 g cm^{-3} at 6 MV and the agreement is even closer at 15 MV. At a density of 5 g cm^{-3} around ≈ 60% at 6 MV and ≈ 40% at 15 MV of the cavity dose is

[22] Data derived from unpublished computations of depth-doses in water for 6 and 15 MV beams.

due to photon interactions in the silicon cavity. At the highest density, 10 g cm^{-3}, the Burlin weighting factor, $(1 - d)_{\mathrm{MC}}$, for the 15 MV photon beam has only reached 0.56 which is still far from the 'large photon cavity' condition. The Monte-Carlo dose ratio, $\left(D_{\mathrm{w}} / \overline{D}_{\mathrm{Si}}\right)_{\mathrm{MC}}$, at this density is 1.109, approximately halfway between the 'small cavity' and 'large cavity' limiting cases of 1.242 (i.e. $s^{\mathrm{SA}}_{\mathrm{w,Si},\Delta}$) and 0.996 (see below) respectively as one would expect. In case of the 6 MV photon beam, at ρ_{Si} = 10 g cm^{-3} $\left(D_{\mathrm{w}} / \overline{D}_{\mathrm{Si}}\right)_{\mathrm{MC}}$ = 1.133 which is within 1.7% of the 'large cavity' limiting case of 1.114 (see below). At this highest density the Monte-Carlo-derived 'Burlin' weighting factor, $(1 - d)_{\mathrm{MC}}$ for the 6 MV beam has reached 0.76 i.e. significantly closer to unity than for the more energetic 15 MV quality.

A further point can be made regarding the Burlin cavity expression (equation (7.12)). For detectors with 'intermediate' cavity sizes, the energies of those electrons in the cavity which originate in the surrounding medium will predominantly be above Δ in energy; therefore it is entirely appropriate that the (Spencer-Attix) integrals used to evaluate the stopping-power ratio (see equation (7.11)) do *not* extend below Δ. Conversely the electrons liberated by photon interactions in the cavity material should predominantly have energies *below* Δ; this will not be the case if the μ_{en}/ρ-ratio in equation (7.12) is evaluated in the conventional manner using equation (7.13). Instead what is ideally required in this expression is a special form of the $\mu_{\mathrm{en}}(k)/\rho$ restricted to energy transfers to electrons below Δ (Brahme 1978).

In the Appendix - C an expression for a photon-fluence perturbation factor was developed. This has been evaluated for the silicon cavity with ρ_{Si} = 10 g cm^{-3}, the highest value attained in present simulation, even though, as shown above, the 'large photon cavity' situation has not yet been reached, especially at 15 MV. Nevertheless the product of the mass-energy absorption coefficient ratio and this perturbation factor (equation (C.3)) has been evaluated. At 6 MV, $\left(\overline{\mu}_{\mathrm{en}}/\rho\right)^{\mathrm{w}}_{\mathrm{Si}}$ = 1.076 and $p^{\mathrm{ph}}_{\mathrm{w,Si}}$ = 1.035 yielding a 'large photon cavity' ratio of 1.114 which is indicated by an arrow in figure 7.3(b). At 15 MV, $\left(\overline{\mu}_{\mathrm{en}}/\rho\right)^{\mathrm{w}}_{\mathrm{Si}}$ = 0.974 and $p^{\mathrm{ph}}_{\mathrm{w,Si}}$ = 1.022, yielding a 'large photon cavity' factor of 0.996 which falls below the range of values on the right hand ordinate in figure 7.3(c). Figures 7.3(b) and 7.3(c) also show the Burlin weighting factor, $(1 - d)$. It is observed that there is good agreement between $(1\text{-}d)_{\mathrm{MC}}$ and $(1\text{-}d)_{\mathrm{Bu}}$, especially at the lower end and upper end of the curves.

Figure 7.3(d) compares the Burlin 'd' weighting factor computed by Monte-Carlo, d_{MC}, with $(D_{\mathrm{S\text{-}A}}(\Delta)/D_{\mathrm{MC}})$ for a water phantom as a function of the Spencer-Attix cut-off energy, Δ for the 6 and 15 MV qualities; d_{MC} for the Si cavity with the various pseudo-densities was linked to Δ using equations (7.9) and (7.10), applying the electron detour factor for silicon. The excellent agreement between these two quantities (differences never more than 5.1 %) can be interpreted as a strong validation of the new ($D_{S-A}(\Delta)/D_{MC}$) metric. Note however that if *DF* is set to unity the agreement is poor.

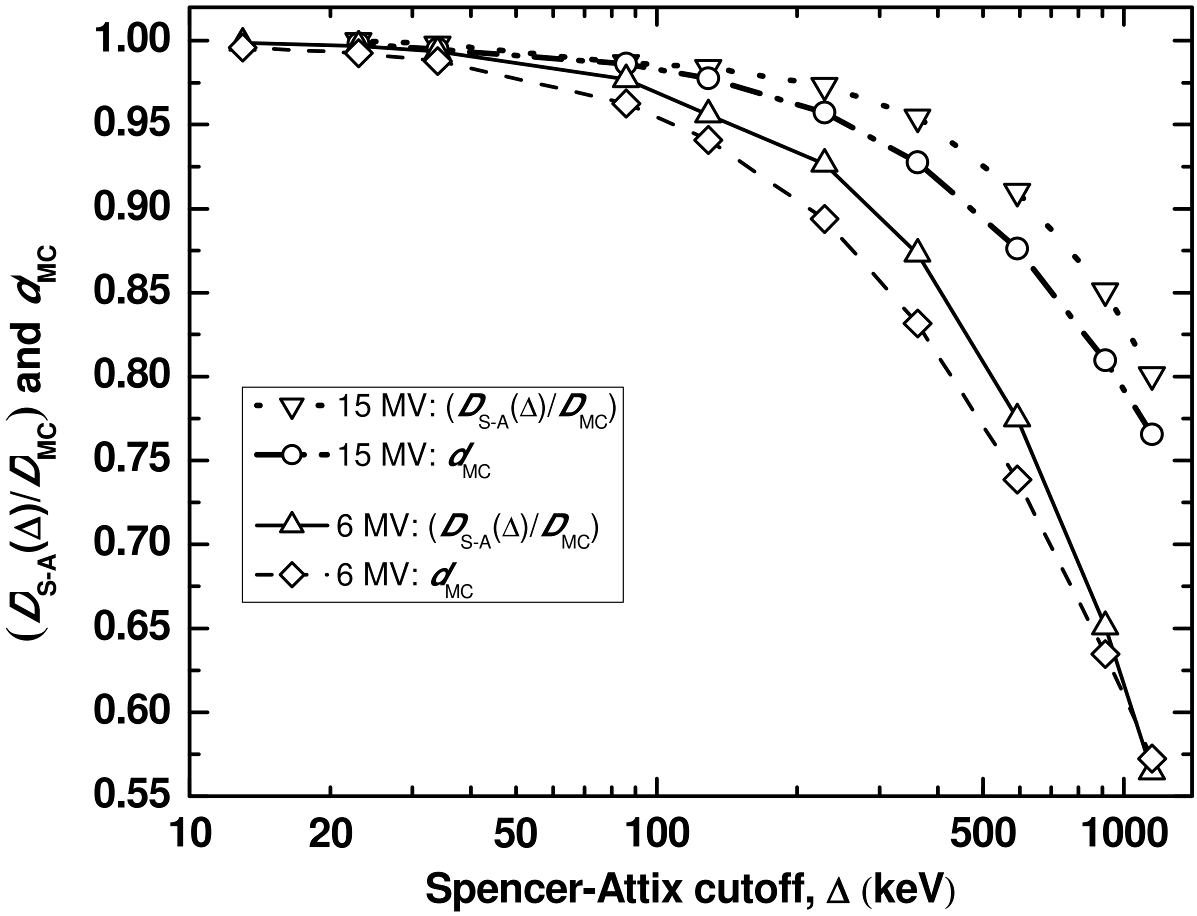

Figure 7.3: **(d) For 6 MV and 15 MV photon beams: comparison of the Burlin '*d*' computed by Monte-Carlo, d_{MC}, for cavities of each silicon pseudo-density, with ($D_{S-A}(\Delta)/D_{MC}$) as a function of Δ; the detour factor for silicon at each Δ has been applied in linking the silicon pseudo-density to Δ using equation (7.10); the Si cavity has diameter 0.23 cm and height 0.2 cm.**

7.4 Summary and Conclusions

The main findings of this work are summarized here:

1. It has been confirmed that the three main forms of 'cavity integral' ('large photon detector' or collision kerma, Bragg-Gray or cema, Spencer-Attix or restricted cema for Δ < 20 keV), are

consistent with each other and closely equal to the 'direct Monte-Carlo-derived dose in water, aluminium and copper media irradiated by 1- and 10-MeV photons under quasi-CPE.

2. The decrease in the quantity $D_{S\text{-}A}(\Delta)/D_{MC}$ as Δ increases above ≈20 keV in photon-irradiated media is investigated in detail. By reference to the Klein-Nishina differential cross-section it is explicitly demonstrated that this Δ-dependence is due to the non-inclusion of secondary electrons with initial kinetic energies below Δ.

3. The value of Δ above which $D_{S\text{-}A}(\Delta)/D_{MC}$ falls below ≈ 0.95-0.98 can be used as a metric for the maximum size of a cavity exhibiting Bragg-Gray behaviour.

4. For a small silicon cavity with pseudo-density varying from that of a gas to 10 g cm^{-3} situated at a depth in a water phantom irradiated by 6 and 15 MV photon beams, the transition from Bragg-Gray through 'intermediate', or Burlin, towards 'large photon detector' behaviour has been demonstrated. A Monte-Carlo-derived electron detour factor has been applied to link silicon density with the Spencer-Attix Δ. The MC-derived water-to-silicon dose ratio agrees closely with the Spencer-Attix ratio at gas-like densities and the agreement with the Burlin ratio at higher densities is satisfactory.

5. The close agreement between $D_{S\text{-}A}(\Delta)/D_{MC}$ and the Monte-Carlo-derived Burlin weighting factor, *d*, as a function of Si pseudo-density, provided that the electron detour factor is applied, suggests that $D_{S\text{-}A}(\Delta)/D_{MC}$ can be used to estimate *d*.

CHAPTER 8

Summary and Conclusions

This chapter summarizes the major findings of the thesis and outlines the scope for *future* work.

In chapter 2, a set of D/K, D/K_{col} and $\overline{X}$ values has been generated in a consistent manner by Monte-Carlo simulation for water, aluminium and copper and for photon energies from 50 keV to 25 MeV (including 6-15 MV). Beyond the build-up region D/K is almost always less than or equal to unity and D/K_{col} greater than unity, and these ratios are virtually constant with increasing depth. D/K decreases and D/K_{col} increases with increasing beam quality. The difference between K and K_{col} increases with energy and with the atomic number of the irradiated materials. A simple analytical expression for $\overline{X}$, denoted by $\overline{X}_{\mathrm{emp}}$, the distance 'upstream' from a given voxel to the mean origin of the secondary electrons depositing their energy in this voxel, was proposed: $\overline{X}_{\mathrm{emp}} \approx 0.5R_{\mathrm{csda}}(\overline{E_0})$, where $\overline{E_0}$ is the mean initial secondary electron energy, and validated. Expressions for D/K and D/K_{col} based on the above expression for $\overline{X}_{\mathrm{emp}}$ are also given (Paper III).

In chapter 3, it has been demonstrated that over a large volume the 'area under the kerma, K, curve' vs depths exceeds the 'area under the dose curve', i.e. the energy content integrated from the kerma distribution exceeds the energy content integrated from the dose distribution over a large volume. Therefore over large irradiated volumes kerma does not conserve energy whereas collision kerma and a special form of kerma, which is denoted by K_{ncpt}, (ncpt $\equiv$'no charged-particle transport'), do conserve energy. For a 25 MeV broad, parallel photon beam this 'violation' amounts to 8.6%, 14.2% and 25.5% in large volumes of water, aluminium and copper respectively but only 0.6% for a 'clinical' 6 MV beam in water. This analysis has highlighted the role played by secondary bremsstrahlung in determining kerma at large depths and also quantified the magnitude of the errors made in deriving kerma by setting a high electron/positron kinetic energy cut-off *ECUT* (Paper V).

In chapter 4, it was demonstrated that the *physical density* of the active volume of a detector is the key factor in its response in a medium irradiated by beams of non-equilibrium field size, rather than atomic number differences between detector and medium. Relative to wide-field readings, it was found that *high*-density detectors *over*-read, and *low*-density detectors *under*-read (relative to the density of water, the reference medium) in non-equilibrium small photon fields (Paper I).

Based on the findings in chapter 4, a modified form of cavity theory has been developed in chapter 5 to take account the 'density effect' in small fields. It has been shown that when compared to water, the over-reading of *high*-density detectors is the result of an increased number of internally generated electrons that do not escape from the active volume. The density-dependence can be minimized either by constructing detectors with sensitive volumes having similar densities to water, or by limiting the thickness of sensitive volumes in the direction of the beam. Regular 3 × 3 cm^2 or 4 × 4 cm^2 fields are useful for small-field detector calibration (Paper II).

Following on from chapters 4 and 5, with the aid of Monte-Carlo simulations the major deviations from Bragg-Gray behaviour exhibited by ionization chambers with small (air) volumes (e.g. the 'PinPoint 3D' chamber) in small megavoltage photon fields are quantified in chapter 6; the EGSnrc Monte Carlo code system has been employed to investigate this 'Bragg-Gray breakdown'. A water-to-air perturbation factor has been defined and computed as the ratio of the photon-generated 'total' electron fluence, integrated over all energies, in undisturbed water to that in a small air cavity; the values are 1.323 and 2.139 for the 0.25 x 0.25 cm^2 field size in 6 MV and 15 MV 'full linac' geometry (FLG) respectively. For the 15 MV FLG, for field sizes of 1 × 1 cm^2 and smaller, not only the magnitude but also the 'shape' of the 'total' electron fluence spectra in the air cavity differs from that in the water cavity, due to the combined effect of electronic disequilibrium, source occlusion and volume-averaging. The consequences of differences in spectral shape are explored in terms of cavity theory and a theoretical expression for this 'shape factor' has been formulated. The physics of this 'Bragg-Gray breakdown' in low-density (gas) detectors in non-equilibrium field sizes is fully explained both diagrammatically and theoretically, making explicit reference to the Fano theorem (Paper IV).

In chapter 7, the self-consistency of conventional cavity theories (large photon detector, Bragg-Gray and Spencer-Attix) has been examined by evaluating the so-called 'cavity integrals' ('large photon detector' or collision kerma, Bragg-Gray or cema, Spencer-Attix or restricted cema) in different materials (water, aluminium and copper) for photon beams of 1 MeV and 10 MeV under quasi-CPE. These three forms of 'cavity integral' (for Δ < 20 keV in the case of Spencer-Attix) are shown to be consistent with each other. The ratio of Spencer-Attix dose to direct Monte-Carlo dose ($D_{S\text{-}A}(\Delta)/D_{MC}$) decreases steadily as Spencer-Attix cut-off energy Δ increases about ≈ 20 keV in photon-irradiated media. It is explicitly demonstrated that this dependence on Δ is due to the non-inclusion of secondary electrons with initial kinetic energies below Δ. The value of Δ above which $D_{S\text{-}A}(\Delta)/D_{MC}$ falls below ≈ 0.95-0.98 can be used as a metric for the maximum size of a detector behaving in a *Bragg-Gray* manner in a medium irradiated by a given photon-beam quality (under quasi CPE); a typical air-filled ion chamber is a Bragg-Gray detector at all (monoenergetic) photon beam energies ≥ 260 keV. Excellent agreement between $D_{S\text{-}A}(\Delta)/D_{MC}$ and the Monte-Carlo-derived Burlin weighting factor, '*d*' at different Si pseudo-densities (provided a correction for electron 'detours' is made) suggests a further application for the $D_{S\text{-}A}(\Delta)/D_{MC}$ ratio: as an alternative way to estimate *d* (Paper VI).

The scope for future work includes (i) formulating a composite expression for a 'quasi-Burlin dose ratio' for an intermediate cavity in a bremsstrahlung beam by recognising that the cavity response can be characterized as a quasi-perfect 'large photon detector' for the lowest energies, an (approximate) ‘Burlin’ detector for the intermediate energies, and a quasi Bragg-Gray detector for the highest energies of the bremsstrahlung beam spectra; (ii) a critical evaluation of the validity of the Fano theorem when the density-dependence of the interaction cross-sections in various media (e.g. the density or polarization effect in condensed media) is explicitly modelled by Monte-Carlo codes.

Appendix-A

A.1 Approximating ε(FS) as being independent of cavity density

In obtaining the link between $P_{\rho-}$ and s_{ee} described by equation (5.22), a multiplicative factor ε(FS) was used to model the field-size dependence of the dose imparted to a cavity by electrons energized outside it. In particular ε(FS) was approximated as being independent of density, leading to equation (5.19)

$$\overline{D}_{\text{external}}\left(\text{FS}, 5, \rho, \frac{\text{MU}_{\text{ref}}}{\left(\text{OF}(\text{FS})/s_{ee}(\text{FS})\right)}\right) \approx D\left(1-J_{\text{cav}}(\rho)\right)\varepsilon(\text{FS})$$

To justify this approximation consider the geometry of figure 5.2, initially replacing the spherical cavity with a long, narrow *cylindrical* cavity of the same radius r, aligned coaxially with the radiation beam. Electrons generated more than d_{equilib} off-axis fail to reach the cavity, and so in fields wider than $2d_{\text{equilib}}$ (practically around 2-3 cm, see *Methods 5.2.3* and figure 5.4) lateral electronic equilibrium exists throughout the cavity, which therefore absorbs the full external dose contribution $D\left(1-J_{\text{cav}}(\rho)\right)$ from electrons energized outside it.

On the other hand in circular fields narrower than $2r$ the paths of primary photons lie entirely within the cylindrical cavity, and so (ignoring photon scatter) no electrons will be generated outside the cavity by these fields, meaning that their external dose component is zero. Regardless of cavity density, then, equation (5.19) correctly represents $\overline{D}_{\text{external}}$ for the cylindrical cavity in fields narrower than $2r$ ($\varepsilon = 0$) or wider than $2d_{\text{equilib}}$ ($\varepsilon = 1$) while describing a smoothly rising curve in between – a reasonable approximation to the real situation.

Of course a *spherical* cavity of radius r will absorb a non-zero $\overline{D}_{\text{external}}$ dose from a circular field of diameter $2r$, because some photon interactions occurring above the cavity will energize electrons that go on to deposit dose within it. When the cavity is filled with unit density water it follows from equation (5.17) that the externally derived dose absorbed by the cavity from the $2r$ diameter field is given exactly by

$$\overline{D}_{\text{external}} = D\left(1-J_{\text{cav}}(\rho)\right)\varepsilon(2r) \quad \text{(A.1)}$$

whereas when the cavity is filled with water of density ρ the externally-derived dose that it absorbs is given approximately, according to equation (5.19), by

$$\overline{D}_{\text{external}} \approx D\left(1-J_{\text{cav}}(\rho)\right)\varepsilon(2r) \quad \text{(A.2)}$$

In the next section it is shown that doses absorbed by the spherical cavity from externally energized electrons in narrow fields actually vary with cavity density as $(1 - 0.64\, J_{\text{cav}}(\rho))$ rather than as $(1 - J_{\text{cav}}(\rho))$, where $J_{\text{cav}}(\rho)$ is the fractional cavity dose arising from internally energized electrons in a wide field. Consequently the real external dose absorbed from the circular field of diameter $2r$ by the cavity when filled with water of density ρ is

$$\overline{D}_{\text{external}} = D\big(1 - J_{\text{cav}}(\rho)\big)\varepsilon(2r)\frac{\big(1 - 0.64J_{\text{cav}}(\rho)\big)}{\big(1 - 0.64J_{\text{cav}}(1)\big)} \tag{A.3}$$

and so the fractional error in the approximate $\overline{D}_{\text{external}}$ value obtained from equation (5.19) is

$$\frac{\overline{D}_{\text{external}}\big[\text{equation (A.2)}\big]}{\overline{D}_{\text{external}}\big[\text{equation (A.3)}\big]} - 1 = \left(\frac{1 - 0.64J_{\text{cav}}(1)}{1 - 0.64J_{\text{cav}}(\rho)}\right)\left(\frac{1 - J_{\text{cav}}(\rho)}{1 - J_{\text{cav}}(1)}\right) - 1$$

$$\approx 0.36\big(J_{\text{cav}}(1) - J_{\text{cav}}(\rho)\big) \tag{A.4}$$

Using either the directly computed J_{cav} values of table 5.3 or the fitted I_{cav} values set out in the *Results,* the fractional error in $\overline{D}_{\text{external}}$ values obtained for narrow fields from equation (5.19) works out at 2.5% for a spherical cavity having the same wide field $J_{\text{cav}}(\rho)$ values as those of the modelled diamond cavity when both are filled with water of unit or diamond density. Similarly for a spherical cavity having the same $J_{\text{cav}}(\rho)$ values as the modelled PinPoint 3D cavity filled with water of unit or air density, the fractional error in $\overline{D}_{\text{external}}$ works out around 4.0%. Consequently the errors introduced by equation (5.19) into narrow field $P_{\rho\_}$ values modelled for these two cavities in equation (5.22) are less than 2.5% and 4%,which are inconsequential in comparison to the calculated departures of $P_{\rho\_}$ from one at small field-sizes (figure 5.4).

Furthermore the spherical cavity, like the cylindrical cavity, absorbs the full external dose $D\big(1 - J_{\text{cav}}(\rho)\big)$ from fields wider than $2d_{\text{equilib}}$, meaning that $\varepsilon(\text{FS})$ is unity in these fields and equation (5.19) is accurate. And so for the spherical cavity equation (5.19) introduces inconsequential errors into $\overline{D}_{\text{external}}$ in fields narrower than $2r$, correctly represents $\overline{D}_{\text{external}}$ in fields wider than $2d_{\text{equilib}}$, and smoothly rises in between – again providing a reasonable approximation to the real situation.

A.2 Doses absorbed from electrons energized outside the cavity in small fields

The whole dose D absorbed by an ideal Bragg-Gray cavity comes from externally energized electrons, which fully traverse its small volume. However some externally energized electrons stop within larger cavities of modified density water, which reduces the mean dose absorbed by these cavities from D to

$D(1 - J_{cav}(\rho))$ – a reduction exactly offset by the dose $DJ_{cav}(\rho)$ absorbed from electrons energized by photon interactions taking place within the cavity.

Just above the Bragg-Gray region, J_{cav} values are given by the formula $\left(\rho/\left(1-\bar{g}\right)\right)\left(\bar{L}_{\Delta(\rho)\mathrm{int}}/\rho\right)_{\mathrm{w}}\left(\frac{\bar{l}(\rho)}{\bar{T}_{\mathrm{ep}}}\right)$ (equation (5.13)) in which $\left(1/\bar{T}_{\mathrm{ep}}\right)$ represents the average reciprocal kinetic energy of newly generated electrons. In a broad field externally energized electrons enter the cavity from all directions, and so $\left(1/\bar{T}_{\mathrm{ep}}\right)$ is an average over the Klein-Nishina differential cross-sections (Attix1986) of Compton interactions which generate electrons travelling at between 0°and 90° with respect to the incident photon direction. For electrons energized by the 4.1 MeV photons typical of a 15 MV beam (*Methods 5.2.3*) the average value of $\left(1/\bar{T}_{\mathrm{ep}}\right)$ obtained for a spherical cavity is 0.40 MeV^{-1}. However in very narrow fields, only those externally energized electrons that travel in roughly the straight-ahead (0°) direction enter the cavity. And for straight-ahead Compton electrons energized by 4.1 MeV photons, $\left(1/\bar{T}_{\mathrm{ep}}\right)$ is 0.26 MeV^{-1}, 64% of the $\left(1/\bar{T}_{\mathrm{ep}}\right)$ value averaged across all electron angles. Consequently spherical cavities in narrow fields will absorb a dose $(1 - 0.64\, J_{cav}(\rho))$ from externally energized electrons, compared to $(1 - J_{cav}(\rho))$ in wide fields.

A.3 Doses absorbed from electrons energized inside the cavity in small fields

The change from $(1 - J_{cav}(\rho))$ to $(1 - 0.64\, J_{cav}(\rho))$ in the density-dependence of the external dose component absorbed by a spherical cavity seen when moving from broad to narrow fields is *not* accompanied by an associated reduction from $J_{cav}(\rho)$ to $0.64\, J_{cav}(\rho)$ in the density-dependence of the internal dose component absorbed from electrons energized by photon interactions occurring within the cavity – because in both narrow and broad beams the trajectories of these internally energized electrons cover a wide angular range rather than being limited to the forwards direction.

Provided that the number of monitor units is chosen to hold the average kerma within the cavity at its broad field level, the cavity will continue to absorb a dose $DJ_{cav}(\rho)$ from the internally energized electrons of a narrow field. However in fields so narrow that the photon fluence profile varies across the cavity, being peaked at its centre, the $DJ_{cav}(\rho)$ dose absorbed from internally energized electrons will actually rise above its broad field value. This amounts to an increase in J_{cav} at small fields-sizes (as noted in the *Results*), in contradistinction to the fall in J_{cav} seen for externally energized electrons.

Appendix-B

Simplified theory of the response of a low-density cavity in a narrow non-equilibrium field

The arguments given in sub-section 6.4.3.2 will now be expressed analytically. Consider the dose at point '×' in Figure 6.6. Simplifying the cavity integrals (e.g. ignoring any difference in mean energy between the 'in' and 'out' components of electron/positron fluence (see below) and using the *unrestricted* electronic mass stopping powers, evaluated at a single effective electron energy), for the uniform medium (upper half of the figure) it can be written

$$D_{\mathrm{med}}(\times) = \left[\Phi(\times)\right]_{\mathrm{med}}^{\mathrm{in+out}} \left[\bar{S}_{\mathrm{el}}/\rho\right]_{\mathrm{med}} = \left\{\left[\Phi(\times)\right]_{\mathrm{med}}^{\mathrm{in}} \left[\bar{S}_{\mathrm{el}}/\rho\right]_{\mathrm{med}}\right\} + \left\{\left[\Phi(\times)\right]_{\mathrm{med}}^{\mathrm{out}} \left[\bar{S}_{\mathrm{el}}/\rho\right]_{\mathrm{med}}\right\} \quad \text{(B.1)}$$

where 'in' denotes the electron (+ positron) fluence (in a small volume centred on '×') arising from photon interactions *inside* the 'cavity' volume and 'out' denotes the electron (+ positron) fluence (in the same volume) arising from photon interactions in the volume *outside* the cavity.

The corresponding expression for the gas cavity centred on '×' is

$$D_{\mathrm{gas}}(\mathrm{cav}) = \left\{\left[\Phi(\mathrm{cav})\right]_{\mathrm{gas}}^{\mathrm{in}} \left[\bar{S}_{\mathrm{el}}/\rho\right]_{\mathrm{gas}}\right\} + \left\{\left[\Phi(\mathrm{cav})\right]_{\mathrm{gas}}^{\mathrm{out}} \left[\bar{S}_{\mathrm{el}}/\rho\right]_{\mathrm{gas}}\right\} \quad \text{(B.2)}$$

where in this case the relevant volume over which the fluence and the dose are expressed is the gas cavity, denoted by 'cav', as opposed to a single point at its centre.

The ratio of doses, medium-to-gas is therefore given by

$$\frac{D_{\mathrm{med}}(\times)}{D_{\mathrm{gas}}(\mathrm{cav})} = \frac{\left\{\left[\Phi(\times)\right]_{\mathrm{med}}^{\mathrm{in}} \left[\bar{S}_{\mathrm{el}}/\rho\right]_{\mathrm{med}}\right\} + \left\{\left[\Phi(\times)\right]_{\mathrm{med}}^{\mathrm{out}} \left[\bar{S}_{\mathrm{el}}/\rho\right]_{\mathrm{med}}\right\}}{\left\{\left[\Phi(\mathrm{cav})\right]_{\mathrm{gas}}^{\mathrm{in}} \left[\bar{S}_{\mathrm{el}}/\rho\right]_{\mathrm{gas}}\right\} + \left\{\left[\Phi(\mathrm{cav})\right]_{\mathrm{gas}}^{\mathrm{out}} \left[\bar{S}_{\mathrm{el}}/\rho\right]_{\mathrm{gas}}\right\}} \quad \text{(B.3)}$$

Note that at *megavoltage* photon qualities, $\left[\Phi(\mathrm{cav})\right]_{\mathrm{gas}}^{\mathrm{in}} \ll \left[\Phi(\mathrm{cav})\right]_{\mathrm{gas}}^{\mathrm{out}}$ because, in a wide, equilibrium field, the low-density (gas) cavity acts in a Bragg-Gray manner (Ma and Nahum 1991).

CASE A: wide, 'equilibrium' field

To a very good approximation $\left[\Phi(\mathrm{cav})\right]_{\mathrm{gas}}^{\mathrm{in+out}} = \left[\Phi(\times)\right]_{\mathrm{med}}^{\mathrm{in+out}}$ due to the Fano theorem, as there is quasi-CPE, given that $\left[\Phi(\mathrm{cav})\right]_{\mathrm{gas}}^{\mathrm{in}}$ is negligible. Therefore it follows from (B.3) that $\left\{D_{\mathrm{med}}(\times) / D_{\mathrm{gas}}(\mathrm{cav})\right\} =$

$\left\{\left[\overline{S}_{\text{el}}/\rho\right]_{\text{med}} / \left[\overline{S}_{\text{el}}/\rho\right]_{\text{gas}}\right\}$ (averaged over the electron spectrum at × in the medium); this is the standard Bragg-Gray result.

CASE B: narrow, non-equilibrium field

In the narrow-field geometry, in marked contrast to that for the wide field, the *secondary-electron generation volumes* outside the cavity for the uniform medium and gas are identical (see the right-hand side of figure 6.6). However, the electrons/positrons entering the virtual cavity in the uniform medium will be 'attenuated' by the medium inside the cavity and therefore $\left[\Phi(\times)\right]_{\text{med}}^{\text{out}}$ will only be approximately equal to $\left[\Phi(\text{cav})\right]_{\text{gas}}^{\text{out}}$. As in CASE A $\left[\Phi(\text{cav})\right]_{\text{gas}}^{\text{in+out}} \approx \left[\Phi(\text{cav})\right]_{\text{gas}}^{\text{out}}$, therefore the (electron + positron) fluence ratio, medium-to-gas, is given by

$$\frac{\left[\Phi(\times)\right]_{\text{med}}^{\text{in+out}}}{\left[\Phi(\text{cav})\right]_{\text{gas}}^{\text{in+out}}} \approx \frac{\left[\Phi(\times)\right]_{\text{med}}^{\text{in}} + \left[\Phi(\times)\right]_{\text{med}}^{\text{out}}}{\left[\Phi(\text{cav})\right]_{\text{gas}}^{\text{out}}} \tag{B.4}$$

As the field size becomes smaller and smaller, $\left[\Phi(\times)\right]_{\text{med}}^{\text{out}}$ will decrease further and further and therefore the (quasi-constant) $\left[\Phi(\times)\right]_{\text{med}}^{\text{in}}$ will increasingly dominate, thus increasing the fluence ratio given by (B.4). Expressed another way, the low-density cavity will significantly 'under-respond', as demonstrated here and in Scott *et al* (2012).

The medium-to-gas dose ratio can be written as

$$\frac{D_{\text{med}}(\times)}{D_{\text{gas}}(\text{cav})} = \frac{\left[\overline{S}_{\text{el}}/\rho\right]_{\text{med}}}{\left[\overline{S}_{\text{el}}/\rho\right]_{\text{gas}}} \times \left(p_{\text{fl}}\right)_{\text{gas}}^{\text{med}} \tag{B.5}$$

where the first term is the (conventional) Bragg-Gray stopping-power ratio and

$$\left(p_{\text{fl}}\right)_{\text{gas}}^{\text{med}} \approx \left\{\left[\Phi(\times)\right]_{\text{med}}^{\text{in}} + \left[\Phi(\times)\right]_{\text{med}}^{\text{out}}\right\} / \left[\Phi(\text{cav})\right]_{\text{gas}}^{\text{out}} \tag{B.6}$$

By contrast, $\left(p_{\text{fl}}\right)_{\text{gas}}^{\text{med}} \approx 1$ in case A.

Appendix-C

A correction for photon-fluence perturbation in a 'large photon detector'

The use of the mass-energy-absorption coefficient ratio, as evaluated from equation (7.13), to yield the ratio of the medium to detector dose for a cavity behaving as a 'large photon detector' (Nahum 2007b) assumes that the photon (energy) fluences in the detector and the uniform medium are *identical* in magnitude and energy distribution, analogous to the assumption regarding the charged-particle fluence in a Bragg-Gray detector. However, for finite-size, non-medium-equivalent detectors there are likely to be differences between detector and medium photon fluences; a *photon fluence perturbation correction factor* (Beddar *et al* 1992, Mobit *et al* 2000) can be applied.

From Kumar *et al* (2015a) it is written

$$\left(\frac{D}{K_{\text{col}}}\right)_{\text{med}} = \beta_{\text{med}} = \left(1 + \left[\mu_{\text{eff}}(\bar{k})\right]_{\text{med}} \left[0.5 \times R_{\text{csda}}^{\text{med}}\left(\overline{E_{\text{o}}}\right)_{\bar{k}}\right]\right) \tag{C.1}$$

where R_{csda} is here in units of length and $\left[\mu_{\text{eff}}(\bar{k})\right]_{\text{med}}$ is the 'effective' attenuation coefficient at photon energy $\bar{k}$ for the medium of interest. In the case of a photon spectrum, e.g. an x-ray beam, the photon energy in equation (C.1) is a *collision-kerma-weighted* mean value over the photon fluence spectrum, $\bar{k}$, and $\overline{E_0}$ is the mean initial electron energy of the electrons set in motion by photons. One can write an equivalent expression for $(D/K_{\text{col}})_{\text{det}}$.

Now by definition,

$$\left(\frac{\overline{\mu_{\text{en}}}}{\rho}\right)_{\text{det}}^{\text{med}} = \frac{(K_{\text{col}})_{\text{med}}}{(K_{\text{col}})_{\text{det}}}$$

If the photon fluence spectra in the detector and uniform medium, at identical depths, were equal then we would have

$$\frac{D_{\text{med}}}{D_{\text{det}}} = \frac{\beta_{\text{med}}(K_{\text{col}})_{\text{med}}}{\beta_{\text{det}}(K_{\text{col}})_{\text{det}}} = \left(\frac{\beta_{\text{med}}}{\beta_{\text{det}}}\right) \times \left(\frac{\overline{\mu_{\text{en}}}}{\rho}\right)_{\text{det}}^{\text{med}}$$

However, a correction will also be necessary for difference in attenuation of the photon fluence between the detector material and the medium. If the distance from the front face of the detector (in the case of a cylindrical volume perpendicular to the beam direction), or from the most 'upstream' depth of the curved front surface, to the detector centre is denoted by $(t_{1/2})_{\mathrm{det}}$ then this difference will be given to a good approximation by $e^{-(t_{1/2})_{\mathrm{det}}\left[\left(\mu_{\mathrm{eff}}\left(\bar{k}\right)\right)_{\mathrm{med}}-\left(\mu_{\mathrm{eff}}\left(\bar{k}\right)\right)_{\mathrm{det}}\right]}$ which in turn is well approximated by $\left\{1-\left(t_{1/2}\right)_{\mathrm{det}}\left[\left(\mu_{\mathrm{eff}}\left(\bar{k}\right)\right)_{\mathrm{med}}-\left(\mu_{\mathrm{eff}}\left(\bar{k}\right)\right)_{\mathrm{det}}\right]\right\}$.

The final expression for the medium-to-(large photon) detector dose ratio becomes therefore

$$\frac{\left[D(\mathrm{P})\right]_{\mathrm{med}}}{\left[\overline{D}\right]_{\mathrm{det}}} \simeq \left(\frac{\overline{\mu_{\mathrm{en}}}}{\rho}\right)_{\mathrm{det}}^{\mathrm{med}} \left(\frac{\beta_{\mathrm{med}}}{\beta_{\mathrm{det}}}\right) \left\{1-\left(t_{1/2}\right)_{\mathrm{det}}\left[\left(\mu_{\mathrm{eff}}\left(\bar{k}\right)\right)_{\mathrm{med}}-\left(\mu_{\mathrm{eff}}\left(\bar{k}\right)\right)_{\mathrm{det}}\right]\right\} \tag{C.2}$$

where P is the position of the detector centre.

We can then define a photon-fluence perturbation factor by

$$\frac{\left[D(\mathrm{P})\right]_{\mathrm{med}}}{\left[\overline{D}\right]_{\mathrm{det}}} = \left(\frac{\overline{\mu_{\mathrm{en}}}}{\rho}\right)_{\mathrm{det}}^{\mathrm{med}} p_{\mathrm{med,det}}^{\mathrm{ph}} \tag{C.3}$$

Comparing the above with equation (C.2) yields

$$p_{\mathrm{med,det}}^{\mathrm{ph}} \simeq \left(\frac{\beta_{\mathrm{med}}}{\beta_{\mathrm{det}}}\right) \left\{1-\left(t_{1/2}\right)_{\mathrm{det}}\left[\left(\mu_{\mathrm{eff}}\left(\bar{k}\right)\right)_{\mathrm{med}}-\left(\mu_{\mathrm{eff}}\left(\bar{k}\right)\right)_{\mathrm{det}}\right]\right\} \tag{C.4}$$

Finally, for the case of a silicon detector in water, it is written

$$p_{\mathrm{w,Si}}^{\mathrm{ph}} \simeq \left(\frac{\beta_{\mathrm{w}}}{\beta_{\mathrm{Si}}}\right) \left\{1-\left(t_{1/2}\right)_{\mathrm{Si}}\left[\left(\mu_{\mathrm{eff}}\left(\bar{k}\right)\right)_{\mathrm{w}}-\left(\mu_{\mathrm{eff}}\left(\bar{k}\right)\right)_{\mathrm{Si}}\right]\right\} \tag{C.5}$$

References

Agostinelli S *et al* 2003 GEANT4: a simulation toolkit *Nucl. Instrum. Methods* A **506** 250–303

Alfonso R, Andreo P, Capote R, Huq M S, Kilby W, Kjäll P, Mackie T R, Palmans H, Rosser K, Seuntjens J Ullrich W and Vatnitsky S 2008 A new formalism for reference dosimetry of small and nonstandard fields *Med. Phys.***35** 5179-5186

Ali E S M and Rogers D W O 2008 Benchmarking EGSnrc in the kilovoltage energy range against experimental measurements of charged particle backscatter coefficients *Phys. Med. Biol.* **53** 1527–1543

Andreo P and Nahum A E 1985 Stopping-power ratio for a photon spectrum as a weighted sum of the values for monoenergetic photon beams *Phys. Med. Biol.* **30** 1055-65

Andreo P 1991 Monte Carlo techniques in medical radiation physics *Phys. Med. Biol.* **36** 861-920

Andreo P, Burns D T, Hohlfeld K, Huq M S, Kanai T, Laitano F, Smyth V G and Vynckier S 2000 *Absorbed dose determination in External Beam Radiotherapy: an International Code of Practice for Dosimetry Based on Standards of Absorbed Dose to Water IAEA Technical Report Series No*. 398 (Vienna: International Atomic Energy Agency)

Attix F H 1968 Basic γ-ray dosimetry *Health Phys*. **15** 49-56

Attix F H 1979a The partition of Kerma to account for bremsstrahlung *Health Phys*. **36** 347-54

Attix F H 1979b Addendum to the partition of kerma to account for bremsstrahlung *Health Phys*. **36** 536

Attix F H 1983 Energy imparted, energy transferred and net energy transferred *Phys. Med. Biol.* **28** 1385-1390

Attix F H 1984 A simple derivation of N_{gas}, a correction in A_{wall}, and other comments on the AAPM Task Group 21 protocol *Med. Phys.* **11** 725-728

Attix F H 1986 *Introduction to Radiological Physics and Radiation Dosimetry* (New York: Wiley)

Battistoni G, Cerutti F, Fasso A, Ferrari A, Muraro S, Ranft J, Roesler S, and Sala P R 2007 The FLUKA code: description and benchmarking *Proc. Hadronic Shower Simulation Workshop 2006: AIP Conf. Proc*. **896** pp 31-49

Beddar A S, Mackie T R and Attix F H 1992 Water-equivalent plastic scintillation detectors for high-energy beam dosimetry: I. Physical characteristics and theoretical considerations *Phys. Med. Biol.***37** 1883-1900

Beddar A S, Mason D J, and O'Brien P F 1994 Absorbed dose perturbation caused by diodes for small field photon dosimetry. *Med. Phys.* **21** 1075-1079

Benedict S H, Yenice K M, Followill D, Galvin J M *et al* 2010 Stereotactic body radiation therapy: The report of AAPM Task Group 101*Med. Phys*. **37** 4078- 4101

Benmakhlouf H, Sempau J and Andreo P 2014 Output correction factors for nine small field detectors in 6 MV radiation therapy photon beams: A PENELOPE Monte Carlo study *Med. Phys.* **41** 041711

Benmakhlouf H, Johansson J, Paddick I and Andreo P 2015 Monte Carlo calculated and experimentally determined output correction factors for small field detectors in Leksell Gamma Knife Perfexion beams *Phys. Med. Biol.* **60** 3959-3973

Berger MJ, Coursey JS, Zucker MA and Chang J 2005 ESTAR, PSTAR, and ASTAR: computer programs for calculating stopping-power and range tables for electrons, protons, and helium ions (version 1.2.3) National Institute of Standards and Technology, (Gaithersburg, MD: NIST) Available online: http://physics.nist.gov/Star

Berger M J, Hubbell J H, Seltzer S M, Chang J, Coursey J S, Sukumar R, Zucker D S and Olsen K 2010 XCOM: photon cross section database (version 1.5) *Technical Report* (Gaithersburg, MD:NIST) (http://physics.nist.gov/xcom)

Bethe H A, Rose M E and Smith L P 1938 The multiple scattering of electrons *Proc. Am. Phil. Soc.* **78** 573-85

Bjärngard B E, Tsai J S and Rice R K 1989 Attenuation in very narrow photon beams *Radiat. Res.* **118** 195-200

Blomgren H, Lax I, Näslund I, Svanströms R, 1995 Stereotactic high dose fraction radiation therapy of extracranial tumors using an accelerator. Clinical experience of the first thirty one patients *Acta. Oncol.* **34** 861-70

Borg J, Kawrakow I, Rogers D W O and Seuntjens J P 2000 Monte Carlo study of correction factors for Spencer-Attix cavity theory at photon energies at or above 100 keV *Med. Phys.* **27** 1804-1813

Bouchard H, Seuntjens J, Carrier J F, Kawrakow I 2009 Ionization chamber gradient effects in nonstandard beam configurations *Med. Phys.* **36** 4654-63

Boutillon M and Niatel M T 1973 A study of a graphite cavity chamber for absolute exposure measurements of ^{60}Co gamma rays *Metrologia* **9** 139-46

Bragg W H 1912 *Studies in Radioactivity* (London: MacMillan)

Brahme A 1978 Restricted energy absorption coefficients for use in dosimetry *Radiat. Res.* **73** 420-29

Brahme A 1984 Dosimetric precision requirements in radiation therapy *Acta Radiol. Oncol.* **23** 379-391

Brahme A, Ed. 1988 Accuracy requirements and quality assurance of external beam therapy with photons and electrons *Acta. Oncol. (*suppl 1) 5-76

Brown F B 2003 MCNP - A general Monte Carlo particle transport code, version 5 *Report LA-UR-03-1987* (Los Alamos, NM: Los Alamos National Laboratory)

Buckley L, Kawrakow I and Rogers D W O 2003 An EGSnrc investigation of the cavity theory for ion chambers measuring air kerma *Med. Phys.* **30** 1211–1218

Buckley L A 2005 An EGSnrc investigation of correction factors for ion chamber dosimetry *PhD Thesis* Carleton University, Canada

Buckley L A and Rogers D W O 2006 Wall correction factors, P_{wall}, for thimble ionization chambers *Med. Phys.* **33** 455–64

Burlin T E 1966 A general theory of cavity ionisation *Br. J. Radiol.* **39** 727-34

Burns D T, Allisy P J and Kessler C 2007 Re-evaluation of the BIPM international standard for air kerma in ^{60}Co gamma radiation *Metrologia* **44** L53-56

Cao D, Afghan M K, Ye J et al 2009 A generalized inverse planning tool for volumetric-modulated arc therapy *Phys. Med. Biol.* **54** 6725-38

Capote R, Sánchez-Doblado F, Leal A, Lagares J I, and Arráns R 2004 An EGSnrc Monte Carlo study of the microionization chamber for reference dosimetry of narrow irregular IMRT beamlets *Med. Phys.* **31** 2416-2422

Chalkley A and Heyes G 2014 Evaluation of a synthetic single-crystal diamond detector for relative dosimetry measurements on a CyberKnife™ *Br. J. Radiol.* **87** 20130768

Chang J Y, Balter P A, Dong L, *et al* 2008 Stereotactic body radiation therapy in centrally and superiorly located Stage I or isolated recurrent non-small-cell lung cancer *Int. J. Radiat. Oncol. Biol. Phys.* **72** 967–971

Charles P H, Crowe S B, Kairn T, Kenny J, Lehmann J, Lye J, Dunn L, Hill B, Knight R T, Langton C M and Trapp J V 2012 The effect of very small air gaps on small field dosimetry *Phys. Med. Biol.* **57** 6947-6960

References

Charles P H, Crowe S B, Kairn T, Knight R T, Hill B, Kenny J, Langton C M and Trapp J V 2013 Monte Carlo-based diode design for correction-less small field dosimetry *Phys. Med. Biol.* **58** 4501-4512

Charles P H, Cranmer-Sargison G, Thwaites D I, Kairn T, Crowe S B, Pedrazzini G, Aland T, Kenny J, Langton C M and Trapp J V 2014 Design and experimental testing of air slab caps which convert commercial electron diodes into dual purpose, correction-free diodes for small field dosimetry *Med. Phys.* **41** 101701

Clivio A, Fogliata A, Franzetti-Pellanda A, Nicolini G, Vanetti E, Wyttenbach R, Cozzi L 2009 Volumetric-modulated arc radiotherapy for carcinomas of the anal canal: A treatment planning comparison with fixed field IMRT *Radiother. Oncol.* **92** 118-24

Cranmer-Sargison G,Weston S, Evans J A, Sidhu N P and Thwaites D I 2011a Implementing a newly proposed Monte Carlo based small field dosimetry formalism for a comprehensive set of diode detectors *Med. Phys.* **38** 6592–602

Cranmer-Sargison G, Weston S, Sidhu N P and Thwaites D I 2011b Experimental small field 6 MV output ratio analysis for various diode detector and accelerator combinations *Radiother. Oncol.* **100** 429–35

Cranmer-Sargison G, Weston S, Evans J A, Sidhu N P and Thwaites D I 2012 Monte Carlo modelling of diode detectors for small field MV photon dosimetry: detector model simplification and the sensitivity of correction factors to source parameterization *Phys. Med. Biol.* **57** 5141–53

Crop F, Reynaert N, Pittomvils G, Paelinck L, Wagter C D, Vakaet L and Thierens H 2009 The influence of small field sizes, penumbra, spot size and measurement depth on perturbation factors for microionization chambers *Phys. Med. Biol.* **54** 2951-2969

Czarnecki D and Zink K 2013 Monte Carlo calculated correction factors for diodes and ion chambers in small photon fields *Phys. Med. Biol.* **58** 2431-2444

Dance D and Carlsson G A 2007 Interactions of photons with matter *Handbook of Radiotherapy Physics: Theory and Practice* ed P Mayles, A E Nahum and J C Rosenwald (London: Taylor & Francis) pp 58-74

Das I J, Downes M B, Corn B W, Curran B J, Wasik M W, and Andrews D W 1996 Characteristic of a dedicated linear accelerator-based stereotactic radiosurgery-radiotherapy unit *Radiother. Oncol.* **38** 61-68

Das I J, Cheng C W, Watts R J, Ahnesjö A, Gibbons J, Li X A, Lowenstein J, Mitra R K, Simon W E and Zhu T C 2008a Accelerator beam data commissioning equipment and procedure: report of the TG-106 of the therapy physics committee of the AAPM *Med. Phys.***35** 4186-4215

Das I J, Ding G X and Ahnesjö A 2008b Small fields: nonequilibrium radiation dosimetry *Med. Phys.***35** 206-15

Dawson D J, Schroeder N J and Hoya J D 1986 Penumbral measurements in water for high-energy x rays *Med. Phys.* **13** 101-104

Day M J and Aird E G A 1996 The equivalent field method for dose determinations in the rectangular fields *Br. J. Radiol. Suppl.* **25** appendix A pp 138-151

Delaney G, Jacob S, Featherstone C *et al* 2005 The role of radiotherapy in cancer treatment: estimating optimal utilization from a review of evidence-based clinical guidelines *Cancer* **104** 1129-37

Dieterich S, Cavedon C, Chuang C F, Cohen A B, Garrett J A, Lee C L, Lowenstein J R, d,Souza M F, Taylor D D, Wu X and Yu C 2011 Report of AAPM TG 135: Quality assurance for robotic radiosurgery *Med. Phys.* **38** 2914-2936

Ding G K and Ding F 2012 Beam characteristics and stopping-power ratios of small radiosurgery photon beams *Phys. Med. Biol.***57** 5509-5521

Dutreix M D, Dutreix A and Tubiana M 1965 Electronic equilibrium and transition stages *Phys. Med. Biol.* **10** 177-90

Eklund K and Ahnesjö A 2010 Spectral perturbations from silicon diode detector encapsulation and shielding in photon fields *Med. Phys.* **37** 6055-6060

Ezzell G A, Gavin J M, Low D, Palta J R *et al* 2003 Guidance document on delivery, treatment planning, and clinical implementation of IMRT: report of the IMRT Subcommittee of the AAPM Radiation Therapy Committee *Med. Phys.* **30** 2089-2115

Fano U 1954 Note on the Bragg-Gray cavity principle for measuring energy dissipation *Radiat. Res.* **1** 237-240

Fenwick J D, Kumar S, Scott A J D and Nahum A E 2013 Using cavity theory to describe the dependence on detector density of dosimeter response in non-equilibrium small fields *Phys. Med. Biol.***58** 2901-2923

Ferlay J, Shin H R, Bray F, Forman D, Mathers C, Parkin D M 2008 Estimates of worldwide burden of cancer in 2008: GLOBOCAN 2008 *Int. J. Cancer* **127** 2893 – 2917

Fernández-Varea J M, Andreo P and Tabata T 1996 Detour factors in water and plastic phantoms and their use for range and depth scaling in electron-beam dosimetry *Phys. Med. Biol.* **41** 1119-39

Fontenot J D, King M L, Johnson S A, Wood C G, Price M J, Lo K K 2012 Single-arc volumetric-modulated arc therapy can provide dose distributions equivalent to fixed-beam intensity-modulated radiation therapy for prostatic irradiation with seminal vesicle and/or lymph node involvement *Br. J. Radiol.* **85** 231-6

Fowler J F, Tome W A, Fenwick J D, Mehta M P 2004 A challenge to traditional oncology *Int. J. Radiat. Oncol. Biol. Phys.* **60** 1241 – 1256

Francescon P, Cora S and Satariano N 2011 Calculation of $k_{Q_{\mathrm{clin}},Q_{\mathrm{msr}}}^{f_{\mathrm{clin}},f_{\mathrm{msr}}}$ for several small detectors and for two linear accelerators using Monte Carlo simulations *Med. Phys.* **38** 6513-6526

Fu Y and Luo Z 2002 Application of Monte Carlo simulation to cavity theory based on the virtual electron source concept *Phys. Med. Biol.***47** 3263-3274

Gagliardi G, Nahum A E and Muren L 2011 'Small-field (photon-beam) dosimetry' in *Physics Corner*, ESTRO NEWSLETTER nr. **80**

Gray L H 1936 An ionization method for the absolute measurement of gamma ray energy *Proc. R. Soc. Lond.* A **156** 578–98

Greening J R 1981 *Fundamentals of Radiation Dosimetry* (*Medical Physics Handbooks*) (Bristol: Adam Hilger)

Goldsmith C and Gaya A 2012 Stereotactic ablative body radiotherapy (SABR) for primary and secondary lung tumours *Cancer Imaging* **12** 351-360

Górka B, Nilsson B, Fernández-Varea J M, Svensson R and Brahme A 2006 Influence of electrodes on the photon energy deposition in CVD-diamond dosimeters studied with the Monte Carlo code PENELOPE *Phys. Med. Biol*. **51** 3607-3623

Haider J A, Skarsgard L D and Lam G K Y 1997 A general cavity theory *Phys. Med. Biol.***42** 491-500

Hall E J and Giaccia A J 2006 *Radiobiology for the Radiologist* (Lippincott Williams & Wilkins)

Hannallah D, Zhu T C, and Bjarngard D E 1996 Electron disequilibrium in high-energy x- ray beams *Med. Phys.* **23** 1867-71

Harder D 1970 Some general results from the transport theory of electron absorption *Proc. 2nd Symp. on Microdosimetry Report no. 4452 (Stressa, Italy, 1969)* ed H G Ebert (Brussels: Euratom) pp 567-93

Harder D 1974 Fano's Theorem and the Multiple Scattering Correction *Proc. 4th Symp. Microdosimetry* (1973) ed J. Booz, H. G. Ebert, R. Eickel, and A. Walker (*Verbania Pallanza, Italy*) pp. 677–693

Haryanto F, Fippel M, Laub W, Dohm O and Nüsslin F 2002 Investigation of photon beam output factors for conformal radiation therapy Monte Carlo simulations and measurements *Phys. Med. Biol.* **47** N133-N143

Heydarian M, Hoban P W and Beddoe A H 1996 A comparison of dosimetry techniques in stereotactic radiosurgery *Phys. Med. Biol.***41** 93-110

Hosmer D W and Lemeshow S 1989 *Applied logistic regression* (New York: Wiley) pp 135-45

Hubbell J H and Seltzer S M 2004 *Tables of x-ray mass attenuation coefficients and mass energy-absorption coefficients (version 1.4)* (Gaithersburg, MD: NIST) (http://physics.nist.gov/xaamdi)

ICRU 1976 Determination of absorbed dose in a patient irradiated by beams of X or gamma rays in radiotherapy procedures *ICRU Report 24* (Bethesda, MD: International Commission on Radiation Units and Measurements)

ICRU 1993 Stopping powers and ranges for protons and alpha particles *ICRU Report 49* (Bethesda, MD: International Commission on Radiation Units and Measurements)

ICRU 2011 Fundamental quantities and units for ionizing radiation *ICRU Report 85* (Bethesda, MD: International Commission on Radiation Units and Measurements)

IPEM 2010 Small field MV photon dosimetry *IPEM Report 103* (York, UK: Institute of physics and Engineering in Medicine)

Iwasaki A 1994 Characteristic of ^{60}Co γ-ray SPR (Scatter-primary ratio), sf (scatter factor), β (dose-kerma ratio), and $d_{\max}$ (depth of maximum dose) *Phys. Med. Biol.* **39** 1081-88

Janaki M G, Kadam A R, Mukesh S, Nirmala, Ponni A, Ramesh B S, Rajeev AG 2010 Magnitude of fatigue in cancer patients receiving radiotherapy and its short term effect on quality of life *J Cancer Res. Ther*. **6** 22-26

Janssens A and Eggermont G 1974 Spectrum perturbation and energy deposition models for stopping power ratio calculations in general cavity theory *Phys. Med. Biol.***19** 619-630

Kawrakow I 2000a Accurate condensed history Monte Carlo simulation of electron transport. I. EGSnrc, The new EGS4 version Med. Phys. **27** 485-498

Kawrakow I 2000b Accurate condensed history Monte Carlo simulation of electron transport. II. Application to ion chamber response simulations *Med. Phys.* **27** 499-513

Kawrakow I, Mainegra-Hing E and Rogers D W O 2006 EGSnrcMP: the multi-platform environment for EGSnrc *NRCC Report* PIRS-877 (Ottawa: National Research Council of Canada)

Kawrakow I, Mainegra-Hing E, Rogers D W O, Tessier F and Walters B R B 2011 The EGSnrc code system: Monte Carlo simulation of electron and photon transport *NRCC Report* PIRS-*701* (Ottawa: National Research Council of Canada)

Khan F M 2010 *The Physics of Radiation Therapy*, 4th ed. (Lippincott Wiliams & Wilkin, Baltimore, MD)

Kilby W, Dooley J R, Kuduvalli G, Sayeh S and Maurer C R Jr 2010 The CyberKnife robotic radiosurgery system in 2010 *Technol. Cancer Res. Treat.* **9** 433-52

Kosunen A and Rogers D W O 1993 Beam quality specification for photon beam dosimetry *Med. Phys.* **20** 1181–8

Kumar S, Deshpande D D and Nahum A E 2015a Monte-Carlo-derived insights into dose-kerma-collision kerma inter-relationships for 50keV to 25MeV photon beams in water, aluminium and copper *Phys. Med. Biol.***60** 501-519

Kumar S, Fenwick J D, Underwood T S A, Deshpande D D, Scott A J D and Nahum A E 2015b Breakdown of Bragg-Gray behaviour for low-density detectors under electronic disequilibrium conditions in small megavoltage photon fields *Phys. Med. Biol.* **60** 8187-8212

Kumar S and Nahum A E 2015 Secondary bremsstrahlung and the energy-conservation aspects of Kerma in photon-irradiated media *Phys. Med. Biol.* **61** 1389-1402

Lagerwaard F J, Haasbeek C J, Smit E F, *et al* 2008 Outcomes of risk-adapted fractionated stereotactic radiotherapy for Stage I non-small-cell lung cancer *Int. J. Radiat. Oncol. Biol. Phys.* **70** 685 – 692

La Russa D J and Rogers D W O 2006 An EGSnrc investigation of the P_{TP} correction factor for ion chambers in kilovoltage x-rays *Med. Phys.* **33** 4590–4599

La Russa D J and Rogers D W O 2008 Accuracy of EGSnrc calculations of the response of various ion chambers to ^{60}Co beams *Med. Phys.* **35** 5629–5640

La Russa D J and Rogers D W O 2009 Accuracy of Spencer-Attix cavity theory and calculations of fluence correction factors for the air kerma formalism, *Med. Phys.* **36** 4173-83

References

Lax I, Blomgren H, Näslund I, Svanströms R, 1994 Stereotactic radiotherapy of malignancies in the abdomen. Methodological aspects *Acta. Oncol.* **33** 677-83

Lee T F, Chao P J, Ting H M, Lo S H, Wang Y W, Tuan C C, Fang F M, Su T J 2011 Comparative analysis of SmartArc-based dual arc volumetric-modulated arc radiotherapy (VMAT) versus intensity-modulated radiotherapy (IMRT) for nasopharyngeal carcinoma *J. Appl. Clin. Med. Phys.* **12** 158-174

Li X A, Soubra M, Szanto J and Gerig L H 1995 Lateral electron equilibrium and electron contamination in measurements of head-scatter factors using miniphantoms and brass caps Med. Phys. **22** 1167-1170

Loevinger R 1981 A formalism for calculation of absorbed dose to a medium from photon and electron beams *Med. Phys.* **8** 1-12

Looe H K, Stelljes T S, Foschepoth S, Harder D, Willborn K and Poppe B 2013 The dose response functions of ionization chambers in photon dosimetry—Gaussian or non-Gaussian? *Z. Med. Phys.* **23** 129–43

Loo B W, Chang J Y, Dawson L A *et al*, 2011 Stereotactic ablative radiotherapy: what's in a name? *Pract. Radiat. Oncol.* **1** 38-39

Low D A, Moran J M, Dempsey J F, Dong L, and Oldham M 2011 Dosimetry tools and techniques for IMRT *Med. Phys.* **38** 1313-1338

Mackie T R, Bielajew A F, Rogers D W O, and Battista J J 1988 Generation of photon energy deposition kernals using the EGS Monte Carlo code *Phys. Med. Biol.* **33** 1-20

Mackie T R 1990 Applications of the Monte Carlo Method in Radiotherapy *The Dosimetry of Ionizing Radiation* vol 3 ed K R Kase, B E Bjärngard and F H Attix (New York: Academic) pp 541–620

Mackie T R, Holmes T, Swerdloff S, Reckwerdt P, Deasy J O, Yang J, Paliwal B and Kinsella T 1993 Tomotherapy: A new concept for the delivery of dynamic conformal radiotherapy *Med. Phys.* **20** 1709-1719

Mackie T R, Balog J, Ruchala K *et al* 1999 Tomotherapy *Semin. Radiat. Oncol.* **9** 108-117

Mackie T R 2006 History of Tomotherapy *Phys. Med. Biol.* **51** R427-R453

Ma C-M and Nahum A E 1991 Bragg-Gray theory and ion chamber dosimetry for photon beams *Phys. Med. Biol.* **36** 413-28

McEwen M R 2010 Measurement of ionization chamber absorbed dose k_Q factors in megavoltage photon beams *Med. Phys.* **37** 2179-2193

Mainegra-Hing E, Kawrakow I, and Rogers D W O 2003 Calculations for plane-parallel ion chambers in ^{60}Co beams using the EGSnrc Monte Carlo code *Med. Phys.* **30** 179–189

Malamut C, Rogers D W O and Bielajew A F 1991 Calculation of water/air stopping-power ratios using EGS4 with explicit treatment of electron-positron differences *Med. Phys.* **18** 1222–1228

Marsolat F, Tromson D, Tranchant N, Pomorski M *et al* 2013a A new single crystal diamond dosimeter for small beam: comparison with different commercial active detectors *Phys. Med. Biol.* **58** 7647-7660

Marsolat F *et al* 2013b Diamond dosimeter for small beam stereotactic radiotherapy *Diamond Relat. Mater.* **33** 63–70

Mayles P and Thwaites D 2007 Rationale and management of the quality system *Handbook of Radiotherapy Physics: Theory and Practice* ed P Mayles, A E Nahum and J C Rosenwald (London: Taylor & Francis) pp 793-807

McKerracher C and Thwaites D I 1999 Assessment of new small-field detectors against standard-field detectors for practical stereotactic beam data acquisition *Phys. Med. Biol.* **44** 2143-60

McKerracher C and Thwaites D I 2002 Verification of the dose to the isocentre in stereotactic plans *Radiother. Oncol.* **64** 97-107

McGarry R C, Papiez L, Williams M, *et al* 2005 Stereotactic body radiation therapy of early-stage nonsmall-cell lung carcinoma: phase I study. *Int. J. Radiat. Oncol. Biol. Phys.* **63** 1010 – 1015

Metcalfe P, Kron T and Hoban P 1997 *The physics of Radiotherapy X-rays from Linear Accelerators* (Madison, Wisconsin: Medical Physics publishing)

Mijnheer B, Battermann J and Wambersie A 1987 What degree of accuracy is required and can be achieved in photon and neutron therapy? *Radiother. Oncol.* **8** 237-252

Miah A B, Bhide S A, Guerrero-Urbano M T, *et al* 2012 Dose-escalated intensity-modulated radiotherapy is feasible and may improve locoregional control and laryngeal preservation in laryngo-hypopharyngeal cancers *Int. J. Radiat. Oncol. Biol. Phys.* **82** 539-47

Mobit P N, Mayles P and Nahum A E 1996 The quality dependence of LiF TLD in megavoltage photon beams: Monte Carlo simulation and experiments *Phys. Med. Biol.* **41** 387-398

Mobit P N, Nahum A E and Mayles P 1997 An EGS4 Monte Carlo examination of general cavity theory *Phys. Med. Biol.***42** 1319-1334

Mobit P N, Nahum A E and Mayles P 1997 A Monte Carlo study of the quality dependence of diamond thermoluminescent dosimeters in radiotherapy beams *Phys. Med. Biol.* **42** 1913-1927

Mobit P N, Sandison G A and Nahum A E 2000 Photon fluence perturbation correction factors for solid state detectors irradiated in kilovoltage photon beams *Phys. Med. Biol.***45** 267-277

Mohan R, Chui C and Lidofsky L 1985 Energy and angular distribution of photons from medical linear accelerators *Med. Phys.* **12** 592-597

Morales J E, Crowe S B, Hill R, Freeman N and Trapp J V 2014 Dosimetry of cone-defined stereotactic radiosurgery fields with a commercial synthetic diamond detector *Med. Phys.* **41** 111702

Muir B R and Rogers D W O 2013 Monte Carlo calculations for reference dosimetry of electron beams with the PTW Roos and NE2571 ion chambers *Med. Phys.* **40** 121722

Muir B R and Rogers D W O 2014 Monte Carlo calculations of electron beam quality conversion factors for several ion chamber types *Med. Phys.* **41** 111701

Nagata Y, Takayama K, Matsuo Y, *et al* Clinical outcomes of a Phase I/II study of 48 Gy of stereotactic body radiotherapy in 4 fractions for primary lung cancer using a stereotactic body frame 2005 *Int. J. Radiat. Oncol. Biol. Phys.* **63** 1427 – 1431

Nahum A E 1978 Water/air mass stopping power ratios for megavoltage photon and electron beams *Phys. Med. Biol.* **23** 24-38

Nahum A E 1996 Perturbation effects in dosimetry: Part I. Kilovoltage x-rays and electrons *Phys. Med. Biol.* **41** 1531–1580

Nahum A E 2007a Interactions of charged particles with matter *Handbook of Radiotherapy Physics: Theory and Practice* ed P Mayles, A E Nahum and J C Rosenwald (London: Taylor & Francis) pp 35-55

Nahum A E 2007b Principles and basic concepts in radiation dosimetry *Handbook of Radiotherapy Physics: Theory and Practice* ed P Mayles, A E Nahum and J C Rosenwald (London: Taylor & Francis) pp 89-115

Nahum A E 2009, Cavity Theory, stopping-power ratios, correction Factors *AAPM 2009 Summer School Proc. Clinical Dosimetry Measurements in Radiotherapy* ed D W O Rogers and J E Cygler (Madison, WI: Medical Physics Publishing, Madison) pp 91-136

Nahum A E, Williams T, Panettieri V, A critical examination of Spencer-Attix cavity theory, CN-182-219, Poster at International Symposium on Standards, Applications and Quality Assurance in Medical Radiation Dosimetry (IDOS), IAEA, 9-12 November 2010, Vienna, Austria

Nelson W R, Hirayama H and Rogers D W O 1985 The EGS4 code system *SLAC Report 265* (Stanford, CA: Stanford Linear Accelerator Institute (available at http://www.slac.stanford.edu/pubs/slacreports/slac-r-265.html)

Nilsson B and Brahme A 1983 Relation between kerma and absorbed dose in photons beams *Acta Radiol. Oncology* **22** 77-85

Nutting C, Dearnaley D P, and Webb S 2000 Intensity modulated radiation therapy:a clinical review *Br. J. Radiol.* **73** 459-69

Nutting C M, Morden J P, Harrington K J, *et al* 2011 Parotid-sparing intensity modulated versus conventional radiotherapy in head and neck cancer (PARSPORT): a phase 3 multicentre randomised controlled trial. *Lancet Oncol.* **12** 127 - 36

Otto K 2008 Volumetric modulated arc therapy: IMRT in a single gantry arc *Med. Phys.* **35** 310-7

Palma D, Vollans E, James K, Nakano S, Moiseenko V, Shaffer R, McKenzie M, Morris J, Otto K 2008 Volumetric modulated arc therapy for delivery of prostate radiotherapy: comparison with intensity-modulated radiotherapy and three-dimensional conformal radiotherapy *Int. J. Radiat. Oncol. Biol. Phys.* **72** 996-1001

Papaconstadopoulos P, Tessier F and Seuntjens J 2014 On the correction, perturbation and modification of small field detectors in relative dosimetry *Phys. Med. Biol.***59** 5937-5952

Pappas E, Maris TG, Zacharopoulou F, Papadakis A, Manolopoulos S, Green S, and Wojnecki C 2008 Small SRS photon field profile dosimetry performed using a PinPoint air ion chamber, a diamond detector, a novel silicon-diode array (DOSI), and polymer gel dosimetry: analysis and intercomparison *Med. Phys.* **35** 4640-4648

Pardo-Montero J and Fenwick J D 2009 An approach to multiobjective optimization of rotational therapy *Med. Phys.* **36** 3292-303

Paskalev K A, Seuntjens J P, Patrocinio H J and Podgorsak E B 2003 Physical aspects of dynamic stereotactic radiosurgey with very small photon beams (1.5 and 3 mm in diameter) *Med. Phys.***30** 118-118

Penagaricano J A, Papanikolaou N, and Yan Y 2005 Feasibility of craniospinal axis radiation with the Hi-Art tomotherapy system *Radiother. Oncol.* **76** 72-78

Podgorsak E B 2005 *Radiation Oncology Physics: A Handbook for Teachers and Students* (Vienna: International Atomic Energy Agency)

Ramsey C R, Langen K M, and Kupelian P A 2006 A technique for adaptive image-guided helical tomotherapy for lung cancer *Int. J. Radiat. Oncol. Biol. Phys.* **64** 1237-1244

Roesch W C 1958 Dose for non-electronic equilibrium conditions *Radiat. Res.* **9** 399-410

Rogers D W O 1984 Low energy electron transport with EGS *Nucl. Instrum. Methods Phys. Res.* A **227** 537-548

Rogers D W O and Bielajew A F 1985 Calculated buildup curves for photons with energies up to ^{60}Co *Med. Phys.* **12** 738-744

Rogers D W O, Ewart G M, Bielajew A F and van Dyk G 1988 Calculation of electron contamination in a ^{60}Co therapy beam *Proc. IAEA Int. Symp. on Dosimetry in Radiotherapy (Vienna, Austria)*

Rogers D W O and Bielajew A F 1990 Monte Carlo techniques of electron and photon transport for radiation dosimetry *The Dosimetry of Ionizing Radiation* vol 3 ed K R Kase, B E Bjärngard and F H Attix (New York: Academic) pp 427–539

Rogers D W, Faddegon B, Ding G X, Ma C M, Wei J and Mackie T 1995 BEAM: A Monte Carlo code to simulate radiotherapy treatment units *Med. Phys.***22** 503–524

Rogers D W O and Kawrakow I 2003 Monte Carlo calculated correction factors for primary standards of air-kerma *Med. Phys.* **30** 521–543

Rogers D W O 2006 Fifty years of Monte Carlo simulations for medical physics *Phys. Med. Biol.* **51** R287-R301

Rogers D W O, Walters B and Kawrakow I 2011a BEAMnrc users manual *Technical Report* PIRS 509 rev L (Ottawa: National Research Council of Canada)

Rogers D W O, Kawrakow I, Seuntjens J P, Walters B R B and Mainegra-Hing E 2011b *NRCC Report No.* PIRS-*702 (rev C): NRC user codes for EGSnrc* (Ottawa: National Research Council of Canada)

Salvat F 2014 *PENELOPE, a code system for Monte Carlo simulation of electron and photon transport* (Issy-les-Moulineaux: OECD Nuclear Energy Agency)

Sánchez-Doblado F, Andreo P, Capote R, Leal A, Perucha M, Arráns R, Núñez L, Mainegra E, Lagares J I and Carrasco E 2003 Ionization chamber dosimetry of small photon fields: a Monte Carlo study on stopping-power ratios for radiosurgery and IMRT beams *Phys.Med. Biol.* **48** 2081-99

Sánchez-Doblado F, Hartmann G H, Pena J, Rosello J V, Rusiello G and Gonzalez-Castao D M 2007 A new method for output factor determination in MLC shaped narrow beams *Phys. Medica* **23** 58-66

Saracci R and Wild C P 2015 International Agency for Research on Cancer: the first 50 years, 1965–2015, ISBN 978-92-832-0441-1 (http://www.iarc.fr/en/publications/books/iarc50)

Sander T and Nutbrown R F 2006 The NPL air kerma primary standard TH100C for high dose rate ^{192}Ir brachytherapy sources *NPL Report* DQL-RD 004 NPL, Teddington (http://publications.npl.co.uk)

Sauer O and Wilbert J 2007 Measurement of output factors for small photon beams *Med. Phys*. **34** 1983-8

Scott A J D, Nahum A E and Fenwick J D 2008 Using a Monte Carlo model to predict dosimetric properties of small radiation fields *Med. Phys.* **35** 4671-4684

Scott A J D, Nahum A E and Fenwick J D 2009 Monte Carlo modeling of small photon fields: quantifying the impact of focal spot size on source occlusion and output factors, and exploring miniphantom design for small-field measurements *Med. Phys.***36** 3132-3144

Scott A J D 2009a Monte Carlo modelling of small field dosimetry: non-ideal detectors, electronic disequilibrium and source occlusion *PhD Thesis* University of Liverpool

Scott A J D, Kumar S, Nahum A E and Fenwick J D 2012 Characterizing the influence of detector density on dosimeter response in non-equilibrium small photon fields *Phys. Med. Biol.* **57** 4461-4476

Seco J and Verhaegen F 2013 *Monte Carlo Techniques in Radiation Therapy* (CRC Press, Taylor & Francis Group, ISBN: 9781466507920)

Sempau J and Andreo P 2006 Configuration of the electron transport algorithm of PENELOPE to simulate ion chambers *Phys. Med. Biol.* **51** 3533-3548

Seuntjens J, Kawrakow I, Borg J, Hobeila F and Rogers D W O 2002 Calculated and measured air-kerma response of ionization chambers in low and medium energy photon beams, in *Recent Developments in Accurate Radiation Dosimetry: Proc. Int. Workshop* ed J Seuntjens and P N Mobit (Madison, WI: Medical Physics Publishing) pp 69-84

Shepard D M, Olivera G H, Reckwerdt P J *et al* 2000 Iterative approaches to dose optimization in tomotherapy *Phys. Med. Biol.* **45** 69-90

Smyth V G 1986 Interface effects in the Monte Carlo simulation of electron tracks *Med. Phys.* **13** 196-200

Soisson E T, Tome W A and Richards G M 2006 Comparison of linac based fractioned stereotactic radiotherapy and tomotherapy treatment plans for skull-base tumors *Radiother. Oncol.* **78** 313-321

Sorcini B B and Brahme A 1994 An accurate energy-range relationship for high-energy electron beams in arbitrary materials *Phys. Med. Biol.* **39** 795–811

Spencer L V and Attix F H 1955 A theory of cavity ionization *Radiat. Res.* **3** 239-254

Staffurth J, Radiotherapy Development Board 2010 A review of the clinical evidence for intensity-modulated radiotherapy *Clin. Oncol.* (R Coll Radiol) 22 643-57

Sterzing F, Schubert K and Sroka-Perez G 2008 Evaluating target coverage and normal tissue sparing in the adjuvant radiotherapy of malignant pleural mesothelioma: Helical tomotherapy compared with step-and-shoot IMRT *Radiother. Oncol.* **86** 251-257

Sze H C, Lee M C, Hung W M, Yau T K, Lee A W 2012 RapidArc radiotherapy planning for prostate cancer: single-arc and double-arc techniques vs. intensity-modulated radiotherapy *Med. Dosim.* **37** 87-91

Tabata T and Andreo P 1998 Semiempirical formulas for the detour factor of 1- to 50- MeV electrons in condensed materials *Radiat. Phys. Chem.* **53** 353-360

Thames H D, Rozell M E, Tucker S L, Ang K K, Fisher D R and Travis E L 1986 Direct analysis of quantal radiation response data *Int. J. Radiat. Biol.***49** 999-1009

Thwaites D 2013 Accuracy required and achievable in radiotherapy dosimetry: have modern technology and techniques changed our views? 7th International conference on 3D radiation dosimetry *J Phys Conf Ser* **444** 012006

Timmerman R D 2008 An overview of hypofractionation and introduction to this issue of seminars in radiation oncology *Semin. Radiat. Oncol.* **18** 215 - 222

Treuer H, Boesecke R, Schlegel W, Hartmann G H, Müller R P and Sturm V 1993 The source-density function: determination from measured lateral dose distributions and use for convolution dosimetry *Phys. Med. Biol.* **38** 1895-909

Underwood T S A, Winter H C, Hill M A and Fenwick J D 2013a Detector density and small field dosimetry: Integral versus point dose measurement schemes *Med. Phys.***40** 082102

Underwood T S A, Winter H C, Hill M A and Fenwick J D 2013b Mass-density compensation can improve the performance of a range of different detectors under non-equilibrium conditions *Phys. Med. Biol.***58** 8295-8310

Underwood T 2013c The dosimetry of small, megavoltage photon fields: correction factors, dose area products and detector designs *PhD Thesis* University of Oxford

Underwood T S A, Thompson J, Bird L, Scott A J D, Patmore P, Winter H C, Hill M A and Fenwick J D 2015 Validation of a prototype DiodeAir for small field dosimetry *Phys. Med. Biol.***60** 2939-2953

Verhaegen F 2002 Evaluation of the EGSnrc Monte Carlo code for interface dosimetry near high-Z media exposed to kilovolt and ^{60}Co photons *Phys. Med. Biol.* **47** 1691–1705

Verhaegen F 2003 Interface perturbation effects in high-energy electron beams *Phys. Med. Biol.* **48** 687–705

Vulpen M V, Field C, Raaijmakers C P, 2005 Comparing step-and-shoot IMRT with dynamic helical tomotherapy IMRT plans for head-and-neck cancer *Int. J. Radiat. Oncol. Biol. Phys.* **62** 1535- 1539

Wang L L W and Leszczynski K 2007 Estimation of the focal spot size and shape for a medical linear accelerator by Monte Carlo simulation *Med. Phys.* **34** 485–488

Williams M V, Summers E T, Drinkwater K et al 2007 Radiotherapy dose fractionation, access and waiting times in the countries of the UK in 2005 *Clin. Oncol.* **19** 273-86

Webb S 1993 The Physics of three-Dimensional Radiation Therapy: Conformal Radiotherapy, Radiosurgery and Treatment Planning (Bristol: Institute of Physics)

Webb S 2001 Intensity modulated radiation therapy 2001(Bristol: Institute of Physics)

Welsh J S, Patel R R, Ritter M a *et al* 2002 Helical Tomotherapy: An innovative technology and approach to radiation therapy *Technol. Cancer Res. Treat.* **1** 311-316

Westermark M, Arndt J, Nilsson B and Brahme A 2000 Comparative dosimetry in narrow high-energy photon beams *Phys. Med. Biol.* **45** 685-702

Wong F C, Ng A W, Lee V H, Lui C M, Yuen K K, Sze W K, Leung T W, Tung S Y 2010 Whole-field simultaneous integratedboost intensity-modulated radiotherapy for patients with nasopharyngeal carcinoma *Int. J. Radiat. Oncol. Biol. Phys.* **76** 138 - 45

Wu Q J, Yoo S, Kirkpatrick J P, Thongphiew D, Yin F F 2009 Volumetric arc intensity-modulated therapy for spine body radiotherapy: comparison with static intensity-modulated treatment *Int. J. Radiat. Oncol. Biol. Phys* **75** 1596-604

Wulff J, Heverhagen J T and Zink K 2008 Monte-Carlo-based perturbation and beam quality correction factors for thimble ionization chambers in highenergy photon beams *Phys. Med. Biol.* **53** 2823–2836

Wulff J 2010 Clinical dosimetry in photon radiotherapy - a Monte Carlo based investigation *PhD Thesis* Medzinische Physik, University of Marburg, Germany

Xia T, Li H, Sun Q, *et al* 2006 Promising clinical outcome of stereotactic body radiation therapy for patients with inoperable Stage I/II non-small-cell lung cancer *Int. J. Radiat. Oncol. Biol. Phys.* **66** 117 – 125

Yu C X 1995 Intensity-modulated arc therapy with dynamic multileaf collimation: an alternative to tomotherapy *Phys. Med. Biol.* **40** 1435-49

Yu C X, Li X A, Ma L, Chen D *et al* 2002 Clinical implementation of intensity-modulated arc therapy *Int. J. Radiat. Oncol. Biol. Phys.* **53** 453-63

Zhang P, Happersett L, Hunt M, Jackson A, Zelefsky M, Mageras G 2010 Volumetric modulated arc therapy: planning and evaluation for prostate cancer cases *Int. J. Radiat. Oncol. Biol. Phys.* **76** 1456-62

Zhang Y, Xiao J P, Zhang H Z, *et al* (2011) Stereotactic body radiation therapy favours long-term overall survival in patients with lung metastases: five-year experience of a single institution *Chin. Med. J.* **124** 4132-4137